

Yuri Vassilevski · Maxim Olshanskii  
Sergey Simakov · Andrey Kolobov  
and Alexander Danilov

# PERSONALIZED COMPUTATIONAL HEMODYNAMICS

Models, Methods, and  
Applications for Vascular Surgery  
and Antitumor Therapy



# *Personalized Computational Hemodynamics*

## *Models, Methods, and Applications for Vascular Surgery and Antitumor Therapy*

Yuri Vassilevski

Maxim Olshanskii

Sergey Simakov

Andrey Kolobov

Alexander Danilov



ACADEMIC PRESS

An imprint of Elsevier

Academic Press is an imprint of Elsevier  
125 London Wall, London EC2Y 5AS, United Kingdom  
525 B Street, Suite 1650, San Diego, CA 92101, United States  
50 Hampshire Street, 5th Floor, Cambridge, MA 02139, United States  
The Boulevard, Langford Lane, Kidlington, Oxford OX5 1GB, United Kingdom

Copyright © 2020 Elsevier Inc. All rights reserved.

No part of this publication may be reproduced or transmitted in any form or by any means, electronic or mechanical, including photocopying, recording, or any information storage and retrieval system, without permission in writing from the publisher. Details on how to seek permission, further information about the Publisher's permissions policies and our arrangements with organizations such as the Copyright Clearance Center and the Copyright Licensing Agency, can be found at our website: [www.elsevier.com/permissions](http://www.elsevier.com/permissions).

This book and the individual contributions contained in it are protected under copyright by the Publisher (other than as may be noted herein).

#### Notices

Knowledge and best practice in this field are constantly changing. As new research and experience broaden our understanding, changes in research methods, professional practices, or medical treatment may become necessary.

Practitioners and researchers must always rely on their own experience and knowledge in evaluating and using any information, methods, compounds, or experiments described herein. In using such information or methods they should be mindful of their own safety and the safety of others, including parties for whom they have a professional responsibility.

To the fullest extent of the law, neither the Publisher nor the authors, contributors, or editors, assume any liability for any injury and/or damage to persons or property as a matter of products liability, negligence or otherwise, or from any use or operation of any methods, products, instructions, or ideas contained in the material herein.

#### Library of Congress Cataloging-in-Publication Data

A catalog record for this book is available from the Library of Congress

#### British Library Cataloguing-in-Publication Data

A catalogue record for this book is available from the British Library

ISBN: 978-0-12-815653-7

For information on all Academic Press publications visit our website at <https://www.elsevier.com/books-and-journals>

*Publisher:* Mara Conner

*Acquisitions Editor:* Chris Katsaropoulos

*Editorial Project Manager:* Joshua Mearns

*Production Project Manager:* R. Vijay Bharath

*Cover Designer:* Christian J. Bilbow

Typeset by TNQ Technologies



# Introduction

Cardiovascular system functionality and disease is a core area of medical research due to its impact on the health and wellness of society. Because of its complexity, the understanding and predictive modeling of cardiovascular phenomena requires joint efforts of physicians, engineers, mathematicians, and scientists working in other fields. As a result, over the past few decades, the area became truly interdisciplinary. This book focuses on the mathematical and computational modeling of the blood flows in the heart, arteries, and microcirculatory networks and interactions of blood flow with the surrounding elastic tissues. An emphasis is made on personalizing the models to a specific patient, since the factors to be accounted by the models vary dramatically depending on the individual physiology and health status. Based on the collaboration with medical doctors from the Institute of Personalized Medicine at Sechenov University, a significant part of the book addresses the application of the mathematical and numerical methods to the predictive treatment of cardiovascular pathologies and the optimization of antitumor therapy.

There exists a huge body of literature on the mathematical and computational modeling of cardiovascular system, which includes several recent monographs [1–6]. The bibliography section of this book lists hundreds of references, still a small subset of the existing literature. Distinct features of this book are (1) a concise but rigorous coverage of fundamental principles and equations of mathematical hemodynamics with a smooth passage to concrete applications in vascular surgery and oncology; (2) a focus on the patient-specific modeling; and (3) an explanation of numerical algorithms in sufficient detail to have the complete modeling cycle presented in one place. The thrust of the book is to provide in one place all of mathematical models, a patient-specific tuning up of the models, and examples of practical applications. Therefore, applied mathematicians, biomedical engineers, and medical doctors will find this book useful for research, diagnostics, and therapeutics.

The book consists of 10 chapters. Chapter 2 gives basic knowledge about human cardiovascular system. The structure of the system and its main parts, the heart, and the vessels network are introduced with necessary details. We discuss the main physical and chemical characteristics of the blood, which affect its circulation. Electrical activity of the

heart, other major phenomena, and conditions of normal functioning are reviewed before the chapter proceeds to the discussion of some pathological conditions, which are further addressed in the modeling and computational sections of the book. Mathematical descriptions of the cardiovascular system inevitably deal with generic shapes and complex three-dimensional geometries. Acquiring the geometrical information from clinical data such as medical images is a part of the modeling process. Chapter 3 introduces acquisition techniques, methods to represent the image data sets and basic operations with images. Further we go into details of medical image segmentation, which is applied to extract specific information about particular organs or their parts such as the heart cavities and myocardium or individual blood vessels. Covered approaches include a new technique for the heart ventricles segmentation based on dynamic contrast-enhanced CT images and automatic vessel segmentation techniques. We also include a section that explains a mesh generation technique for the recovered geometries. These meshes are used later in the book to solve numerically the systems of partial differential equations governing the deformation of elastic tissues and the dynamics of blood flow. Mathematical models describing these phenomena are introduced in Chapter 4. The model of blood flow dynamics in the heart and vessels includes the Navier–Stokes equations posed in time-dependent domains. These equations as well as equations governing the motion of deformable elastic medium are derived from basic conservation laws. We next introduce the fluid–structure interaction problem that describes the coupled dynamics of the blood flow and elastic walls of the vessels. For each of the models, the chapter discusses basic mathematical properties required for understanding their performance in cardiovascular applications. Discretization techniques and algorithms to solve these models numerically are the subject of Chapter 5. Besides providing details of the computational techniques and examples of generic and patient-specific simulations, the chapter includes all necessary background information about the finite element method for fluids and elasticity as well as a concise review of the numerical linear algebra algorithms used to solve systems of discretized equations.

Real-time patient-specific simulations are often based on models of reduced complexity. If only basic (averaged) blood flow characteristics are required, then a common approach is to apply spatial reduction techniques. Chapter 6 introduces, classifies, and compares so-called lumped parameter or 0D models of the cardiovascular system. This is the most simplified but still useful modeling approach, where the region of interest (whole organism or its local part) is virtually represented by a set of interconnected compartments. The chapter goes into details of two most popular lumped parameter approaches that explore electrical analogies and mechanical modeling. Numerical integration procedure for finding approximate solutions to these models is considered. Furthermore, the chapter discusses

---

how to make such reduced models to account for certain cardiovascular pathologies. Chapter 7 extends our discussion of reduced models to the simulation of blood flow in large networks of vessels. In such setting, vessels are represented by edges connecting junction nodes and altogether forming a graph. Spatial averaging of the full fluid–structure interaction model leads to a system of 1D hyperbolic equations for averaged blood flow characteristics, posed on the graph. The exposition of the chapter includes the derivation of the system with boundary and junction conditions. Through accounting for all necessary assumptions, we emphasize certain limitations of 1D reduced flow models and consider the numerical procedure to solve the system of ordinary differential equations on the graph. We then proceed with the geometric multiscale modeling, where models of varying spatial dimensions are coupled together for the purpose of the better *local* resolution of the blood flow. Two last sections of the chapter are devoted to the discussion of how different physiological conditions may be incorporated in such reduced models. This includes different mechanical properties of the vessel’s walls, valves, nonhomogenous surrounding tissues, external forces depending on body position and physical load, and also a number of common pathological conditions.

Chapter 8 discusses mathematical models of blood circulation and nutrition transport in normal and angiogenic capillary networks. The development of new microvessels, i.e., angiogenesis, is a vital process for wound healing, embryonic development and growth of muscle or adipose tissue. It also plays a fundamental role in the growth of a malignant tumor, which is accompanied by intense reorganization of a microcirculatory network. The structure of microcirculatory networks is complex with extremely high density of microvessels, thus requiring special models for its description. The chapter starts with reconstruction algorithms of the microcirculatory network structure and continues with microcirculatory flow models. Since it is not feasible to resolve flow details in individual capillary vessels, the models operate with statistical characteristics of the blood flow. The remainder of the chapter is devoted to coupling of microcirculation and tumor growth models.

Chapter 9 addresses several clinical applications of regional patient-specific hemodynamic models. The applications include stenting of leg arteries, coronary arteries, and cerebral arteries. We introduce the notion of fractional flow reserve, an important characteristic for the evaluation of stenosed coronary arteries, and discuss its use in the predictive patient-specific numerical modeling. The book proceeds with applications of cardiovascular models to optimize protocols of antitumor therapy in Chapter 10. In this chapter, the microcirculatory and tumor growth models are coupled with the models of nutrition supply and drug administration. The cumulative model is then applied to predict efficiency and to optimize protocols for the combined antitumor chemo- and antiangiogenic therapy.

## **Acknowledgments**

This book would not be possible without dedications of many colleagues and collaborators. We wish to thank Philip Kopylov, Darya Gognieva, Alexandra Bykova, and Maria Serova for their immense help with clinical data. We owe to our colleagues Tatiana Dobroserdova, Alexander Lozovskiy, Nina Gorodnova, Roman Pryamynosov, Timur Gamilov, and Maxim Kuznetsov for their input to numerical results included in this book. Victoria Salamatova helped us with Section 4.3. We highly appreciate her contribution. We are grateful to Philip Kopylov and Maria Serova for posing the problems addressed in Sections 7.6.3 and 9.3–9.5 and collaboration on these subjects. We also grateful to Dmitry Burenchev for illuminating discussions on medical image processing and to our friends and colleagues Fuyou Liang and Jordi Alastruey for many vigorous discussions about cardiovascular simulation. We are in a great dept to Yuri Kuznetsov, Georgy Kobelkov, Alexander Kholodov, and Andrey Polezhaev, who introduced us to the world of mathematical modeling years ago. A large part of the work presented here was done within the research group in simulation of blood flow and vascular pathologies at the Institute of Numerical Mathematics of the Russian Academy of Sciences. We acknowledge the support of the group by the Russian Science Foundation through the project 14-31-00024 “Multiscale modeling of hemodynamics for patient-specific medical treatments in cardiology, vascular neurology, and oncology”. The Institute of Personalized Medicine at Sechenov University provided a venue for interdisciplinary collaboration. We thank the University for administrative support.

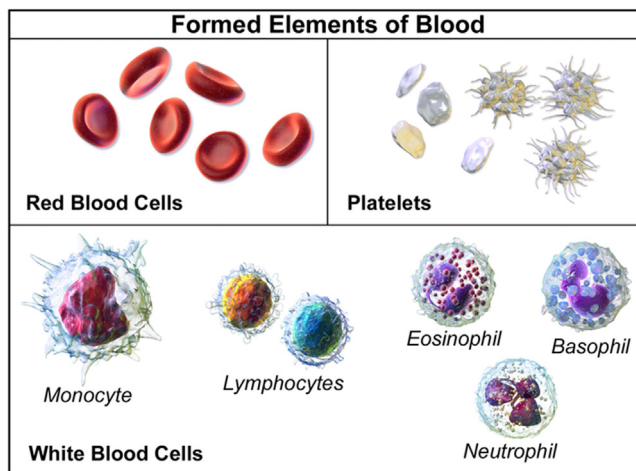
# ***Basic facts about human cardiovascular system***

## ***2.1 Introduction***

The cardiovascular system consists of three main parts: the heart, the vessels, and the blood. These components work together for maintaining living conditions of the body. The heart periodically contracts and pumps the blood through the network of vessels. The vascular network is divided into systemic and pulmonary loops. These two circuits are connected into one closed loop by the heart through its chambers. Each loop has arterial and venous parts. Arterial parts start from the heart ventricles and ramify in the organs and tissues throughout the whole organism. They end up with capillary network. In the venous parts, the capillaries merge into venules, and further into veins and, finally, converge to the vena cava and pulmonary vein, which are joined with the heart auricles (atria).

The following physiological phenomena drive the blood flow through the body: the blood ejection from the heart due to the contraction of its chambers, the peristaltic pumping of blood in the microcirculation, the skeletal–muscle pump, the respiratory pump, and the heart sucking effect. In short, the blood is ejected from the ventricles, and then it goes subsequently through the arterial and venous parts and returns to the heart auricles. In the systemic loop, the blood flows through the organs and tissues. It delivers oxygen, glucose, and other nutrients. In the pulmonary loop, the blood flows through the lungs. It delivers carbon dioxide to the alveoli and gets a new portion of oxygen.

The fraction of blood in an average adult human organism is approximately 6%–8% of the body weight. The two principal types of the components of the blood are plasma and cells suspended in the plasma (formed elements). Plasma is a water solution of low-molecular organic and inorganic substances. Formed elements are classified as red blood cells (RBCs or erythrocytes), white blood cells (WBCs or leukocytes), and platelets (thrombocytes) (see Fig. 2.1). The essential hemodynamical property of the blood is its viscosity. The viscosity strongly depends on the volume fraction of the RBCs (hematocrit), which is about 40%–45% in the normal case.

**Figure 2.1**

The formed elements of the blood. Source: Blausen.com staff (2014). Medical gallery of Blausen Medical 2014. *WikiJournal of Medicine* 1 (2). <http://doi.org/10.15347/wjm/2014.010>.

The primary functions of the blood are nutrients supply (oxygen, glucose, acid fats, amino fats, etc.); metabolic wastes transport to the lungs and kidneys (carbon dioxide, sulfates, phosphates, etc.); other transport (hydrogen ions, hormones, immunoglobulins, drugs, etc.); temperature, and *pH* regulation. Some blood components participate in inflammatory processes: WBCs fight infections, and platelets initiate blood coagulation and clot formation. Almost all oxygen and carbon dioxide are transferred by blood in the bounded state with the RBCs. All other substances are dissolved in plasma.

## **2.2 Heart as a pump**

The heart pumping is the main factor, which enables the blood flow through the whole vascular network. Electric, mechanical, and hydrodynamic mechanisms are responsible for the successful heart functioning. First, the sinoatrial node produces the electrical impulse (action potential). Next, the impulse is transmitted by the electrical conduction system of the heart, which includes bundle of His, bundle branches, fascial branches, and Purkinje fibers (see Fig. 2.3). Further, auricles contract during His bundle and bundle branches excitation, while ventricles contract during Purkinje fibers excitation after a short delay followed by auricles contraction. Finally, the blood is ejected to the aorta and pulmonary artery (see Fig. 2.2, 2.3). This is a complex hydrodynamical process, which is determined by the anatomical features of the ventricles: unidirectional valves, complex shape, trabecules, and complex movement of the ventricular walls. The myocardium perfusion and nutrients supply is performed by a portion of blood, which is directed from the aortic root to the coronary circulation.

## 2.2.1 Anatomy

The principal scheme of the heart is shown in Fig. 2.2. For our modeling purposes, we can think of the heart as a set of two successive pumps, which are also called left and right heart. The pumps are combined together by vascular network. Each pump consists of two successive chambers: auricle and ventricle. The ventricles are larger and thicker than atria and can produce larger stress. The auricles are separated from the ventricles by the unidirectional atrioventricular valves. The left ventricle is separated from the aorta by the unidirectional aortic valve. The right ventricle is separated from the pulmonary artery by the unidirectional pulmonary valve. Thus, the blood flow through the heart is unidirectional. The right ventricle receives the blood from the right auricle and pumps it to the pulmonary circuit. The left ventricle receives the blood from the left auricle and pumps it to the systemic circuit.

All chambers walls have the same material structure. The heart wall is divided into three layers: endocardium, myocardium, and epicardium. Endocardium is a small thin layer of endothelial cells, which is the lining inner surface of the chambers. Endocardium of the ventricles has trabecules, which are rounded or irregular muscular columns. The trabecules protrude from the inner surface of the right and left ventricle of the heart and prevent suction. Myocardium is composed of cardiac muscle fibers (cardiomyocytes), which

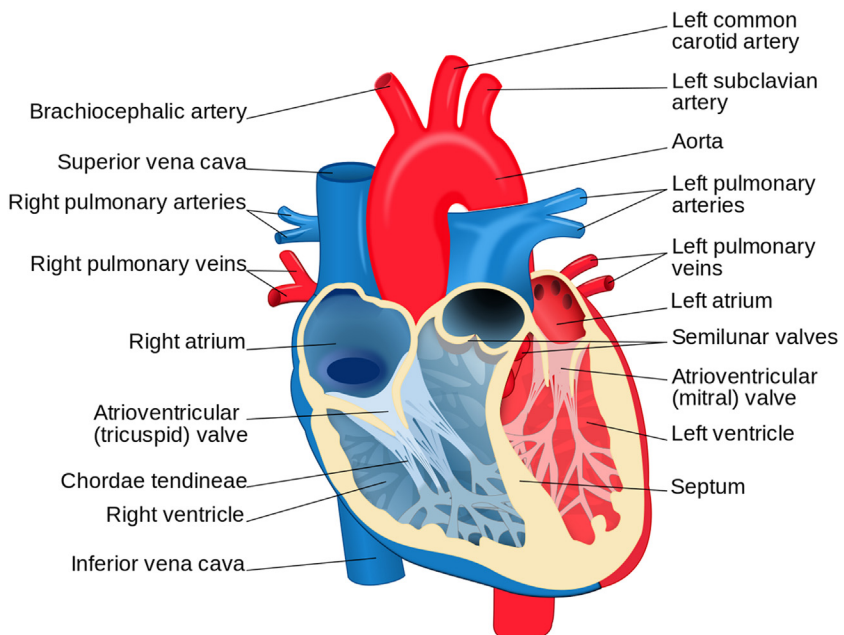


**Figure 2.2**

The heart. Source: ZooFari, available at [https://commons.wikimedia.org/wiki/File:Heart\\_diagram-en.svg](https://commons.wikimedia.org/wiki/File:Heart_diagram-en.svg).

enable heart contractions. Cardiomyocytes are connected to each other by gap junctions. They are organized in fibers, which in turn are organized in sheets. The sheets are separated by cleavage planes. The fiber and sheet orientation varies throughout the ventricles. At any small segment of myocardium, there always exist some fibers, which respond to the stress in any direction. The structure of the atria and ventricular orientation has been recently studied by 3D diffusion tensor magnetic resonance imaging [7,8].

The outer layer of the heart is epicardium. It consists of a thin layer of connective tissue and fat. Pericardium is the thick, membranous sac, which surrounds the heart. Together with endocardium, it protects and lubricates the heart with the pericardial fluid. It helps to reduce friction between pericardial membranes.

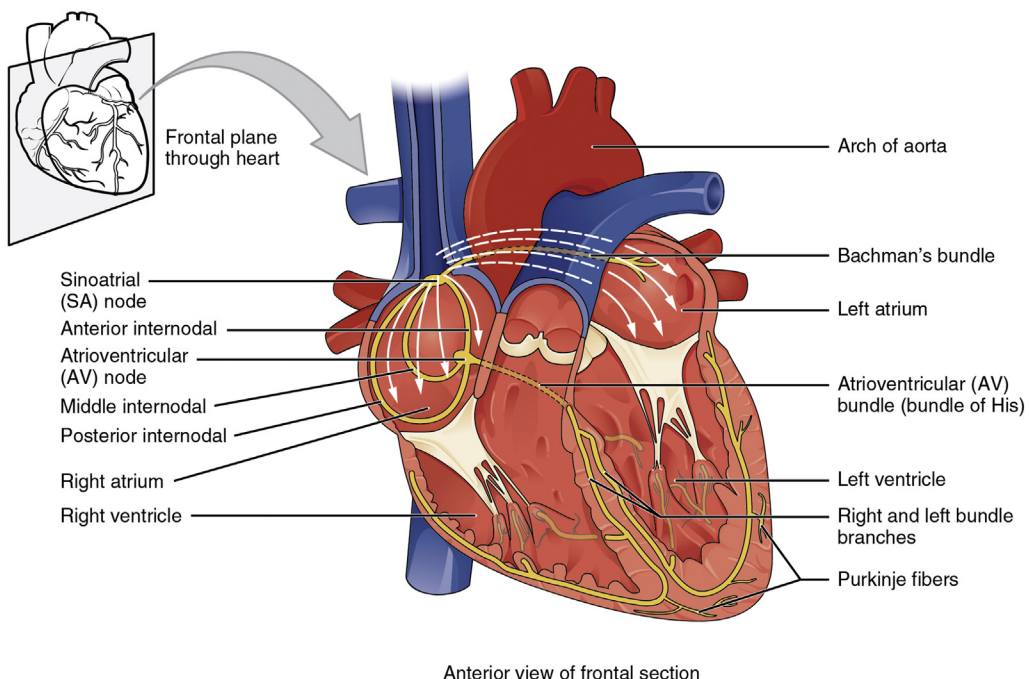
### **2.2.2 Electrical activity**

Cardiomyocytes are the muscle fibers that form the chambers walls of the heart. They are spatially organized for optimal adenosine triphosphate (ATP) and calcium delivery to sarcomeric myosin and ionic pumps during every excitation-contraction cycle. The 3D structure of the human left ventricular myocyte has been recently studied in Ref. [9].

Interactions of actin and myosin filaments are responsible for the cell contraction, which is regulated by the electrical activity of the cell through the cellular membrane permeability. There is interconnection of the membrane potential and membrane permeability to some small inorganic ions: permeability varies during the heart cycle due to the change of the potential difference across the membrane, whereas the potential difference depends on the relative permeability to the ions. This complex interplay of coupled physiological processes is often addressed by numerical simulations [10–15].

The fluid inside the heart cells contains mainly potassium ( $K^+$ ) ions together with some amount of sodium ( $Na^+$ ), chlorine ( $Cl^-$ ), and calcium ( $Ca^{2+}$ ) ions. The extracellular fluid contains mostly  $Na^+$  and  $Cl^-$  ions with some amount of  $K^+$  ions. The depolarization and repolarization of the cell membrane during an action potential is driven by the flow of current carried by  $Na^+$ ,  $Ca^{2+}$ , and  $K^+$  ions. The steep upstroke in the beginning of the action potential results from the rapid opening of  $Na^+$  channels following a stimulus and the consequent inward flow of  $Na^+$  ions, which depolarizes the membrane. It is followed by a smaller inward current of  $Ca^{2+}$  ions. It balances an outward current of  $K^+$  ions and maintains the plateau of the action potential. Finally, the outward current carried by  $K^+$  ions becomes significant, which causes repolarization of the membrane and returns it to the initial resting state.

The principal scheme of the conducting system of the heart is shown in Fig. 2.3. The sinoatrial node (SA node) spontaneously generates electrical impulse (action potential), which initiates myocardium excitation and, thus, cardiac cycle. The rate of the impulses is



Anterior view of frontal section

**Figure 2.3**

Conducting system of the heart. Source: OpenStax, Anatomy and Physiology. OpenStax CNX. Available at <http://cnx.org/content/col11496/>.

controlled by the nerves. The SA node is located in the myocardial wall near the junction of sinus venarum and right atrium. Electrical signals arising in the SA node causes auricles contraction. Then, they travel to the atrioventricular node (AV node), which is located between the auricles and the ventricles. The action potential is conducted through the left and right His bundles to the appropriate Purkinje fibers on each side of the ventricles, which causes ventricular contractions [16].

An action potential is conducted along the muscle fibers at a speed that depends on the diameter of the fiber, its branching, and electric current available to depolarize the next section of the fiber represented by a cardiomyocyte. The fiber and fiber sheet orientation also cause substantial effect to the propagation of the action potential. It propagates two to three times faster along the fibers, than across it within the sheet. The speed of action potential propagation orthogonal to sheets is two to three times slower than orthogonal to fibers within the sheets.

Electrical impulses from the SA node propagate through all tissues in the body and attenuate with the distance from the SA node. The electrical activity of the heart can be recorded by the electrodes placed on the surface of the thorax. This process is called electrocardiography (ECG). Computational simulations of ECG help to reveal the features

of impulse propagation from the SA node and provide new insights to the diagnostic of arrhythmia and other heart diseases [17,18].

### ***2.2.3 Myocardial perfusion, ischemia, and infarction***

The blood supply of the myocardium is maintained by the coronary arteries, which are mostly located in epicardium. Coronary blood flow is well autoregulated. It remains stable in a wide range of perfusion pressure. Therefore, it maintains sufficient myocardium supply with nutrients.

Ischemia is insufficient tissue supply with oxygen and other nutrients. Infarction is the tissue necrosis due to the prolonged ischemia. Myocardial ischemia is characterized by an unbalanced myocardial oxygen supply and demand. It leads to the loss of myocardial contractility, changes in the membrane potential, ventricular fibrillation, and complete heart block. Irreversible damage includes ATP decrease, stop of anaerobic glycolysis,  $pH$  and lactate increase, high level of osmolality, membrane damage, cellular and mitochondrial swelling, amorphous densities in the mitochondria, etc. [19]. These changes are the reasons for cardiac dysfunction, arrhythmias, myocardial infarction, and a sudden death.

The usual mechanism for the development of acute myocardial infarction is the rupture or erosion of a vulnerable atherosclerotic coronary plaque with the subsequent totally occluding thrombus. The other possible scenarios are partial occlusion or occlusion in the presence of collateral circulation. Acute myocardial infarction is classified into six types [20].

Microvascular dysfunction in patients with hypercholesterolemia, hypertension, and diabetes mellitus may be a reason for abnormal myocardial perfusion even in the absence of epicardial coronary artery disease (CAD) [21]. Microvascular dysfunction is related to the endothelial function abnormality, which causes autoregulatory mechanisms disorder.

Typically, the overture to the obstructive CAD is a long-term process. Patients are often asymptomatic for decades. Then, the process rapidly develops in less than an hour. The ischemia duration is an important factor of its severity. Ischemia duration less than 40 min results in reversible cellular and functional alterations. Ischemia lasting for more than 40 min often leads to the progressive functional loss and irreversible damage [19]. Ischemic tissue indicates the following pathological abnormalities: loss of oxidative phosphorylation, accumulation of the toxic compounds due to anaerobic metabolism, and acidosis resulted from catabolic reaction [19].

Thus, urgent reperfusion of coronary flow must be provided for the patients with acute myocardial infarction. The invasive treatments such as stenting, angioplasty, thrombolysis,

and coronary bypass may be applied. The no-reflow phenomenon may be observed in the patients with coronary microvascular dysfunction. Therefore, both epicardial coronary flow and microvascular perfusion should be considered and restored [21].

A range of noninvasive testing tools have been developed for clinical evaluation of coronary flow and perfusion, which provide the benefits of increased comfort and less pain. They include single-photon emission computerized tomography, myocardial contrast echocardiography, positron emission tomography (PET), stress cardiovascular magnetic resonance imaging, and cardiac computed tomography. Noninvasive cardiac imaging plays an important role in the diagnosis of coronary artery disease and in the decision-making for surgical interventions [22].

## **2.3 Large vessels**

The heart supplies blood with the energy. The vessels conduct the blood through all parts of the organism. The vessels carrying blood from the heart ventricles to the microcirculation are called arteries, and the vessels carrying blood from the microcirculation to the auricles are called veins. At first glance, vessels are just elastic tubes. However, they have many additional features. Vascular wall may contain different amount of elastin fibers, collagen fibers, and muscle cells. The vascular wall may be affected by the regulatory and autoregulatory mechanisms, muscles, sphincters, and chemicals. Some vessels have a system of unidirectional valves.

### **2.3.1 Vascular network anatomy**

There are two loops, which are formed by the vessels (see Fig. 2.4). In the systemic loop the aorta starts upward from the left ventricle, and then it turns to the 180° and goes downward. Two coronary arteries are started immediately from the aortic root. They supply the heart. There are three branches coming from the aortic arch: brachiocephalic artery, left common carotid artery, and left subclavian artery. These arteries supply the head and upper extremities. The descending part of the aorta is divided into thoracic and abdominal parts. The radius of the descending aorta decreases with the distance from the heart. The thoracic aorta supplies the lung's muscles and other tissues of the thoracic region. The abdominal aorta supplies the organs and tissues of the abdominal cavity (stomach, kidneys, liver, etc.). The abdominal aorta is divided into two common iliac arteries, which supply the lower extremities.

The structure of veins is similar to that of arteries. The average radius of the arteries and veins decreases with the distance from the heart. However, the total cross section of the vessels increases with the distance from the heart. Approximately 80% of the total blood volume is located in the systemic circulation. Veins contain approximately 80% of the

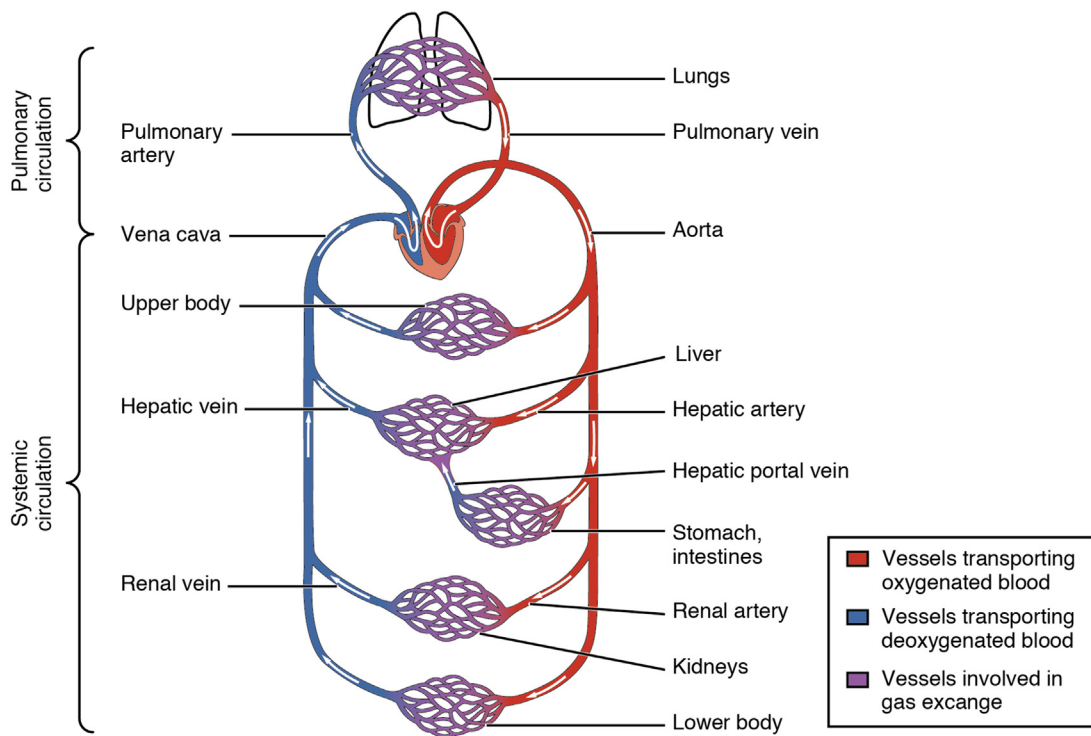


Figure 2.4

The scheme of the cardiovascular system. Source: OpenStax, Anatomy and Physiology. OpenStax CNX. Available at <http://cnx.org/content/col11496/>.

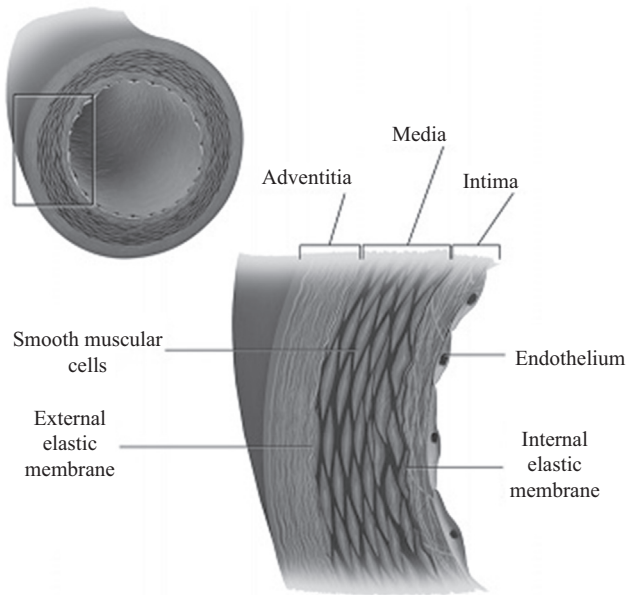
total blood volume. Systemic arteries and veins are organized into networks due to numerous anastomoses. Pulmonary arteries and veins are organized into trees.

### 2.3.2 Vascular wall structure, elasticity, viscoelasticity

The vessel walls can change their cross-sectional shape and area in response to the applied stresses, e.g., by transmural pressure. Elastic properties and thickness of the vessel depend on its proximity to the heart and on its function. The elasticity is determined by the structure and composition of the vascular wall. Regulatory mechanisms also affect vascular elasticity (see Section 2.3.3).

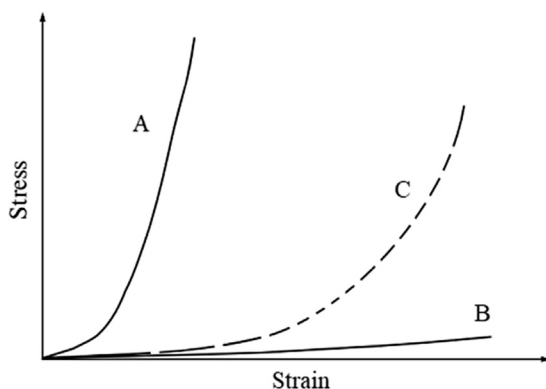
The walls of all large vessels in the human body are structurally decomposed into three layers: intima, media, and adventitia (see Fig. 2.5).

Intima and adventitia are much thinner than media. Intima is primarily composed of a layer of endothelial cells lining the vessel wall. Adventitia primarily consists of fibroblasts, fibrocytes, and bundles of collagen fibers. Medium is composed of elastic membranes, collagen fibers, and smooth muscle cells. The relative ratio of these three components in

**Figure 2.5**

Typical structure of the blood vessel. Source: Blausen.com staff (2014). Medical gallery of Blausen Medical 2014. *WikiJournal of Medicine* 1 (2). <http://doi.org/10.15347/wjm/2014.010>.

the media accounts for the elastic properties of particular vessel. Elastin fibers have a modulus of elasticity of 0.6 MPa. They can stretch up to 250% of their original length. Collagen fibers are much stiffer with a modulus of elasticity approximately 500 MPa [23]. The pressure load is distributed between the elastin and collagen. For the low pressure, the major role in the elastic response is played by elastin fibers. Contribution of collagen fibers increases with the pressure increase (Fig. 2.6).

**Figure 2.6**

Stress-strain relationship for elastin (A), collagen (B), and mixed (C) fibers.

Arteries and superficial veins are generally thicker and have more smooth muscle cells and more elastic fibers than deep veins. Arteries can be classified into elastic and muscular according to the composition of a vessel wall. Elastic arteries have a relatively large diameter and are closer to the heart (e.g., aorta or carotid artery). Generally, the number of elastic membranes decreases with the decrease of the vessel diameter. Muscular arteries (e.g., femoral artery, abdominal artery, cerebral arteries) have few elastic membranes. In veins of medium and large size, the media typically consist of two or three layers of smooth muscle cells and bundles of collagen and elastin fibers. Their external layer is the thickest one. The walls of the deep veins are thin. Primarily, they consist of collagen. The shape of the cross section of the deep veins substantially changes depending on transmural pressure. It may be circular, elliptic, dumbbell-like, or almost collapsed.

Vascular wall elasticity was studied in many clinical and laboratory researches [23–29]. The mechanical properties of blood vessels are classified as passive (accounting for elastin and collagen fibers contractions) and passive-active (accounting also for smooth muscles contractions). In the most experimental studies, passive properties are considered. Passive-active properties are related to the regulatory processes (see [Section 2.3.3](#)).

Vascular wall exhibits both instant elastic and time-dependent viscous response to the stress. The stress–strain relationship of the vascular wall material depends on the stress rate. The aortic pressure profile is not symmetrical. The steep pressure increase with high stress rate is observed during early systole, which turns to smooth decrease and lower stress rate in late systole and diastole. As a result, the load and unload stress–strain curves are different as the pressure-time profile is not symmetrical. In addition, viscous behavior is responsible for the energy dissipation. Viscoelastic properties may be estimated based on the measurements and numerical simulations [30,31].

In continuum mechanics, elastic properties of a material are characterized by the constitutive equation quantifying the nonlinear relationship between applied stress and responded strain. This relationship can be derived using various different approximations of the vessel wall material. For example, the vascular wall can be considered as complex composite, which is described by isotropic matrix reinforced by oriented sets of fibers. This approach describes nonlinear, anisotropic behavior of the material [28,122]. It is capable to account for response of the collagen fibers to high blood pressure. The other possible approach exploits microstructure of vessel walls as a basis for deriving constitutive equation for the specific vessel [505–507]. Due to significant differences in the structure of the vessel’s walls, none of the proposed approaches is universal for all types of arteries.

### 2.3.3 Arterial regulation and autoregulation

Internal physiological and pathological conditions and external environmental conditions of the body may vary in a wide range. They may cause substantial change in the blood pressure and in the tissues and organs metabolic demand. The regulatory mechanisms tend to maintain blood flow despite the changes of the arterial perfusion pressure or increase blood flow due to increased metabolic demands (e.g., working hyperemia). The blood vessels adapt to these changes by adjustment of their diameter through contraction (vasoconstriction) or relaxation (vasodilation) of the smooth muscle cells. As a result, hydraulic resistance and elasticity are changed, which, in turn, helps to control required perfusion rate, as well as nutrients and oxygen consumption. Vasoconstriction results in the decrease of the diameter and elasticity and in the increase of the hydraulic resistance. Vasodilation causes an opposite effect.

Various regulatory mechanisms of vessel networks have been studied. These mechanisms can be divided into neurogenic regulation, humoral regulation, and autoregulation.

Neurogenic regulation modulates the blood flow by the perivascular nerves activity due to autonomic nervous system signals. Humoral regulation causes both vasomotor effect through the chemical substances in the blood and the systemic effect achieved by the calcium, potassium, sodium ions, hormones, etc. The local effect is achieved by the histamine, serotonin, acetylcholine, etc. [32].

Myogenic, metabolic, tissue pressure, and tubuloglomerular feedback (TGF) hypotheses are considered as the major mechanisms of autoregulation. According to myogenic hypothesis, the diameter of arteriole is directly related to the intravascular pressure through the smooth muscle cells stimulation and response. Thus, myogenic mechanism is the vascular wall response to the normal stress exerted by the blood flow. In addition, the vascular wall diameter is inversely related to the shear stress exerted by the blood flow due to friction between the blood and the wall through the process referred to as “mechanotransduction” [33,34]. Increased shear stress results in increased NO production by the endothelial cells and subsequent relaxation of the smooth muscular cells. These two processes in balance provide stability of the integrated vascular response to the mechanical interaction of the wall with the blood flow for a wide range of pressure and flow rate values. Both processes may be of a transient or sustained nature.

According to the metabolic hypothesis, reduction in arterial inflow causes an elevation of vasodilator metabolites in the tissue and associated increase of the diameter. Decreased blood flow results in a reduced washout of metabolites such as CO<sub>2</sub>, lactic acid, and/or increased production of vasodilator substances due to stagnant hypoxia. In addition, partial pressure of oxygen in the tissues is responsible for autoregulation in organs with high oxygen consumption (e.g., heart and brain) [35].

The kidney regulation is aimed at maintaining electrolyte concentrations, osmolality, and acid–base balance of blood plasma. Kidney participates in blood pressure regulation and in the maintenance of the water volume in the whole organism. According to the TGF hypothesis, an increase in arterial pressure leads to increased glomerular filtration. In turn, the increase in glomerular filtration rate increases the solute and electrolyte concentration in the tubular fluid. The muscle tension in the afferent arterioles is adjusted proportional to the difference between the actual and target concentration. Relaxation (vasodilation) of the afferent arterioles results in increased glomerular filtration pressure and tubular fluid flow. Thus, this is a negative feedback loop process.

#### **2.3.4 Pulse wave propagation and reflection**

The heart ventricles eject the blood by discrete portions in an almost periodical manner. One part of the ejected blood goes immediately to the arterial network. Due to limited flow capacity, another part is accumulated in the aorta and large arteries and causes their elastic expansion due to the pressure, which was supplied by the heart. This portion goes to the arterial network during diastole due to the elastic contraction of the arteries. Thus, a pressure wave is generated, which travels along arterial network in forward direction (from heart to microcirculation). The secondary backward pressure waves are generated due to reflection of the forward wave from the bifurcations and microcirculation, where low-resistance conduit arteries join high-resistance arterioles. The pulse wave (PW) is the total of these forward and backward waves. Pulse wave velocity (PWV) is the velocity of the propagation of the PW peak through the arterial network.

Elasticity of the arteries substantially affects the velocity of the forward and backward waves, and, thus, it affects shape and amplitude of the PW and PWV. The decrease of arterial elasticity causes early return of the backward wave to the aortic root. It results in the pressure increase during later systole instead of diastole, which makes the blood ejection more difficult and requires more work of the heart muscle. A variety of cardiovascular diseases (CVDs) may follow the persistent late systolic pressure increase. Some factors cause arterial elasticity increase and, thus, decrease risk of CVD: exercise, vasodilator administration. Other factors cause arterial elasticity decrease and, thus, increase risk of CVD: aging, food and drink preferences, smoking, heart rate, gender, atherosclerosis, hypertension, diabetes, aortic degeneration, aneurysms, and heart failure [36].

It is important to study all these factors. For example, abdominal aortic aneurysms (AAA) are rarely detected at early stages by conventional methods. On the other hand, the

influence of AAA on PW shape is now well established. Recent physical and computational experiments allow to reveal several indicators that characterize the impact of an aneurysm on waveforms [37].

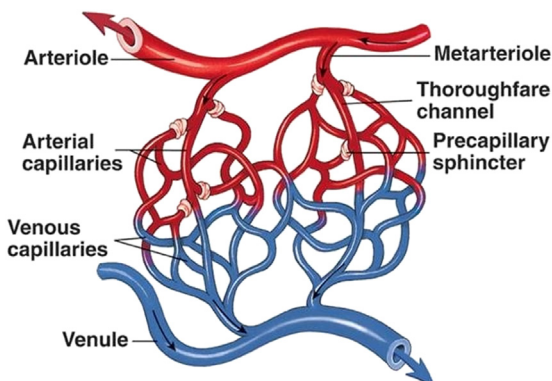
While pulse palpation is an important diagnostic tool in traditional Chinese medicine, nowadays it can be observed as solving the inverse problem of detecting the properties of (the health of) vessel walls and the heart function from the PW measurements. In modern implementation, PW shape is analyzed using 27 complex pulse images, which can be parameterized by six basic variables: frequency, rhythm, wideness, length, deepness, and qualities. Such analysis allows to differentiate a number of diseases somehow related to the change of arterial elasticity, endothelial function, and microcirculatory properties, thus causing the change in backward waves reflection and PW shape. This technique was analyzed by numerical simulation [38] and was applied for studying hypertension [39], atherosclerosis, diabetes, etc.

## **2.4 Microvasculature**

Microcirculatory network is an essential part of the cardiovascular system. It is responsible for all exchange processes in the body and for the regulation of blood flow in individual organs. The microcirculatory network is substantially different from the vascular network of large vessels. It consists of a huge number of very small vessels. The lumen of these vessels is close to the RBC size. The blood flow is substantially lower than in large vessels. Thus, the role of blood composition, its non-Newtonian behavior, and biological properties of RBC and WBC become important for the flow. The structure of the microvasculature may be modified due to normal processes (e.g., natural growth and development) and pathological conditions (e.g., tumor growth, wound healing), which affects perfusion of the tissues.

### **2.4.1 Anatomy**

Microcirculation network is the part of cardiovascular system, which directly performs its basic function of supplying cells of an organism with nutrients. It consists of arterioles, capillaries, and venules. Arterioles branch out of the smallest arteries, and after several successive bifurcations, each terminal arteriole leads to a cluster of capillaries, which then converge to venules, leading to veins (see [Fig. 2.7](#)). The structure of microcirculation network demonstrates significant variety throughout the body. It is adjusted to every specific organ where it is embedded in a way that every cell is usually within 20  $\mu\text{m}$  distance from a microvessel. Microcirculation density increases in the metabolically active tissues.

**Figure 2.7**

Schematic representation of a region of microcirculation network. Source: Tafner PFA, Chen FK, Rabello R, Correa TD, Chaves RCF, Serpa A. Recent advances in bedside microcirculation assessment in critically ill patients. *Revista Brasileira de Terapia Intensiva* (2017).

Arterioles are the microvessels with the diameter of 10–100 µm. Muscular layer predominates in their walls. Its thickness is comparable with the size of the lumen. Relative narrowness and limited amount of arterioles in organism results in the pressure drop, which is about 50%–80% of the total blood pressure drop between auricles and ventricles. Large arterioles are highly innervated with vasomotor nerves. The nerves control the diameter and the muscle tone. It allows to maintain systemic blood flow in a wide range of the blood pressure. Small arterioles contain few vasomotor nerves. They control local blood flow by hormonal stimulation. In skin and nasal mucosa, arteriovenous anastomoses exist, which directly connect arterioles with venules. They participate in the thermal regulation. Microcirculation of the mesentery includes metarterioles. Their smooth muscle cells are arranged in precapillary sphincters, which also control the blood flow.

Capillaries are the smallest vessels in the body. The size of a single capillary is less than 10 µm in diameter and less than 1 mm in length. The main substance exchange between the blood and the tissues takes place in these vessels through their walls. The function of the capillaries determines their ubiquity throughout the body and their structure. The width of their walls is about 0.5 µm, and it is simply a layer of endothelial cells, supported by special cells (pericytes) and wrapped in basement membrane. The diameter of a red blood cell is larger than the diameter of a capillary, so they move through them one by one in deformed state, which brings additional friction to the flow of blood plasma. Moreover, the capillary part in total possesses considerable resistance due to the large total cross-sectional area of all capillaries, which in total makes capillary blood flow rather slow—its velocity is usually no more than 1 mm/s. The pulsations of blood flow are already damped in arterial part of circulatory system.

Venules differ from veins primarily in their size (50–200  $\mu\text{m}$  in diameter), but not in wall structure. Small postcapillary venules lack smooth muscle cells, unlike larger venules.

Approximately 25% of the human blood is contained in venules, which walls are rather extensible. Together with veins, they serve as repository of blood. Contraction of venules and veins allows to enhance blood supply to organs when needed, e.g., during extensive exercise or stress.

### 2.4.2 Blood rheology

In continuum mechanics, all viscous fluids are classified as Newtonian and non-Newtonian. The viscosity of Newtonian fluids is independent of shear rate and shear stress. In non-Newtonian fluids, the apparent viscosity is not a constant. It can be calculated as the ratio of shear rate to shear stress, which is nonlinear. The flow of non-Newtonian fluids is different from the Newtonian one due to the internal molecular structure and interaction.

The blood flow is the major determinant of sufficient tissue perfusion. Thus, it is important to understand the factors affecting the blood flow as continuum. In different cases, blood is considered as a single-phase fluid, a two-phase fluid, suspension (fluid–solid mixture), or emulsion (fluid–fluid mixture) [40]. In any case, one part of the blood is plasma, and the other part consists of different cells. Plasma is a Newtonian fluid. The normal range of plasma viscosity is between 1.10 and 1.35 cP at 37  $^{\circ}\text{C}$ . The RBCs are substantially greater than the other blood components. Normally, RBC is a biconcave disc with typical dimensions of 6–8  $\mu\text{m}$  in diameter and 2  $\mu\text{m}$  thick. WBCs vary in size. Inactivated neutrophil is almost spherical with a diameter of 8  $\mu\text{m}$ . Platelet is a disc with a diameter of 2  $\mu\text{m}$ . These cells occupy less than 1% of the total blood volume. Hence, in microcirculation, the sizes of blood vessels are the same order or even smaller than the sizes of blood cells.

The integrated rheological properties of the blood are primary determined by the plasma viscosity, hematocrit, RBC rheology, RBC membrane elasticity, RBCs interaction (e.g., aggregation), WBC, and other cells type and state. Reviews on the physical and mathematical description of blood viscosity can be found in Refs. [41–44].

Cellular components disturb the flow streamlines and thereby increase the total blood viscosity relative to the plasma one. Thus, a larger number of cellular components in the blood cause the increase of the viscosity. For example, blood viscosity is exponentially proportional to hematocrit. Under most conditions, RBCs behave in the blood like fluid drops, which are oriented along the streamlines. Increased shear rate results in deformation and reorientation of RBCs relative to the streamlines, which also causes viscosity increase. At moderate to high shear rates, RBCs tends to align and form layers in the flow, which results in the decrease of the viscosity. Low flow conditions and the presence of fibrinogen and globulins cause RBCs aggregation in a structure similar to coin stacks (rouleaux).

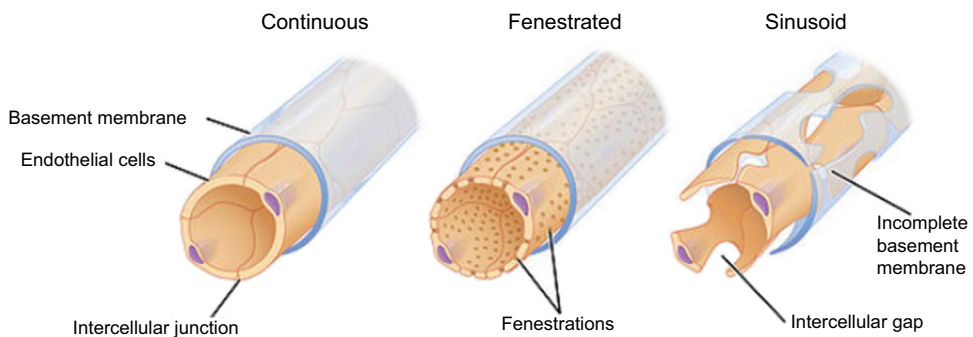
Rouleaux and its branched 3D aggregates behave like huge single particles, thereby significantly increasing viscosity. Normally, WBCs produce a negligible effect on total blood viscosity. Nevertheless, biologically activated by inflammation or by extraneous molecules, WBCs and platelets may cause substantial changes to the flow due to their extensive biochemical, morphological, and mechanical alterations. The near-zero flow or stasis conditions may result in the flow termination under nonzero shear stress (yield stress phenomenon).

One may conclude that, in normal conditions, in most parts of the arterial system, blood flow exhibits the properties of the Newtonian fluid. Non-Newtonian effects become noticeable in high and low flow conditions: in small vessels, in venous system, downstream stenoses, and in saccular aneurysms.

### **2.4.3 Transvascular transport**

The exchange of solutes and water between blood plasma and interstitial fluid takes place mainly via two physical processes: diffusion, which rate is proportional to the difference in substance concentrations, and convection, which is driven by hydrostatic and oncotic pressures. To a much lesser extent, some transport may occur due to the temporary fusion of vesicles in endothelial cells of microvessels, which are connected to both luminal and abluminal cell sides [45]. The transport of specific substance depends on their chemical properties and the structure of microvessels. Small lipid-insoluble molecules, the most important example of which is oxygen, are able to penetrate freely through the microvessel wall. A large amount of oxygen exchange happens already across the walls of arterioles [46]. The high rate of transvascular transfer leads to the situation in which concentrations of free oxygen in blood and in surrounding tissue come to equilibrium along the length of exchange. Thus, the inflow of oxygen in tissue is flow based, and the increase in blood velocity directly leads to its enhanced supply.

The transport of lipid-insoluble molecules is confined to the holes in walls of capillaries. There are three structural types of capillaries in human body (see Fig. 2.8). The most prevalent and less permeable type is continuous capillaries, which possess only small pores in their walls. The actual nature of pores is controversial; however, their main location is believed to be the gaps between junctional strands of adjacent endothelial cells, which sizes are 5–11 nm [47]. The passage of large molecules is hindered by the layer of glycocalyx, which is a net of fibrous molecules, and by the basement membrane. For practical purposes, it may be considered that continuous capillaries possess cylindrical pores of radius 4–5 nm [48]. However, the fact that the transport rate of bigger molecules is nonzero even across the walls of continuous capillaries has led to the concept of less numerous “large pores,” which nature is, however, even more unclear at this moment. Fenestrated capillaries possess additional perforations of 50–80 nm in diameter in their

**Figure 2.8**

Types of capillaries. Source: OpenStax, Anatomy and Physiology. OpenStax CNX. Available at <http://cnx.org/content/col11496/>.

endothelial lining. They are situated mainly in tissues, which functions involve active fluid exchange. The walls of sinusoidal capillaries have even larger windows up to 40  $\mu\text{m}$  in diameter, and their basement membrane is also perforated. Capillaries of this type are located in tissues, where blood cells need to pass through the capillary wall, e.g., bone marrow, lymph nodes, spleen, and liver.

Transvascular exchange of lipid-insoluble molecules is governed primarily by diffusion rather than convection, e.g., studies in Ref. [49] for glucose (which radius is  $\approx 0.35 \text{ nm}$ ) demonstrate that convection results in less than 2% of its transfer across the capillary wall. Since the transport of glucose, as well as other metabolites, is restricted by pores, permeability of capillaries' walls for glucose is much lesser than that for oxygen, and alterations of blood flow do not affect significantly the inflow of glucose in tissue, which is diffusion limited. Note that in contrast to oxygen, which levels in human arteries and veins even under normal conditions differ more than twice [50], glucose concentrations in arterial and venous blood under normal conditions differ only by 2% [51]. Microvascular permeability for different substances can be affected by various chemical factors, depends on the charge of substances' molecules, and, obviously, rises with the increase in number and sizes of pores and falls with the increase in size of the molecules. For larger molecules, convective movement with water starts playing a significant role in their transvascular transfer. Water molecules diffuse rapidly across the capillary wall, but since this process is bidirectional, net diffusion of water is equal to zero. Filtration of water is driven by hydrostatic pressures in the capillary and in the intercellular space and by oncotic pressure in the capillary. Note that the interstitial oncotic pressure has been found to have negligible effect on the net filtration rate [52]. The excess of interstitial fluid is carried away by lymphatic system. Abnormal accumulation of fluid in tissue, i.e., edema, may be caused by various reasons, among which are the increased capillary permeability, the fall of capillary oncotic pressure, and impaired lymphatic drainage.

### **2.4.4 Angiogenesis**

Two main processes of blood vessel formation are distinguished: vasculogenesis, i.e., their *de novo* formation, and angiogenesis, i.e., formation of new blood vessels from preexisting ones, which in turn has two types: sprouting and intussusception (nonsprouting) angiogenesis. During embryonic development, the vasculogenesis leads to the formation of early vascular plexus, after which the majority of vessels are formed through angiogenesis. Sprouting angiogenesis includes degradation of extracellular matrix, followed by proliferation and migration of tip endothelial cells, and lumen formation. Intussusception is the splitting of a single vessel into two. Pruning, maturation, and remodeling of vessels complete the process of angiogenesis. All these steps are subtly orchestrated by the balanced action of large amount of factors [53]. One of the most important of these factors is the vascular endothelial growth factor, which stimulates proliferation and migration of endothelial cells, as well as branching of vessels, and causes the increase in their permeability.

Angiogenesis plays a central role in several important physiological processes, among which are wound healing, formation of new muscle or adipose tissue and menstrual cycle. It has been recognized as a therapeutic target for the treatment of diseases characterized by poor vascularization and, conversely, abnormal vasculature, among which are ischemic heart disease, peripheral arterial disease, and macular degeneration. Angiogenesis has been identified as one of the major hallmarks of cancer, since malignant cells actively stimulate this process to obtain more nutrients, thus increasing their proliferation rate [54]. Antiangiogenic therapy is a relatively new promising approach in oncology.

## **2.5 Vascular pathologies**

Normal blood flow is the vitally important factor for a living organism. Vascular pathologies may significantly change the blood flow distribution and, thus, tissue supply with nutrients. Some of the vascular pathologies (aneurism rupture, thromboembolism) may progress rapidly causing acute ischemic events and death. Others (stenosis, aneurism growth, vascular aging) have an insidious onset. In most cases, they develop without symptoms for 10–20 years. The choice between pharmacological and surgical treatment in the particular case requires individual analysis of possible pros and cons, which is difficult to perform using standard clinical measurements.

### **2.5.1 Stenosis**

An arterial stenosis is a narrowing of the vascular lumen due to extrinsic or intrinsic reasons. It decreases the local and distal (downstream) blood flow and prevents the normal perfusion of a tissue region. Extrinsic stenosis is caused by external compression of the

surrounding tissues due to their inflammation, edema, tumor growth, etc. Intrinsic stenosis is related to atherosclerosis. Atherosclerosis is the process of the lipids accumulation in the subendothelial layer of the vessel during the vessel wall inflammation or dyslipidemia. As a result, the atheromatous plaque is developed.

One of the two possible scenarios of the atherosclerosis progression is the plaque rupture with the clotting and subsequent emboli formation. Emboli are taken by the flow to a smaller downstream artery, which may be a reason of sudden interruption of the perfusion in a tissue region and, thereby, a reason of acute ischemia and infarction. The other scenario is the severe narrowing of the lumen due to the repeated plaque rupture and healing responses. It results in the substantial decrease of the downstream blood flow and insufficient delivery of oxygen to a tissue region (ischemic hypoxia).

The most frequent regions affected by the atherosclerosis are the large and medium thick-walled systemic arteries, especially near and in branching regions. The vitally important regions are coronary and brachiocephalic arteries. The damage of these regions results in failure of the heart and brain functions.

The treatment of stenotic arterial segments may rely on pharmacologic therapy, surgical minimally invasive procedures such as stenting, balloon remodeling, or more complex surgical interventions such as shunting, endarterectomy, and laminectomy. The decision on particular type of the treatment for the particular patient is complicated. It depends on the estimate of hemodynamical importance of the stenosis. The various factors should be considered: possible variations of the procedure (e.g., type and place of stenting, especially in the case of multiple stenosis), regional blood flow redistribution after the treatment (e.g., coronary stealing effect), and possible intensive blood flow conditions in everyday life (e.g., intensive physical activity, mental stress).

Various techniques are used to estimate the hemodynamical importance of the stenosis: Doppler ultrasound measurements; angiography and computed tomography (CT), which exploit X-ray beams; magnetic resonance imaging (MRI), which exploits strong magnetic field and radio frequency pulses; PET; etc. All methods have some limitations. The use of regular Doppler ultrasound is limited for the blood flow measurements in the coronary and cerebral arteries due to the strong reflection from the bones of the chest and skull.

Angiography and CT cause radiation injury. MRI measurements are safer but longer than CT and produce noisy output. Therefore, computer (*in silico*) modeling based on the physical principles of the blood flow in the vascular network is important for the extended analysis of the possible treatment and side effects.

Multiple stenosis of coronary arteries is a common CVD. It can cause myocardial ischemia, which frequently results in disability or death. In this case, the fractional flow reserve (FFR) became the basic parameter for making decision on surgical treatment.

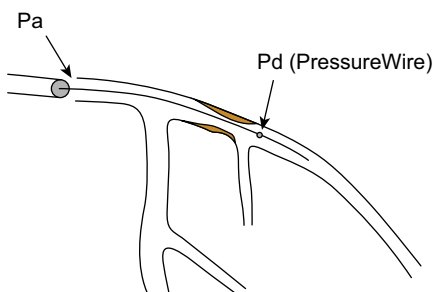


**Figure 2.9**  
Fractional flow reserve measurement.

FFR is calculated as the ratio of mean pressure distal to stenosis ( $P_d$ ) to mean aortic pressure during hyperemia after vasodilator administration (see Fig. 2.9). The values below 0.8 are associated with hemodynamic importance of the stenosis and recommendation of surgical treatment. The FFR-based decisions allow reducing the number of unnecessary invasive treatments relative to the previous conventional parameter, which is lumen cross-sectional area ratio.

Clinical measurement of FFR has two disadvantages. It requires a minimally invasive endovascular procedure. Also it requires an expensive ultrasound probe. Modern methods of *in silico* FFR estimation involve 3D blood flow modeling in the local region of the studied vessel. It requires complex simulations of local coronary region with high computational cost. Another approach is based on the 1D hemodynamic simulation in the coronary region. It allows to simulate substantial part of coronary region with multiple stenosis, calculate FFR, separately estimate hemodynamic importance of every stenotic region, and estimate the possible blood stealing effects and intensive blood flow effects. The 1D patient-specific coronary vessels network structure can be reconstructed from individual CT scans.

### 2.5.2 Aneurysms

The details of biomechanics and hemodynamics of arterial aneurysms can be found in Refs. [55,56].

Aneurysm is an abnormal bulge of the vessel wall due to its degradation and permanent pathological dilation. Aneurysms mainly appear in arteries, especially in thoracic and abdominal parts of the aorta, intracranial, and leg and spleen arteries. The most serious consequence of aneurysm progression is its rupture and associated internal hemorrhage. In turn, it results in high morbidity and mortality rate. Aneurysms often do not produce any symptoms before the rupture.

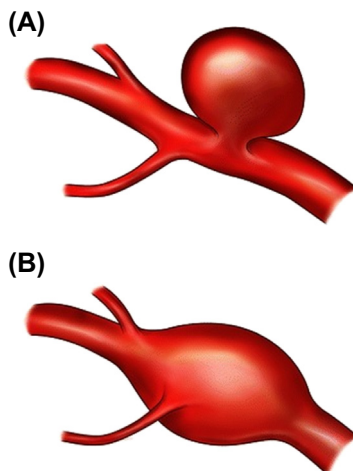


**Figure 2.10**

Aneurysms: (A) saccular, (B) fusiform. Reprinted by permission from Springer Nature Customer Service Centre GmbH: Springer Nature, Applied Health Economics and Health Policy, Pipeline™ Embolization Device for the Treatment of Complex Intracranial Aneurysms, Kathleen Withers, Grace Carolan-Rees, Megan Dale, © 2013.

Aneurysms are classified according to their shape as fusiform (spindle-shaped) or saccular (berry-like) (see Fig. 2.10). Fusiform aneurysms are mostly formed in the thoracic and abdominal aorta or in the popliteal artery behind the knee. They are primarily found at the upstream of bifurcations. Saccular aneurysms are generally found in the main cerebral arteries, intracranial arteries, and leg and spleen arteries. They are primarily found at the apex of bifurcations, at the origin of small arteries branching from large ones, and on the sidewall of arteries with sharp curvatures.

The causes of aneurysms occurrence include one or several following factors: hemodynamic factors, increased wall shear stress (WSS), infection on the arterial wall, genetic disorders, hypertension, atherosclerosis, structural vascular wall defects due to aging, cigarette smoking, and alcohol consumption. The aneurysm progression is a complex process regulated by mechanical, hemodynamical, and biological factors. The forces exerted by the pulsatile blood flow pressure on the weakened vessel wall cause a gradual expansion. The mechanotransduction effects result in progressive degradation of the wall. The aneurysm progression and rupture depends on the cooperative effect of several factors: the blood flow pulsatile pressure, the mechanical properties of the aneurysm wall, and interaction of the aneurysm with the surrounding environment, such as bones and brain tissue.

Numerical simulations help to observe that blood flow in aneurysm depends on the neck diameter, its angle relative to the parent vessel, the parent vessel diameter, the diameter and the angle of the efferent vessels, and the aneurysm shape. The progression and rupture of aneurysms is associated with the regions of the aneurysm wall exposed to both high and low WSS.

Stable elevation of maximal WSS causes endothelial injury, which, in turn, initiates wall remodeling and subsequent degeneration. On the biological level, it causes an overexpression of endothelium-dependent NO production and associated stable decrease of the arterial tonus and apoptosis of the vascular smooth muscle cells.

There is a region of blood flow stagnation with low WSS in the dome of the developed saccular aneurysms. It causes loss of permeability of the endothelial cell membrane and dysfunction of flow-induced NO production. This dysfunction results in the aggregation of red blood cells, accumulation and adhesion of platelets and leukocytes along the intimal surface, and subsequent inflammatory events inside the aneurism wall. The aneurysm wall becomes progressively thinner, which results in a lower pressure threshold at which tensile forces can be supported.

Aneurysm diameter is the currently used statistics for estimating the risk of rupture. Nevertheless, there is no apparent general decision regarding the specific factors determining aneurysm enlargement. More accurate analysis requires the calculation of the tensile stresses on the aneurysms wall, which is a matter of numerical simulations. Current treatment of fusiform aneurysm is a surgical procedure of placing a graft to the affected area. Thus, the fusiform aneurysm walls are reinforced. Saccular aneurysm is treated by clipping its neck with a metallic clip (craniotomy) or by packing the aneurysm sac with platinum coil, hydrocoil, hardening polymers, etc. The objectives of such techniques are either total occlusion of the sac or the activation of stable thrombus formation by the reduction of the flow velocity inside the sac. Thus, the ultimate goal is to exclude saccular aneurysm from the circulation.

### **2.5.3 *Vascular aging***

The walls of the vessels change over life time. The diameters of the elastic systemic arteries increase with the age; they become stiffer and thicker due to the proliferation of smooth muscle cells. The main changes occur in the median layer, which thins out and loses the orderly arrangement of elastin fibers. Elastin sheets are very stable for approximately 40 years. The cycle stresses due to blood pulsations cause the fracture of the load-bearing elastic sheets. The tearing of the elastin sheets and fibers causes a

progressive permanent dilatation of the vessel and, possibly, aneurysm. The ratio of elastin to collagen is decreased due to both elastin decrease and collagen increase. It results in the decrease of elasticity and in an increase in the PWV. For example, PWV of the aorta almost doubles during the lifetime (from about 6.5 m/s in a 10 years to about 11 m/s in 60 years). As a result, the backward pressure waves, reflected from bifurcations and peripheral resistances, reach the aortic root in the end systole, thereby increasing the total pressure wave amplitude and cardiac afterload, which promotes hypertension, decrease of coronary circulation, and other related diseases.

#### **2.5.4 Pressure-related diseases: hypertension and hypotension**

Pathological persistent elevation of the arterial pressure is called hypertension. Hypotension is opposite to the hypertension. Hypotension is a pathological decrease of the arterial pressure.

The blood pressure may elevate due to lifestyle conditions (e.g., high salt, caffeine or alcohol consumption, smoking, low physical activity, obesity, stress) or pathological conditions (e.g., kidney disease, endocrine conditions, renal artery stenosis, etc.).

Prolonged increase of blood pressure is a risk factor for many diseases: stroke, heart failure, atrial fibrillation, coronary arteries disease, peripheral vascular disease, etc. The reasons of the systolic aortic pressure increase may be different and include the stenosis of large arteries (e.g., aorta coarctation), increase of the arterial stiffness due to aging, degenerative arterial dilatation, atherosclerosis, regulatory or autoregulatory mechanisms failure, vasoconstrictor drugs administration, peripheral resistance increase due to improper functioning of sympathetic nervous system, and a decrease of tissue oxygen partial pressure or an increase in carbon dioxide partial pressure.

Arterial stiffness and/or the increase of peripheral resistance produce an effect, which is similar to the vascular aging processes (see [Section 2.5.3](#)). These factors affect PWV and systolic pressure wave amplitude. Thus, the backward-reflected wave reaches the aortic root during late systole instead of diastole.

The heart can adjust to the short-term pressure increase. However, the structural remodeling of the myocardium is observed during the long-term systolic afterload. A sudden increase in systolic pressure at the aortic root causes reduction in left ventricular output. The excessive blood volume within the ventricle pushes and stretches the myocardial fibers. According to Starling's law, the energy of contraction is directly related to the length of the myocardial fibers in diastole. Thus, as a result of stretching of the fibers, the energy of myocardial contraction increases sufficiently to restore a normal

cardiac output under the conditions of the increased systolic arterial pressure. The prolonged retention of excess blood leads to the permanent left ventricular dilatation and its wall thickening. The hypertension causes an additional load to the heart. Cardiac work increases and the oxygen requirement of the heart elevates, which may be a possible cause of further ischemic events [57].

The persistently low arterial pressure (hypotension) results in insufficient blood and, thus, oxygen and nutrients supply of the organs and tissues. Hypotension may be a reason of dizziness, fainting, heart, endocrine, or neurological disorders. Hypovolemia (reduced blood volume) is one of the main reasons of hypotension. It can result from hemorrhage, insufficient fluid intake, and excessive fluid losses. The other reasons may include the use of different medications (diuretics, vasodilators, alpha- or beta-blockers). The failure of regulatory mechanisms may result in orthostatic hypotension, which occurs after a change in body position.

Hemodynamic compensatory responses to the hypotension and hypovolemia include the mechanisms of decreasing venous capacity, the increasing of cardiac contractility and rate, and the mechanisms of increasing vascular resistance. The latter mechanism relates to the blood centralization, which ensures perfusion of critical organs.

### ***2.5.5 Vein thrombosis***

Venous thromboembolism is a potentially fatal condition. Standard treatment includes prompt administration of anticoagulation medications. In the absence of effective anticoagulation, the risk of thrombosis recurrence, progression, or embolization is estimated to be 50% in 3 months. For the patients with a contraindication to anticoagulation, a mechanical interruption of the inferior vena cava with a filter is an acceptable method for minimization of the embolic events. Possible indications for filter installation include free-floating thrombus in deep veins, presence of a pulmonary embolism, recurrent venous thromboembolism despite anticoagulation, venous thromboembolism with reduced cardiopulmonary reserve, and chronic thromboembolic pulmonary hypertension undergoing pulmonary endarterectomy [58]. Retrievable cava filters can be used if temporary protection is needed. The accurate indications of the filter installation are still discussed.

Development of proper endovascular devices is one of the modern challenges in biomedical engineering. The installed device with trapped thrombus should minimize hemodynamic perturbations in the vessel and drag damage to the vessel wall. This requires optimization of the device shape, the choice of materials with suitable properties as well

as the place and the method of the device fixation. Other important factors one has to account for are the thrombus dissolving, the impact on the global circulation, and chemical species transport in the case of dissolvable devices. Such analysis requires complex multimodeling and multiscale computational techniques [59,60].

# Patient-specific geometric modeling

## 3.1 Introduction

This section briefly discusses the use of medical imaging in scientific research. The overview of human-like phantoms development is followed by the introduction to patient-specific geometric modeling in biomedical applications.

### 3.1.1 Development of human-like phantoms for scientific research

The history of anthropomorphic models starts from the radiation dosimetry problems [61]. In the first half of the 20th century, so-called “material phantoms” were used for experimental measurements. These are real models made of solid materials, with shape and density close as possible to the shape and density of imitated anatomical structures.

The use of such models was expensive, the preparation of experiments required considerable effort and time. Later in the 1960s, first “computational phantoms” appeared. In these models the shape of anatomical structures is described mathematically, and each domain is attributed with a set of specific properties, such as material density and conductivity. The first mathematical models of human anatomy were developed in the Oak Ridge National Laboratory. They were created using constructive geometry from the combinations of primitives: planes, cubes, prisms, cylinders, spheres, cones, and ellipsoids [62].

The use of primitives failed to provide an accurate representation of real anatomy. However, it made possible the parameterization of anthropometric data in the description of the phantom. This allowed researchers to obtain models that take into account age and gender characteristics. Adjusting the model parameters helped to design a whole family of phantoms of people of different ages and complexion.

Rapid development and active application of computer and magnetic resonance imaging technologies lead to the emergence of a new method for constructing “computational phantoms,” also called *tomographic models*. The method consists in identifying boundaries between the organs and tissues depicted in the tomography images and further assigning every image voxel (i.e., a three-dimensional pixel) to a particular anatomical part or structure.

This process is called segmentation. We shall define it more precisely below. Compared with methods based on the combination of primitives, this approach has its own problems:

1. Segmentation requires the input of medical images (results of examination) of the patient. The availability of images may be limited due to the expensive hardware needed for examination.
2. Typically available medical images do not cover the entire body; they are cropped to specific regions, either due to hardware limitations or for other reasons such as keeping the radiation dose limited.
3. The process of identifying tissue and organs borders is by far not straightforward and time-consuming.

Despite this, the “computational phantoms” obtained by the segmentation method continue to gain recognition due to their anatomical accuracy, which is important in many applications. The problem of completely automatic segmentation at this moment remains unresolved. We refer the reader to Refs. [61,63] for a comprehensive review of the evolution of computational models of human anatomy.

### ***3.1.2 Image-based patient-specific models***

Personalized numerical simulations of physiological processes in the human body received a great deal of attention over several last decades, and a vast number of models have been described in the literature. Contemporary resolution of medical images and new algorithms for their postprocessing allow us to develop high-resolution numerical models of various processes at cellular, organ, and the whole-organism scale [64–68]. For a given imaging data set, one is commonly interested in image segmentation, volume reconstruction, and numerical discretization.

The cornerstone of medical image processing is the segmentation process that assigns labels to the voxels. Each biomedical application imposes special restrictions on both the input medical images and the output patient-specific model and, therefore, calls for a specific class of 3D segmentation methods. Various medical image segmentation techniques have been developed (see, e.g., Refs. [69–71]). The most promising fully automatic segmentation methods belong to the class of atlas-based segmentation techniques [72–74]. The patient-specific segmentation is obtained from the atlas of presegmented images of other individuals. This atlas should contain enough different cases for accurate mapping of the new patient data. Thus, the atlas-based approach requires a large amount of manual segmentation by an expert for the preparation of atlases and the development of algorithms dealing with big data. The application area of atlas-based methods is, however, limited due to lack of the specialized presegmented atlases.

Semiautomatic or supervised segmentation technologies require some interaction with an expert. They are used primarily for the segmentation of particular organs and tissues.

## 3.2 Basics of medical imaging

This section covers medical imaging, in general. The specifics about heart and vessel segmentation are covered in consequent sections. We start from the basic principles of several medical images acquisition techniques. Then, we move to the underlying representation of the image data sets and general operations with images.

### 3.2.1 Image modalities

One of the most widespread medical image acquisition techniques is an ultrasound imaging, or *ultrasonography* (US). An ultrasound device emits high-frequency sound waves in different directions and captures the reflected waves.

Ultrasonography is a low-cost, informative, safe, reliable, and accessible diagnostic procedure. Several modes of ultrasound scanning are used conventionally. The B-mode (brightness mode) represents ultrasound echo as two dimensional; it is the most commonly used mode in medical diagnostics and study of morphological condition of organs and tissues. The brightness represents the intensity of the echo. The transit time of the acoustic pulse determines the distance and position of the echo.

Doppler ultrasonography mode is based on the Doppler effect. It is capable of movement detection. The direction and speed of moving sample is calculated from the pulse frequency shift. The computed velocity is color-coded (Color Doppler mode) and is usually combined with B-mode images (duplex mode).

Typically the US device is applied from the outside of the body. However, the *intravascular ultrasound* (IVUS) may be used to visualize the inner wall of blood vessels using a miniaturized ultrasound probe introduced inside the vessels through the catheter.

*Computed tomography* (CT) scan is a tomography technique, which produces images of the structures of the body. In CT, a beam of X-rays from multiple angles penetrates the examined object and is recorded by sensitive radiation detectors. This information is analyzed by computer using the Radon transform equations; the result of analysis is a detailed image reconstruction of the examined object and its contents.

*Computed tomography angiography* (CTA) is a CT technique with additional contrast, e.g., iodine-based contrast agent, intravenously injected to highlight arterial and venous vessels in the body.

*Cone beam computed tomography* (CBCT) differs from CT in the divergent conical shape of X-ray beams. CBCT is widely used in diagnosis and treatment planning in interventional radiology, patient positioning, and verification in image-guided radiation therapy.

In *magnetic resonance imaging* (MRI), a radio frequency pulse from powerful magnets excites and polarizes hydrogen nuclei of water molecules. Following the pulse, the radiowaves emitted from the protons relaxation are registered and analyzed during image reconstruction. MRI is believed to have minimal side effects since it does not use the ionizing radiation, unlike CT. A variety of different excitation and measuring protocols result in several MRI modalities: T1-weighted (T1-MRI), T2-weighted (T2-MRI), diffusion-weighted imaging, and dynamic contrast enhancement MRI.

In this chapter, we focus on CT and MRI techniques, which are able to provide three-dimensional images. Both CT and MRI are sensitive to different tissue properties; therefore, the CT and MRI images may differ significantly. CT images have low contrast in soft tissues, since they are not dense and do not block X-rays. At the same time, MRI produces excellent images of soft tissues, since MRI imaging uses the hydrogen nuclei, which are abundant in fluid and fat of soft tissues.

### **3.2.2 Contrast enhancement protocols and phases**

Contrast enhancement is used to improve the visibility and distinguishability of specific organs, tissues, and blood vessels. Generally, an iodine-based radiocontrast agent is used. Often, images are taken both with and without radiocontrast. The time interval between contrast administration and image acquisition is standardized in specific protocols for visualization of different organs and tissues. The main phases of CT enhancement are as follows: without contrast (nonenhanced CT), early arterial, late arterial, portal, and late phase. The contrast propagation starts from the arteries. Next, the organs that get their blood supply from the arteries receive the contrast. The contrast propagates to the veins and highlights the liver parenchyma. Later, all parenchyma organs and veins are enhanced.

Different contrast agents may be used for specific studies. Gadolinium is the key component of the contrast material most often used in MRI exams; it alters the magnetic properties of tissues and enhances the MRI images.

One can use oral contrast solutions for gastrointestinal tract enhancement in abdominal CT images. In this case, barium sulfate contrast materials are commonly used; however, in some cases, a plain water or milk may be used as an alternative.

### **3.2.3 The voxel-based representation of the medical images**

Medical images are associated with virtual physical space inside the CT/MRI machines. Image is exported as a three-dimensional  $N_1 \times N_2 \times N_3$  array of voxels. Each voxel has the same size and represents a small  $h_1 \times h_2 \times h_3$  rectangular box. Voxels are indexed throughout array by integer tuples  $(k_1, k_2, k_3)$ . Assume the indexes start from zero:

$$k_1 \in [0\dots N_1 - 1], k_2 \in [0\dots N_2 - 1], k_3 \in [0\dots N_3 - 1].$$

We denote voxel spacing by  $\mathbf{h} = (h_1, h_2, h_3)^T$ , image dimensions by

$$\mathbf{N} = (N_1, N_2, N_3)^T, N_i \in \mathbb{Z}, \quad i \in [1 \dots 3],$$

and voxel coordinates by

$$\mathbf{k} = (k_1, k_2, k_3)^T, k_i \in \mathbb{Z}, \quad i \in [1 \dots 3].$$

The physical coordinates of the first voxel are called the image origin; we denote it by  $\mathbf{o} = (o_1, o_2, o_3)^T$ .

One can also think about the voxel  $\mathbf{k}$  as the rectangular domain in  $\mathbb{R}^3$  consisting of all points  $\mathbf{x} = (x_1, x_2, x_3)$  such that:

$$o_i + k_i h_i < x_i < o_i + (k_i + 1) h_i, \quad i = 1, 2, 3.$$

We define the set of possible image indexes by  $\Pi$ :

$$\Pi = \{\mathbf{k} | k_i \in [0 \dots N_i - 1], \quad i = 1, 2, 3\}.$$

Image dimensions, origin, and voxel spacing are the core information, which is incorporated in the image auxiliary data.

Medical images are usually grayscale, so we can represent them as mappings  $G: \Pi \rightarrow \mathbb{R}$ . In most cases, CT and MRI machines export the color intensity as an *integer* value, in which case, one can assume  $G: \Pi \rightarrow \mathbb{Z}$ .

Typically, MRI images have significant variation in intensity across patients and scanners. This makes it hard or even impossible to determine a tissue-specific absolute intensity numerical meaning, even within the same MRI protocol, body region, for images obtained on the same scanner, and for the same patient.

The radiodensity in CT images is measured in *Hounsfield units* (HU). The Hounsfield scale is a linear scale, such that the radiodensity of water is taken as zero HU, and radiodensity of air is taken as  $-1000$  HU. The Hounsfield scale clearly distinguishes lungs with high negative values ( $-900$  to  $-500$  HU), fat with small negative values ( $-100$  to  $-80$  HU), and bones with high positive values (higher than  $+200$  HU). However, most of other organs and tissues lie in one range of small positive values ( $+10$  to  $+90$  HU).

For computational purposes, the most memory efficient numerical type is an 8-bit integer. However, due to its low resolution, it is mostly used only in the segmentation images. A wider range is usually required for MRI and CT images. A signed 12-bit integer represents values from  $-2048$  to  $+2047$  and is suitable for most medical images. Each voxel can be represented using 2 bytes in computer memory. Note that one can reduce the memory usage by combining two 12-bit integers as 24-bit data and store it using 3 bytes.

The following information is necessary to define the image: image origin, voxel spacing, and the image as the mapping  $G$ . Additional image information is preferable, such as protocol description, image acquisition-specific parameters, patient orientation, patient identifier, acquisition date and time, and other useful information. Digital Imaging and Communications in Medicine (DICOM) was developed as a standard for storing and transmitting medical images enabling the intercommunication between medical imaging devices and applications. Usually, DICOM images are organized in a tree-like structure with DICOMDIR file in the root, holding references to all other files. The DICOM information model itself is hierarchical. The levels of the model are the Patient, Study, Series, and Image/Instance level. 3D images may be saved as a stack of files, one per each slice inside the Series directory. Each image file includes the header with all metadata information, including Series identifier.

Other popular formats for working with image and segmentation data include Analyze image data format, Neuroimaging Informatics Technology Initiative (NIfTI) file format, Nearly Raw Raster Data (Nrrd) file format, and Insight Toolkit MetaImage (ITK MetaImage) file format. In some cases, the stack of ordinary image files may be used. However, in this case, the spatial information should be saved separately.

Most of the file formats support saving 2D and 3D images with signed/unsigned 8-bit and 16-bit integers, floats, and RGB tuples. The segmentation image may be saved in the same format with unsigned 8-bit integer as voxel type.

### 3.2.4 Basic operations with images and masks

Consider an input grayscale image  $G$ , and assume that the intensities are integers or floats if not stated otherwise. Segmentation images are denoted by  $S$ . Usually, all operations with grayscale images can be applied to segmentation images as well. Segmentation images are treated as nonnegative integer images, where zero value has a special meaning—the background label. The binary mask is a special case of a segmentation image with only one label.

The basic arithmetic operations with images include addition, subtraction, and multiplication. These operations are performed voxel-wise:

$$\begin{aligned}\text{sum}(G_1, G_2) &: \mathbf{k} \mapsto G_1(\mathbf{k}) + G_2(\mathbf{k}), \\ \text{diff}(G_1, G_2) &: \mathbf{k} \mapsto G_1(\mathbf{k}) - G_2(\mathbf{k}), \\ \text{mul}(G_1, G_2) &: \mathbf{k} \mapsto G_1(\mathbf{k}) \cdot G_2(\mathbf{k}).\end{aligned}$$

The voxel-wise min and max operators are defined similarly:

$$\text{min}(G_1, G_2) : \mathbf{k} \mapsto \min(G_1(\mathbf{k}), G_2(\mathbf{k})),$$

$$\max(G_1, G_2) : \mathbf{k} \mapsto \max(G_1(\mathbf{k}), G_2(\mathbf{k})).$$

The clipping operator is used to clip the intensity of the image to the range  $[a, b]$ :

$$\text{clip}(G, a, b) : \mathbf{k} \mapsto \max(a, \min(G(\mathbf{k}), b)).$$

The threshold operator is used to extract regions with image intensity in the range  $[a, b]$ :

$$\text{thresh}(G, a, b) : \mathbf{k} \mapsto \begin{cases} 1, & \text{if } G(\mathbf{k}) \in [a, b] \\ 0, & \text{otherwise.} \end{cases}$$

Let us consider a special case of segmentation image, the *binary mask* image  $M : \Pi \rightarrow \{0, 1\}$ . For simplicity of the following presentation, we will allow the binary mask  $M$  to be used as a set of voxels:

$$\mathbf{k} \in M \Leftrightarrow M(\mathbf{k}) = 1.$$

In some cases, we need a complement of the binary mask:

$$\overline{M} : \mathbf{k} \mapsto 1 - M(\mathbf{k}) \text{ or } \overline{M} = \Pi / M.$$

Operators on sets can be easily replaced by voxel-wise operators:

$$\begin{aligned} M_1 \cap M_2 &= \min(M_1, M_2) = \text{mul}(M_1, M_2), \\ M_1 \cup M_2 &= \max(M_1, M_2). \end{aligned}$$

We need some further notations. Let us start with the definition of adjacent voxels. For each voxel, we introduce two sets of adjacent voxels. Set  $N_6(\mathbf{k})$  denotes the set of voxels adjacent to voxel  $\mathbf{k}$  and sharing a face; this connectivity rule is called *6-adjacency*. Set  $N_{26}(\mathbf{k})$  denotes the set of voxels adjacent to voxel  $\mathbf{k}$ , and sharing either a face, or an edge, or a vertex, this connectivity rule is called *26-adjacency*.

We can rewrite these definitions in the following way:

$$\begin{aligned} N_6(\mathbf{k}) &= \left\{ \mathbf{m} \left| \sum_{i=1,2,3} |m_i - k_i| = 1 \right. \right\}, \\ N_{26}(\mathbf{k}) &= \left\{ \mathbf{m} \left| \max_{i=1,2,3} |m_i - k_i| = 1 \right. \right\}. \end{aligned}$$

A subset of binary mask is called a connected component when all voxels inside this component are connected with a path of 26-adjacent voxels. The classical algorithm to enumerate all connected components in the binary mask uses two passes to mark voxels in the same component by a unique label. An improved algorithm from Ref. [75] for labeling connected component can be adopted to 3D binary images. The algorithm is based on run-length encoding [76]. For convenience, the labels of the connected components may be reordered from the largest to the tiniest component size.

Several mathematical morphology operators are quite useful in image processing. Here, we discuss the basic ones: dilation, erosion, opening, and closing. These operators are closely related to Minkowski addition described in the following.

First, let us define an auxiliary set representing the index offsets of voxels in the neighboring ball of radius  $r$ :

$$B_r = \{\mathbf{k} \mid \|\mathbf{k}\| \leq r\},$$

where indices may be negative, and  $\|\cdot\|$  is Euclidean norm of vector

$$\|\mathbf{k}\| = (k_1^2 + k_2^2 + k_3^2)^{1/2}.$$

The *dilation* of binary mask is the enlarging of the mask by substituting each voxel with the ball. The results can be obtained as the Minkowski sum of the initial mask  $M$  and the neighboring ball  $B$ :

$$M \oplus B = \{\mathbf{k} + \mathbf{m} \mid \mathbf{k} \in M, \mathbf{m} \in B\}.$$

The *erosion* of binary mask is the shrinking of the mask by keeping only voxels, which neighborhood balls are inside the mask. This result may be obtained as a Minkowski difference of the initial mask  $M$  and neighborhood ball  $B$ :

$$M \ominus B = \{\mathbf{k} \mid \mathbf{k} \oplus B \subseteq M\}.$$

The *opening* of the binary mask is obtained by the erosion, followed by the dilation of the resulting mask:

$$M \circ B = (M \ominus B) \oplus B.$$

The *closing* of the binary mask is similar, but obtained by performing dilation first followed by erosion:

$$M \bullet B = (M \oplus B) \ominus B.$$

Efficient computation of morphological operations for 3D images [77] is based on the following theorem [78]:

$$A \oplus B = A \cup (\text{surf}(A) \oplus B),$$

where  $\text{surf}(A)$  is the boundary of  $A$ .

The set  $B$  is sometimes called the kernel of the morphological operator.

### 3.3 Heart segmentation

This section covers the segmentation techniques for the heart. We discuss the segmentation of heart cavities and myocardium. New technique for dynamic heart ventricles segmentation using dynamic contrast-enhanced CT images is presented in the end of the section.

### 3.3.1 Segmentation of heart cavities

Heart cavities and blood vessels can be segmented using active contours method and random forest classifier [79]. These regions are filled with blood and usually have a distinct intensity in the contrast-enhanced images. Once the connected region of blood vessels and cavities is segmented, it is advisable to split it into parts corresponding to right atrium (RA), left atrium (LA), right ventricle (RV), left ventricle (LV), aorta, pulmonary trunk, superior vena cava, and inferior vena cava (Fig. 3.1).

### 3.3.2 Segmentation of myocardium

Myocardium segmentation is performed in the vicinity of segmented heart cavities. Myocardium tissue differs in texture and intensity compared with neighboring fat tissue, bones, and lungs (Fig. 3.2). This segmentation step is also performed using active contours method and random forest classifier [79].

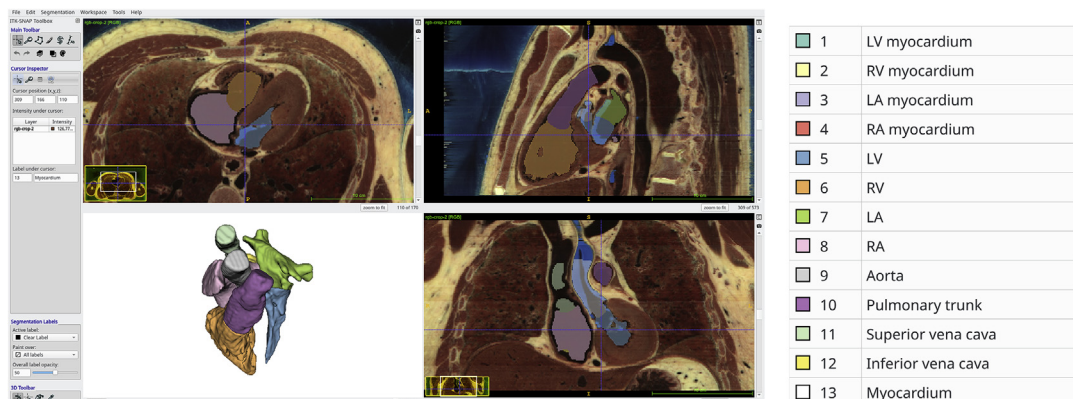


Figure 3.1

Segmentation of cardiac cavities and blood vessels. Snapshot of ITK-SNAP software.

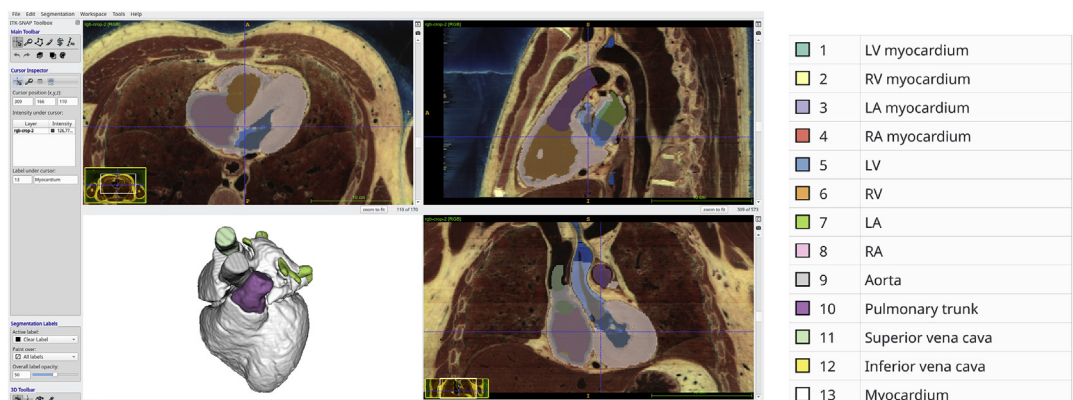


Figure 3.2

Myocardium segmentation. Snapshot of ITK-SNAP software.

The final step involves segmentation smoothing. The myocardium tissue was divided into four parts using mathematical morphology operations: right atrium, left atrium, right ventricle, and left ventricle (Fig. 3.3). This division can be used in modeling algorithms for synthetic computation of myocardium fiber orientation.

### 3.3.3 Segmentation of dynamic images

One can take a step further and segment a dynamic 4D chest contrast enhanced CT (ceCT) data set. In this section, we go through a segmentation process of the left ventricle suitable for generation of the dynamic mesh. In the present example, we start with an anonymized dynamic chest ceCT data set of 100 images with  $512 \times 512 \times 480$  voxels and  $0.625 \times 0.625 \times 0.25$  mm resolution (Fig. 3.4).

At the first stage, we apply 3D nonlocal means smoothing [80], crop, and resample the input images. Resulting smoothed images have  $96 \times 96 \times 96$  voxels and  $1.25 \times 1.25 \times 1$  mm resolution (Fig. 3.5).

We select several images for manual segmentation at different stages of cardiac cycle: the beginning of systole (image #0), the end of systole (image #30), and the middle of rapid inflow during diastole (image #50). We use level-set method from ITK-SNAP package [81] for user-guided segmentation and segment four materials: left ventricle, left atrium, aorta, and right ventricle and atrium combined (Fig. 3.6).

At the next stage, we apply machine learning techniques to segment all images. To this end, we construct the random forest classifier [79], trained on the manually segmented images. The result of classification is postprocessed using a combination of mathematical

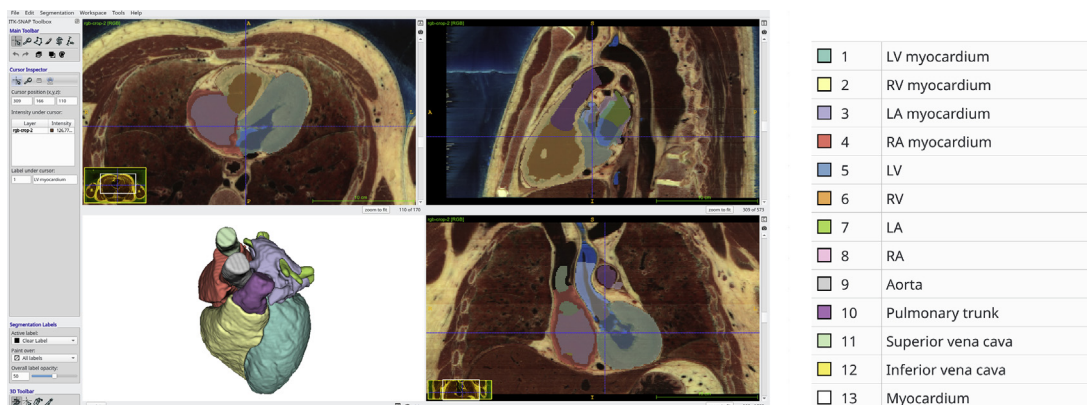


Figure 3.3

Final segmented model. Snapshot of ITK-SNAP software.



**Figure 3.4**

Initial CT data set, image #50, the middle of rapid inflow during diastole: *A*, aorta; *CT*, computed tomography; *LA*, left atrium; *LV*, left ventricle; *RV*, right ventricle. Snapshot of ITK-SNAP software.

operations: dilation, erosion, and construction of connected regions (Fig. 3.7). This step allows us to fill possible holes inside the segmented regions, to remove small isolated spots appearing from segmentation of too noisy image, and provides smoothed boundaries of the segmented regions.

At the final stage, we reconstruct the position and orientation of valve planes by the principal component analysis (PCA) method [82]. For mitral valve, we use PCA to compute the *best-fitting* plane for the union of all voxels forming interface between left ventricle and left atrium across all time series images. The same method is used to compute the *best-fitting* plane of aortic valve for the voxels forming interface between left ventricle and aorta. We assume that these planes will be fixed during the cardiac cycle for simplicity of mesh generation and numerical modeling.

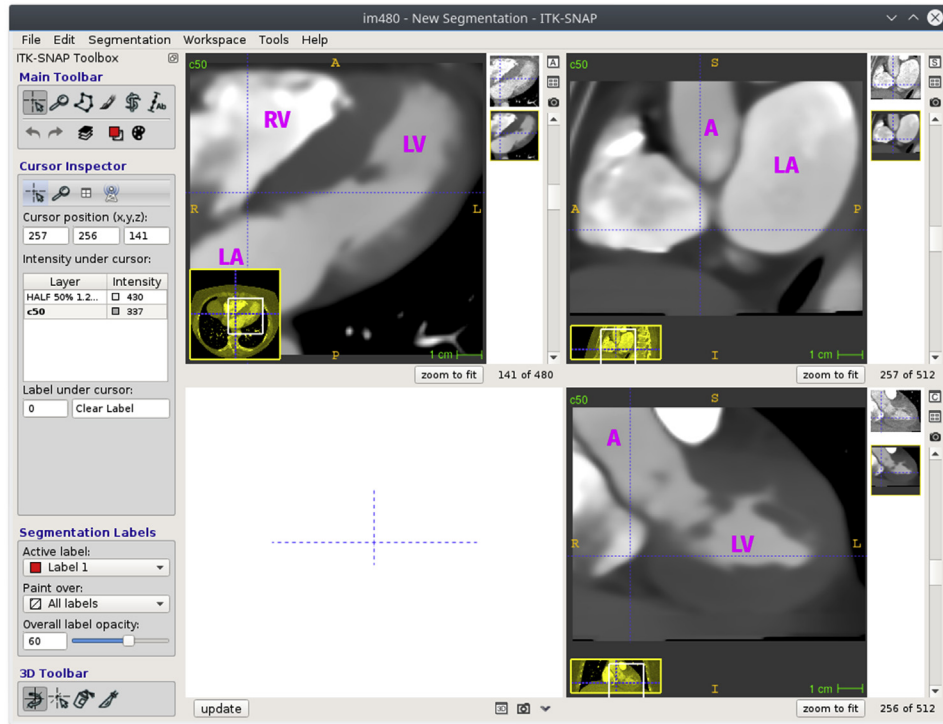


**Figure 3.5**

Cropped and smoothed CT image #50: *A*, aorta; *CT*, computed tomography; *LA*, left atrium; *LV*, left ventricle; *RV*, right ventricle. Snapshot of ITK-SNAP software.

### 3.4 Blood vessels segmentation

This section covers automatic vessel segmentation techniques. We start from the aorta segmentation and then proceed to the segmentation of coronary arteries and cerebral vessels.

#### 3.4.1 Automatic segmentation of aorta

The first step in our automated segmentation algorithm for coronary arteries is obtaining the binary mask of aorta. As discussed in Ref. [83], the aorta segmentation algorithm is based on isoperimetric distance trees (IDT) method [84]. The IDT method is fast and robust and provides anatomically correct results. On input, it takes an initial mask and a voxel from this mask, cuts the mask at *bottlenecks*, i.e., thin structures connecting significant parts of the mask, and outputs a submask of the initial mask containing the

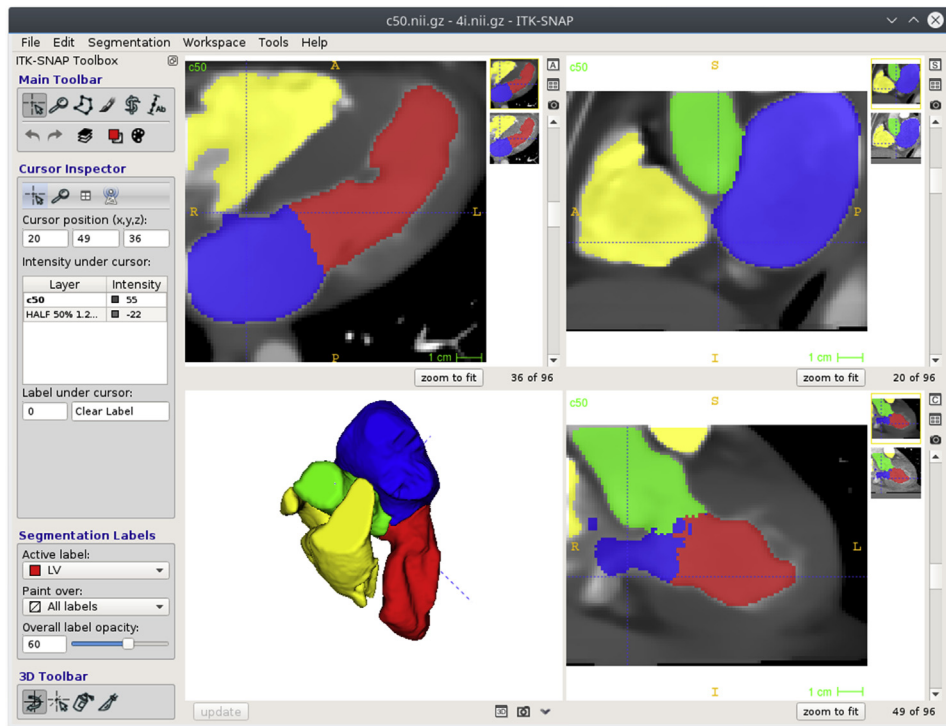


**Figure 3.6**

Manual segmentation of CT image #50: red (dark gray in print version)—left ventricle, blue (black in print version)—left atrium, green (gray in print version)—aorta, yellow (light gray in print version)—right atrium and right ventricle. Snapshot of ITK-SNAP software. CT, computed tomography.

input voxel. The fully automated aorta segmentation is defined by the following algorithm illustrated in Fig. 3.8:

**Algorithm 3.1.** Aorta segmentation.

1. Find a slice with largest bright disk, and compute the radius  $r_A$  and the center  $\mathbf{k}_c$  of the largest bright disk using the circle Hough transform (CHT) (Fig. 3.8A).
2. Find the threshold  $T$  as the minimal intensity inside the disk.
3. Extract the connected mask  $M$  according to the threshold  $T$  (Fig. 3.8B).
4. Apply the IDT to  $M$  and  $\mathbf{k}_c$ , and obtain the mask of aorta  $M_A$  (Fig. 3.8C).
5. Apply opening morphology operator to  $M_A$  using neighborhood ball  $B_r$  (Fig. 3.8D,E).

The largest bright disk detected by CHT [85] at the first CT slice corresponds to the uppermost aorta cut. Apart of the aorta, mask  $M$  contains contrast-enhanced parts of the heart and other vessels, and therefore, the IDT algorithm is needed.

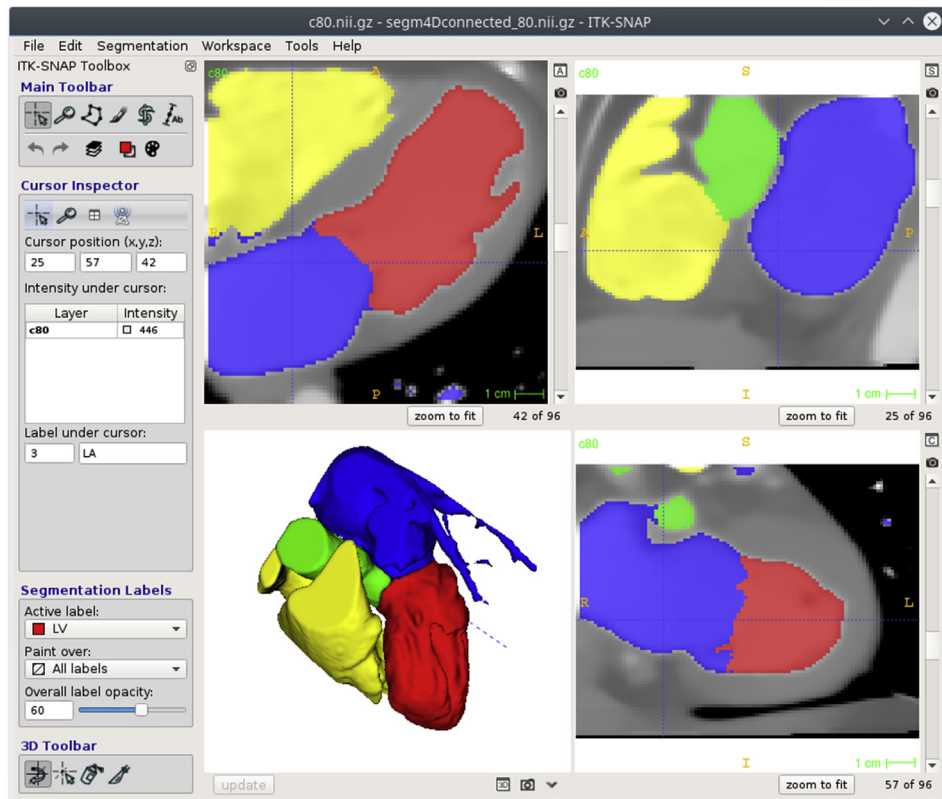


**Figure 3.7**

Automatic segmentation of CT image #80: red (dark gray in print version)—left ventricle, blue (black in print version)—left atrium, green (gray in print version)—aorta, yellow (light gray in print version)—right atrium and right ventricle. Snapshot of ITK-SNAP software. *CT*, computed tomography.

The last step of the aorta segmentation algorithm smooths the mask  $M_A$  and denoises its boundary. The noise may occur due to inappropriate choice of the threshold  $T$  and a wrong assignment of coronary vessels parts to the mask of aorta at the IDT stage. Therefore, a smoothing parameter  $r$  should not be less than the maximum radius  $r_{\max}$  of coronary vessels and significantly less than  $r_A$ . In practice, instead of computing  $r_{\max}$ , we set  $r = 15 \geq r_{\max}$ : for general CT datasets with different noisiness, such choice provided successful aorta segmentation.

### 3.4.2 Automatic segmentation of coronary arteries

For vascular segmentation, we exploit the Frangi vesselness filter [86]. The filtering is based on the information given by eigenvalues of the Hessian of an image function  $G(\mathbf{x})$  where  $\mathbf{x}$  is a 3D coordinate vector. The filter measures similarity to a tubular structure with

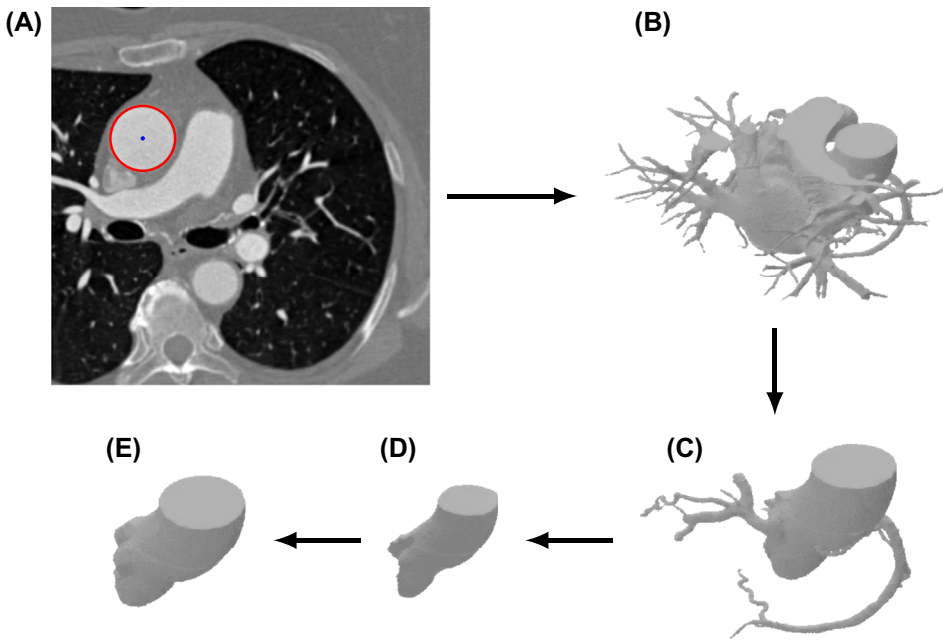


**Figure 3.8**

Aorta segmentation workflow: (A) red circle (dark gray circle in print version) with radius  $r_A$  and center  $\mathbf{k}_c$  corresponds to aorta cut, (B) connected initial mask  $M$  containing  $\mathbf{k}_c$ , (C) output of IDT contains a noisy mask of aorta and parts of coronary vessels, (D) erosion of  $M_A$  by  $B_r$ , (E) dilation of  $M_A$  by  $B_r$  provides the aorta segmentation. IDT, isoperimetric distance trees.

specific diameter and assigns vesselness value to each input voxel. Thresholding of the vesselness values provides a binary mask of vascular structures. The approach gives anatomically correct segmentation of all input voxels regardless of possible image discontinuities. The general idea of the local analysis of image  $G(\mathbf{x})$  is based on its Taylor expansion. For the computation of the Hessian  $H_s(\mathbf{x})$  of  $G$ , one uses normalized derivatives in accordance with the linear scale space theory [87]:

$$\frac{\partial}{\partial x_i} G_s(\mathbf{x}) = s^\gamma G(\mathbf{x}) * \frac{\partial}{\partial k_i} K(\mathbf{x}, s),$$

where  $*$  denotes the convolution,  $K(\mathbf{x}, s) := \frac{1}{\sqrt{2\pi s^3}} \exp\left(-\frac{\|\mathbf{x}\|^2}{2s^2}\right)$  is the 3D Gauss kernel

with scale  $s$ , and  $\|\mathbf{x}\|$  is the Euclidean norm of vector  $\mathbf{x} \in \mathbb{R}^3$ . Here and further in the text, the length is measured in voxels, i.e., the voxel size is assumed to be equal to 1. Scale parameter  $s$  with length dimension is used to limit the Frangi filter to vessels with

approximate radius  $s$  [86]. Parameter  $\gamma$  defines a family of normalized derivatives [88]. This normalization is important for a fair comparison of the response of differential operators at multiple scales. For each voxel, the vesselness  $V(s)$  at scale  $s$  is computed from the eigenvalues  $|\lambda_1| \leq |\lambda_2| \leq |\lambda_3|$  of the Hessian  $H_s$ :

$$V(s) = \begin{cases} 0, & \text{if } \lambda_2 > 0 \text{ or } \lambda_3 > 0, \\ \left(1 - \exp\left(-\frac{\mathcal{R}_A^2}{2\alpha^2}\right)\right) \exp\left(-\frac{\mathcal{R}_B^2}{2\beta^2}\right) \left(1 - \exp\left(-\frac{\mathcal{S}^2}{2c^2}\right)\right), & \text{otherwise.} \end{cases}$$

Here,  $\mathcal{R}_B = |\lambda_1| / \sqrt{|\lambda_2 \lambda_3|}$  accounts for the deviation from a blob-like structure,  $\mathcal{R}_A = |\lambda_2| / |\lambda_3|$  is ratio distinguishing between plate-like and line-like structure, and

$\mathcal{S} = \|H\|_F = \sqrt{\lambda_1^2 + \lambda_2^2 + \lambda_3^2}$  is the Frobenius norm of  $H_s$ . Frangi parameters  $\alpha$ ,  $\beta$ , and  $c$  define thresholds that control the sensitivity of filter to quantities  $\mathcal{R}_A$ ,  $\mathcal{R}_B$ , and  $\mathcal{S}$ , respectively.

Segmentation of vessels with various radii is easily performed with the scale range  $[s_{\min}, s_{\max}]$ :

$$V = \max_{s_{\min} \leq s \leq s_{\max}} V(s).$$

In practice, the vesselness filter detects both vessels and bones. Therefore, the Frangi filter segmentation of large vessels requires such preprocessing of the input image that hides all bones. Note that a typical heart imaging data set has relatively low resolution, and the filter computation is not time-consuming in this case.

Given the mask of aorta, we apply the Frangi filter with parameters  $\alpha = 0.5$ ,  $\beta = 0.5$ ,  $c = 300$  for three scales  $s = 1, 2, 3$ . Ostia points are detected as two distinct local maxima of the Frangi vesselness inside the mask of aorta. The coronary arteries are defined as components of vascular trees rooting at ostia points.

### 3.4.3 Automatic segmentation of cerebral arteries

Now we extend the above algorithm to cerebral data sets. Pulmonary arteries are removed by morphological operations proposed in Ref. [89]. Bone elimination is an essential step for cerebral artery segmentation due to vertebral arteries and cervical vertebrae proximity. Assuming both CT and ceCT data sets are available for the same patient, bones can be automatically darkened with the multiscale-matched mask bone elimination algorithm [90]. Otherwise, bones should be segmented and eliminated manually. Ostia points are detected as two distant vesselness maxima near aorta border. Aortic arch branches are defined as connected components of voxels with high vesselness, lying close to aorta border. Aorta border cleaning is the final step, which is necessary since high vesselness

values may falsely occur near big bright structures. We will describe the details of these steps in the following.

After the IDT stage, some parts of aortic arch branches or coronary arteries may still be included in  $M_A$ . In the coronary case, a simple morphological smoothing of  $M_A$  is sufficient to remove coronary parts and to keep the mask intact. However, carotid and subclavian arteries are bigger than the coronary arteries, and thus, algorithm requires more sophisticated approach for their removal.

Next, we use three parameters  $r$ ,  $R$ , and  $t$  to remove coronary and cerebral arteries from the aorta mask  $M_A$ . We assume that the mask  $M_A$  is already smoothed by opening morphological operator with kernel  $B_r$ , and coronary vessels are already excluded. To remove the aortic arch branches, the mask  $M_A$  is copied to the mask  $M_s$ , and  $M_s$  is opened with a bigger kernel  $B_R$ . After that step,  $M_s$  is distorted, but no longer contains any parts of carotid or subclavian arteries. We apply dilation with kernel  $B_t$  to the mask  $M_s$  and intersect it with the mask  $M_A$ . The last step allows resulting mask to keep intact the border of the mask  $M_A$ . To summarize, we suggest the following algorithm:

**Algorithm 3.2.** Aortic arch segmentation.

1. Compute the radius and the center  $\mathbf{c}$  of the largest bright disk  $D$  on transverse planes using CHT method.
2. Construct the connected region mask  $M_0$  containing voxel  $\mathbf{c}$  with the minimal intensity inside of  $D$  as the lower threshold.
3. Obtain  $M_A$  as a result of the IDT method applied to the mask  $M_0$  and the seed  $\mathbf{c}$ .
4. Apply opening morphological operator to the mask  $M_A$  with the kernel  $B_r$ .
5. (Cerebral case only) Copy mask  $M_A$  to mask  $M_s$ . Apply erosion with kernel  $B_R$ , apply dilation with kernel  $B_{R+t}$ .
6. (Cerebral case only) Intersect the mask  $M_A$  with the mask  $M_s$ .

The Frangi vesselness filter is a useful instrument for vessel segmentation since it results in high vesselness values inside the vessels and low values elsewhere. The filter may also produce high values near large bright structures like aorta. The authors of Ref. [89] proposed the modified vesselness function. However, in practice, we observed false filter response only near the aorta. Thus, we propose alternative approach for segmentation correction only near the aorta border. It should be noted that conventional remove-islands procedure may not eliminate the segmentation errors, since false regions are attached to the correctly identified arteries.

We define the *distance map*  $dmap_M(v)$  as the distance to the mask  $M$  for each voxel  $v$ . The detailed description of distance maps and its construction process are presented below in [Section 3.5.3](#). We assume that the mask  $M_V$  represents the vessels, and the mask  $M_A$  represents only the aorta. We define the voxel layer  $L_d = \{\mathbf{k} \in M_V \mid dmap_{M_A}(\mathbf{k}) = d\}$  as a

subset of mask  $M_V$ , distanced from the mask  $M_A$  by the distance  $d$ . Note that the distance is measured in voxels, and it depends on the metric used in the distance map construction. For each voxel layer  $L_d$  for  $d = d_{\max}, \dots, 0$ , we apply the following procedure: remove all voxels from  $L_d$  that have no adjacent voxels in  $L_{d+1}$ . The parameter  $d_{\max}$  should be big enough, so that voxel layer  $L_{d_{\max}}$  contains no segmentation errors. In practice, we set  $d_{\max} = 15$ .

We should note that the proposed algorithms were designed for the vessels without pathological tortuosity. However, our experiments show that Frangi vesselness filter works for segmentation of tortuous vessels with S-like and C-like tortuosity, kinking, and coiling (Fig. 3.9).

### 3.5 Generation of computational meshes

This section covers mesh generation technique for solving numerically the systems of partial differential equations describing the deformation of elastic tissues and the dynamics of blood. Computational mesh is used to represent the model domain in a discrete form as the union of mesh elements. One way to treat the computation domain is to use voxel-based representation, where each voxel is a cubic mesh element. Unstructured adaptive tetrahedral meshes can be used to decrease the number of mesh elements and for more accurate approximation of complex geometries.

A 1D graph network of blood vessels can be considered as a special case of a computational mesh, with 1D segments as mesh elements.

#### 3.5.1 Tetrahedral mesh generation techniques

A computational mesh may be generated by several methods. One can start from generating a surface mesh using the marching cubes algorithm for recovering the zero of the distance function [91]. Next, one can postprocess the surface mesh by triangulation smoothing and coarsening algorithm [92]. Once the surface mesh is available, one can use

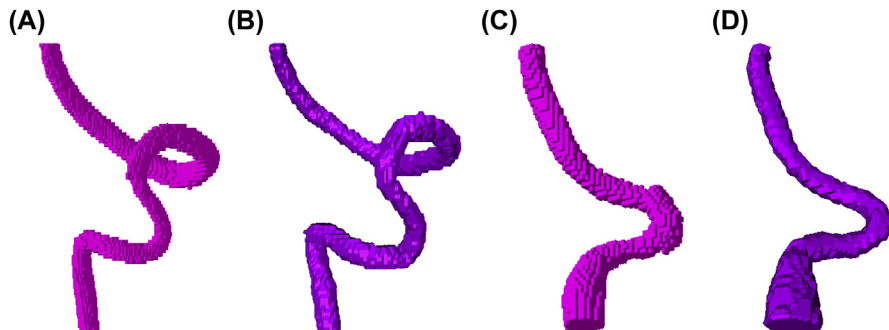


**Figure 3.9**

Segmentation of tortuous vessels: (A, B)—coiling, (C, D)—kinking, (A, C)—Frangi vesselness segmentation, (B, D)—manual reference segmentation.

3D Delaunay triangulation [93] and advancing front technique for volume mesh generation [93,94].

We suggest the application of the Delaunay triangulation algorithm from the CGAL-Mesh library [95]. The domain is defined implicitly by a segmentation image. Mesh generation is based on Delaunay refinement, followed by global optimization, perturbation, and sliver exudation. The surface mesh is generated along with volume mesh. This algorithm also enables the definition of a mesh size for each model material, thus generating adaptive meshes. One can assign a smaller mesh size to blood vessels and a larger mesh size to fat and muscle tissues to preserve geometric features of the segmented model while keeping the number of mesh elements minimal. Mesh cosmetics algorithms from the Ani3D library are used to improve mesh quality. This last step is essential to reduce the error of the finite element discretization and the condition number of the resulted matrices.

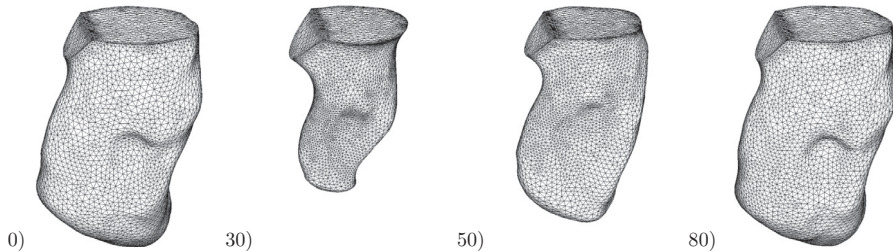
### ***3.5.2 Dynamic 3D mesh generation***

We illustrate the performance of our method for solving the Navier–Stokes equations in a moving domain. The method is applied to simulate a flow in a model of the left ventricle of a human heart. We consider the left ventricle due to its hemodynamic significance, but the method is equally applicable to the right ventricle.

The motion of the ventricle is recovered from a sequence of ceCT images of a real patient. The input data was a data set of 100 images with  $512 \times 512 \times 480$  voxels and  $0.625 \times 0.625 \times 0.25$  mm resolution. The images were taken from a chest ceCT of a 50-year-old female.

The dynamic grid model is built in several steps.

On the first step, the application of Delaunay triangulation from CGAL Mesh library [95] for the first segmented image yields an unstructured tetrahedral mesh with typical mesh size 0.7 mm. The left ventricle domain is defined implicitly by segmented image. This domain is also explicitly restricted by two valve planes. We enforce each tetrahedron to have at least one internal node by splitting each cell with four boundary nodes. The main requirement for a 3D dynamic grid model of the heart ventricle is to preserve mesh connectivity: In the sequence of grids, only nodal positions change. We deform the mesh by moving nodes for each subsequent image. At the first stage, we move only boundary nodes while simultaneously propagating and smoothing the surface mesh. This procedure is performed iteratively. At each iteration, each boundary node is shifted in the direction of the weighted sum of two vectors: the surface normal vector (weight 0.2) and the vector pointing at the center of surrounding nodes (weight 0.4). This procedure is repeated until the maximum node displacement at the current iteration drops below  $\varepsilon = 0.001$  mm, or until the maximum number of 2000 iterations is exceeded. Note that the above algorithm

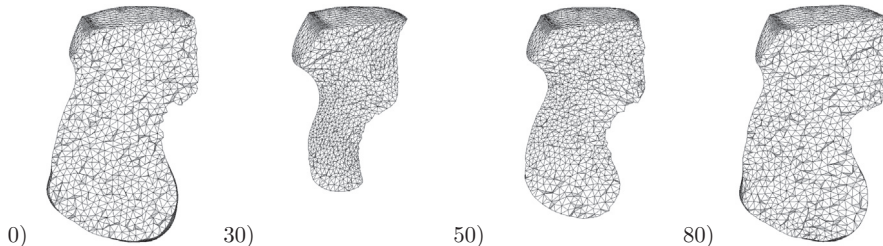
**Figure 3.10**

Surface triangular mesh of the left ventricle for several computed tomography images.

does not recover the material trajectories of ventricle points and therefore may produce spurious tangential velocities on the boundary. We pay a special attention to the nodes on the valve planes: they should always stay on the planes (Fig. 3.10). At the second stage, we simultaneously apply untangling and smoothing algorithm [96]; the boundary nodes are fixed, and only the internal nodes are shifted. The untangling stage is robust due to the presence of internal nodes in all tetrahedra. The final output is the series of *topologically invariant* meshes with 14,033 nodes, 88,150 edges, and 69,257 tetrahedra for the left ventricle recovered from the dynamic ceCT images (Fig. 3.11).

### 3.5.3 1D meshes

It is convenient to describe tubular structures using a notion of centerline. There exist several methods of centerlines extraction without image segmentation. Since our objective is to generate 1D vascular networks and 3D reconstruction of local vascular regions, we shall not address these methods. Skeletonization is a fully automatic approach for centerline extraction. The thinning method generates vascular skeletonization. The input for the method is a binary mask of segmented object. The output is a skeleton (one-voxel thick set of connected voxels). The postprocessing step is used for automatic centerlines extraction and graph construction.

**Figure 3.11**

Volume cut of the tetrahedral mesh of the left ventricle for several computed tomography images.

Among different implementations of the thinning idea, we adopt the distance-ordered homotopic thinning proposed in Ref. [97]. The algorithm starts with a binary mask  $M$  and outputs the skeleton topologically equivalent to  $M$  and centered with respect to the shape of  $M$ . Voxel  $\mathbf{k}$  is called *simple*, if it can be deleted from  $M$  by setting  $M(\mathbf{k}) = 0$  without topology modification of the shape of  $M$ . The rule for determining whether voxel is simple or not can be found in Ref. [98].

The centeredness of the skeleton is determined by the order of voxel elimination from  $M$ . Following [97], we define a chamfer distance transform approximating Euclidean distance transform:

$$\text{dmap}(\mathbf{k}) = \begin{cases} 0, & \text{if } M(\mathbf{k}) = 0, \\ \min_{\mathbf{k}_0 \in N_{26}(\mathbf{k})} (\text{dmap}(\mathbf{k}_0) + \text{dist}(\mathbf{k}, \mathbf{k}_0)), & \text{if } M(\mathbf{k}) = 1. \end{cases}$$

The initial value for all foreground voxels  $\mathbf{k}$  in this recursive definition is defined as  $\text{dmap}(\mathbf{k}) = \text{inf}$ , the value of  $\text{inf}$  is big enough (e.g., the threefold total number of foreground voxels), and  $\text{dist}(\mathbf{k}, \mathbf{k}_0)$  is defined as

$$\text{dist}(\mathbf{k}, \mathbf{k}_0) = \begin{cases} n_1, & \text{if } \|\mathbf{k} - \mathbf{k}_0\|^2 = 1, \\ n_2, & \text{if } \|\mathbf{k} - \mathbf{k}_0\|^2 = 2, \\ n_3, & \text{if } \|\mathbf{k} - \mathbf{k}_0\|^2 = 3. \end{cases}$$

In Ref. [99], it is shown that setting  $n_1 = 3$ ,  $n_2 = 4$ , and  $n_3 = 5$  minimizes the upper bound on the difference between the chamfer and Euclidean distances. In the definition of  $\text{dist}(\mathbf{k}, \mathbf{k}_0)$ , we use Euclidean norm, assuming that voxel is a unit cube.

During the thinning process, the voxels are sorted by dmap values in the ascending order and are deleted in groups with equal values. The paper [97] defines a center of a maximal ball using the chamfer transform definition and introduces the following two *deletability* rules:

1. A voxel is deletable if it is simple and not the center of a maximal ball with distance value greater than a user-defined threshold.
2. A voxel is deletable if it is simple and not the end of a medial axis (i.e., it is 6-adjacent to one and only one foreground voxel).

In the original work, the first rule is used at the first stage of thinning process, and the second rule is used at the second stage. In practice, this approach leads to a skeleton with several false twigs, usually near bifurcations and flattened vessels, which do not correspond to any actual vessel. False twigs are attributed to superfluous topology features caused by initial image noises and irregularities of vessel shape.

We developed an alternative approach: we use the algorithm from Ref. [97] with the second deletability rule, and then we apply a postprocessing stage to eliminate false twigs. This technique allows us to identify vessel structure using a postprocessed skeleton.

As described above, the skeletonization process preserves the network topology but may produce false twigs to be eliminated. For mathematical definition of false twigs, we will use the following notations. Two voxels are called *adjacent*, if one of them is 26-adjacent to another.

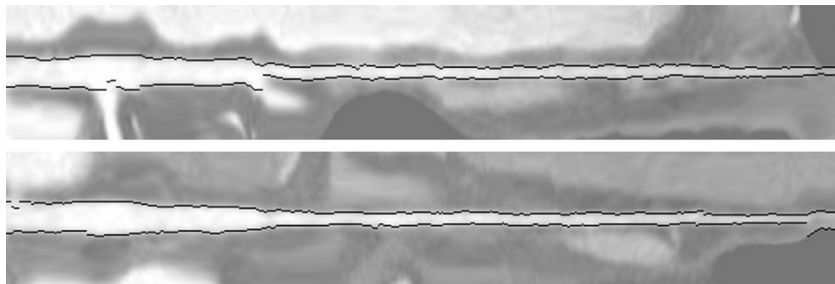
Skeleton voxel is called *inner*, if it has exactly two adjacent voxels. Skeleton voxel that is not inner is called *voxel node*. Skeleton voxel with at most one adjacent voxel is called *end node*. The connectivity component of inner voxels along with two bounding voxel nodes defines the *skeletal segment*. The voxel nodes of a skeletal segment are called *segment ends*. The *length* of a skeletal segment is defined as a number of voxels in the skeletal segment. Finally, a *false twig* is a skeletal segment with one of the segment ends being an end node, and the length of the skeletal segment is smaller than a user-defined threshold parameter.

The algorithm for false twigs elimination was developed in Ref. [100]. It consists of the following steps. All skeletal segments with end nodes as segment ends are identified. All segments with length smaller than the threshold are eliminated simultaneously. The skeleton thickness is enforced: voxel nodes adjacent to eliminated skeletal segments are analyzed, and excessive voxel nodes are eliminated. If at least one skeletal segment is eliminated, we start over. Importantly, all existing false twigs should be eliminated simultaneously; otherwise, valid vessel branches may be accidentally eliminated.

Once the skeleton is cleared from false twigs, the 1D graph reconstruction is straightforward. Each skeletal segment corresponds to a centerline of a vessel segment. The centers of voxels along the skeletal segment define the centerline of the segment.

The connectivity component of voxel nodes is used to define the graph node coordinates. The latter are coordinates of the barycenter of the connectivity component of the voxel nodes. Each skeletal segment has two associated segment ends, which belong to some voxel nodes components, which in turn correspond to graph nodes. This information is used to specify the connectivity of the graph.

For each skeletal segment, we need to compute the length of the segment and measure local diameter and curvature across the segment. Since skeleton is a voxel structure, the segments are represented as zigzag lines, due to the sequential connection of the voxels of the skeleton. Therefore, we should first smooth the discrete line of the skeleton segment, to calculate the derivatives along the curve. Splines are generally a good choice for fitting curved lines to discrete points [101]. A lot of algorithms are available for spline reconstruction. Here, we use multilevel B-splines [102].

**Figure 3.12**

Two straightened reformatted images of a coronary vessel with lumen contours.

The local curvature of the line is calculated by the conventional formula for Cartesian coordinates. Let the curve  $\gamma$  be parameterized in the form  $\gamma(t) = (x(t), y(t), z(t))$ , then the local curvature is

$$k = \frac{\sqrt{(z''y' - y''z')^2 + (x''z' - z''x')^2 + (y''x' - x''y')^2}}{(x'^2 + y'^2 + z'^2)^{\frac{3}{2}}}.$$

To compute the vessel lumen, we use the curved planar reformation [103]. This technique allows us to generate straightened reformatted images, representing the vessel as a straight line ([Fig. 3.12](#)). The lumen contours are detected by a minimum cost path algorithm [104].

# *Equations of fluid dynamics and elasticity*

## 4.1 Introduction

Blood is composed primarily of red blood cells (RBCs) suspended in plasma with volume fraction about 40%. In the traditional approach, blood is considered as a two-component fluid (RBCs and plasma). Therefore, one can apply the laws of continuum mechanics to model its motion on macroscopic length and time scales.

Soft biological tissues reveal a wide spectrum of material structures and properties. In this chapter, we deal with those whose response to a load can be described by the principles of continuum mechanics.

### 4.1.1 Basics of continuum mechanics

To describe the motion of a continuum medium, one operates with the notions of the *deformation* of a body with respect to a reference configuration and the *velocity* of material points constituting the body. Following the principles of Newtonian mechanics, the motion of a continuum medium is produced by the action of forces, where one distinguishes between *body forces* and *surface forces* applied to an arbitrary volume of the medium. The surface forces are exerted by neighboring particles of the medium along imaginary internal surfaces and are called *stress*. A material-depended *constitutive law* is then formulated to provide the relation between deformations and stresses for a given medium. Based on these fundamental principles, one derives partial differential equations (PDEs) that describe the kinematics of the medium (fluid or elastic body). In this section, we review main steps and arrive at basic equations used further in this book.

We start with some notations. Denote by  $\hat{\mathbf{x}} \in \mathbb{R}^3$  an Euclidean coordinate of a given material particle in a reference configuration of continuum body (for the reference, we can take the configuration at time  $t = 0$ ), and let  $\mathbf{x}(t, \hat{\mathbf{x}})$  be its position at time instance  $t \geq 0$ . Then,  $\mathbf{u}(t, \hat{\mathbf{x}}) = \mathbf{x}(t, \hat{\mathbf{x}}) - \hat{\mathbf{x}}$  is the *displacement* vector field,  $\hat{\mathbf{v}} = \dot{\mathbf{x}}_t$  is the *velocity in reference coordinates*, and  $\hat{\mathbf{v}}_t$  is the acceleration. The motion of the body can be defined through the one-to-one mapping  $\xi$  from the reference coordinates to the actual ones,  $\mathbf{x} = \xi(t, \hat{\mathbf{x}})$ , leading to the *Lagrangian* description of the motion. Alternatively, one can use the mapping from the actual coordinates to the reference coordinates,  $\hat{\mathbf{x}} = \xi^{-1}(t, \mathbf{x})$  ending up with the *Eulerian* description of the motion.

Same quantities can be written in both the reference (Lagrangian) and physical (Eulerian) coordinates. For example,  $\mathbf{v}(t, \mathbf{x}) = \hat{\mathbf{v}}(t, \xi^{-1}(t, \mathbf{x}))$  for the velocity of a particle in position  $\mathbf{x}$  at time  $t$ . In more general, we shall use notation  $\hat{f}$  for a quantity defined in Lagrangian coordinates and  $f$  for its Eulerian counterpart. We always assume they are related through  $f(t, \mathbf{x}) = \hat{f}(t, \xi^{-1}(t, \mathbf{x}))$  identity. Since we are interested in derivatives of  $f$ , we always assume that  $\xi$  is sufficiently smooth.

For relating derivatives in Lagrangian and Eulerian coordinates, one applies the product rule. Thus, the rate of change of a quantity  $\hat{f}$  for material point  $\hat{\mathbf{x}}$  is, obviously,  $\dot{\hat{f}}_t$  in the reference coordinates, whereas in the Eulerian coordinates, one obtains

$$\dot{\hat{f}}_t = [f(t, \xi(t, \hat{\mathbf{x}}))]_t = f_t + \xi_t \cdot \nabla_{\mathbf{x}} f = f_t + \hat{\mathbf{v}}(t, \hat{\mathbf{x}}) \cdot \nabla_{\mathbf{x}} f = f_t + \mathbf{v} \cdot \nabla_{\mathbf{x}} f. \quad (4.1)$$

The Eulerian quantity on the right-hand side is known as the *material derivative* of  $f$ ,

$$\dot{f} := f_t + \mathbf{v} \cdot \nabla_{\mathbf{x}} f. \quad (4.2)$$

The material derivative can be observed as the rate of change of a quantity  $f$  along the material path of a particle.

The conservation laws for mass and momentum will lead us to governing equations written in terms of basic quantities characterizing the behavior of the continuous medium such as displacement, velocity vector field, and their derivatives. These conservation laws can be written for arbitrary *material volume*  $V$  of the medium, which is an open subset of Euclidean space consisting for all times of the same material particles (thus,  $\hat{V} = \xi^{-1}(V)$  is fixed in reference coordinates, but  $V$  depends on time in physical coordinates). Further,  $\partial V$  denotes the boundary of  $V$ . In physical (Eulerian) coordinates, the conservation of mass for  $V$  then reads

$$\frac{d}{dt} \int_{V(t)} \rho(t, \mathbf{x}) d\mathbf{x} = 0, \quad (4.3)$$

where  $\rho(t, \mathbf{x})$  is the *density* of mass distribution. The conservation of linear momentum can be written as

$$\frac{d}{dt} \int_{V(t)} \rho(t, \mathbf{x}) \mathbf{v}(t, \mathbf{x}) d\mathbf{x} = \int_{\partial V(t)} \mathbf{f}_v(t, \mathbf{x}) ds + \int_{V(t)} \rho(t, \mathbf{x}) \mathbf{f}(t, \mathbf{x}) d\mathbf{x}, \quad (4.4)$$

where  $\mathbf{f}_v$  are the contact (surface) forces on  $\partial V(t)$ ,  $\mathbf{f}$  are the volume (body) forces.

Equality (4.4) can be seen as a generalization of the second Newton law.

To represent the surface forces, one introduces the *Cauchy stress tensor*  $\boldsymbol{\sigma}$ . Let  $\mathbf{n}$  denote the external unit normal vector on  $\partial V$ ; then from the basic principles of continuum mechanics, it follows that there exists such  $\boldsymbol{\sigma} : (t, \mathbf{x}) \rightarrow \mathbb{R}^{3 \times 3}$  that  $\mathbf{f}_v = \boldsymbol{\sigma} \mathbf{n}$  on

$\partial V(t)$  (cf. [166]). Thus,  $\sigma(t, \mathbf{x})$  is the tensor field defined in a continuum body such that for any unit vector  $\mathbf{n}$ ,  $\sigma\mathbf{n}$  defines forces acting on the elementary area around  $\mathbf{x}$  with the normal  $\mathbf{n}$  to  $\partial V(t)$  at time  $t$ . The normal component of the vector  $\sigma\mathbf{n}$ , i.e.,  $\mathbf{n}^T\sigma\mathbf{n}$ , is called the *normal stress*, and the tangential component of  $\sigma\mathbf{n}$ , i.e.,  $\sigma\mathbf{n} - (\mathbf{n}^T\sigma\mathbf{n})\mathbf{n}$ , is called *shear stress*.

Using the notion of Cauchy stress tensor, the conservation of linear momentum for the material volume  $V$  takes the form:

$$\frac{d}{dt} \int_{V(t)} \rho \mathbf{v} \, d\mathbf{x} = \int_{\partial V(t)} \sigma \mathbf{n} \, ds + \int_{V(t)} \rho \mathbf{f} \, d\mathbf{x}. \quad (4.5)$$

#### 4.1.2 From conservation laws to partial differential equations

Conservation laws written in terms of integral equalities as in Eqs. (4.3) and (4.5) are not always convenient to design numerical algorithms. The next step would be to rewrite them in terms of *pointwise* identities for  $\mathbf{v}$ ,  $\sigma$ ,  $\rho$ , and their derivatives. Furthermore, we shall always assume that these quantities are smooth in time and space. Two well-known results from vector calculus will be of help. The first one is the *Stokes theorem*,

$$\int_{\partial V} \mathbf{f} \cdot \mathbf{n} \, ds = \int_V \operatorname{div} \mathbf{f} \, d\mathbf{x} \quad (4.6)$$

for a sufficiently smooth vector field  $\mathbf{f}$  in  $V$ . The second is the *Reynolds transport theorem*,

$$\frac{d}{dt} \int_{V(t)} f \, d\mathbf{x} = \int_{V(t)} (f_t + \operatorname{div}(f\mathbf{v})) \, d\mathbf{x}, \quad (4.7)$$

where  $f$  is a sufficiently smooth function in  $V$  and  $\mathbf{v}$  is the velocity of material points constituting the volume  $V$ , as defined above.

With the help of Eqs. (4.6) and (4.7), we rewrite the conservation of mass (Eq. 4.3) and linear momentum (Eq. 4.5) as

$$\int_{V(t)} (\rho_t + \operatorname{div}(\rho\mathbf{v})) \, d\mathbf{x} = 0 \quad (4.8)$$

and

$$\int_{V(t)} ((\rho\mathbf{v})_t + \operatorname{div}(\rho\mathbf{v}\mathbf{v}^T) - \operatorname{div} \sigma - \rho \mathbf{f}) \, d\mathbf{x} = 0, \quad (4.9)$$

where we applied the Reynolds transport theorem componentwise (for each component of vector  $\mathbf{v}$  separately) to the integral on the left-hand side of Eq. (4.5). We note that in Eq. (4.9), the  $\operatorname{div}$  operator is applied to each row vector in tensors  $\mathbf{vv}^T$  and  $\boldsymbol{\sigma}$ . We also recall that the notation  $\mathbf{vv}^T = \mathbf{v} \otimes \mathbf{v}$  is used for the direct products of two vectors, i.e.,  $\mathbf{vv}^T$  is the symmetric  $3 \times 3$  matrix (tensor) with entries  $(\mathbf{vv}^T)_{i,j} = (\mathbf{v} \otimes \mathbf{v})_{i,j} = v_i v_j$ .

Finally, we use the following fact from analysis: for a continuous function  $f$  in  $\mathbb{R}^3$ ,  $\int_V f \, dx = 0$  for arbitrary volume  $V \in \mathbb{R}^3$  implies  $f = 0$  everywhere (see, e.g., [184]). The

same holds true if instead of  $\mathbb{R}^3$  we define  $f$  in a domain  $\Omega \subset \mathbb{R}^3$  and consider all subdomains  $V \subset \Omega$ . Applying this result to Eqs. (4.8) and (4.9) allows one to rewrite the balance laws in terms of PDEs defined pointwise,

$$\rho_t + \operatorname{div}(\rho \mathbf{v}) = 0 \quad (4.10)$$

and

$$(\rho \mathbf{v})_t + \operatorname{div}(\rho \mathbf{v} \mathbf{v}^T) - \operatorname{div} \boldsymbol{\sigma} = \rho \mathbf{f}. \quad (4.11)$$

Equalities (4.10) and (4.11) are defined in physical domains for each observation instance  $t$  and represent the conservation of mass and linear momentum in the Eulerian coordinates. Noting  $\operatorname{div}(\rho \mathbf{v} \mathbf{v}^T) = \operatorname{div}(\rho \mathbf{v}) \mathbf{v} + \rho(\mathbf{v} \cdot \nabla) \mathbf{v}$ , one can use Eq. (4.10) to simplify Eq. (4.11). Using this and the notion of material derivative, one can write Eqs. (4.10) and (4.11) as

$$\dot{\rho} + \rho \operatorname{div} \mathbf{v} = 0 \quad (4.12)$$

and

$$\rho \dot{\mathbf{v}} - \operatorname{div} \boldsymbol{\sigma} = \rho \mathbf{f}. \quad (4.13)$$

It is clear that the system of one equation in (4.12) and three equations in (4.13) is not complete, since we have more unknowns than equations. To close the system, one has to specify constitutive equations, which relate stress and density to  $\mathbf{v}$  or  $\mathbf{u}$  (recall that  $\mathbf{v}$  can be defined through  $\mathbf{u}$ ). Finding suitable constitutive equations, which are material dependent, is a part of modeling. For fluids, such as blood, the constitutive equation typically relates stress to the *rate-of-deformation* tensor:

$$\mathbf{D}(\mathbf{v}) = \frac{1}{2} (\nabla \mathbf{v} + (\nabla \mathbf{v})^T),$$

and its invariants, pressure  $p$ , and possibly other thermodynamic or chemical states of the medium. For elastic solids, such as wall of blood vessels or soft tissues, the stress depends on the *deformation gradient tensor*:

$$\mathbf{F} = \nabla_{\hat{\mathbf{x}}} \xi = \mathbf{I} + \nabla_{\hat{\mathbf{x}}} \mathbf{u}$$

and other material parameters. Density may also depend on pressure, temperature, etc. However, we shall see that, in many practical cases, it can be treated as a material parameter rather than unknown.

It is instructive to write [Eqs. \(4.12\) and \(4.13\)](#) in the Lagrangian coordinates. To this end, we introduce determinant of  $\mathbf{F}$ ,  $J = \det(\mathbf{F})$ , which defines the relative change of volume under the deformation. From the reversibility and orientation preserving property of  $\xi$  (cf. [191]), it follows that  $\mathbf{F}$  is nonsingular and  $J > 0$  for all  $\hat{\mathbf{x}}$  and  $t$ . Since the Lagrangian coordinates preserve the material points, the mass conservation [Eq. \(4.12\)](#) reduces to

$$\hat{\rho}(\hat{\mathbf{x}}, t) = \rho(\mathbf{x}(\hat{\mathbf{x}}, t), t)J(\hat{\mathbf{x}}, t). \quad (4.14)$$

The linear momentum conservation equation in Lagrangian coordinates is discussed in [Section 4.2.4](#).

Next, we discuss in more detail equations describing the dynamics of blood flows, the Navier–Stokes equations, and the set of equations we use to model the motion of elastic vessels and soft tissues, the elasticity equations. In [Section 4.4](#), we discuss the coupling of these two models.

## 4.2 The Navier–Stokes equations

### 4.2.1 Governing equations

Many biological fluids, such as blood, can be treated as *incompressible*. This refers to the property that any material volume of fluid does not change in time  $J = 1$ , i.e., the density  $\hat{\rho}(t, \hat{\mathbf{x}})$  for any material point  $\hat{\mathbf{x}}$  of fluid does not change,  $\hat{\rho}_t = 0$ . In the Eulerian coordinates, this implies that the material derivative of  $\rho$  vanishes, that is,

$$\dot{\rho} = 0. \quad (4.15)$$

It is often plausible to assume that the fluid is homogeneous, i.e., the density distribution at the initial moment is uniform; then, [Eq. \(4.15\)](#) implies that  $\rho = \text{const}$  for all times and so can be treated as a material parameter. Together with the mass conservation [Eq. \(4.12\)](#), the equality [\(4.15\)](#) leads to

$$\text{div } \mathbf{v} = 0. \quad (4.16)$$

[Eq. \(4.16\)](#) is often referred to as the incompressibility condition for a fluid flow with velocity field  $\mathbf{v}$ .

Blood is a viscous fluid. Its simplest model is given by the constitutive equation of the *Newtonian viscous fluid*,

$$\boldsymbol{\sigma} = -p\mathbf{I} + \lambda \text{div } \mathbf{v} \mathbf{I} + 2\mu \mathbf{D}(\mathbf{v}),$$

where  $\lambda$  and  $\mu$  are fluid (viscosity) parameters and  $p$  is the pressure. We assume no dependence of material parameters, density, and pressure on the temperature. The assumption is valid for the fluids of constant temperature (isothermal), which is relevant for many blood flows. For the incompressible fluid, the constitutive equation reduces to

$$\boldsymbol{\sigma} = -p \mathbf{I} + 2\mu\mathbf{D}(\mathbf{v}). \quad (4.17)$$

Summarizing Eqs. (4.13), (4.15)–(4.17), we arrive at the following set of equations for the basic fluid model used in this book, the system of *the Navier–Stokes equations* for the incompressible viscous Newtonian isothermal fluid,

$$\begin{cases} \rho \left( \frac{\partial \mathbf{v}}{\partial t} + (\mathbf{v} \cdot \nabla) \mathbf{v} \right) - 2\mu \operatorname{div} \mathbf{D}(\mathbf{v}) + \nabla p = \rho \mathbf{f} \\ \operatorname{div} \mathbf{v} = 0 \end{cases} \quad (4.18)$$

with constant density and viscosity coefficients  $\rho > 0$  and  $\mu > 0$  and given body forces  $\mathbf{f}$ , e.g., gravity force. Eq. (4.18) is written in the Eulerian coordinates. Later, we discuss other useful formulations of the Navier–Stokes equations and introduce initial and boundary conditions necessary to close the system.

In Newtonian fluids, the viscosity coefficient  $\mu$  in Eq. (4.17) does not depend on the rate of strain. For flows of blood plasma and blood flows in arteries with diameters larger than  $\sim 1$  mm, it is plausible to assume that  $\mu$  is constant, and experimental measurements show  $\mu \in [0.003, 0.004]$  Pa·s [43]. In smaller vessels, in particular vessels with diameters below 0.1 mm, the blood may exhibit non-Newtonian fluid behavior, and more accurate models should include a dependence of  $\mu$  on the invariants of the rate of strain tensor [193, 43]. For hemorheology in the microcirculation, we refer to the review paper [42].

### 4.2.2 Energy balance

Conservation of energy is a fundamental law of nature, which was not explicitly used so far to deduce the governing Eq. (4.18). It is, however, easy to show that any (smooth) solutions to Eq. (4.18) satisfy suitable energy balance. To see this, let us consider any material volume  $V(t)$  consisting of fluid particles. We further take an inner product of the momentum equation (4.18) with  $\mathbf{v}$  and integrate over  $V(t)$ . Using the notion of the material derivative, we get

$$\int_{V(t)} (\rho \dot{\mathbf{v}} \cdot \mathbf{v} - 2\mu \operatorname{div} \mathbf{D}(\mathbf{v}) \mathbf{v} + \mathbf{v} \cdot \nabla p) \, d\mathbf{x} = \int_{V(t)} \rho \mathbf{f} \cdot \mathbf{v} \, d\mathbf{x}.$$

Now we apply the Reynolds transport theorem (4.7) to  $f = |\mathbf{v}|^2$ , the incompressibility condition (4.16), and integrate by parts the viscous and pressure terms. Recalling the relation for the stress tensor (Eq. 4.17), we get the following energy balance:

$$\underbrace{\frac{1}{2} \frac{d}{dt} \int_{V(t)} \rho |\mathbf{v}|^2 d\mathbf{x}}_{\text{rate of change of kinetic energy}} = -2\mu \underbrace{\int_{V(t)} |\mathbf{D}(\mathbf{v})|^2 d\mathbf{x}}_{\text{viscous energy dissipation}} + \underbrace{\int_{\partial V(t)} (\boldsymbol{\sigma} \mathbf{n}) \cdot \mathbf{v} ds}_{\text{work of surface forces}} + \underbrace{\int_{V(t)} \rho \mathbf{f} \cdot \mathbf{v} d\mathbf{x}}_{\text{work of body forces}}. \quad (4.19)$$

Thus, all smooth solutions to the Navier–Stokes Eq. (4.18) obey the fundamental energy balance (Eq. 4.19). The identity (4.19) can take slightly different forms, depending on boundary conditions and the choice of  $V(t)$ . For numerical methods, it is important to ensure that computed (approximate, discrete) solutions satisfy an analog of the energy balance (Eq. 4.19).

### 4.2.3 Boundary conditions

For the system of fluid equations to be closed, we need to supply it with initial and boundary conditions. For the initial condition, it is common to assume that the velocity of fluid is known everywhere in the flow domain,  $\mathbf{v}(0, \mathbf{x}) = \mathbf{v}_0(\mathbf{x})$  with some given  $\mathbf{v}_0$ .

Although in many cases knowing the initial state  $\mathbf{v}_0$  is not feasible, the influence of the error in the initial guess on the computed solution is not significant for larger  $t$ . For obvious reasons, practically important blood flows happen and being computed in bounded volumes. We introduce the notation  $\Omega$  for the domain in Eulerian coordinate system where the fluid equations are posed ( $\Omega$  may depend on  $t$ ). The choice of suitable boundary conditions on  $\partial\Omega$  is important.

We shall distinguish between the no-slip, no-penetration, inflow, outflow, and interface conditions. Interface conditions are imposed on interfaces between fluid and other continuum medium (e.g., a different fluid or elastic body), which motion is unknown and finding it is a part of the problem. Interface conditions relevant for cardiovascular applications will be discussed in Section 4.4.1. To introduce other conditions, recall that the mapping  $\xi(t): \widehat{\Omega} \rightarrow \Omega$  from the reference domain  $\widehat{\Omega}$  to the physical domain  $\Omega$  defines the material trajectories for all  $\widehat{\mathbf{x}} \in \widehat{\Omega}$ . The condition that fluid does not penetrate through the part of the boundary,  $\partial\Omega^{ns} \subset \partial\Omega$ , then reads

$$\mathbf{n} \cdot \mathbf{v} = \mathbf{n} \cdot (\xi_t \circ \xi^{-1}) \quad \text{on } \partial\Omega^{ns}, \quad (4.20)$$

i.e., the normal fluid velocity equals the normal velocity of the boundary. The *no-penetration condition* (4.20) is not enough and should be supplemented with a tangential condition. For viscous fluids, the most common is the *no-slip condition*,

$$\mathbf{n} \times \mathbf{v} = \mathbf{n} \times (\xi_t \circ \xi^{-1}) \quad \text{on } \partial\Omega^{ns}, \quad (4.21)$$

which states that the tangential component of fluid velocity coincides with the tangential velocity of the boundary (fluid particles attach to the boundary). Conditions (4.20) and (4.21) together, of course, mean that the velocity of fluid along  $\partial\Omega$  is the same as the velocity of material points on the boundary,

$$\mathbf{v} = \xi_t \circ \xi^{-1} \quad \text{on } \partial\Omega^{ns}. \quad (4.22)$$

One can recognize  $\mathbf{v} = \mathbf{0}$  on  $\partial\Omega^{ns}$  for the case of *stationary* fluid domain.

The Dirichlet condition,

$$\mathbf{v} = \mathbf{v}_D \quad \text{on } \partial\Omega^D, \quad (4.23)$$

is often imposed on *inflow* parts of the boundary  $\partial\Omega^D$ , where the flow profile  $\mathbf{v}_D$  is assumed to be known. The Neumann condition,

$$\boldsymbol{\sigma}\mathbf{n} = \mathbf{g} \quad \text{on } \partial\Omega^N, \quad (4.24)$$

is useful on artificial *outflow* boundaries, where one lacks any suitable information on flow profile. It is common to set  $\mathbf{g}$  equal to zero or an approximate average value of normal stress exerted by an exterior medium on the fluid. If  $\partial\Omega^N = \emptyset$ , then one should ensure the consistency condition  $\int_{\partial\Omega^{ns}} \mathbf{n} \cdot \xi_t \circ \xi^{-1} \, ds + \int_{\partial\Omega^D} \mathbf{n} \cdot \mathbf{v}^D \, ds = 0$ .

No-penetration, no-slip, inflow (4.23), and outflow (4.24) conditions are the most often used boundary conditions in the modeling of blood flows. It is not rare, however, that other type of boundary conditions is better suited for modeling and simulations. On fluid–solid interfaces, the no-slip condition (4.21) models the adherence of fluid to the solid. This assumption is sometimes argued as not sufficiently justified, especially on the macroscopic level (see [201] and references therein). In certain situations, it makes sense to assume that the fluid may slip along a part  $\partial\Omega^{\text{slip}}$  of the solid boundary possibly generating friction forces. To model this phenomenon, one applies the *Navier boundary condition* also known as *slip with friction* condition [178]:

$$(\boldsymbol{\sigma}\mathbf{n} + \alpha\mathbf{v}) \times \mathbf{n} = 0 \quad \text{on } \partial\Omega^{\text{slip}}, \quad (4.25)$$

where  $\alpha > 0$  is a coefficient and  $\alpha^{-1}$  is known as slip length, which measures the ability of the fluid to slip along the boundary. We see that slip with friction condition assumes a linear resistance of fluid to slip. In even more general situations, nonlinear relations between normal stress and slip velocity can be used (see, e.g., [201]).

Next boundary condition looks more *ad hoc* but is proved to be useful in numerical simulations of many cardiovascular blood flow problems with artificial boundaries. For numerical purposes, it is common to cut a fluid domain along an imaginary surface  $\partial\Omega^{aux}$  (artificial boundary). It is a well-known problem to prescribe suitable boundary conditions on such a boundary, since little a priori information is available about a flow there. One popular option is setting the normal stresses to zero, i.e., Eq. (4.24) with  $\mathbf{g} = \mathbf{0}$ . It appears that, for problems with incoming (reverse) flows through artificial boundaries setting, Eq. (4.24) leads to energetically unstable models, since incoming flow may lead to a blowup of energy or nonphysical oscillations for the computed solution. To compensate for this inflow of excessive energy, one adds extra term to Eq. (4.24), which models boundary forces that diffuse the energy in the case of incoming flow [118, 114]:

$$\boldsymbol{\sigma}\mathbf{n} + \frac{\alpha}{2}(\mathbf{v}\cdot\mathbf{n})_-\mathbf{v} = \mathbf{0} \quad \text{on } \partial\Omega^{aux}, \quad (4.26)$$

with a parameter  $\alpha \in [0, 1]$  and  $(x)_- = \frac{1}{2}(|x| - x)$ . Condition (4.26) is known in the literature as *directional do-nothing* boundary condition. For other options of stabilizing boundary conditions for physiological flows on artificial boundaries, see, e.g., [110] and references therein.

#### 4.2.4 Fluid equations in Lagrangian and quasi-Lagrangian coordinates

One can rewrite fluid equations in the reference domain, using Lagrangian velocity and pressure variables. In Lagrangian coordinates system, the inertia terms in Eq. (4.18) simplify, but the viscous terms and incompressibility constrain get more complicated. In this section, all derivatives are assumed with respect to the reference coordinates  $\hat{\mathbf{x}}$ . Recall the notations  $\mathbf{F} = \nabla\xi$  for deformation gradient tensor and  $J = \det(\mathbf{F})$  for its determinant. Changing variables and applying the product rule for computing derivatives in Eq. (4.18), one obtains the set of the Navier–Stokes equations in Lagrangian coordinates:

$$\begin{cases} \hat{\rho}\hat{\mathbf{v}}_t - J^{-1}\operatorname{div}(J(\boldsymbol{\sigma}\circ\xi)\mathbf{F}^{-T}) = \hat{\rho}\hat{\mathbf{f}} \\ \operatorname{div}(J\mathbf{F}^{-1}\hat{\mathbf{v}}) = 0 \end{cases} \quad (4.27)$$

with body forces  $\hat{\mathbf{f}} = \mathbf{f}\circ\xi$ . Note that we have  $\dot{\mathbf{v}}\circ\xi = \hat{\mathbf{v}}_t$ . The constitutive relation (4.17) in the reference domain reads

$$\boldsymbol{\sigma}\circ\xi = -\hat{p}\mathbf{I} + \mu\left(\nabla\hat{\mathbf{v}}\mathbf{F}^{-1} + \mathbf{F}^{-T}(\nabla\hat{\mathbf{v}})^T\right). \quad (4.28)$$

In practice, it may happen that the motion of  $\Omega$  is given by a *non-Lagrangian* mapping from the reference domain to  $\Omega$ , i.e.,  $\xi(\hat{\mathbf{x}}, t)$  does not define a material trajectory for any  $\hat{\mathbf{x}} \in \hat{\Omega}$ . One example of non-Lagrangian mapping  $\xi$  is considered in Section 5.4.4 where it is recovered from a sequence of medical images of the motion of heart walls. Let such

mapping  $\xi$  be level preserving, i.e.,  $\xi(\hat{\Omega}, t) = \Omega(t)$  for all  $t \in [0, T]$ , and  $J > 0$ . If one uses such a non-Lagrangian mapping to formulate the fluid system in the reference coordinates, then the identity  $\dot{\mathbf{v}} \circ \xi = \hat{\mathbf{v}}_t$  is no longer true, and using Eq. (4.1) and the product rule, we get

$$\begin{aligned}\dot{\mathbf{v}} \circ \xi &= (\mathbf{v}_t + (\nabla_{\mathbf{x}} \mathbf{v}) \mathbf{v}) \circ \xi = \hat{\mathbf{v}}_t - \xi_t \cdot (\nabla_{\mathbf{x}} \mathbf{v}) \circ \xi + (\nabla_{\hat{\mathbf{x}}} \hat{\mathbf{v}}) \mathbf{F}^{-1} \hat{\mathbf{v}} \\ &= \hat{\mathbf{v}}_t + (\nabla_{\hat{\mathbf{x}}} \hat{\mathbf{v}}) (\mathbf{F}^{-1} (\hat{\mathbf{v}} - \xi_t)).\end{aligned}$$

We see that the inertia term does not simplify as in Eq. (4.27), and the momentum equation reads

$$\hat{\rho} (\hat{\mathbf{v}}_t + (\nabla \hat{\mathbf{v}}) (\mathbf{F}^{-1} (\hat{\mathbf{v}} - \xi_t))) - J^{-1} \operatorname{div} (J (\boldsymbol{\sigma} \circ \xi) \mathbf{F}^{-T}) = \hat{\rho} \hat{\mathbf{f}}. \quad (4.29)$$

#### 4.2.5 Arbitrary Lagrangian–Eulerian formulation

Eq. (4.27) shows that inertia terms in Lagrangian formulation look simpler than in the Eulerian form, but viscous terms become more complicated. From computational point of view, it is sometimes convenient to handle the time derivative in the reference domain, but to treat all other terms in the physical domain. For doing this, it is sufficient to know any smooth mapping  $\xi(t) : \hat{\Omega} \rightarrow \Omega(t)$  (not necessary Lagrangian) as in Eq. (4.29). Then identifying  $\hat{\mathbf{v}}(t, \hat{\mathbf{x}}) = \mathbf{v}(t, \xi(t, \hat{\mathbf{x}}))$ , one computes  $\mathbf{v}_t = \hat{\mathbf{v}}_t - \xi_t \cdot \nabla \mathbf{v}$ . This leads to the formulation of Eq. (4.18) known as Arbitrary Lagrangian–Eulerian (ALE) formulation

$$\left\{ \begin{array}{l} \rho \left( \frac{\partial \hat{\mathbf{v}}}{\partial t} + ((\mathbf{v} - \xi_t) \cdot \nabla) \mathbf{v} \right) - 2\mu \operatorname{div} \mathbf{D}(\mathbf{v}) + \nabla p = \rho \mathbf{f}, \\ \operatorname{div} \mathbf{v} = 0. \end{array} \right. \quad (4.30)$$

Vector field  $\xi_t$  is called ALE velocity.

#### 4.2.6 Flow regimes

The quantities in the flow problem (4.18) have the following physical units:  $\text{kg}/\text{m}^3$  for density  $\rho$ ,  $\text{kg}/(\text{s} \cdot \text{m})$  for viscosity coefficient  $\mu$ , and  $\text{m}/\text{s}$  for velocity  $\mathbf{v}$ . Assuming for a moment, that the domain is stationary and  $L$  is a characteristic linear dimension for this problem (for example,  $L = \operatorname{diam}(\Omega)$ ), one can define the dimensionless quantity,

$$Re = \frac{\rho V L}{\mu},$$

where  $V$  is a characteristic velocity for this problem (for example, the maximum of the inflow velocity  $\mathbf{v}_D$ ). In fluid dynamics, this important dimensionless quantity is known as *Reynolds* number. It helps to predict flow patterns and dynamic similarity in different fluid flow situations.

To see its role, one may rescale unknowns and variables in Eq. (4.18) to make them nondimensional,  $\mathbf{x} = L\mathbf{x}'$ ,  $\mathbf{v} = V\mathbf{v}'$ ,  $t = LV^{-1}t'$ ,  $p = \rho V^2 p'$ . We arrive at the nondimensional form of the Navier–Stokes equations,

$$\begin{cases} \frac{\partial \mathbf{v}}{\partial t} + (\mathbf{v} \cdot \nabla) \mathbf{v} - \frac{2}{Re} \operatorname{div} \mathbf{D}(\mathbf{v}) + \nabla p = \mathbf{f} \\ \operatorname{div} \mathbf{v} = 0. \end{cases} \quad (4.31)$$

From Eq. (4.31), we see that the Reynolds number is the ratio of inertial forces to viscous forces in the momentum equation.

When the viscous forces dominate (Re number is small), then one can neglect the nonlinear terms in Eq. (4.31) and arrive at the *Stokes system*. After further rescaling of pressure, right-hand side, and time variable, the Stokes problem takes the form:

$$\begin{cases} \frac{\partial \mathbf{v}}{\partial t} - \operatorname{div} \mathbf{D}(\mathbf{v}) + \nabla p = \mathbf{f} \\ \operatorname{div} \mathbf{v} = 0. \end{cases} \quad (4.32)$$

The Stokes system (Eq. 4.32) is used to model slow flows such as blood flow in capillary vessels.

In more general, for lower Reynolds numbers, fluid flows are characterized by low velocities, regular flow patterns, and dynamics happening over a narrow range of spatial and temporal scales. Such flows are called *laminar*. When the Reynolds number increases, the flow eventually becomes *turbulent*. The turbulent flow regime is characterized by complex vortical flow patterns, chaotic fluctuations in flow velocity and pressure, and the presence of flow dynamics over a wide range of length and time scales. One can also identify *transitional* flow regimes between very regular laminar and chaotic turbulent flows (see, e.g., [167]).

Most of hemodynamics is characterized by laminar blood flows (Fig. 4.1). Flows in aneurysms, aorta, and stenosed arteries are often classified as transitional [203, 197]. Turbulent blood flow regimes may be observed in the presence of some pathologies such as severe stenoses [197].

Direct numerical simulation of turbulent flows can be prohibitively expensive in terms of computational resources since one, in general, needs too many degrees of freedom to

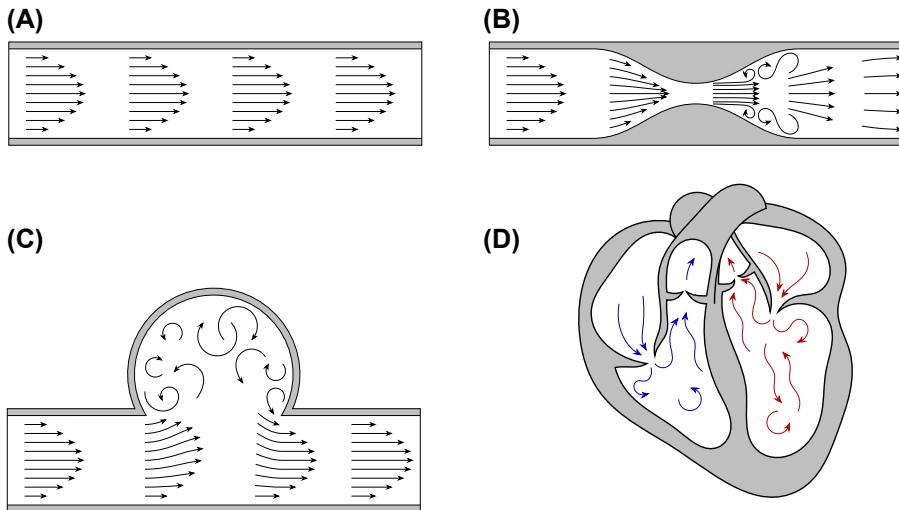


Figure 4.1

Blood flow: (A) laminar flow in vessel, (B) turbulent flow behind stenosis, (C) turbulent flow near aneurysm, (D) flow pattern in heart cavities may be complex.

resolve all spatial and temporal scales in the solution. Most often, one solves for averaged flow statistics such as averaged velocity and pressure. Deducing a complete set of equations for such averaged quantities is a well-known challenge, and available models of turbulence are based on certain empirical modeling assumptions. We do not elaborate this topic further in the book and instead refer the interested reader to the literature (see, e.g., [168]).

### 4.3 Equations for deformable bodies

In mathematical biomechanics, soft biological tissues are treated as deformable elastic bodies. Equations governing the motion of elastic medium are derived from the fundamental principles already discussed in [Section 4.1](#). In fact, all equations we deduced in that section remain valid. There are, however, two important differences between how one proceeds from [Eqs. \(4.12\) and \(4.13\)](#) in the case of fluids and solids. First, the equation of motion for deformable elastic bodies is conventionally written and treated numerically in Lagrangian coordinates, i.e., in the reference domain  $\hat{\Omega}$ . Thus, we consider the conservation of momentum equation in the Lagrangian form ([Eq. 4.27](#)):

$$\hat{\rho}\hat{\nabla}_t - J^{-1} \operatorname{div}(J\boldsymbol{\Sigma}\mathbf{F}^{-T}) = \hat{\rho}\hat{\mathbf{f}}. \quad (4.33)$$

Hereafter, we shall use the short notation  $\boldsymbol{\Sigma} = \boldsymbol{\sigma} \circ \boldsymbol{\xi}$  for the stress tensor in Lagrange coordinates and refer to  $J\boldsymbol{\Sigma}\mathbf{F}^{-T}$  as the *Piola–Kirchhoff tensor*.

Second, the constitutive equation for solids relates stress and *deformation*, rather than stress and rate of deformation as happens for fluids. Finding a constitutive law, which would be the best to describe a material at hand, is an important modeling question. In the following, we discuss a general framework and several models that have been proved to be useful in cardiovascular simulations.

### 4.3.1 General framework for hyperelastic materials

We further consider general constitutive laws for deformable bodies that relate the Cauchy stress  $\Sigma$  and the deformation gradient  $\mathbf{F}$ . The dependence of  $\Sigma$  on material properties and  $\mathbf{F}$  is very diverse depending on a material. To present many useful models within a single framework, we take advantage of the notion of hyperelasticity. Recall that a material is *elastic* if its constitutive law is defined entirely by the current deformation:  $\Sigma = \Sigma(\mathbf{F}, \hat{\mathbf{x}})$ . A material is said to be *hyperelastic* if the mechanical work spent for its deformation depends on the initial and final states only, i.e., the work is independent of the loading path and, therefore, is spent to change an energy of the material. Although, for many solids, hyperelasticity is only an idealized model, it was experimentally found to describe material properties of most biological tissues rather accurately [122].

Hyperelastic materials are characterized by an elastic potential (also known as a strain energy density function or a stored energy function)  $\Psi(\mathbf{F})$ , which defines the Cauchy stress tensor as

$$\Sigma = \frac{1}{J} \frac{\partial \Psi}{\partial \mathbf{F}} \mathbf{F}^T, \quad (4.34)$$

where matrix  $\frac{\partial \Psi}{\partial \mathbf{F}}$  has entries  $\left[ \frac{\partial \Psi}{\partial \mathbf{F}} \right]_{ij} = \frac{\partial \Psi}{\partial \mathbf{F}_{ij}}$ . Indeed, the mechanical work for deformation of the unit volume of a nondeformed body is [113, Section 5.2]

$$\Psi(\mathbf{F}) = \int_{t_0}^t (J \Sigma \mathbf{F}^{-T}) : \mathbf{F}_t dt \quad (4.35)$$

from which we have  $\Psi_t = (J \Sigma \mathbf{F}^{-T}) : \mathbf{F}_t$ . On the other hand, the chain rule gives us  $\Psi_t = \frac{\partial \Psi}{\partial \mathbf{F}} : \mathbf{F}_t$ , and therefore, we obtain Eq. (4.34).

Material is said to be *isotropic* at point  $\hat{\mathbf{x}}$  if its constitutive law is independent of any rotation  $\mathbf{Q}$  of the coordinate frame with origin at  $\hat{\mathbf{x}}$ ,  $\Sigma(\mathbf{F}, \hat{\mathbf{x}}) = \Sigma(\mathbf{F}\mathbf{Q}, \hat{\mathbf{x}})$ , i.e., its elastic properties are the same in all directions. Material is isotropic if it is isotropic at any point  $\hat{\mathbf{x}}$ . The elastic potential of an isotropic material should be independent of any rotation transformation as well,  $\Psi(\mathbf{F}) = \Psi(\mathbf{Q}\mathbf{F})$ . It is shown [124] that in this case  $\Psi$  is a function of the *right Cauchy–Green tensor*  $\mathbf{C} = \mathbf{F}^T \mathbf{F}$ , which defines the change of distance between two material points during the deformation. Therefore, we further assume that  $\Psi$  is given as a function of  $\mathbf{C}$ . One can use the chain rule to compute

$$\begin{aligned}\frac{\partial \Psi}{\partial \mathbf{F}_{ij}} &= \sum_{k,m=1}^3 \frac{\partial \Psi}{\partial \mathbf{C}_{km}} \frac{\partial \mathbf{C}_{km}}{\partial \mathbf{F}_{ij}} = \sum_{k,m=1}^3 \frac{\partial \Psi}{\partial \mathbf{C}_{km}} (\mathbf{F}_{im} \delta_j^k + \mathbf{F}_{ik} \delta_j^m) \\ &= \sum_{m=1}^3 \frac{\partial \Psi}{\partial \mathbf{C}_{jm}} \mathbf{F}_{im} + \sum_{k=1}^3 \frac{\partial \Psi}{\partial \mathbf{C}_{kj}} \mathbf{F}_{ik} = 2\mathbf{F} \frac{\partial \Psi}{\partial \mathbf{C}_{ij}}.\end{aligned}$$

Hence, Eq. (4.34) can be rewritten in the equivalent form:

$$\boldsymbol{\Sigma} = \frac{2}{J} \mathbf{F} \frac{\partial \Psi}{\partial \mathbf{C}} \mathbf{F}^T. \quad (4.36)$$

The  $3 \times 3$  right Cauchy–Green tensor  $\mathbf{C}$  has three principal invariants under a rigid coordinate transformation:

$$I_1 = \text{tr } \mathbf{C}, \quad I_2 = \frac{1}{2} ((\text{tr } \mathbf{C})^2 - \text{tr } \mathbf{C}^2), \quad I_3 = \det \mathbf{C} = J^2. \quad (4.37)$$

The principal invariants can be written in the componentwise notations:

$$I_1 = \sum_{i=1}^3 \mathbf{C}_{ii}, \quad I_2 = \frac{1}{2} \sum_{i,j=1}^3 (C_{ii}C_{jj} - C_{ij}C_{ji}), \quad I_3 = \sum_{i,j,k=1}^3 \epsilon_{ijk} C_{i1} C_{j2} C_{k3},$$

where  $\epsilon_{ijk}$  is 1 for even permutation of  $i, j, k$ ,  $-1$  for odd permutation of  $i, j, k$ , and 0 for  $i = j$  or  $j = k$  or  $i = k$ . One also defines the *left Cauchy–Green tensor*  $\mathbf{B} = \mathbf{F}\mathbf{F}^T$ , which has the same invariants  $I_1, I_2, I_3$ . We recall that  $J = \det \mathbf{F}$  shows the relative change of volume under the deformation. Materials featuring  $J = 1$  are called incompressible.

It is shown [124] that the elastic potential of an isotropic and homogeneous hyperelastic material is a function of the principal invariants of the right Cauchy–Green tensor  $\mathbf{C}$  (Eq. 4.37),  $\Psi = \Psi(I_1, I_2, I_3)$ . Therefore, the constitutive relation becomes

$$\boldsymbol{\Sigma} = \frac{2}{J} \mathbf{F} \left( \sum_{i=1}^3 \frac{\partial \Psi}{\partial I_i} \frac{\partial I_i}{\partial \mathbf{C}} \right) \mathbf{F}^T,$$

where

$$\frac{\partial I_1}{\partial \mathbf{C}} = \mathbf{I}, \quad \frac{\partial I_2}{\partial \mathbf{C}} = I_1 \mathbf{I} - \mathbf{C}, \quad \frac{\partial I_3}{\partial \mathbf{C}} = I_2 \mathbf{I} - I_1 \mathbf{C} + \mathbf{C}^2 \equiv I_3 \mathbf{C}^{-1}.$$

The last identity follows from Cayley–Hamilton theorem. Using these identities, one derives the general constitutive law for isotropic and homogeneous hyperelastic material:

$$\boldsymbol{\Sigma} = \frac{2}{J} \mathbf{F} \left[ \left( \frac{\partial \Psi}{\partial I_1} + I_1 \frac{\partial \Psi}{\partial I_2} + I_2 \frac{\partial \Psi}{\partial I_3} \right) \mathbf{I} - \left( \frac{\partial \Psi}{\partial I_2} + I_1 \frac{\partial \Psi}{\partial I_3} \right) \mathbf{C} + \frac{\partial \Psi}{\partial I_3} \mathbf{C}^2 \right] \mathbf{F}^T, \quad (4.38)$$

or in terms of  $\mathbf{B}$ :

$$\boldsymbol{\Sigma} = \frac{2}{J} \left( \frac{\partial \Psi}{\partial I_1} + I_1 \frac{\partial \Psi}{\partial I_2} \right) \mathbf{B} - \frac{2}{J} \frac{\partial \Psi}{\partial I_2} \mathbf{B}^2 + 2J \frac{\partial \Psi}{\partial I_3} \mathbf{I}. \quad (4.39)$$

A practically important group is *incompressible* elastic materials, i.e., the ones preserving the volume under the deformation. In laboratory tests, incompressible materials are more easy-to-handle. Therefore, it is a common practice that a basic elastic potential  $\Psi_{\text{inc}}$  for incompressible material is known. Then, a generalization of the potential to the compressible case is built as a “perturbation” of the incompressible potential:

$$\Psi_{\text{cmp}} = \Psi_{\text{inc}} + \Psi_{\text{vol}}(J), \quad (4.40)$$

where the last term is added to capture the pressure–volume response. The incompressibility constrain  $J = 1$  requires an extra term  $-p(J - 1)$  to be added to the incompressible elastic potential  $\Psi_{\text{inc}}$ , where  $p$  is the Lagrange multiplier. Although this term vanishes for  $J = 1$ , its derivative with respect to  $I_3 = J^2$  in Eq. (4.39) generates an extra “pressure” type term  $-p\mathbf{I}$  in the constitutive law.

We briefly mention heterogeneous materials. If the body material is *heterogeneous*, then it can be decomposed into homogeneous patches described by their own constitutive laws. The final problem formulations should take into account matching conditions on interfaces between different materials. The physically motivated interface conditions are the continuity of displacements and stresses.

Many biological tissues are considered to be composed of an isotropic matrix and elastic fibers, which introduce material anisotropy. In this case, the elastic potential can be represented in the form [122,152]:

$$\Psi = \Psi_{\text{iso}} + \Psi_{\text{aniso}}, \quad (4.41)$$

where the first term describes the isotropic part of the material and the second term involves additional rigidity of particular directions.

Let an anisotropic incompressible material have one family of fibers whose direction is given by a unit vector  $\mathbf{a}$  in the undeformed reference configuration. If the material demonstrates rotational symmetry about the direction of  $\mathbf{a}$ , then it is called locally transversally anisotropic. Elastic potential  $\Psi$  of locally transversally anisotropic material is a function of the right Cauchy–Green tensor  $\mathbf{C}$  and the structure tensor  $\mathbf{a} \otimes \mathbf{a}$ . Incompressibility of the material ( $I_3 = J^2 = 1$ ) yields dependence of  $\Psi$  on two (instead of three) invariants  $I_1, I_2$ , whereas dependence on  $\mathbf{a} \otimes \mathbf{a}$  leads to dependence on two invariants of the structure tensor,  $I_4 = \mathbf{a} \cdot (\mathbf{Ca}), I_5 = \mathbf{a} \cdot (\mathbf{C}^2\mathbf{a})$ :

$$\Psi(\mathbf{F}) = \Psi(I_1, I_2, I_4, I_5) = \Psi_{\text{iso}}(I_1, I_2) + \Psi_{\text{aniso}}(I_4, I_5).$$

According to Eq. (4.39), the Cauchy stress is given by

$$\Sigma = -p\mathbf{I} + 2\Psi_1\mathbf{B} + 2\Psi_2(I_1\mathbf{B} - \mathbf{B}^2) + 2\Psi_4\mathbf{a}_F \otimes \mathbf{a}_F + 2\Psi_5(\mathbf{a}_F \otimes \mathbf{B}\mathbf{a}_F + \mathbf{B}\mathbf{a}_F \otimes \mathbf{a}_F), \quad (4.42)$$

where  $\Psi_i := \frac{\partial \Psi}{\partial I_i}$ ,  $\mathbf{a}_F := \mathbf{F}\mathbf{a}$ . In laboratory, one performs four independent tests to find  $\Psi_1$ ,  $\Psi_2$ ,  $\Psi_4$ ,  $\Psi_5$  and to set up the constitutive law for a locally transversally anisotropic material.

Some biological tissues (e.g., artery wall with collagen fibers) are strengthened by *two* families of fibers given by unit vectors  $\mathbf{a}, \mathbf{a}'$  in the undeformed reference configuration. Elastic potential

$$\Psi(\mathbf{F}) = \Psi(I_1, I_2, I_4, I_5, I_6, I_7, I_8) = \Psi_{\text{iso}}(I_1, I_2) + \Psi_{\text{aniso}}(I_4, I_5, I_6, I_7, I_8)$$

has three additional invariants  $I_6 = \mathbf{a}' \cdot (\mathbf{C}\mathbf{a}')$ ,  $I_7 = \mathbf{a}' \cdot (\mathbf{C}^2\mathbf{a}')$ , and  $I_8 = \mathbf{a} \cdot (\mathbf{C}\mathbf{a}')( \mathbf{a} \cdot \mathbf{a}' )$ , and application of Eq. (4.39) yields constitutive relation:

$$\begin{aligned} \Sigma &= -p\mathbf{I} + 2\Psi_1\mathbf{B} + 2\Psi_2(\mathbf{I}_1\mathbf{B} - \mathbf{B}^2) \\ &\quad + 2\Psi_4\mathbf{a}_F \otimes \mathbf{a}_F + 2\Psi_5(\mathbf{a}_F \otimes \mathbf{B}\mathbf{a}_F + \mathbf{B}\mathbf{a}_F \otimes \mathbf{a}_F) \\ &\quad + 2\Psi_6\mathbf{a}'_F \otimes \mathbf{a}'_F + 2\Psi_7(\mathbf{a}'_F \otimes \mathbf{B}\mathbf{a}'_F + \mathbf{B}\mathbf{a}'_F \otimes \mathbf{a}'_F) + \Psi_8(\mathbf{a}_F \otimes \mathbf{a}'_F + \mathbf{a}'_F \otimes \mathbf{a}_F). \end{aligned} \quad (4.43)$$

The sum of any isotropic incompressible elastic potential  $\Psi_{\text{iso}}$  and  $\Psi_{\text{aniso}}$  can be used in Eq. (4.43) to define the Cauchy stress tensor. An example of the elastic potential (Eq. 4.41) for the artery wall was suggested in [152]:

$$\Psi_{\text{iso}} = \frac{\mu}{2}(I_1 - 3), \quad \Psi_{\text{aniso}} = \frac{\mu_2}{2\mu_3} \left\{ \exp[\mu_3(I_4 - 1)^2] + \exp[\mu_3(I_6 - 1)^2] - 2 \right\},$$

with matrix elasticity parameter  $\mu$  and fiber elasticity parameters  $\mu_2$  and  $\mu_3$ . Note that  $\Psi_{\text{aniso}}$  is active only if fibers are stretched,  $I_4 > 1$  or  $I_6 > 1$ .

Now we are ready to consider several popular choices of the isotropic elastic potentials, which are motivated by different assumptions on the medium behavior.

### 4.3.2 Models of hyperelastic materials

The Green–Lagrange strain tensor is given by

$$\mathbf{E} = \frac{1}{2}(\mathbf{C} - \mathbf{I}) = \frac{1}{2}(\nabla\mathbf{u} + \nabla\mathbf{u}^T + \nabla\mathbf{u}^T \nabla\mathbf{u}).$$

Tensor  $\mathbf{E}$  measures the deformation relative to the reference (undeformed) configuration. It is defined completely by  $\mathbf{C}$  and reduces to the linear strain tensor  $\frac{1}{2}(\nabla\mathbf{u} + \nabla\mathbf{u}^T)$  in case of small deformations. Using the definition of  $\mathbf{E}$ , one can rewrite Eq. (4.36) as:

$$\Sigma = \frac{1}{J} \mathbf{F} \frac{\partial \Psi}{\partial \mathbf{E}} \mathbf{F}^T. \quad (4.44)$$

The Saint Venant–Kirchhoff model of a compressible isotropic material is given by

$$\Psi_{SVK} = \frac{\lambda}{2}(\text{tr } \mathbf{E})^2 + \mu \text{tr } \mathbf{E}^2. \quad (4.45)$$

The *Saint Venant–Kirchhoff material* is the simplest compressible model with the Hooke's constitutive law applicable for finite (but not necessarily small) deformations:

$$\Sigma_{SVK} = \frac{1}{J} \mathbf{F} (\lambda(\text{tr } \mathbf{E}) \mathbf{I} + 2\mu \mathbf{E}) \mathbf{F}^T. \quad (4.46)$$

The linear elasticity model follows from Eqs. (4.44)–(4.46) under the assumption of infinitesimal deformation, when  $\|\mathbf{u}\| \ll 1$  and  $\|\nabla \mathbf{u}\| \ll 1$ . In this case, the second-order term in  $\mathbf{E}$  can be neglected and the Green–Lagrange strain tensor becomes linear:

$$\mathbf{E}_L = \frac{1}{2} (\nabla \mathbf{u} + \nabla \mathbf{u}^T).$$

An isotropic linear material is defined by the elastic potential:

$$\Psi_{L,\text{iso}} = \frac{\lambda}{2}(\text{tr } \mathbf{E}_L)^2 + \mu \text{tr } \mathbf{E}_L^2, \quad (4.47)$$

where the *Lamé parameters*  $\lambda$  and  $\mu$  are defined from the experimentally observed *Poisson's coefficient*  $\nu$  and *Young's modulus*  $E$ :

$$\lambda = \frac{E\nu}{(1+\nu)(1-2\nu)}, \quad \mu = \frac{E}{2(1+\nu)}.$$

Eqs. (4.44) and (4.47) lead to the constitutive law of *linear elasticity*:

$$\Sigma_{L,\text{iso}} = \frac{1}{J} \mathbf{F} (\lambda(\text{tr } \mathbf{E}_L) \mathbf{I} + 2\mu \mathbf{E}_L) \mathbf{F}^T = \frac{1}{J} \mathbf{F} (\lambda(\text{div } \mathbf{u}) \mathbf{I} + \mu(\nabla \mathbf{u} + \nabla \mathbf{u}^T)) \mathbf{F}^T. \quad (4.48)$$

Under the assumption of linear elasticity, the strain is infinitesimal, and one has  $J \approx 1 + \text{tr } \mathbf{E}_L$ ,  $\mathbf{F} \approx \mathbf{I}$ , and  $\mathbf{F}^T \approx \mathbf{I}$ . After simplifications based on these approximations, Eq. (4.48) becomes the standard Hooke's law:

$$\Sigma_{L,\text{iso}} = \lambda(\text{tr } \mathbf{E}_L) \mathbf{I} + 2\mu \mathbf{E}_L. \quad (4.49)$$

Another popular model for isotropic biological tissues is the *neo-Hookean model* of a compressible isotropic material [122]:

$$\Psi_{NH} = \frac{\mu}{2} (I_1 - 3 + d(J^2 - 1) - 2(d+1)(J-1)), \quad (4.50)$$

which gives rise to the neo-Hookean constitutive relation:

$$\Sigma_{NH} = \mu \mathbf{B} + \mu(dJ - d - 1) \mathbf{I}. \quad (4.51)$$

The neo-Hookean model is used in surgical simulators for modeling of mechanical behavior of kidney and liver [159]. However, the model cannot describe stiffening of soft tissue at very large deformations. An often adopted rule of thumb is to use the neo-Hookean model at range of deformation up to 100%.

Now, we consider several practical incompressible models. We already mentioned that, for incompressible materials, the constitutive law contains the extra term  $-p\mathbf{I}$ .

If deformations are small, the incompressibility condition  $J = 1$  can be written in the form of the constrain  $\text{div } \mathbf{u} = 0$  or  $\text{tr } \mathbf{E}_L = 0$ . Therefore, for the linear incompressible elastic model, the elastic potential (Eq. 4.47) and the constitutive law (Eq. 4.48) reduce to

$$\Psi_{L,\text{inc}} = \mu \text{tr } \mathbf{E}_L^2, \quad \Sigma_{L,\text{inc}} = 2\mu \mathbf{E}_L - p\mathbf{I}, \quad (4.52)$$

whereas, for the neo-Hookean model (finite deformations), the elastic potential and constitutive relation are

$$\Psi_{NH,\text{inc}} = \frac{\mu}{2}(I_1 - 3), \quad \Sigma_{NH,\text{inc}} = \mu \mathbf{B} - p\mathbf{I}. \quad (4.53)$$

Incompressible models applicable at large deformations are the *Gent model* [153] with parameter  $J_m \gg 1$ :

$$\Psi_{G,\text{inc}} = -\frac{\mu J_m}{2} \ln \left( 1 - \frac{I_1 - 3}{J_m} \right), \quad (4.54)$$

and the *Yeoh model* with  $C_1 = \mu/2$  and parameters  $C_2, \dots, C_n$  [210],

$$\Psi_{Y,\text{inc}} = \sum_{i=1}^n C_i (I_1 - 3)^i. \quad (4.55)$$

The Gent model can be used for soft tissues containing reinforcing fibers such as arterial walls. The Yeoh model was shown to be adequate for a wide range of deformations [176].

The incompressible Gent and Yeoh constitutive laws are

$$\Sigma_{G,\text{inc}} = \frac{\mu J_m}{J_m - I_1 + 3} \mathbf{B} - p\mathbf{I}, \quad \Sigma_{Y,\text{inc}} = 2 \sum_{i=1}^n i C_i (I_1 - 3)^{i-1} \mathbf{B} - p\mathbf{I}. \quad (4.56)$$

These equations are readily reduced to Eq. (4.53) when  $J_m \rightarrow \infty$  and  $n = 1$ .

#### 4.4 Fluid–structure interaction

In cardiovascular simulations, one is often interested in numerical simulation of blood dynamics and tissues deformation at once. Such a problem involves mutual interaction of a fluid (blood) and an elastic structure (tissue): Fluid flow depends on the structure

displacement, whereas structure motion is influenced by the fluid dynamics. In mathematical modeling, such setup is known as a *fluid–structure interaction (FSI)* problem. Examples of FSI problems arising in computational hemodynamics include blood flow in a compliant elastic vessel and flow passing heart valves or vascular stent.

In the previous sections, we separately considered equations governing the fluid dynamics and the motion of elastic materials. For a complete description of an FSI problem, one needs to prescribe coupling conditions on the fluid–structure interface and the evolution of the fluid domain due to the motion of the structure. In the following, we discuss interface conditions and equations constituting a standard FSI problem.

Trying to understand or simulate numerically an FSI problem, one should keep in mind that equations of fluid dynamics are commonly given in the Eulerian coordinates, whereas, for solids motion, one usually uses Lagrangian description.

#### 4.4.1 Interface conditions

Assume that the fluid and solid motion takes place in a time-dependent domain  $\Omega(t) \subset \mathbb{R}^3$  that is partitioned into subdomain  $\Omega^f(t)$  occupied by the fluid and subdomain  $\Omega^s(t)$  occupied by the solid medium (structure). Let  $\Gamma^{fs}(t) := \partial\Omega^f(t) \cap \partial\Omega^s(t)$  be the interface where the interaction of the fluid and solid material happens. The initial configuration will be further used to define the reference domains in the Lagrangian framework,

$$\widehat{\Omega}_f = \Omega^f(0), \quad \widehat{\Omega}_s = \Omega^s(0), \quad \widehat{\Gamma}_{fs} = \Gamma^{fs}(0).$$

The first condition, which is commonly assumed on the fluid–structure interface, is the continuity of fluid and structure velocities, i.e., the fluid does not penetrate through the structure, and fluid particles adhere to it (no slip). Mathematically, this condition can be written as

$$\mathbf{v}^f = \mathbf{v}^s \quad \text{on } \Gamma^{fs}(t).$$

Since the solid motion is often defined in terms of displacements with respect to the reference configuration,  $\mathbf{u}^s(\widehat{\mathbf{x}}, t)$ , it is common to write the continuity of velocity interface condition in the form:

$$\mathbf{v}^f = \mathbf{u}_t^s \circ \xi^{-1} \quad \text{on } \Gamma^{fs}(t) \quad \text{or} \quad \mathbf{v}^f \circ \xi = \mathbf{u}_t^s \quad \text{on } \widehat{\Gamma}_{fs}, \quad (4.57)$$

where  $\xi(\widehat{\mathbf{x}}, t) = \widehat{\mathbf{x}} + \mathbf{u}$  is the Lagrangian mapping from  $\widehat{\Omega}_s$  to  $\Omega^s(t)$  ([Fig. 4.2](#)).

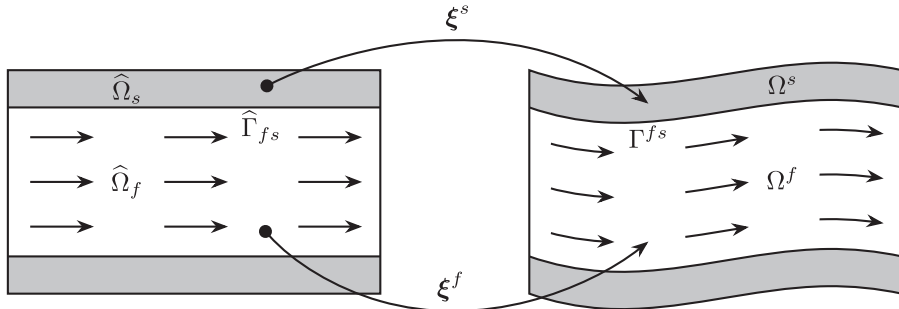


**Figure 4.2**  
Reference (initial) and deformed (current) configurations.

The second condition results from the balance of contact forces on  $\Gamma^{fs}(t)$ . Equating surface forces acting on an elementary area of  $\Gamma^{fs}(t)$  from the solid and fluid sides leads to the balance of the normal stresses:

$$\boldsymbol{\sigma}^f \mathbf{n} = \boldsymbol{\sigma}^s \mathbf{n} \quad \text{on } \Gamma^{fs}(t),$$

where  $\boldsymbol{\sigma}^f$ ,  $\boldsymbol{\sigma}^s$  are fluid and surface Cauchy stress tensors, and  $\mathbf{n}$  is the normal vector to  $\Gamma^{fs}(t)$ . Again switching from physical to reference coordinates, we can equivalently write

$$(\boldsymbol{\sigma}_f \circ \xi) \mathbf{F}^{-T} \hat{\mathbf{n}} = \boldsymbol{\Sigma}_s \mathbf{F}^{-T} \hat{\mathbf{n}} \quad \text{on } \hat{\Gamma}_{fs}, \quad (4.58)$$

where  $\hat{\mathbf{n}}$  is the normal vector to  $\hat{\Gamma}_{fs}$ .

#### 4.4.2 Fluid domain motion

In an FSI problem, fluid equations are solved in a time-dependent domain. There is, however, an important difference to the situation discussed in [Section 4.2](#). The evolution of  $\Omega^f(t)$  is not given *a priori* any more, and finding it is a part of the FSI problem.

Assuming for the sake of clarity that only  $\Gamma_{fs}$  part of the boundary  $\partial\Omega^f(t)$  depends on time, we see that the evolution of fluid domain is completely determined by the motion of the elastic structure and that the velocity of  $\hat{\Gamma}_{fs}(t)$  is equal to the velocity of solid particles on the interface. To formulate this observation mathematically, we recall that the evolution of  $\Omega^f(t)$  can be described through the mapping from the reference domain to the physical domain occupied by the fluid,  $\xi^f : \hat{\Omega}_f \rightarrow \Omega^f(t)$ . Thus, we have the condition:

$$\xi^f = \hat{\mathbf{x}} + \mathbf{u}^s \quad \text{on } \hat{\Gamma}_{fs}. \quad (4.59)$$

This is, of course, equivalent to  $\xi^f = \xi^s$  on  $\hat{\Gamma}_{fs}$ , i.e., the mapping  $\xi$  is continuous over the interface. This mapping is Lagrangian and is defined by the displacement field  $\mathbf{u}$  as  $\xi^s = \hat{\mathbf{x}} + \mathbf{u}^s$  in the solid part  $\hat{\Omega}_s$ . In the fluid part, however, the mapping does not have to follow material trajectories, and one has an option to choose any sufficiently smooth

mapping  $\xi^f : \widehat{\Omega}_f \rightarrow \Omega^f(t)$  that satisfies Eq. (4.59) and  $\xi^f = \widehat{\mathbf{x}}$  on  $\partial\widehat{\Omega}_f - \widehat{\Gamma}_{fs}$  (other parts of the fluid domain boundary are static). In fact, one needs to define a smooth *extension of the displacement field* from the solid to the flow reference domains:

$$\mathbf{u}^f := \text{Ext}(\mathbf{u}^s) \quad \text{in } \widehat{\Omega}_f, \quad (4.60)$$

which is *continuous* over the interface (a consequence of Eq. (4.59)) and such that

$$\mathbf{u}^f = 0 \quad \text{on } \partial\widehat{\Omega}_f - \widehat{\Gamma}_{fs}. \quad (4.61)$$

Furthermore, one may set  $\xi^f(\widehat{\mathbf{x}}, t) = \widehat{\mathbf{x}} + \mathbf{u}^f$ . Now, when  $\Omega^f(t)$  is defined through the mapping  $\xi^f$ , one can opt for the Eulerian formulation of the fluid equations in the physical domain or, as alternative, one can use quasi-Lagrangian or arbitrary Lagrangian–Eulerian formulation of the fluid problem.

The extension in Eq. (4.60) can be defined in different ways. For numerical stability, one is interested in an extension with possibly small gradients and such that its Jacobian in  $\widehat{\Omega}_f$  is strictly positive and well separated from zero. Finding a suitable extension in the case of not small deformations may be a challenging task. One popular extension method consists in finding  $\mathbf{u}^f$  as a solution to an auxiliary elliptic PDE in  $\widehat{\Omega}_f$  with boundary conditions:

$$\mathbf{u}^f = \mathbf{u}^s \quad \text{on } \widehat{\Gamma}_{fs} \quad (4.62)$$

and Eq. (4.61). One standard choice of PDE is the linear elasticity equation (see, e.g., [188]):

$$-\text{div} (\lambda_m(\text{div } \mathbf{u})\mathbf{I} + \mu_m(\nabla\mathbf{u} + \nabla\mathbf{u}^T)) = 0 \quad \text{in } \widehat{\Omega}_f, \quad (4.63)$$

with space-dependent auxiliary Lame parameters  $\lambda_m, \mu_m$ . However, other options including nonlinear elasticity and biharmonic equations are available (see, for example, [188, 194, 207]).

#### 4.4.3 Complete system of equations and energy balance

Once we defined a (auxiliary) displacement field  $\mathbf{u}^f$  in the fluid domain, it is convenient to write out the FSI system of PDEs using the continuous displacement and velocity fields defined in the reference domain:

$$\mathbf{u} = \begin{cases} \mathbf{u}^s & \text{in } \widehat{\Omega}_s, \\ \mathbf{u}^f & \text{in } \widehat{\Omega}_f, \end{cases} \quad \mathbf{v} = \begin{cases} \mathbf{v}^s & \text{in } \widehat{\Omega}_s, \\ \mathbf{v}^f & \text{in } \widehat{\Omega}_f. \end{cases}$$

In this section, we shall omit hats in notations of Lagrangian velocities in  $\widehat{\Omega}$ . Velocity is continuous due to the interface condition (4.57) and  $\mathbf{u}$  is continuous by construction of the

extension operator. In the reference solid domain (but not in fluid domain), one, of course, has the relation:

$$\mathbf{u}_t = \mathbf{v} \text{ in } \widehat{\Omega}_s. \quad (4.64)$$

Hence,  $\mathbf{v}$  is the Lagrangian velocity for the solid and quasi-Lagrangian for the fluid. The deformation gradient is  $\mathbf{F} = \mathbf{I} + \nabla \mathbf{u}$ , and its determinant  $J := \det(\mathbf{F})$  is also defined globally in  $\widehat{\Omega}$ .

Denote by  $\rho_s$  and  $\rho_f$  the densities of solid and fluid. The momentum Eqs. (4.29) and (4.33) for the fluid and the solid in the reference subdomains can be combined:

$$\frac{\partial \mathbf{v}}{\partial t} = \begin{cases} \rho_s^{-1} \operatorname{div}(J \boldsymbol{\Sigma}_s \mathbf{F}^{-T}) + \hat{\mathbf{f}} & \text{in } \widehat{\Omega}_s, \\ (J \rho_f)^{-1} \operatorname{div}(J(\boldsymbol{\sigma}_f \circ \boldsymbol{\xi}^f) \mathbf{F}^{-T}) - (\nabla \mathbf{v}) \left( \mathbf{F}^{-1} \left( \mathbf{v} - \frac{\partial \mathbf{u}}{\partial t} \right) \right) + \hat{\mathbf{f}} & \text{in } \widehat{\Omega}_f. \end{cases} \quad (4.65)$$

If the fluid is incompressible, then we also have the mass conservation equation:

$$\operatorname{div}(J \mathbf{F}^{-1} \mathbf{v}) = 0 \text{ in } \widehat{\Omega}_f, \quad (4.66)$$

and an additional variable, the fluid pressure  $p^f$ . For the complete FSI system, one complements Eqs. (4.65) and (4.66) with Eq. (4.64), extension rule (Eq. 4.60), interface conditions (4.57), (4.58), and (4.62), as well as suitable initial and boundary conditions.

It is instructive to find the total energy balance of the FSI system. For the brevity, we consider the homogeneous boundary conditions in Eqs. (4.23) and (4.24) for fluid and the free-stress boundary condition for the solid on  $\partial\widehat{\Omega}_s - \widehat{\Gamma}_{fs}$ . Using integration by parts, one checks the identity:

$$\begin{aligned} & \int_{\widehat{\Omega}_f} ((\mathbf{w} \cdot \nabla u)v) + \frac{1}{2} ((\operatorname{div} \mathbf{w})uv) d\mathbf{x} \\ &= \int_{\widehat{\Omega}_f} \frac{1}{2} ((\mathbf{w} \cdot \nabla u)v) - ((\mathbf{w} \cdot \nabla v)u) d\mathbf{x} + \frac{1}{2} \int_{\partial\widehat{\Omega}_f} (\mathbf{n} \cdot \mathbf{w})uv \, d.s. \end{aligned} \quad (4.67)$$

Multiplying the first equality in Eq. (4.65) by  $\rho_s \mathbf{v}$ , the second one by  $J \rho_f \mathbf{v}$ , integrating over the reference domain, and employing Eq. (4.67) give

$$\begin{aligned}
 & \frac{1}{2} \frac{d}{dt} \left( \int_{\widehat{\Omega}_s} \rho_s |\mathbf{v}|^2 d\mathbf{x} + \rho_f \int_{\widehat{\Omega}_f} J |\mathbf{v}|^2 d\mathbf{x} \right) - \frac{\rho_f}{2} \int_{\widehat{\Omega}_f} \frac{\partial J}{\partial t} |\mathbf{v}|^2 d\mathbf{x} \\
 & + \int_{\widehat{\Omega}_s} J \boldsymbol{\Sigma}_s \mathbf{F}^{-T} : \nabla \mathbf{v} d\mathbf{x} + \int_{\widehat{\Omega}_f} J (\boldsymbol{\sigma}_f \circ \xi^f) \mathbf{F}^{-T} : \nabla \mathbf{v} d\mathbf{x} \\
 & - \frac{\rho_f}{2} \int_{\widehat{\Omega}_f} \operatorname{div} \left( J \mathbf{F}^{-1} \left( \mathbf{v} - \frac{\partial \mathbf{u}}{\partial t} \right) \right) |\mathbf{v}|^2 d\mathbf{x} + \frac{\rho_f}{2} \int_{\Gamma_{out}} \mathbf{v} \cdot \mathbf{n} |\mathbf{v}|^2 ds = \int_{\widehat{\Omega}} \widehat{\mathbf{f}} \cdot \mathbf{v} d\mathbf{x}.
 \end{aligned}$$

Now note that the Reynolds transport equality (4.7) applied to  $f = J$  brings us to the identity:

$$\frac{\partial J}{\partial t} + \operatorname{div} \left( J \mathbf{F}^{-1} \left( \mathbf{v} - \frac{\partial \mathbf{u}}{\partial t} \right) \right) = 0 \quad \text{in } \widehat{\Omega}_f. \quad (4.68)$$

This identity leads to some cancellations and we get

$$\begin{aligned}
 & \frac{1}{2} \frac{d}{dt} \left( \int_{\widehat{\Omega}_s} \rho_s |\mathbf{v}|^2 d\mathbf{x} + \rho_f \int_{\widehat{\Omega}_f} J |\mathbf{v}|^2 d\mathbf{x} \right) + \int_{\widehat{\Omega}_s} J \boldsymbol{\Sigma}_s \mathbf{F}^{-T} : \nabla \mathbf{v} d\mathbf{x} \\
 & + \int_{\widehat{\Omega}_f} J (\boldsymbol{\sigma}_f \circ \xi^f) \mathbf{F}^{-T} : \nabla \mathbf{v} d\mathbf{x} + \frac{\rho_f}{2} \int_{\Gamma_{out}} \mathbf{v} \cdot \mathbf{n} |\mathbf{v}|^2 ds = \int_{\widehat{\Omega}} \widehat{\mathbf{f}} \cdot \mathbf{v} d\mathbf{x}.
 \end{aligned}$$

The third term corresponds to the variation of the elastic energy. To see this, we can rewrite it using the elastic potential  $\Psi$ . From the principle of the mechanical work (Eq. 4.35), we have  $\Psi_t(\mathbf{F}) = (J \boldsymbol{\Sigma} \mathbf{F}^{-T}) : \mathbf{F}_t$ . With the help of this equality, we get

$$\begin{aligned}
 & \int_{\widehat{\Omega}_s} J \boldsymbol{\Sigma}_s \mathbf{F}^{-T} : \nabla \mathbf{v} d\mathbf{x} = \int_{\widehat{\Omega}_s} J \boldsymbol{\Sigma}_s \mathbf{F}^{-T} : \nabla \frac{\partial \mathbf{u}}{\partial t} d\mathbf{x} \\
 & = \int_{\widehat{\Omega}_s} J \boldsymbol{\Sigma}_s \mathbf{F}^{-T} : \frac{\partial \mathbf{F}}{\partial t} d\mathbf{x} = \int_{\widehat{\Omega}_s} \frac{\partial \Psi(\mathbf{F})}{\partial t} d\mathbf{x} = \frac{d}{dt} \int_{\widehat{\Omega}_s} \Psi(\mathbf{F}) d\mathbf{x}.
 \end{aligned}$$

Now we need the Piola identity  $\operatorname{div}(J\mathbf{F}^{-1}) = 0$ , which implies the following equality:

$$\operatorname{div}(J\mathbf{F}^{-1}\mathbf{v}) = J(\nabla\mathbf{v}) : \mathbf{F}^{-T} \quad \text{in } \widehat{\Omega}_f. \quad (4.69)$$

Using the notation  $\widehat{\mathbf{D}}(\mathbf{v}) = \frac{1}{2}(\nabla\mathbf{v}\mathbf{F}^{-1} + \mathbf{F}^{-T}(\nabla\mathbf{v})^T)$  for the rate of deformation tensor in the (quasi)-Lagrangian coordinates, we get with the help of Eqs. (4.28), (4.66), and (4.69):

$$\int_{\widehat{\Omega}_f} J(\boldsymbol{\sigma}_f \circ \boldsymbol{\xi}^f) \mathbf{F}^{-T} : \nabla\mathbf{v} \, d\mathbf{x} = 2\mu_f \int_{\widehat{\Omega}_f} J|\widehat{\mathbf{D}}(\mathbf{v})|_F^2 \, d\mathbf{x}.$$

Here and in the remainder,  $|\cdot|_F$  stands for the Frobenius norm. Therefore, the final energy equality takes the form:

$$\begin{aligned} & \frac{1}{2} \frac{d}{dt} \left( \int_{\widehat{\Omega}_s} \rho_s |\mathbf{v}|^2 \, d\mathbf{x} + \rho_f \int_{\widehat{\Omega}_f} J|\mathbf{v}|^2 \, d\mathbf{x} + \int_{\widehat{\Omega}_s} \Psi(\mathbf{F}) \, d\mathbf{x} \right) \\ & + 2\mu_f \int_{\widehat{\Omega}_f} J|\widehat{\mathbf{D}}(\mathbf{v})|_F^2 \, d\mathbf{x} + \frac{\rho_f}{2} \int_{\Gamma_{\text{out}}} \mathbf{v} \cdot \mathbf{n} |\mathbf{v}|^2 \, ds = \int_{\widehat{\Omega}} \widehat{\mathbf{f}} \cdot \mathbf{v} \, d\mathbf{x}, \end{aligned} \quad (4.70)$$

i.e., the variation of the total system energy is balanced by the fluid viscous dissipation, and the energy rate at the open boundary and the work of external forces.

In case of Saint Venant–Kirchhoff material (Eq. 4.45), the elastic energy is

$$\int_{\widehat{\Omega}_s} \Psi(\mathbf{F}) \, d\mathbf{x} = \frac{1}{2} \int_{\widehat{\Omega}_s} \left( \lambda_s \operatorname{tr}(\mathbf{E})^2 + 2\mu_s |\mathbf{E}|_F^2 \right) \, d\mathbf{x}.$$

In case of incompressible neo-Hookean material (Eq. 4.53), the elastic energy is

$$\int_{\widehat{\Omega}_s} \Psi(\mathbf{F}) \, d\mathbf{x} = \frac{1}{2} \int_{\widehat{\Omega}_s} \mu_s (|\mathbf{F}|_F^2 - 3) \, d\mathbf{x}.$$

# ***3D vascular and heart hemodynamics***

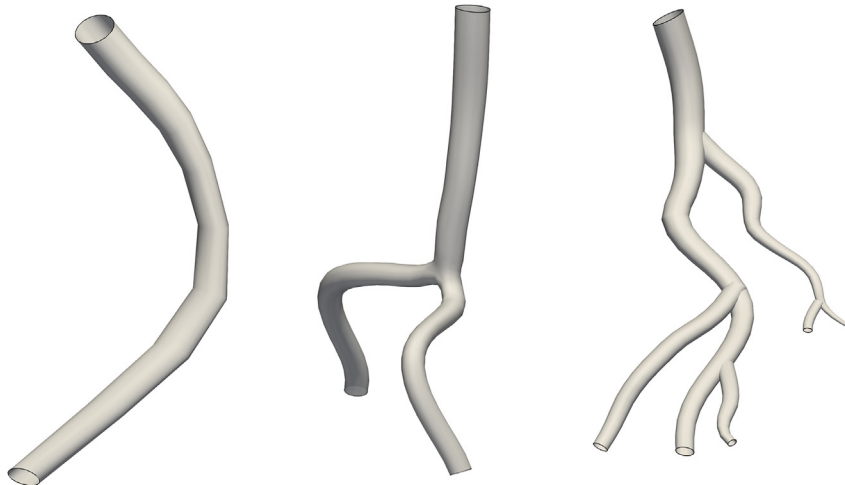
## ***5.1 Introduction***

In Chapter 4, we reviewed some fundamental laws and equations of fluid dynamics and the physics of deformable media. Building on this basis, this chapter introduces mechanical models of (different parts of) a human cardiovascular system. We further apply computational methods to solve these models numerically. Numerical simulation of a complete cardiovascular system would include interaction of elastic vessels, deformable tissues, and blood flows on a range of spatial scales from aortic to capillary flows. Such direct computations look unfeasible even with modern supercomputers. To address this computational challenge, model order reduction techniques can be used, and we discuss some of them in Chapters 6 and 7. At the same time, it is often required to simulate in full detail local phenomena, such as a blood flow in the heart chambers or the interaction of the blood flow with a vascular stent. In this case, full-scale 3D models should be used to set up a numerical experiment. Such models and methods are the subject of this chapter. We first discuss blood flow modeling in the case of noncompliant boundaries, which is a reasonable approximation for flows when the vessel walls lack elasticity due to a pathology or no sufficient information about their elastic properties is available. Furthermore, we continue with fluid–structure models for the blood flows in compliant vessels and blood flow in the heart. We complete the chapter with a more detailed discussion about numerical procedures used to compute for solutions of these models.

## ***5.2 Simulation of blood flow in vessel with nondeformable walls***

### ***5.2.1 Mathematical model***

The setup of a mathematical model requires definitions of equations, a domain where the equations are posed, as well as boundary and initial conditions. We start with the domain definition. The simulation domain  $\Omega$  is represented by a 3D tube with rigid walls, which may have one or several bifurcations (see Fig. 5.1). The rigid wall defines a part of the boundary  $\Gamma_{wall}$ . The vessel inlet  $\Gamma_{in}$  is represented by a cross section of the tube. The vessel outlet  $\Gamma_{out}$  or several outlets,  $\Gamma_{out}^k, k = 1, \dots, N_{out}$  are also given by the tube cross sections.

**Figure 5.1**

Variants of the computational domain: vessel without bifurcations, vessel with one bifurcation, network of vessels.

The equations in the domain  $\Omega$  are the Navier–Stokes equations (4.18)

$$\begin{cases} \rho \left( \frac{\partial \mathbf{v}}{\partial t} + (\mathbf{v} \cdot \nabla) \mathbf{v} \right) - 2\mu \operatorname{div} \mathbf{D}(\mathbf{v}) + \nabla p = \rho \mathbf{f} \\ \operatorname{div} \mathbf{v} = 0 \end{cases} \quad (5.1)$$

where  $\mathbf{v}$  is the fluid velocity,  $p$  is the pressure,  $\rho$  is the density,  $\mu$  is the viscosity coefficient, and  $\mathbf{f}$  is a given external body force. The initial condition is set for the velocity field in  $\Omega$ :

$$\mathbf{v}|_{t=0} = \mathbf{v}_0. \quad (5.2)$$

On the rigid walls, we pose the no-slip condition (4.21) that implies (due to  $\xi = 0$ )

$$\mathbf{v} = \mathbf{0} \text{ on } \Gamma_{wall} \quad (5.3)$$

due to fixed position of  $\Gamma_{wall}$ . Slip and slip with friction boundary conditions are also considered on vessels wall, but Eq. (5.3) is the most common.

On the inlet boundary, one conventionally sets the Dirichlet condition (4.23):

$$\mathbf{v} = \mathbf{v}_D \text{ on } \Gamma_{in} \quad (5.4)$$

where  $\mathbf{v}_D$  is a given cross-sectional profile of the velocity. One can use for  $\mathbf{v}_D$  either analytical Poiseuille or Womersley profiles for the normal component of  $\mathbf{v}_D$ , or velocity profiles reconstructed from MRI data. For the inlet of the ascending aorta, one can use a

numerical velocity profile from a patient-specific model of blood flow in the left ventricle [127].

On the outlet boundary, the typical boundary condition has the Neumann type (Eq. 4.24):

$$\sigma \mathbf{n} = \mathbf{0} \text{ on } \Gamma_{out}, \quad (5.5)$$

or the Robin type (Eq. 4.26)

$$\sigma \mathbf{n} + \frac{\alpha}{2} (\mathbf{v} \cdot \mathbf{n})_- \mathbf{v} = \mathbf{0} \text{ on } \Gamma_{out} \quad (5.6)$$

with  $\alpha \in [0, 1]$  and  $(x)_- := \frac{1}{2}(|x| - x)$ . Condition (5.6) stabilizes the solution in case of backward flows through  $\Gamma_{out}$ .

It is also common to let the right-hand side in Eq. (5.5) be nonzero:

$$\sigma \mathbf{n} = p_{out} \mathbf{n} \text{ on } \Gamma_{out}. \quad (5.7)$$

In this case,  $p_{out}$  has the physical sense of prescribed averaged pressure on  $\Gamma_{out}$ ,  $p_{out} = |\Gamma_{out}|^{-1} \int_{\Gamma_{out}} p(t, x) dx$ , and Eq. (5.7) implies the equilibrium of the normal stress and the normal force produced by exterior pressure.

When pressure boundary conditions (5.7) are given both on inflow and outflow boundaries,

$$\sigma \mathbf{n} = p_{in} \mathbf{n} \text{ on } \Gamma_{in}, \quad \sigma \mathbf{n} = p_{out} \mathbf{n} \text{ on } \Gamma_{out}, \quad (5.8)$$

they model the so-called *pressure drop* boundary condition. The corresponding mathematical problem is well posed (at least in 2D), and models embedded flows driven by the averaged pressure difference at inflow and outflow boundaries [140,151]. Besides prescribing averaged pressures, one may be interested in setting averaged fluxes on  $\Gamma_{in}$  and  $\Gamma_{out}$ ,

$$\int_{\Gamma_{in}} \mathbf{v} \cdot \mathbf{n} ds = Q_{in}, \quad \int_{\Gamma_{out}} \mathbf{v} \cdot \mathbf{n} ds = Q_{out}. \quad (5.9)$$

This can be realized through conditions on normal stresses as in Eq. (5.8), but this time  $p_{in}$  and  $p_{out}$  should be treated as unknowns and mathematically can be interpreted as Lagrange multipliers corresponding to the additional linear constraints (5.9) for the velocity [140].

### 5.2.2 Finite element method for blood flow equations

Finite element method (FEM) is one of the most powerful, versatile, and mathematically sound discretization techniques for models written in terms of partial differential equations [140,151]. In this book, we apply it for numerical simulation of blood flows and elastic deformations of blood vessels. There exists an overwhelming literature on practice and

theory of FEMs; the interested reader can consult, for example, monographs [115,135,147]. Here, we briefly explain how FEM is used for the problems of our interest. We start with the model of a flow in a fixed nondeformable domain, consisting of governing equations and initial and boundary conditions (5.1)–(5.5).

The first step of applying FEM would be to rewrite the problem in the weak form. To do this, one takes an inner product of the momentum Eq. (5.1) with a generic smooth vector function  $\Psi$ , which vanishes at  $\Gamma_{wall} \cup \Gamma_{in}$  and integrates over  $\Omega$ . Furthermore, one integrates by parts the terms representing stresses (viscous and pressure terms in this case) and uses boundary conditions for  $\mathbf{v}$  and  $\Psi$ . This readily leads to the following integral equality:

$$\int_{\Omega} (\rho \dot{\mathbf{v}} \cdot \Psi - 2\mu \mathbf{D}(\mathbf{v}) : \mathbf{D}(\Psi) + p \operatorname{div} \Psi) dx = \int_{\Omega} \rho \mathbf{f} \cdot \Psi dx. \quad (5.10)$$

The divergence free velocity field  $\mathbf{v}$  and pressure  $p$  should satisfy Eq. (5.10) for any sufficiently smooth  $\Psi$  vanishing on  $\Gamma_{wall} \cup \Gamma_{in}$ . It is crucial to note that integrals in the identity (5.10) make sense if  $p$  is from the Lebesgue space  $L^2(\Omega)$  and  $\Psi$  is from  $L^2(\Omega)^3$  together with  $\nabla \Psi \in L^2(\Omega)^{3 \times 3}$  (we shall write  $\Psi \in \mathbf{H}^1(\Omega)$  for such vector functions), while  $\mathbf{v}(t)$  should be from  $\mathbf{H}^1(\Omega)$  for almost all  $t \geq 0$  and  $\mathbf{v}_t \in L^2(\Omega)^3$ . The above smoothness conditions can be weakened, but this is not important for what follows.

In the FEM, one seeks for approximations to  $\mathbf{v}$  and  $p$  (finite element velocity  $\mathbf{v}_h$  and pressure  $p_h$ ) in a suitable *finite dimensional subspaces*  $\mathbb{V}_h$  and  $\mathbb{Q}_h$  of  $\mathbf{H}^1(\Omega)$  and  $L^2(\Omega)$ , respectively, and claims them to satisfy Eq. (5.10) for any  $\Psi$  from a finite dimensional subspace of  $\mathbf{H}^1(\Omega)$  vanishing on  $\Gamma_{wall} \cup \Gamma_{in}$ . Choosing bases in those subspaces and decomposing  $\mathbf{v}_h$  and  $p_h$  in those bases allow to reduce Eq. (5.10) to an ordinary differential equation (ODE) system for unknown coefficients in the decompositions. The ODE system is further integrated numerically in time. To carry out this plan, we now briefly review how one builds FE spaces  $\mathbb{V}_h$  and  $\mathbb{Q}_h$ .

We define a *triangulation*  $\mathcal{T}_h$  of domain  $\Omega$  as a collection of shape regular simplexes (triangles for  $d = 2$  and tetrahedra for  $d = 3$ ) forming a consistent tessellation of  $\Omega$ . The *mesh size* is the maximum diameter of the simplex in the triangulation,  $h = \max_{T \in \mathcal{T}_h} \operatorname{diam}(T)$ . We define FE spaces  $\mathbb{V}_h \subset \mathbf{H}^1(\Omega)$  and  $\mathbb{Q}_h \subset L^2(\Omega)$  composed of piecewise polynomial functions:

$$\begin{aligned} \mathbb{V}_h &= \left\{ \mathbf{u}_h \in C(\Omega)^d : \mathbf{u}_h|_T \in [P^{m+1}(T)]^d, \forall T \in \mathcal{T}_h \right\}, \\ \mathbb{Q}_h &= \left\{ q_h \in C(\Omega) : q_h|_T \in P^m(T), \forall T \in \mathcal{T}_h \right\}, \end{aligned} \quad (5.11)$$

where integer  $m \geq 1$  is some fixed polynomial degree. The polynomial degree of FE velocities from  $\mathbb{V}_h$  is intentionally one degree higher than the polynomial degree of FE pressure functions.

The FE discretization of Eqs. (5.1)–(5.5) is as follows. We look for  $p_h \in \mathbb{Q}_h$ ,  $\mathbf{v}_h \in \mathbb{V}_h$ , satisfying  $\mathbf{v}_h = I_h(\mathbf{v}_D)$  on  $\Gamma_{in}$ ,  $\mathbf{v}_h = 0$  on  $\Gamma_{wall}$ , such that

$$\begin{aligned} & \int_{\Omega} \left( \rho \left( \frac{\partial \mathbf{v}_h}{\partial t} + \mathbf{v}_h \cdot \nabla \mathbf{v}_h \right) \cdot \boldsymbol{\Psi}_h - 2\mu \mathbf{D}(\mathbf{v}_h) : \mathbf{D}(\boldsymbol{\Psi}_h) + p_h \operatorname{div} \boldsymbol{\Psi}_h \right) dx \\ &= \int_{\Omega} \rho \mathbf{f} \cdot \boldsymbol{\Psi}_h dx \end{aligned} \quad (5.12)$$

for all  $\boldsymbol{\Psi}_h \in \mathbb{V}_h$  satisfying  $\boldsymbol{\Psi}_h = 0$  on  $\Gamma_{wall} \cup \Gamma_{in}$ .

It is clear that problem (5.12) is underdetermined (unknowns are given by  $\mathbf{v}_h$  and  $p_h$ , while constraints are only enforced through  $\boldsymbol{\Psi}_h \in \mathbb{V}_h$ ). Missing constraints come from the divergence-free condition for the blood velocity in Eq. (5.1). It turns out that building practically useful FE spaces  $\mathbb{V}_h$  such that  $\operatorname{div} \mathbf{v}_h = 0$  for  $\mathbf{v}_h \in \mathbb{V}_h$  is a difficult task with little options known so far [158]. A common approach is to enforce the divergence-free condition for  $\mathbf{v}_h \in \mathbb{V}_h$  only in the integral sense,

$$\int_{\Omega} q_h \operatorname{div} \mathbf{v}_h dx = 0 \quad \text{for all } q_h \in \mathbb{Q}_h. \quad (5.13)$$

It is clear that Eq. (5.13) implies  $\operatorname{div} \mathbf{v}_h = 0$  if  $\mathbb{V}_h \subset \mathbb{Q}_h$ , but the latter does not hold for most commonly used pairs of  $\mathbb{V}_h$  and  $\mathbb{Q}_h$ .

Eqs. (5.12) and (5.13) and  $\mathbf{v}_h = I_h(\mathbf{v}_D)$  on  $\Gamma_{in}$ ,  $\mathbf{v}_h = 0$  on  $\Gamma_{wall}$  constitute the discrete (FE) model of blood flow in a nondeformable domain.

### 5.2.3 Numerical stability

There are several subtle numerical stability issues related to applying FEM for blood flow simulations. One originates from the incompressibility constraint. Looking at Eq. (5.13), we realize that if the dimension of  $\mathbb{Q}_h$  is large enough, then it may happen that only  $\mathbf{v}_h = 0$  satisfy Eq. (5.13), thus leading to physically meaningless velocity field. For sure, this happens if  $\dim(\mathbb{Q}_h) > \dim(\mathbb{V}_h)$ , but may also happen if  $\dim(\mathbb{V}_h)$  is larger than  $\dim(\mathbb{Q}_h)$  [111]. On the other hand,  $\mathbb{Q}_h$  should be large enough to resolve the pressure variable. The balance is delicate, and mathematical assumptions for the right choice of  $\mathbb{V}_h$  and  $\mathbb{Q}_h$  consist of approximation properties and the following compatibility condition, which is known as the LBB (from Ladyzhenskaya–Babuška–Brezzi) condition: There exists a constant  $\kappa(\Omega) > 0$  independent of  $h$  such that

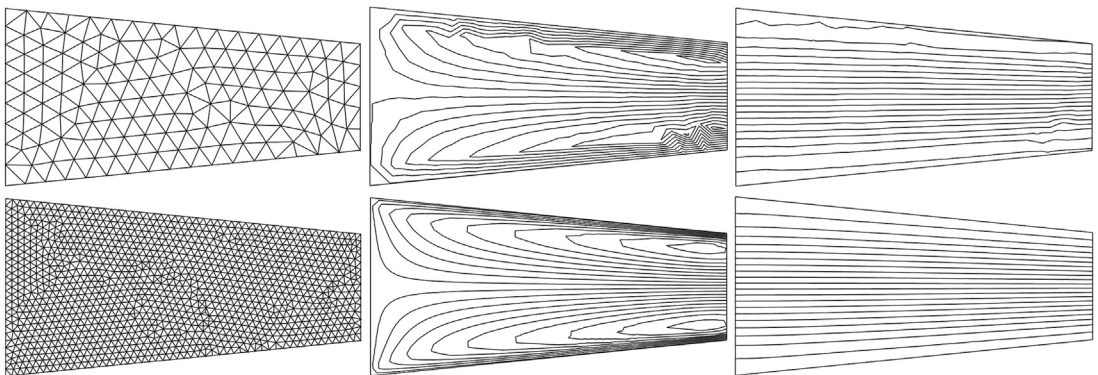
$$\kappa(\Omega) \leq \inf_{q_h \in \mathbb{Q}_h} \sup_{\mathbf{v}_h \in \mathbb{V}_h} \frac{(q_h, \operatorname{div} \mathbf{v}_h)}{\|q_h\| \|\mathbf{v}_h\|_1}. \quad (5.14)$$

Here and further,  $(f, g) = \int_{\Omega} fg \, dx$  is the inner product in  $L^2(\Omega)$  and  $\|\cdot\|$  is the corresponding norm;  $\|f\|_1 = (\|f\|^2 + \|\nabla f\|^2)^{1/2}$  is the norm in the Sobolev space  $H^1(\Omega)$ .

Some simple and naive choices of velocity–pressure FEs may fail to satisfy Eq. (5.14). For example, condition (5.14) does not hold if  $\mathbb{V}_h$  consists of piecewise linear continuous functions and  $\mathbb{Q}_h$  consists of piecewise linear continuous or piecewise constant functions. The corresponding FE pairs are commonly denoted by  $P_1 - P_1$  and  $P_1 - P_0$ . Examples of FE pairs satisfying Eq. (5.14) include the family of Taylor–Hood elements  $P_{m+1} - P_m, m \geq 1$  (both velocity and pressure are continuous, and on each mesh cell, they are polynomials of degree  $m+1$  and  $m$ , respectively) and  $P_{m+1} - P_{m-1}^{\text{disc}}$  (in 2D) and  $P_{m+2} - P_{m-1}^{\text{disc}}$  (in 3D). Here,  $P_{m-1}^{\text{disc}}$  denotes the space of pressure functions, which are polynomials of degree  $k-1$  in each simplex, but not necessarily continuous across faces (edges) of tetrahedra (triangles). Another popular example is the nonconforming  $\widetilde{P}_1 - P_0$  Crouzex–Raviart element (piecewise constant pressure  $p_h$  and piecewise linear velocity  $\mathbf{v}_h$  on the same triangulation; here,  $\mathbf{v}_h$  is not globally continuous, its continuity holds at midedges in 2D). Since, for the nonconforming elements, the discrete velocity  $\mathbf{v}_h$  can be discontinuous across the edges of the triangulation, the integrals in Eqs. (5.12) and (5.13) should be defined elementwise. Monographs [111, 144, 147] discuss in detail why the LBB condition is important and how it can be verified for given elements and consider other suitable velocity–pressure FE pairs.

Another potential source of numerical instability arises if inertia forces dominate over viscous forces in a fluid flow. Such flow regimes are characterized by higher Reynolds numbers and feature complex flow patterns, sharp boundary and internal layers, transitional dynamics, and eventually turbulence (see also Section 4.2.6). In hemodynamics, higher Reynolds number flows can be observed in large arteries and the heart (in contrast, in capillaries blood flows are creeping, see Chapter 8). The ability of the computational mesh to resolve fine features of such flows is often characterized by the mesh Reynolds number defined individually for each cell  $T \in \mathcal{T}_h$ ,  $Re_T = h_T \|\mathbf{v}\|_{L_\infty(T)} / \mu$ . If  $Re_T \gg 1$  holds, then the mesh may fail to adequately resolve blood flow dynamics, and the FEM is prone to produce nonphysical flow patterns (see Fig. 5.2) and even energy blow-up (numerical instability). Refining the mesh sufficiently to guarantee  $Re_T \ll 1$  is not always the option since the resulting number of degrees of freedom leads to prohibitively expensive computations. In particular, real-time patient-specific simulations are currently not feasible with fine 3D meshes. The question of reliable and stable numerical methods for higher Reynolds number flows has been extensively addressed in the literature from both computational and modeling sides.<sup>1</sup> Possible solutions include Petrov–Galerkin and

<sup>1</sup> Still the numerical simulation of flows with high Reynolds numbers, e.g., turbulent, is a grand challenge of computational physics. The situation is partially explained by insufficient (mathematical) understanding of underlying system of equations [209].

**Figure 5.2**

Instability of the P2–P1 finite element solution of the 2D Navier–Stokes equations with Poiseuille profile (Eq. 5.4) on inlet ( $x = 0$ ) and “do-nothing” boundary condition (5.5) on outlet ( $x = 1$ ). From left to right: mesh, isolines of  $v_y$  velocity component, streamlines for  $\max_{T \in \mathcal{T}_h} Re_T \approx 62$  (top row) and  $\max_{T \in \mathcal{T}_h} Re_T \approx 21$  (bottom row). Note unphysical oscillations of the computed solutions for higher  $Re_T$ .

stabilized FEM, multiscale numerical methods, and turbulence models; the recent monograph [157] provides in-depth overview of these topics. In the following, we recall three useful approaches for numerical simulations of high-speed flows: streamline upwind Petrov–Galerkin (SUPG) formulation, variational multiscale (VMS) stabilization, and Smagorinsky turbulence model.

In the Petrov–Galerkin FEM, one uses different spaces for trial and test functions, i.e., for  $\mathbf{v}_h$ ,  $p_h$ ,  $\Psi_h$ , and  $q_h$  in Eqs. (5.12) and (5.13). The minimum requirement, of course, is that the dimensions of trial and test spaces are the same. From the earlier papers [117,141], it follows that the solution-dependent choice of velocity trial functions on each cell  $T$ ,  $\Psi_h = \mathbf{w}_h + \sigma_T \mathbf{v}_h \nabla \mathbf{w}_h$ ,  $\mathbf{w}_h \in \mathbb{V}_h$  improves the stability of the FEM for large mesh Reynolds numbers. Due to some similarities to numerical schemes based on upwind differences, the method got its name: SUPG method. In practice, to define  $\mathbf{v}_h$ , one considers a known velocity field from the previous time step or iteration and does not contribute extra nonlinearity to the discrete problem. The *stabilization parameter*  $\sigma_T$  for each cell  $T$  depends on the cell diameter  $h_T$  and  $\mathbf{v}_h$ . While various receipts for the choice of  $\sigma_T$  can be found in the literature, for our simulations, we use

$$\sigma_T = \begin{cases} \bar{\sigma} \frac{h_T}{2\|\mathbf{v}_h\|_{L_\infty(T)}} \left(1 - \frac{1}{Re_T}\right), & \text{if } Re_T > 1 \\ 0, & \text{if } Re_T \leq 1, \end{cases} \quad \text{with } 0 \leq \bar{\sigma} < 1.$$

Note that the local mesh-dependent parameter  $\sigma_T$  makes test functions discontinuous across element boundaries. This requires certain care with integration by parts, and so with formulation of the method. For further detail, we refer the interested reader to the literature, e.g., the monograph [183]. This is not the only reasonable option of defining trial functions in Petrov–Galerkin FEM for the incompressible Navier–Stokes equations. For example,  $\nabla q_h$  and/or  $\mu \nabla \mathbf{w}_h$  terms can be also included in the definition of  $\Psi_h$ , which renders the method closer to least-squares formulations.

One can explain numerical instability of the plain FEM for higher Reynolds number flows as a failure of the method to diffuse excessive energy due to poor grid resolution of small scales in the true solution. This unresolved small scale dynamics contributes significantly to the energy balance of the original problem (Navier–Stokes equations), mainly through the viscous forces. Thus, one may try to model explicitly the effect of “missing” small scales in the numerical method. This can be done either by modifying the original system of PDEs (giving rise to a plethora of turbulent models) or by modifying the FE formulation (5.12) to accommodate this need. One consistent way of modifying Eq. (5.12) is given by the VMS formulation [156]. In the VMS methods, one typically separates the scales of interest in two groups of coarse (resolved) and fine (unresolved) scales. Furthermore, coarse scales can be defined in terms of projections into appropriate functional spaces, which are often FE spaces for a fixed given mesh. A system of equations for the coarse scales follows from a variational problem formulation and a set of explicitly formulated assumptions about the space decomposition and local properties of the involved operators. In the context of blood flow simulations, the VMS method is often used to stabilize numerical modeling of the heart and aorta blood flows (see, e.g., Refs. [123,181,195,196]). Again, currently, there is no single VMS formulation, but rather a group of numerical approaches, which center around the idea of modeling the effect of scales unresolved in  $\mathbb{V}_h$  and  $\mathbb{Q}_h$  through the additional terms in the FE formulation commonly depending on the residual of the FE solution (see, e.g., the review paper [105]).

The modeling of missing scales can be done at the level of formulating a system of governing equations. One prominent class of such models is given by LES (large eddy simulation) turbulence models (see, e.g., Ref. [189]). One classical LES model is the Smagorinsky turbulence model. In this model, the effect of unresolved scales is modeled by additional nonlinear diffusion term added to the Navier–Stokes system (5.1) with the Smagorinsky turbulent viscosity coefficient  $\mu_T$  instead of the dynamic viscosity  $\mu$ :

$$\mu_T = \mu + (C_s h_T)^2 \sqrt{2\mathbf{D}(\mathbf{v}) : \mathbf{D}(\mathbf{v})}, \quad (5.15)$$

where  $C_s$  is a constant (we use  $C_s = 0.2$ ) and  $h_T = \text{diam}(T)$ , for any mesh cell  $T \in \mathcal{T}_h$ .

### 5.2.4 Examples

Solutions to Eq. (5.1) can be explicitly written out only for few simple flows. These analytical solutions are used for the accuracy analysis of numerical schemes for the Navier–Stokes equations before one applies them to simulate more complex flows.

Analytical solutions are known for  $\mathbf{f} = \mathbf{0}$  in the straight tube (representing an idealized vessel) with a circular cross section of radius  $R$  and the centerline belonging to  $[0, A]$  on  $Ox_1$ -axis and the following boundary conditions: no-slip on the tube wall (Eq. 5.3), a given velocity profile (Eq. 5.4) at inlet  $x_1 = 0$ , and free normal stress condition (5.5) at outlet  $x_1 = A$ .

The steady version of Eq. (5.1) with the parabolic inflow profile

$\mathbf{v}_D = (v_D, 0, 0)^T$ ,  $v_D = v_{\max} \left( 1 - R^{-1} \sqrt{x_2^2 + x_3^2} \right)$ , has the exact solution with the only nonzero velocity component  $v_1 = v_D$  and  $p(x) = \mu \Delta v x_1$  known as the Poiseuille flow.

Another physiologically interesting flow is the Womersley flow [208]. This solution predicts velocity profile of a flow in a circular cylinder subjected to the longitudinal oscillating pressure gradient. This may model two repeating phases of the cardiac cycle. The exact solution is written in terms of Bessel functions (we refer, e.g., to Refs. [148,208] for details). The interplay between inertia, viscous, and oscillating pressure forces gives rise to W-shape of the Womersley flow profile, which one observes in more practical physiological settings, as we illustrate by the following experiment. We consider an idealized model of the aortic bifurcation [112,132,209] with an inlet cylindrical segment (abdominal aorta) and two equal branches of cylindrical segments (iliac arteries) forming the angle 47.9 degrees. On inlet of aorta, a time-dependent velocity profile  $u_x(r, \theta, t) = U(t)V(r, \theta)$  is given, each iliac artery is coupled with a three-element 0D Windkessel model representing the downstream vasculature [209]. The inlet velocity may have negative axial component; in this case, the Windkessel model provides blood inflow to the iliac arteries. The unsteady iliac backflow is averaged on the cross section, so the velocity profile obtains a W-shaped profile shown in Fig. 5.3.

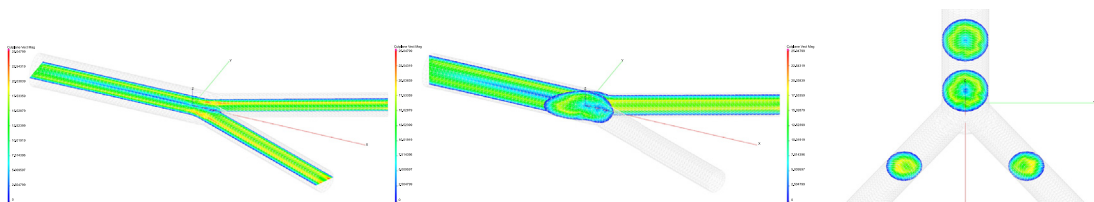
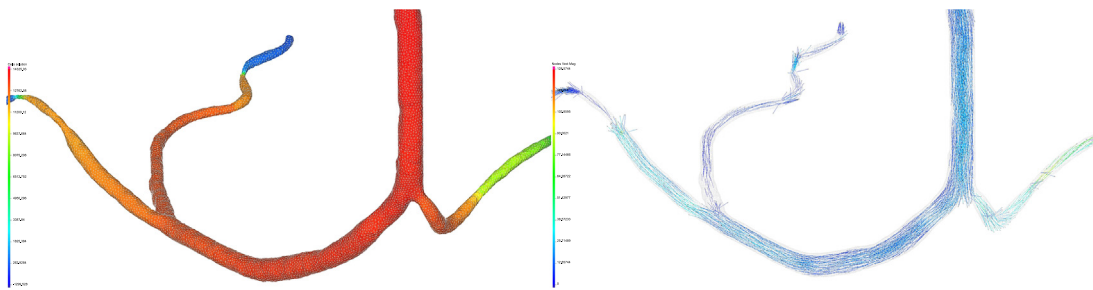


Figure 5.3

Womersley velocity fields of blood flow in idealized aortic bifurcation:  $oxy$  plane (left),  $ozx$  planes (middle),  $oyz$  (right).

**Figure 5.4**

Pressure (left) and vector velocity (right) fields in a patient-specific simulation of right coronary blood flow.

The final example in this section is the simulation of blood dynamics in a 3D domain recovered from a real patient coronary CT angiography. The right coronary artery branches, and we cut it to embed in the box of  $6.5 \text{ cm} \times 6.8 \text{ cm} \times 5 \text{ cm}$ . The diameter of the inlet cross section is about 0.27 cm. A shape-regular tetrahedral mesh with 63K tetrahedra approximates the vessel. On inlet and outlet boundary, we set conditions (5.4) and (5.5), respectively. In Fig. 5.4, we show the pressure field and the vector velocity field in the artery at time 0.15 s, which corresponds to the maximum inlet systolic velocity of 6.8 cm/s. Blood viscosity and density are set to  $\mu = 0.025 \text{ cm}^2/\text{s}$  and  $\rho = 1 \text{ g/cm}^3$ , respectively. The numerical method requires SUPG stabilization, whereas for more viscous blood  $\mu = 0.04 \text{ cm}^2/\text{s}$ , the stabilization is not needed [162,163].

## 5.3 Simulation of blood flow in vessel with compliant wall

### 5.3.1 Mathematical model

We now extend the blood flow model by allowing for the deformation of the elastic wall of the blood vessel. This brings us to the fluid–structure interaction (FSI) problem as discussed in Section 4.4. The problem addresses a more complex coupled phenomenon, which includes both blood dynamics and elastic deformation of vessel wall. The mathematical model includes Eqs. (4.64)–(4.66) posed in the reference (time-independent) flow and structure domains and interface conditions (4.57)–(4.58) and (4.62). On the inflow–outflow boundaries, one may prescribe the pressure drop boundary condition as in Eq. (5.8) rewritten in the reference coordinates. It is also common for FSI problems to distinct between outflow and inflow boundaries so that we have boundary conditions (5.4) and (5.7). We put normal stress equal to zero on the part of the structure boundary, which does not interact with fluid. Zero deformation and the fluid at rest is a common initial condition for the blood flow in a vessel FSI problem. Since such initial state is not

physiologically relevant, one often needs to simulate a few cardiac cycles to minimize the influence of the initial condition on the computed statistics. We also remind that one needs to define mapping from the reference flow domain to the physical flow domain with the help of a smooth extension of the displacement field from the reference structure domain (Eq. 4.60). For this purpose, we shall use the auxiliary elasticity equation (4.63) or its modification [165]

$$-\operatorname{div} \left[ J \left( \lambda_m \operatorname{tr} \left( \nabla \left[ \frac{\partial \mathbf{u}}{\partial t} \right]^k \mathbf{F}^{-1} \right) \mathbf{I} + \mu_m \left( \nabla \left[ \frac{\partial \mathbf{u}}{\partial t} \right]^k \mathbf{F}^{-1} + \left( \nabla \left[ \frac{\partial \mathbf{u}}{\partial t} \right]^k \mathbf{F}^{-1} \right)^T \right) \right) \mathbf{F}^{-T} \right] = 0 \text{ in } \widehat{\Omega}_f. \quad (5.16)$$

For Eq. (5.16), the boundary condition  $\left[ \frac{\partial \mathbf{u}}{\partial t} \right]^k = \mathbf{v}^k$  is used on the interface. The elasticity parameters are set to  $\mu_m = \mu_s |\Delta_e|^{-1.2}$ ,  $\lambda_m = 16\mu_m$ , where  $|\Delta_e|$  denotes the physical volume of a mesh cell  $\Delta_e$  subjected to displacement from the previous time step.

We are now ready to introduce a FEM for the discretization of the FSI problem.

### 5.3.2 Monolithic finite element method for fluid–structure interaction

Since Eqs. (4.64)–(4.66) are written in the reference coordinates, for a numerical method, one can build the computational mesh in the reference domain. This avoids meshes and FE function spaces dependent on time. Alternatively, one can use an integral formulation of the governing equations, where integration is done in both space and time. This leads to a family of space–time FEMs (see, for example, [299,200]). Here, we, however, consider a consistent regular triangulation/tetrahedrization of the reference domain  $\overline{\Omega}(0) = \overline{\Omega}_s \cup \overline{\Omega}_f$  and FE spaces  $\mathbb{V}_h \subset \mathbf{H}^1(\Omega(0))$  and  $\mathbb{Q}_h \subset L^2(\Omega(0))$  for trial functions and the following two subspaces for the test functions:  $\mathbb{V}_h^0 = \left\{ \mathbf{v} \in \mathbb{V}_h : \mathbf{v}|_{\Gamma_{s0} \cup \Gamma_{f0}} = 0 \right\}$  and

$\mathbb{V}_h^{00} = \left\{ \mathbf{v} \in \mathbb{V}_h^0 : \mathbf{v}|_{\Gamma_{sf}} = 0 \right\}$ . Following discussion of numerical stability in Section 5.2, we choose FE pressure and velocity spaces to satisfy Eq. (5.14).

We need some further notations. For a tensor  $\mathbf{A} \in \mathbb{R}^{N \times N}$ , we denote its symmetric part as  $\{\mathbf{A}\}_s = \frac{1}{2}(\mathbf{A} + \mathbf{A}^T)$ . We shall emphasize the dependence of  $\mathbf{F}$  on a displacement field in  $\mathbf{F}(\mathbf{u}) := \mathbf{I} + \nabla \mathbf{u}$  and set  $J := \det(\mathbf{F}(\mathbf{u}))$ ,  $\mathbf{D}_{\mathbf{u}} \mathbf{v} = \left\{ (\nabla \mathbf{v}) \mathbf{F}^{-1}(\mathbf{u}) \right\}_s$ . To formulate a FEM, we multiply Eq. (4.65) by some  $\boldsymbol{\Psi} \in \mathbf{H}_0^1(\widehat{\Omega})$ , such that  $\boldsymbol{\Psi} = \mathbf{0}$  on  $\Gamma_{s0} \cup \Gamma_{f0}$ , and integrate over  $\widehat{\Omega}$  and by parts. Likewise, we test Eq. (4.66) with  $q \in L^2(\widehat{\Omega})$ . The resulting integral identities state that the solution  $\mathbf{u}$ ,  $\mathbf{v}$ ,  $p$  to Eqs. (4.64)–(4.66) with interface conditions (4.57)–(4.58) and (4.62) satisfies

$$\begin{aligned}
& \int_{\hat{\Omega}_s} \rho_s \frac{\partial \mathbf{v}}{\partial t} \cdot \boldsymbol{\Psi} \, dx + \int_{\hat{\Omega}_s} J \Sigma_s \mathbf{F}^{-T} : \nabla \boldsymbol{\Psi} \, dx \\
& + \int_{\hat{\Omega}_f} \rho_f J \frac{\partial \mathbf{v}}{\partial t} \cdot \boldsymbol{\Psi} \, dx + \int_{\hat{\Omega}_f} \rho_f J(\nabla \mathbf{v}) \mathbf{F}^{-1}(\mathbf{u}) \left( \mathbf{v} - \frac{\partial \mathbf{u}}{\partial t} \right) \cdot \boldsymbol{\Psi} \, dx \\
& + \int_{\hat{\Omega}_f} 2\mu_f J \mathbf{D}_{\mathbf{u}} \mathbf{v} : \mathbf{D}_{\mathbf{u}} \boldsymbol{\Psi} \, dx + \int_{\hat{\Omega}_f} p J \mathbf{F}^{-T}(\mathbf{u}) : \nabla \boldsymbol{\Psi} \, dx = 0
\end{aligned} \tag{5.17}$$

for all  $\boldsymbol{\Psi} \in \mathbf{H}_0^1(\hat{\Omega})$ , such that  $\boldsymbol{\Psi} = \mathbf{0}$  on  $\Gamma_{s0} \cup \Gamma_{f0}$ ,

$$\int_{\hat{\Omega}_s} \frac{\partial \mathbf{u}}{\partial t} \cdot \boldsymbol{\phi} \, dx - \int_{\hat{\Omega}_s} \mathbf{v} \cdot \boldsymbol{\phi} \, dx = 0 \tag{5.18}$$

for all  $\boldsymbol{\phi} \in \mathbf{H}_0^1(\hat{\Omega})$ , such that  $\boldsymbol{\phi} = \mathbf{0}$  on  $\Gamma_{s0} \cup \Gamma_{f0} \cup \Gamma_{sf}$  and

$$\int_{\hat{\Omega}_f} J(\nabla \mathbf{v}) : \mathbf{F}^{-T}(\mathbf{u}) q \, dx = 0 \tag{5.19}$$

for all  $q \in L^2(\hat{\Omega})$ . Note that integrals over the interface in Eq. (5.17) cancel out due to the interface condition (4.58). Moreover, we have  $\mathbf{u} = \mathbf{0}$  on  $\Gamma_{s0} \cup \Gamma_{f0}$ ,  $\mathbf{v} = \mathbf{v}_D$  on  $\Gamma_{f0}$ ,  $\mathbf{v} = \mathbf{0}$  on  $\Gamma_{s0}$ .

Equalities (5.17)–(5.20) serve to define the FEM, which consists of finding  $\{\mathbf{u}_h, \mathbf{v}_h, p_h\} \in \mathbb{V}_h^0 \times \mathbb{V}_h \times \mathbb{Q}_h$  such that  $\mathbf{v}_h = \mathbf{v}_{D,h}$  on  $\Gamma_{f0}$ ,  $\mathbf{v}_h = \mathbf{0}$  on  $\Gamma_{s0}$  and satisfying Eqs. (5.17)–(5.20) (in place of  $\mathbf{u}$ ,  $\mathbf{v}$ , and  $p$ ) and for all  $\boldsymbol{\Psi} \in \mathbb{V}_h^0$ ,  $\boldsymbol{\phi} \in \mathbb{V}_h^{00}$ , and  $q \in \mathbb{Q}_h$ . The coupling condition on  $\Gamma_{sf}$  is enforced strongly for FE functions:

$$\frac{\partial \mathbf{u}_h}{\partial t} = \mathbf{v}_h \quad \text{on } \Gamma_{sf}. \tag{5.20}$$

We note that the strong enforcement of the interface condition (5.20) together with condition (5.18) implies that the equality  $\frac{\partial \mathbf{u}_h}{\partial t} = \mathbf{v}_h$  is satisfied in the usual sense in  $\hat{\Omega}_s$ . Eqs. (5.17)–(5.20) subject to initial conditions and a choice of continuous extension of  $\mathbf{u}_h$  from  $\hat{\Omega}_s$  onto  $\hat{\Omega}_f$ , ensuring  $\mathbf{u}_h \in \mathbb{V}_h^0$  defines the system of ODEs. Of course, for the fully discrete method, we still have to discretize in time. This, however, decouples from space discretization (in the spirit of *the method of lines*), since the spacial discretization is done in the time-independent reference domain. Time discretizations will be discussed later in Section 5.5.1.

As for the extension equation, the user is free to choose a smooth extension of the displacement field from  $\hat{\Omega}_s$  (Eq. 4.60). However, this freedom is troublesome: in certain

cases, a chosen extension can fail to produce physically meaningful displacements, and the computational mesh becomes tangled in  $\hat{\Omega}_f$ . The choice is often *ad hoc*, as we will see in the next subsection.

If one considers the case of the compressible Saint Venant–Kirchhoff material, the second term in Eq. (5.17) becomes

$$\int_{\hat{\Omega}_s} \mathbf{F}(\mathbf{u}) \mathbf{S}(\mathbf{u}, \mathbf{u}) : \nabla \boldsymbol{\Psi} \, dx$$

where

$$\mathbf{S}(\mathbf{u}_1, \mathbf{u}_2) = \lambda_s \text{tr}(\mathbf{E}(\mathbf{u}_1, \mathbf{u}_2)) \mathbf{I} + 2\mu_s \mathbf{E}(\mathbf{u}_1, \mathbf{u}_2), \quad \mathbf{E}(\mathbf{u}_1, \mathbf{u}_2) = \frac{1}{2} \{ \mathbf{F}(\mathbf{u}_1)^T \mathbf{F}(\mathbf{u}_2) - \mathbf{I} \}_s.$$

Note that  $\mathbf{S}(\mathbf{u}_1, \mathbf{u}_2) = \mathbf{S}^T(\mathbf{u}_1, \mathbf{u}_2) = \mathbf{S}(\mathbf{u}_2, \mathbf{u}_1)$ .

In the case of the incompressible neo-Hookean material, the following modifications to the FE formulation should be made:

- (i) Change the domain of integration in the pressure-dependent term (sixth term in Eq. (5.17)) to the whole  $\hat{\Omega}$ , so it now reads:

$$- \int_{\hat{\Omega}_s \cup \hat{\Omega}_f} p_h J \mathbf{F}^{-T}(\mathbf{u}_h) : \nabla \boldsymbol{\Psi}_h \, dx; \quad (5.21)$$

- (ii) Replace the second term in Eq. (5.17) with

$$\mu_s \int_{\hat{\Omega}_s} \mathbf{F}(\mathbf{u}_h) : \nabla \boldsymbol{\Psi}_h \, dx;$$

- (iii) Consider the incompressibility condition in the form of identity (4.69), and add the following constraint to the FE formulation:

$$\int_{\hat{\Omega}_s} J \nabla \mathbf{v}_h : \mathbf{F}^{-T}(\mathbf{u}_h) q_h \, dx = 0 \quad \forall q_h \in \mathbb{Q}_h.$$

Hence instead of Eq. (5.19), we enforce the constraint in the whole reference domain  $\hat{\Omega}$ :

$$\int_{\hat{\Omega}_s \cup \hat{\Omega}_f} J (\nabla \mathbf{v}_h) : \mathbf{F}^{-T}(\mathbf{u}_h) q_h \, dx = 0 \quad \forall q_h \in \mathbb{Q}_h. \quad (5.22)$$

### 5.3.3 Examples

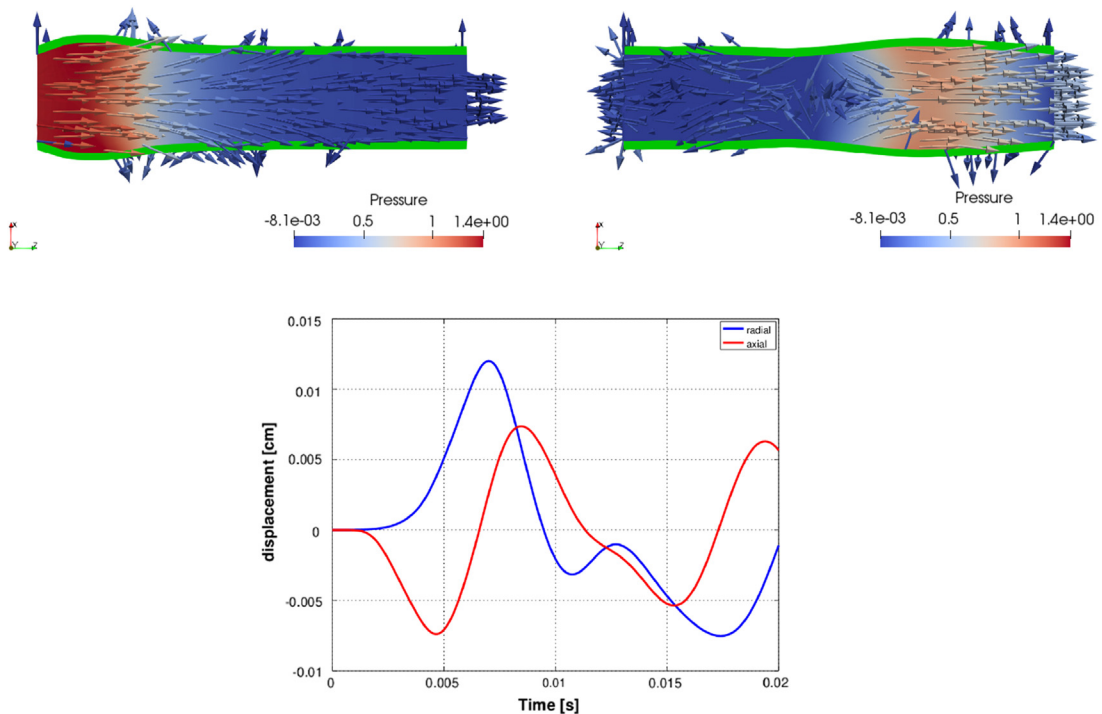
We illustrate the material of [Section 5.3](#) with several numerical examples. For these examples, we use P2–P1 (Taylor–Hood) elements for blood velocity and pressure variables and P2 elements for the vessel wall displacements. FE discretizations are implemented on the basis of the open source packages Ani2D [170] and Ani3D [171]. The time stepping and linearization of nonlinear systems are such as explained in [Section 5.5](#).

For the first experiment, we consider propagation of a pressure impulse in a flexible tube with the circular cross section filled by incompressible viscous fluid [139]. The tube is fixed at both ends. Initially, the tube is nondeformed, and the fluid is at rest. This is the simplest model for the 3D blood flow through a compliant artery, which serves for validating of FSI solvers [128,134,142,143,164,175].

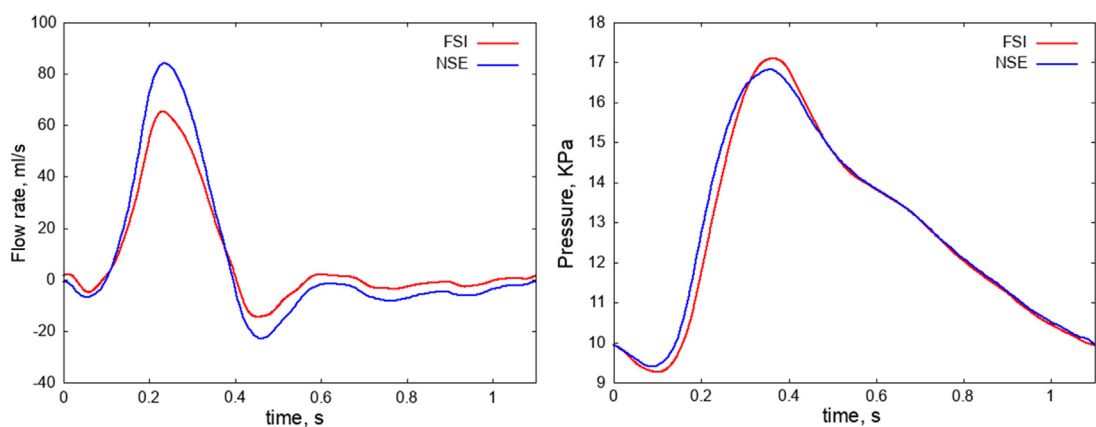
The length and inner diameter of the tube are 50 and 10 mm, respectively, and the tube wall is 1 mm thick. The fluid density is  $10^{-3}$  g/mm<sup>3</sup>, and kinematic viscosity is 3 mm<sup>2</sup>/s. The wall has density  $\rho_s = 1.2 \cdot 10^{-3}$  g/mm<sup>3</sup>. The Saint Venant–Kirchhoff hyperelastic model is used with elastic modulus  $E = 3 \cdot 10^5$  g/mm/s<sup>2</sup> and Poisson's ratio  $\nu = 0.3$ . On the left open boundary of the tube, an impulse of external pressure  $p_{ext} = 1.333 \cdot 10^3$  Pa is applied during first 3 ms, followed by zero pressure  $p_{ext}$ , whereas on the right open boundary, the external pressure  $p_{ext}$  is always zero. These conditions generate a pressure impulse that travels along the tube. [Fig. 5.5](#) demonstrates the velocity field in the middle cross section and wall displacement exaggerated by a factor of 10 for clarity, and the radial and axial components of the displacement of the inner tube wall at half the length of the pipe, as functions of time. The extension [Eq. \(5.16\)](#) was used in the simulation.

For the second experiment, we reconsider the idealized model of the aortic bifurcation, which generates the solution of the incompressible Navier–Stokes equations shown in [Fig. 5.3](#). Although the waveforms in vessels with compliant and rigid walls are different under the same boundary conditions, the aortic bifurcation reflecting severely the pressure wave [120] can be interpreted as if it has stiffer walls and even rigid walls. [Fig. 5.6](#) shows cross-sectionally averaged flow rate waveform and pressure waveform at the bifurcation junction computed from the solutions to [Eqs. \(5.1\) and \(5.17\)](#) with time-dependent boundary conditions [132] and linear elastic model with Young's modulii for inlet and outlet cylinders  $E_a = 500$  kPa,  $E_i = 700$  kPa, density  $\rho_w = 1$  g/cm<sup>3</sup>, blood viscosity  $\mu_b = 4$  mPa s, density  $\rho_b = 1060$  kg/m<sup>3</sup>, and mean flow rate  $\bar{Q}_a = 0.4791$  1/min.

In the third experiment, we consider a 2D vessel model with an aneurysm [202]. The computational domain  $\Omega(0) \subset [-8, 0] \times [0, 8]$  mm<sup>2</sup> is shown in [Fig. 5.7](#). The compliant wall of the vessel is presented by the shaded part, and the rest is the fluid domain. The upper open part of the boundary is the inflow with inlet velocity  $v_1(0, y, t) = -50(8 - y)(y - 6)(1 + 0.75 \sin(2\pi t))$ ,  $6 \leq y \leq 8$ . The bottom open part of

**Figure 5.5**

Pressure wave test: velocity field, pressure distribution, velocity vectors, and 10-fold enlarged structure displacement for  $t = 3\text{ms}$  (top, left)  $t = 9\text{ms}$  (top, right), and the axial and radial components of displacement of the inner wall at half the length of the pipe (bottom).

**Figure 5.6**

Flow rate waveform (left) and pressure waveform (right) at the junction computed from the solutions to Eqs. (5.1) and (5.17).

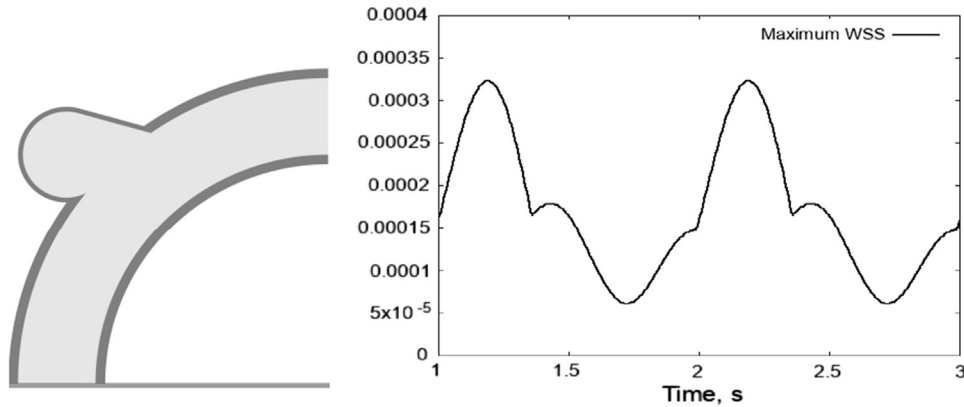


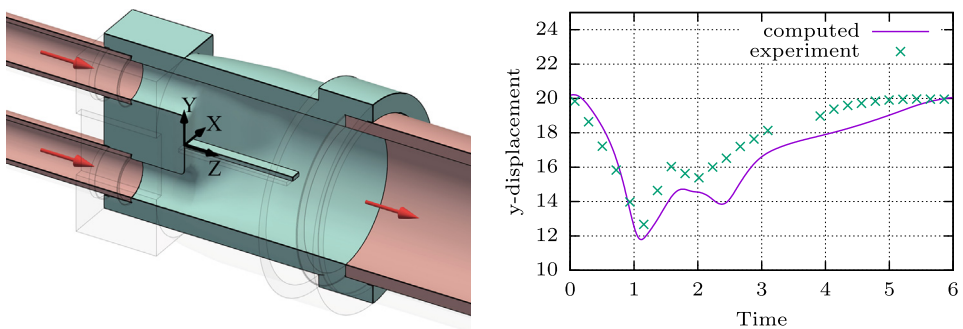
**Figure 5.7**

The computational domain for the 2D model aneurysm and the absolute value of the wall shear stress on the inside of the aneurysm wall.

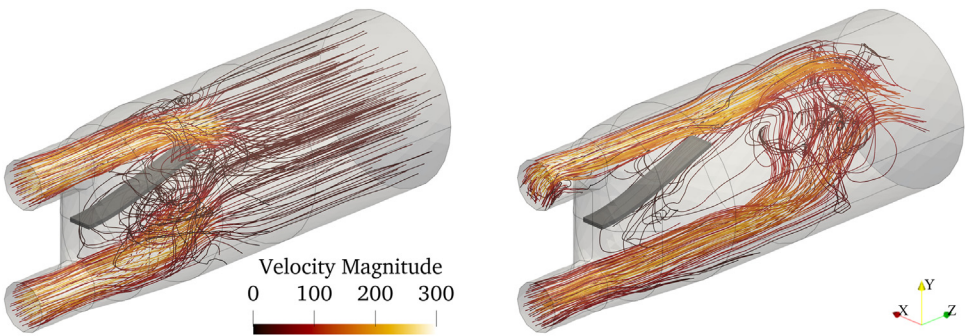
the boundary serves as the outflow with natural boundary condition. The upper and lower ends of the artery walls are fixed. The wall material is assumed to be incompressible neo-Hookean, although compressible neo-Hookean and Saint Venant–Kirchhoff models are applicable as well [173]. We take  $\rho_s = 1.12 \cdot 10^3 \text{ kg/m}^3$ ,  $\rho_f = 1.035 \cdot 10^3 \text{ kg/m}^3$ , and  $\mu_f = 3.4983 \cdot 10^{-3} \text{ Pa}\cdot\text{s}$  from Ref. [202], the shear modulus  $\mu_s = 270 \text{ kPa}$  from Ref. [120], where it was experimentally measured for dog's artery. The extension Eq. (4.63) uses  $\mu_m = \mu_s$  and  $\lambda_m = 4\lambda_s$ . In Fig. 5.7, we present the maximum of the absolute values of the wall shear stress (WSS) evaluated along the dilatation wall. WSS peak values along the vessel wall are crucial in estimating the risk of both aneurysm formation in the initial stages and the eventual rupture.

For the final experiment in this section, we consider the interaction of a three-dimensional clamped beam with a fluid flowing in a pipe [149]. The computational domain is obtained from computer-aided design but is also motivated by biomedical applications. We address transient laminar flow at maximal Reynolds number 1283, which is realistic for cardiovascular flows. The benchmark has been used to validate FSI solvers in Refs. [150,165,172].

Two inlets of diameter 21.9 mm and length 29.5 mm merge smoothly into a cylindrical domain of length 173.55 mm, which terminates with an outlet of diameter 76.2 mm. A silicon filament 2 mm  $\times$  11 mm  $\times$  65 mm is attached to the wall of the flow chamber in the merging section  $z = 0$  (see Fig. 5.8). The parameters of Eqs. (4.64)–(4.66) are  $\rho_s = 1063 \text{ kg/m}^3$ ,  $\rho_f = 1164 \text{ kg/m}^3$ , and  $\mu_f = 11.49 \text{ mm}^2/\text{s}$ . Saint Venant–Kirchhoff material of the filament has the Young modulus  $E = 2.1626 \cdot 10^5 \text{ Pa}$  and Poisson ratio  $\nu = 0.3151$  [165]. The gravity volumetric force acts along the y-direction. The inflow velocities are parabolic and periodic with the frequency  $1/6 \text{ s}^{-1}$ , peak velocities recovered

**Figure 5.8**

Left: flow chamber. Right: comparison of  $y$ -displacement of the point of filament with coordinate  $z \approx 53$ ,  $x = 0$  for  $t \in [0, 6]$  and recorded experimental data (bottom).

**Figure 5.9**

Flow streamlines colored by the velocity magnitude at  $t = 1.153$  s (left) and  $t = 2.449$  s (right).

from the experimental data. On the outflow boundary, we prescribe directional outflow condition as in Eq. (5.6) with  $\alpha = 1$ , but nonzero right-hand side  $\mathbf{g}_N = gy \mathbf{n}$ , where  $g = 9.81$  m/s<sup>2</sup> is the acceleration of gravity.

The dynamics of the filament is driven by normal stresses exerted on the beam by upcoming flow jet and the buoyancy force. Generated unsteady vortical structures interact with the filament and may influence its motion [172]. The swing of the filament computed numerically matches the experimental data (see Fig. 5.8). Fig. 5.9 illustrates the predicted flow at a couple of time instances. Extension Eq. (5.16) was found capable to provide the sequence of untangled meshes.

#### 5.4 Simulation of blood flow in the heart

This section discusses the numerical modeling of blood flow in the heart of a patient. Two major stages are the reconstruction of the flow domain from a sequence of medical images and the numerical solution of flow equations in the reconstructed time-dependent domain.

### 5.4.1 Reconstruction of the heart beat

Our input data are a sequence of 100 contrast-enhanced CT images of beating heart within one cardiac cycle. As discussed in Chapter 3 (Section 3.5.2), these data are processed to a sequence of 100 tetrahedral meshes for the left ventricle cavity. The meshes with 14,033 nodes, 88,150 edges, and 69,257 tetrahedra are topologically invariant in the sense that they have the same nodes, edges, faces, and cells, only node positions are different (see Figs. 3.10, 3.11). The time interval between two consecutive shapes in the sequence is 12.7 ms; this is the best time resolution for the currently available CT measurements. When the deformation is fast, large boundary displacements happen over one time interval, which is the potential cause of numerical error. To cope with this error, we generate a new series of 1981 meshes with 20 times smaller time step  $\Delta t = 0.635$  ms. The mesh  $20(i - 1) + 1$  from the refined series coincides with the mesh  $i$  from the coarse series. The nodal coordinates of intermediate meshes are interpolated by cubic splines from nodal coordinates of available 100 meshes. The meshes from the refined series have good quality. In particular, no cells violate the condition for the Jacobian of the recovered deformation  $J > 0$ , although the ventricle volume varies considerably within the cardiac cycle (see Fig. 5.10).

### 5.4.2 Mathematical model and finite element method

Consider a time-dependent domain  $\Omega(t) \subset \mathbb{R}^3$  occupied by fluid. To formulate a flow problem, we introduce the reference domain  $\widehat{\Omega} = \Omega(0)$  and a mapping from the space–time cylinder  $Q := \widehat{\Omega} \times [0, T]$  to the physical domain,

$$\xi: Q \rightarrow Q^{\text{phys}} := \bigcup_{t \in [0, T]} \Omega(t) \times \{t\}.$$

The mapping is assumed to be level preserving, i.e.,  $\xi(\widehat{\Omega} \times \{t\}) = \Omega(t)$  for all  $t \in [0, T]$ . We assume also that the evolution of  $\Omega(t)$  is sufficiently smooth  $\xi \in C^3(Q)^3$  and that there

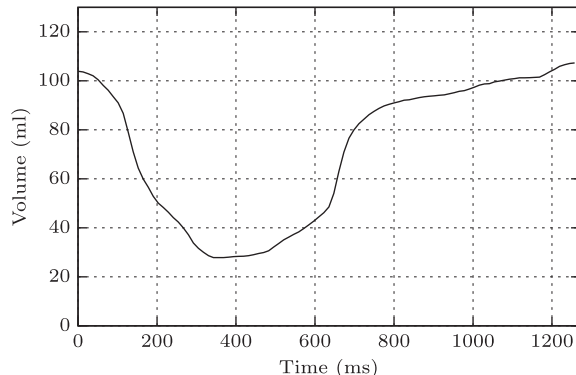


**Figure 5.10**  
Time dependence of ventricle volume.

exist such positive reals  $C_F, c_J$  that, for the spatial gradient matrix of  $\xi$  by  $\mathbf{F} = \nabla_{\mathbf{x}}\xi$  and  $J = \det(\mathbf{F})$ , it holds

$$\inf_Q J \geq c_J > 0, \sup_Q \left( \|\mathbf{F}\|_F + \|\mathbf{F}^{-1}\|_F \right) \leq C_F. \quad (5.23)$$

Given the mapping, the fluid equations can be written in the quasi-Lagrangian form (4.27)–(4.29) for the velocity vector field  $\hat{\mathbf{v}}(\mathbf{x}, t)$  and the pressure function  $\hat{p}(\mathbf{x}, t)$  defined in  $\hat{\Omega}$  for all times  $t \in [0, T]$ . To set up boundary conditions, we first distinguish between different types of the boundaries in the physical flow domain: the no-slip  $\partial\Omega^{ns}(t)$ , Dirichlet  $\partial\Omega^D(t)$ , and outflow  $\partial\Omega^N(t)$  parts of the boundary, and  $\partial\Omega(t) = \partial\Omega^{ns}(t) \cup \partial\Omega^D(t) \cup \partial\Omega^N(t)$ . In the reference domain, we define  $\partial\Omega_0^D = \xi^{-1}\partial\Omega^D(t), \partial\Omega_0^N = \xi^{-1}\partial\Omega^N(t), \partial\Omega_0^{ns} = \xi^{-1}\partial\Omega^{ns}(t)$  and assume that  $\partial\Omega_0^D, \partial\Omega_0^N, \partial\Omega_0^{ns}$  are independent of  $t$  so that we can use notations  $\partial\hat{\Omega}^D, \partial\hat{\Omega}^N, \partial\hat{\Omega}^{ns}$  for them. On  $\partial\Omega^{ns}$ , we impose no-penetration no-slip boundary condition, i.e., the fluid velocity on  $\partial\Omega^{ns}(t)$  is equal to the material velocity of the boundary (see the discussion in the following):

$$\hat{\mathbf{v}} = \xi_t \text{ on } \partial\hat{\Omega}^{ns}, \quad (5.24)$$

while on  $\hat{\Omega}^D$  and  $\hat{\Omega}^N$ , we prescribe Dirichlet and Neumann conditions,

$$\hat{\mathbf{v}} = \hat{\mathbf{v}}_D \text{ on } \partial\hat{\Omega}^D, \quad \hat{\boldsymbol{\sigma}}\hat{\mathbf{n}} = \hat{\mathbf{g}} \text{ on } \partial\hat{\Omega}^N. \quad (5.25)$$

Here,  $\hat{\mathbf{v}}_D$  is a given velocity, and  $\mathbf{n}$  is the exterior unit normal vector on  $\partial\hat{\Omega}$ . If  $\partial\hat{\Omega}^N = \emptyset$ , we assume

$$\int_{\partial\hat{\Omega}^{ns}} \hat{\mathbf{n}} \cdot \xi_t \, ds + \int_{\partial\hat{\Omega}^D} \hat{\mathbf{n}} \cdot \hat{\mathbf{v}}_D \, ds = 0. \quad (5.26)$$

The FEM builds on the weak formulation of Eqs. (4.27)–(4.29). It consists of finding  $\mathbf{v}(t, \mathbf{x})$  and  $p(t, \mathbf{x})$  such that for all  $t \in [0, T]$   $\mathbf{v}(t, \cdot) \in \mathbf{H}^1(\hat{\Omega})$  and  $p(t, \cdot) \in L^2(\hat{\Omega})$ , satisfying  $\mathbf{v} = \xi_t$  on  $\partial\hat{\Omega}^{ns}$ ,  $\mathbf{v} = \mathbf{v}_D$  on  $\partial\hat{\Omega}^D$  and

$$\begin{aligned} & \int_{\hat{\Omega}} J \mathbf{v}_t \Psi_h \, dx + \int_{\hat{\Omega}} J((\nabla \mathbf{v}) \mathbf{F}^{-1} \mathbf{v} - \xi_t) \cdot \Psi \, dx + \int_{\hat{\Omega}} 2\mu J \mathbf{D}_{\xi} \mathbf{v} : \mathbf{D}_{\xi} \Psi \, dx \\ & - \int_{\hat{\Omega}} p J \mathbf{F}^{-T} : \nabla \Psi \, dx + \int_{\hat{\Omega}} q J \mathbf{F}^{-T} : \nabla \mathbf{v} \, dx \\ & = \int_{\hat{\Omega}} J \mathbf{f} \cdot \Psi \, dx + \int_{\partial\hat{\Omega}^N} J \mathbf{g} \cdot \Psi \, ds \end{aligned} \quad (5.27)$$

for all  $\Psi \in \mathbf{H}^1(\widehat{\Omega})$ ,  $\Psi = 0$  on  $\partial\widehat{\Omega}^{ns} \cup \partial\widehat{\Omega}^D$ ,  $q \in L^2(\widehat{\Omega})$ . The FEM, naturally, consists of looking for  $\{\mathbf{v}_h(t), p_h(t)\} \in \mathbb{V}_h \times \mathbb{Q}_h$ , satisfying (5.28) for all  $\Psi_h \in \mathbb{V}_h^0, q_h \in \mathbb{Q}_h$ :

$$\begin{aligned} & \int_{\widehat{\Omega}} J \frac{\partial \mathbf{v}_h}{\partial t} \cdot \Psi_h \, dx + \int_{\widehat{\Omega}} J((\nabla \mathbf{v}_h) \mathbf{F}^{-1} \mathbf{v}_h - \xi_t) \cdot \Psi_h \, dx + \int_{\widehat{\Omega}} 2\mu \mathbf{J} \mathbf{D}_\xi \mathbf{v}_h : \mathbf{D}_\xi \Psi_h \, dx \\ & - \int_{\widehat{\Omega}} p_h J \mathbf{F}^{-T} : \nabla \Psi_h \, dx + \int_{\widehat{\Omega}} q_h J \mathbf{F}^{-T} : \nabla \mathbf{v}_h \, dx \\ & = \int_{\widehat{\Omega}} J \mathbf{f} \cdot \Psi_h \, dx + \int_{\partial\widehat{\Omega}^N} J \mathbf{g} \cdot \Psi_h \, ds. \end{aligned} \quad (5.28)$$

### 5.4.3 Numerical challenges of patient-specific ventricle simulations

The normal velocity of the boundary  $\partial\Omega(t)$  is  $v_\Gamma = \mathbf{n} \cdot (\xi_t \circ \xi^{-1})$ . Both normal  $\mathbf{n}$  and  $v_\Gamma$  can be recovered from the CT data, as discussed in Chapter 3. However, the material tangential velocity of the boundary is defined by the tangential part of  $\xi_t$  only if  $\xi$  is the Lagrangian mapping, i.e.,  $\xi(\mathbf{x}, t)$ ,  $t \in [0, T]$ , which defines the material trajectory for  $\mathbf{x} \in \widehat{\Omega}$  (or at least for  $\mathbf{x} \in \partial\widehat{\Omega}$ ). In some applications, such Lagrangian mapping is not available, and in this case, Eq. (5.24) may produce spurious or zero tangential velocities on the boundary. For example, this may happen if  $\xi$  is reconstructed from medical images. Thus, in practice, one may or may not amend Eq. (5.24) based on any additional information (e.g., tagged MRI, speckle tracking echocardiography) about the tangential motions for a better model.

Besides the ambiguity of tangential motion, the boundary velocities  $\mathbf{v}_h^{ns,D}$  should be compatible with the divergence constraint, i.e., satisfy Eq. (5.26). This additional compatibility is dictated by the integration by parts formula (Gauss's theorem) in the absence of inflow/outflow boundary ( $\partial\widehat{\Omega}^N = \emptyset$ ). Displacements of the ventricle wall contain an error due to roughness of the CT data, its noise, and postprocessing. There is a little chance to satisfy Eq. (5.26) accurately. Therefore, in this case, we let

$$\mathbf{c}_\perp(t) := \int_{\partial\widehat{\Omega}} J \mathbf{F}^{-T} \mathbf{v}_h^{ns,D}(t) \cdot \mathbf{n} \, ds \text{ and update the boundary data } \mathbf{v}_h^{ns,D}(t) := \mathbf{v}_h^{ns,D}(t) - \mathbf{c}_\perp.$$

For the ventricle blood flow, the inflow and outflow parts of the boundary are defined as those representing the mitral and aortic valves, respectively. In the simplest case, the valves function is modeled by the Dirichlet condition for the mitral and aortic valves in their closed state and the homogeneous Neumann condition for the valves in their open state. The latter, however, do not account for the stresses produced by valves on the passing blood flow. To model the resistance of aortic valves to the outflow, the Neumann boundary conditions can be modified as suggested, for example, in Ref. [195] to include the “momentum” flux,

$$(\mathbf{v} \otimes (\mathbf{v} - \xi_t) - \widehat{\boldsymbol{\sigma}}) \mathbf{n} = \widehat{\mathbf{g}},$$

where  $\hat{\mathbf{g}}$  represents the external normal stress, which increases linearly with respect to the flow rate through the aortic orifice. Yet, the most adequate boundary conditions for valves are derived using the geometrical multiscale approach with an FSI model for the blood–valves interaction and a 1D network hemodynamic model to represent the remaining downstream vasculature (see, e.g., Ref. [108]).

It is well known that the systolic contraction and twist of left ventricle produce helical outflow through the aortic valve. The outflow helicity is additionally enforced by the presence of carnel trabecules. The segmentation of the medical images may fail to recover this anatomical detail. If the geometrical model does not contain the network of carnel trabecules, it may produce less helical flow compared with the actual one.

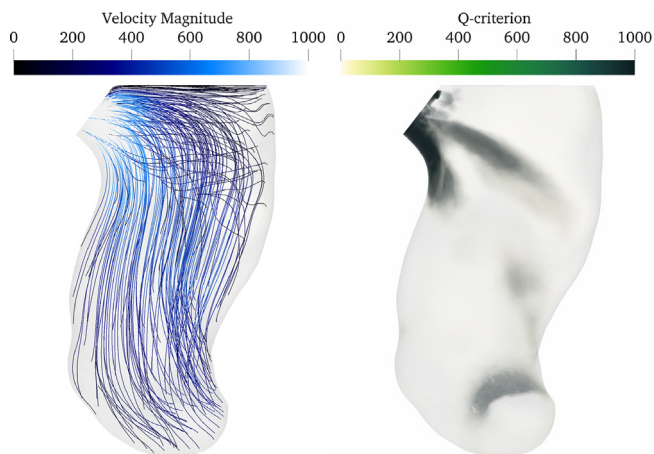
Another challenge of the cardiac hemodynamics is its transitional and even turbulent flow regime [123,136,182]. If the computational mesh is not sufficiently fine to resolve all scales in the flow, then stabilization has to be adopted (see [Section 5.2.3](#)).

#### **5.4.4 Patient-specific simulation of blood flow in the left ventricle**

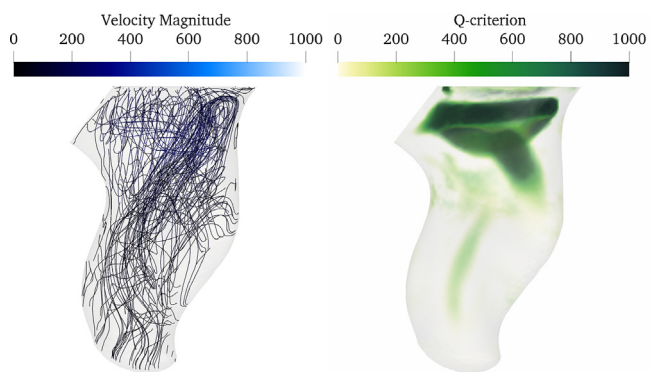
We illustrate the topic of this section by performing numerical simulations of hemodynamics in a simplified model of the human left ventricle. Our main tool is the finite element method ([Eq. 5.28](#)) for solving the Navier–Stokes equations in a moving domain. Simplifications are made by omitting some fine anatomical structures, using simple boundary conditions on the aortic and mitral orifices, and neglecting the ventricle twisting.

The motion of the ventricle  $\Omega(t)$  within one cardiac cycle is given by a sequence of 1981 topologically invariant tetrahedral meshes  $\Omega_h^k$ ,  $k = 1, \dots, 1981$ . We associate with the reference grid the first mesh in the sequence and identify the coordinate of each node  $\mathbf{x}^k$  in  $\Omega_h^k$  with  $\xi^k(\mathbf{x}^1)$ . The mapping  $\xi^k$  is the continuous piecewise linear vector function with prescribed values at the reference grid nodes. The stability and accuracy of the FEM under some smoothness assumptions on the mapping  $\xi$  is analyzed in Ref. [174].

The ventricle boundary is split into aortic valve and mitral valve patches and the remaining part of the boundary. In the systole phase,  $t \in [0, 355]$  ms, we set the “do-nothing” boundary condition ([5.25](#)) with  $\hat{\mathbf{g}} = \mathbf{0}$  (normal stress vanishes) on the patch associated with the aortic valve. In the diastole phase,  $t \in [355, 1257]$  ms, the same boundary condition on the normal stress is imposed on the patch associated with the mitral valve. The zero normal stress condition imitates valve’s opening. On the remaining part of the boundary, including the aortic valve during the diastole phase and the mitral valve during the systole phase, we impose the no-penetration no-slip condition ([5.24](#)),  $\mathbf{v} = \xi_t$ . The viscosity of blood was set  $\mu = 4 \text{ mm}^2/\text{s}$ , and the maximum velocities attain  $1000 \text{ mm}/\text{s}$ , which corresponds to the Reynolds number of order  $10^3$ . Thus, we stabilize the flow using the Smagorinsky turbulent viscosity ([5.15](#)).

**Figure 5.11**

Velocity streamlines and the Q-criterion field at  $t = 180$  ms, horizontal long axis view.

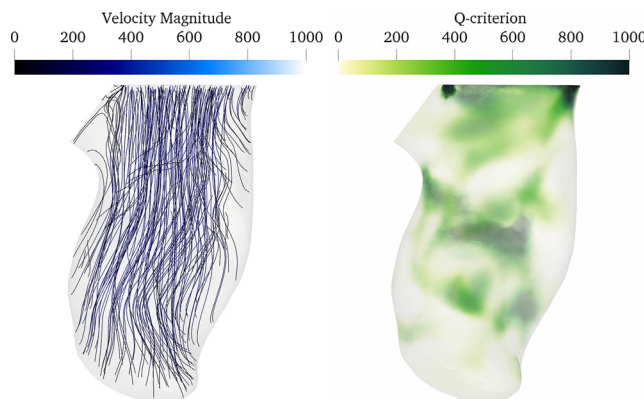
**Figure 5.12**

Velocity streamlines and the Q-criterion field at  $t = 380$  ms, horizontal long axis view.

The computed velocity streamlines and the Q-criterion (Q-criterion is widely used in fluid mechanics to identify flow regions with vortical structures [133]) fields at 180, 380, and 580 ms are shown in Figs. 5.11–5.13, respectively. These instances correspond to the middle of the systole phase, beginning of the diastole phase, and beginning of the second quarter of the diastole phase (cf. Fig. 5.10).

## 5.5 Integration in time and solving systems of algebraic equations

FE models as they were introduced in Sections 5.3.2 and 5.4.2 are not fully computable yet. The approach we use follows the classical method of lines [190]: The application of FEM in space (but not in time) reduces the mathematical model formulated in terms of

**Figure 5.13**

Velocity streamlines and the Q-criterion field at  $t = 580$  ms, horizontal long axis view.

PDEs to a large system of ODEs. Next, we need to handle the time dependence. After discretization in time is done, we obtain systems of algebraic equations, which are solved numerically. We start discussion of time discretizations with the blood flow in the heart model, which does not involve interaction with an elastic structure. For the considerations in the following, the blood flow in vessel with nondeformable walls in [Section 5.2.1](#) can be seen as a particular case of time-independent physical domain and so the mapping  $\xi$  is identity. We further proceed to the full FSI problem.

### **5.5.1 Coupled and splitting methods for the blood flow problem**

Consider a time mesh on  $[0, T]$  with nodes  $t_k = k\Delta t$ ,  $k = 1, \dots, K$ , where  $\Delta t = T/K$  is a constant time step. We use the notation  $\mathbf{v}^k$  to denote approximation of  $\mathbf{v}$  at  $t_k$ ,  $\mathbf{v}^k(\mathbf{x}) \approx \mathbf{v}(t_k, \mathbf{x})$  and similar for  $p$  and other quantities of interest. For approximation of time derivatives, it is convenient to use backward differentiation formulas. We shall need first- and second-order differences:

$$\left[ \frac{\partial f}{\partial t} \right]^k = \frac{f^k - f^{k-1}}{\Delta t} \quad \text{and} \quad \left[ \frac{\partial^2 f}{\partial t^2} \right]^k = \frac{3f^k - 4f^{k-1} + f^{k-2}}{2\Delta t},$$

for a quantity  $f$  defined in time nodes.

Implicit discretizations are very common in computational hemodynamics due to their superior numerical stability. Let  $\mathbf{v}_h^0 = I_h(\mathbf{v}_0)$ , where  $I_h$  stands for FE interpolation operator. The fully implicit FE discretization of (5.28) reads: For  $k = 1, 2, \dots$ , find

$\{\mathbf{v}_h^k, p_h^k\} \in \mathbb{V}_h \times \mathbb{Q}_h$  satisfying  $\mathbf{v}_h^k = I_h(\xi_t^k)$  on  $\partial\widehat{\Omega}^{ns}$ ,  $\mathbf{v}_h^k = I_h(\mathbf{v}_D^k)$  on  $\partial\widehat{\Omega}^D$  and the following equations:

$$\begin{aligned} & \int_{\widehat{\Omega}} J_k \left[ \frac{\partial \mathbf{v}_h}{\partial t} \right]^k \cdot \boldsymbol{\Psi}_h \, dx, + \int_{\widehat{\Omega}} J_k \left( (\nabla \mathbf{v}_h^k) \mathbf{F}_k^{-1} \mathbf{w}_h^k \right) \cdot \boldsymbol{\Psi}_h \, dx \\ & + \int_{\widehat{\Omega}} 2\mu J_k \mathbf{D}_{\xi^k} \mathbf{v}_h^k : \mathbf{D}_{\xi^k} \boldsymbol{\Psi}_h \, dx - \int_{\widehat{\Omega}} p_h^k J_k \mathbf{F}_k^{-T} : \nabla \boldsymbol{\Psi}_h \, dx \\ & + \int_{\widehat{\Omega}} q_h J_k \mathbf{F}_k^{-T} : \nabla \mathbf{v}_h^k \, dx = \int_{\widehat{\Omega}} J_k \mathbf{f}_k \cdot \boldsymbol{\Psi}_h \, dx + \int_{\partial\widehat{\Omega}^N} J_k \mathbf{g} \cdot \boldsymbol{\Psi}_h \, ds \end{aligned} \quad (5.29)$$

for all  $\boldsymbol{\Psi}_h \in \mathbb{V}_h^0$ ,  $q_h \in \mathbb{Q}_h$ , with advection velocity  $\mathbf{w}_h^k := (\mathbf{v}_h^k - \xi_t^k)$  and  $J_k = \det(\mathbf{F}_k)$ ,  $\mathbf{F}_k = \nabla_{\mathbf{x}} \xi^k$ .

On each time step, the method (Eq. 5.29) leads to a large system of nonlinear equations. Newton or inexact Newton method is usually applied to its solution [129]. One may minimize the computational cost of finding  $\{\mathbf{v}_h^k, p_h^k\}$  by making one step of the FEM more explicit. This should be done with certain care, since more explicit schemes may produce numerical instabilities, unless the time step is sufficiently small (sometimes, it is too small that reduces efficiency of simulation). Since the motions of the domain,  $J_k$ ,  $\mathbf{F}_k$ , and  $\xi_k$  are given in Eq. (5.29), the only nonlinear term is the inertia term, the second one in Eq. (5.29). This term is *linearized* by extrapolating advection velocity  $\mathbf{w}_h^k$  from previous time steps, e.g.,  $\mathbf{w}_h^k = (2\mathbf{v}_h^{k-1} - \mathbf{v}_h^{k-2}) - \xi_t(t_k)$  for the linear (second order) extrapolation. With such modification of the inertia term, a *linear* algebraic system should be solved on each time step. The resulting method is proved [174] to be unconditionally stable, which means that numerical stability holds without a restriction on time step  $\Delta t$ . For the rigorous proof, one needs to modify slightly the formulation by including the term:

$$\int_{\widehat{\Omega}} \frac{1}{2} \left( \left[ \frac{\partial J}{\partial t} \right]^k + \operatorname{div}(\mathbf{J}^k \mathbf{F}_k^{-1} \mathbf{w}_h^k) \right) \mathbf{v}_h^k \cdot \boldsymbol{\Psi}_h \, dx,$$

which is consistent due to the identity (4.68). While computations show that in practice this term can be skipped, analysis benefits from including it. In the analysis of FEM for incompressible Navier–Stokes equations, including this term corresponds to the Temam's [1] skew-symmetric form of the convective terms.

One can further reduce the complexity of algebraic problems on each time step of the numerical method for solving Eq. (5.27). One very common way of doing this is decoupling the velocity and pressure update. This can be done by relaxing divergence-free condition and treating pressure explicitly at predictor step and next correcting the velocity field by projecting it back to the space of divergence-free functions. The new pressure or pressure update appears as Lagrange multiplier on this projection step. This idea is developed in the class of so-called projection or quasi-compressibility methods (see Refs. [146,42] for a detailed exposition). An example of such projection is given in

the next section. Another splitting algorithm decouples nonlinearity and incompressibility constraint through decomposition of Eq. (5.27) into the transport diffusion and the Stokes problem on every time step (see, e.g., Ref. [145]).

### 5.5.2 Coupled and splitting methods for the fluid–structure interaction problem

In the same spirit of decoupling, one may integrate in time the FSI problem using the fluid and structure solvers separately. This strategy, however, is well known to have pitfalls. In particular, for certain range of physical parameters, such splitting schemes can be numerically unstable for all values of the time step. This instability is related to so-called “added mass effect” [121]: The presence of the fluid changes the natural vibration frequencies of the elastic structure, which in a simplified setting can be interpreted as adding extra “mass” to the structure. The effect is mostly pronounced if the density of the elastic body is comparable with (or less than) the density of fluid (this is the case of blood and blood vessel wall). Furthermore, geometric anisotropy also plays a role in amplifying the added mass effect. It turns out that a segregate treatment of fluid and structure problems often fails to address adequately this phenomenon and introduces spurious frequencies independently on how small is the time step.

For the reasons outlined above, coupled (also known as *monolithic*) solvers have become popular for the numerical integration of FSI problems (see, e.g., Refs. [154,155,177,185,199]). Of course, the superior numerical stability of monolithic approaches comes with the expense of more computationally demanding algebraic systems to be solved. This extra cost can be somewhat reduced by the linearization of the coupled systems through time-lagging geometric terms. Moreover, nonlinear elasticity models can be also linearized on each time step while keeping the overall stability of the algorithm (we refer to Refs. [107,172,173] for further details).

We now consider a fully discrete method for the FSI FE problem (5.17)–(5.19). This numerical strategy extends semi-implicit schemes for the blood flow problem from Section 5.5.1. However, the FSI problem has stronger nonlinearity due to coupling between the kinematic variables and the evolution of physical domain. In the ALE/Lagrangian formulation (5.17)–(5.19), this evolution is accounted by  $J-s$ ,  $\mathbf{F}-s$ , and  $\mathbf{D}_\mathbf{u}-s$ , which depend on the solution. The fully implicit formulation is built by analog to Eq. (5.29), when all solution-dependent quantities are computed on time step  $t_k$ . The resulting method is computationally expensive. To linearize the formulation, we first make all  $J$ ,  $\mathbf{F}$ , and  $\mathbf{D}_\mathbf{u}$  terms explicit by extrapolating them from previous time steps, i.e., we change  $\mathbf{F}(\mathbf{u}_h^k)$  to  $\tilde{\mathbf{F}}_k = \mathbf{F}(\tilde{\mathbf{u}}_h^k)$ ,  $\tilde{\mathbf{u}}_h^k = \tilde{\mathbf{u}}_h^{k-1} - \tilde{\mathbf{u}}_h^{k-2}$ ,  $J_k$  to  $\tilde{J}_k = \det(\tilde{\mathbf{F}}_k)$ , and  $\mathbf{D}_{\mathbf{u}_h^k}$  to  $\mathbf{D}_{\tilde{\mathbf{u}}_h^k}$ .

We next linearize the advection velocity in the inertia term similar to how we did it above for Eq. (5.29), but now we also have to extrapolate the domain motion:

$$\mathbf{w}_h^k = 2 \left( \mathbf{v}_h^{k-1} - \left[ \frac{\partial \mathbf{u}_h}{\partial t} \right]^{k-1} \right) - \left( \mathbf{v}_h^{k-2} - \left[ \frac{\partial \mathbf{u}_h}{\partial t} \right]^{k-2} \right).$$

The resulting method takes the following form:

$$\begin{aligned}
 & \int_{\Omega_s} \rho_s \left[ \frac{\partial \mathbf{v}_h}{\partial t} \right]^k \cdot \boldsymbol{\Psi}_h \, dx + \int_{\Omega_s} \tilde{\mathbf{F}}_k \mathbf{S}(\mathbf{u}_h^k, \tilde{\mathbf{u}}_h^k) : \nabla \boldsymbol{\Psi}_h \, dx \\
 & + \int_{\Omega_f} \rho_f \tilde{J}_k \left[ \frac{\partial \mathbf{v}_h}{\partial t} \right]^k \cdot \boldsymbol{\Psi}_h \, dx + \int_{\Omega_f} \rho_f \tilde{J}_k (\nabla \mathbf{v}_h^k) \tilde{\mathbf{F}}_k^{-1} \mathbf{w}_h^k \cdot \boldsymbol{\Psi}_h \, dx \\
 & + \int_{\Omega_s} 2\mu_f \tilde{J}_k \mathbf{D}_{\tilde{\mathbf{u}}_h^k} \boldsymbol{\Psi}_h \, dx - \int_{\Omega_f} p_h^k \tilde{J}_k \tilde{\mathbf{F}}_k^{-T} (\tilde{\mathbf{u}}_h^k) : \nabla \boldsymbol{\Psi}_h \, dx = 0
 \end{aligned} \tag{5.30}$$

for all  $\boldsymbol{\Psi}_h \in \mathbb{V}_h^0$ ,

$$\int_{\Omega_s} \left[ \frac{\partial \mathbf{u}_h}{\partial t} \right]^k \boldsymbol{\phi}_h \, dx - \int_{\Omega_s} \mathbf{v}_h^k \boldsymbol{\phi}_h \, dx = 0 \tag{5.31}$$

for all  $\boldsymbol{\phi}_h \in \mathbb{V}_h^{00}$ , and

$$\int_{\Omega_f} \tilde{J}_k (\nabla \mathbf{v}_h^k) : \mathbf{F}_h^{-T} q_h \, dx = 0 \tag{5.32}$$

for all  $q_h \in \mathbb{Q}_h$ . Note that although strong coupling (Eq. 5.20) is imposed on the interface, only a *linear algebraic system should be solved on each time step*.

The added mass phenomenon puts serious restriction on applicability of decoupling to the FSI problem. Nevertheless, splitting schemes are not ruled out entirely. One attractive splitting approach was suggested in Ref. [138] as a natural extension of the projection method for fluid problems. Adopting this decoupling strategy to the ALE/Lagrangian FE formulation with Saint Venant–Kirchhoff material leads to the following three-step algorithm:

**Step 1.** Given  $\mathbf{v}_h^i$ ,  $\mathbf{u}_h^i$ ,  $p_h^i$  for  $i = k-1, k-2, \dots$ , first find intermediate new velocity  $\hat{\mathbf{v}}_h^k$  satisfying

$$\begin{aligned}
 & \int_{\Omega_f} \rho_f \tilde{J}_k \left[ \frac{\partial \hat{\mathbf{v}}_h^k}{\partial t} \right]^k \cdot \boldsymbol{\Psi}_h \, dx + \int_{\Omega_f} \rho_f \tilde{J}_k (\nabla \hat{\mathbf{v}}_h^k) \tilde{\mathbf{F}}_k^{-1} \mathbf{w}_h^k \cdot \boldsymbol{\Psi}_h \, dx \\
 & + \int_{\Omega_f} 2\mu_f \tilde{J}_k \mathbf{D}_{\tilde{\mathbf{u}}_h^k} \hat{\mathbf{v}}_h^k : \mathbf{D}_{\tilde{\mathbf{u}}_h^k} \boldsymbol{\Psi}_h \, dx - \int_{\Omega_f} p_h^{k-1} \tilde{J}_k \tilde{\mathbf{F}}_k^{-T} (\tilde{\mathbf{u}}_h^k) : \nabla \boldsymbol{\Psi}_h \, dx = 0
 \end{aligned} \tag{5.33}$$

for all  $\boldsymbol{\Psi}_h \in \mathbb{V}_h^0$ .

**Step 2.** Find new deformation  $\mathbf{u}_h^k$ , velocity  $\mathbf{v}_h^k$ , and pressure  $\mathbf{p}_h^k$  satisfying

$$\begin{aligned}
 & \int_{\Omega_s} \rho_s \left[ \frac{\partial \mathbf{v}_h}{\partial t} \right]^k \boldsymbol{\Psi}_h \, dx + \int_{\Omega_s} \tilde{\mathbf{F}}_k \mathbf{S}(\mathbf{u}_h^k, \tilde{\mathbf{u}}_h^k) : \nabla \boldsymbol{\Psi}_h \, dx \\
 & + \int_{\Omega_f} \rho_f \tilde{J}_k \frac{\mathbf{v}_h^k - \hat{\mathbf{v}}_h^k}{\Delta t} \cdot \boldsymbol{\Psi}_h \, dx - \int_{\Omega_f} (p_h^k - p_h^{k-1}) \tilde{J}_k \tilde{\mathbf{F}}_k^{-T} (\tilde{\mathbf{u}}_h^k) : \nabla \boldsymbol{\Psi}_h \, dx = 0
 \end{aligned} \tag{5.34}$$

for all  $\Psi_h \in \mathbb{V}_h^0$ ,

$$\int_{\Omega_s} \left[ \frac{\partial \mathbf{u}_h}{\partial t} \right]^k \cdot \boldsymbol{\phi}_h \, dx - \int_{\Omega_s} \mathbf{v}_h^k \cdot \boldsymbol{\phi}_h \, dx = 0 \quad (5.35)$$

for all  $\boldsymbol{\phi}_h \in \mathbb{V}_h^{00}$ , and

$$\int_{\Omega_f} \mathcal{T}^k (\nabla \mathbf{v}_h^k) : \mathbf{F}_k^{-T} q_h \, dx = 0 \quad (5.36)$$

for all  $q_h \in \mathbb{Q}_h$ .

**Step 3.** Extend continuously the deformation field  $\mathbf{u}_h^k$  to the fluid domain, by solving, e.g., auxiliary elasticity equation in  $\Omega_f$ .

We see that on [Step 1](#) only the problem for velocity in  $\Omega_f$  is solved, while on [Step 2](#) velocity, pressure, and deformation serve as unknowns, but the system is greatly simplified in  $\Omega_f$ . The stability of such splitting method was studied in Ref. [138].

### 5.5.3 Systems of linear algebraic equations

Algorithms for solving systems of linear algebraic equations are the cornerstone for the numerical solution of many cardiovascular problems. Both implicit and semi-implicit schemes typically lead to systems of algebraic equations with possibly millions of unknowns. Depending on size, structure, and various algebraic properties of corresponding matrices, direct or iterative methods are used to find (approximate) solution to these systems. We will come across direct solvers later in this chapter. Since the systems of algebraic equations resulting from [Eqs. \(5.29\)](#) or [\(5.30\)–\(5.32\)](#) are, in general, nonsymmetric, generalized minimal residual method (GMRES) [186] is a suitable iterative algorithm for solving them. For the system of equations:

$$Ax = b, \quad A \in \mathbb{R}^{N \times N}, \quad x, b \in \mathbb{R}^N, \quad (5.37)$$

GMRES takes initial guess  $x^0 \in \mathbb{R}^N$  and builds a sequence of approximations (*iterates*)  $x^i, i = 1, 2, \dots$  to the solution  $x$ . For given  $i$ , the iterate  $x^i$  solves the minimization problem:

$$\|Ax^i - b\| = \min_{y \in \mathcal{K}_i} \|A(x^0 + y) - b\|,$$

where  $\mathcal{K}_i$  is the so-called Krylov subspace, defined as

$$\mathcal{K}_i = \text{span}\{r^0, Ar^0, \dots, A^{i-1}r^0\}, \quad r^0 = b - Ax^0.$$

The computational complexity of passing from  $x^{i-1}$  to  $x^i$  is largely defined by complexity of matrix–vector multiplication with the matrix  $A$  (at least for not too large  $i-s$ ).

Therefore, the approach is particularly attractive for solving systems of linear algebraic equations resulting from FEMs, since the corresponding matrices are sparse, i.e., they have very few nonzero entries compared with the total number of entries. The sparsity property

makes the matrix–vector product operation computationally cheap and highly suitable for parallel computing. Another popular choice of the iterative solver for nonsymmetric nondefinite systems is the BiCGstab method [204], which needs less computer memory than GMRES but is less robust: its convergence can be nonmonotone and, in general, is not guaranteed.

Although, in the exact machine arithmetic, the GMRES method would give the exact solution to Eq. (5.37) for some  $i \leq N$ , the method is rarely used as direct (exact) solver. It is much more common to terminate the process for smaller values of  $i$ , when the iterate  $x^i$  is close enough to the true solution  $x$ . The *convergence* of the method (which measures how fast  $x^i$  approaches to  $x$  for increasing  $i$ ), however, strongly depends on algebraic properties of the matrix  $A$ , for example, the bounds on pseudospectrum or field of values for the matrix. Iterative methods based on Krylov subspaces, including their convergence properties, have been extensively addressed in the literature (we refer to the monographs [169,179,187] for further details).

In general, algebraic properties of the matrix  $A$  from Eq. (5.37) should be improved by *preconditioning* for GMRES, BiCGstab, or other iterative method to be efficient. One may think of preconditioning as looking for a matrix  $P \in \mathbb{R}^{N \times N}$ , which is called *preconditioner*, such that

- the equation  $Py = b$  is “easily” solved with any given right-hand side vector  $b$  and
- the product matrix  $P^{-1}A$  or  $AP^{-1}$  is more suitable for applying the iterative method.

Different approaches for building preconditioners have been proposed [206]; some of them explicitly exploit information and properties of the underlying PDE system and FE method, whereas others are entirely based on entries of matrix  $A$ . Both approaches are used for FE discretizations of hemodynamics problems. In particular, for the blood flow problems in nondeformable volumes, it is common to design  $P$  by exploiting the block structure of the matrix  $A$ . This structure is well seen after regrouping velocity unknowns first and pressure unknowns next:

$$\begin{pmatrix} A & B^T \\ B & 0 \end{pmatrix} \begin{pmatrix} v \\ p \end{pmatrix} = \begin{pmatrix} b_v \\ b_p \end{pmatrix} \Leftrightarrow Ax = b, \quad (5.38)$$

$v$  and  $p$  are the vectors of nodal values of FE velocity and pressure functions. Then one may construct  $P$  (or directly  $P^{-1}$ ) through defining preconditioners for the velocity block  $A$  and for the pressure Schur complement matrix  $-BA^{-1}B^T$ , which arise if one applies the blockwise Gauss elimination procedure to the system (5.38). In turn, a preconditioner for  $A$  can be built upon a PDE-based technique such as multigrid or domain-decomposition algebraic solver [116,179], and for  $-BA^{-1}B^T$ , less standard approaches should be used.

Preconditioners exploiting the block structure of system (5.38) in this or other ways are well studied in the literature (see, e.g. Refs. [109,135,179] and references therein).

An alternative to block preconditioners is based on elementwise incomplete factorizations of the  $2 \times 2$  block matrix from Eq. (5.38). Among various factorizations, the ILU factorization is the most commonly considered for the purpose of preconditioning. In this approach, one looks for a left triangle matrix  $L$  and a right triangle matrix  $R$  such that

$$A = LR + E \quad (5.39)$$

where  $E$  is the error matrix of the decomposition. The factors  $L$  and  $R$  are easily “invertible” (assuming all diagonal elements are nonzero); hence,  $LR$  can be a good preconditioner if  $E$  has a small norm compared with  $A$  or/and  $E$  has a small rank [187]. Preconditioners based on incomplete LU factorization are less studied for the discrete fluid system than various block preconditioners. Several approaches to building ILU preconditioners for nonsymmetric saddle-point systems that arise from the FE discretization of the incompressible Navier–Stokes equations have been suggested in Refs. [126,161,162,205]. Numerical results in Section 5.2.4 were computed using the second-order threshold ILU preconditioners [161,162]. In particular, the method was successfully applied to simulate a flow in a reconstruction of the right coronary artery of a real patient. The assessment of block preconditioners in the hemodynamics context can be found in Ref. [131]. Comparison studies of some block and ILU preconditioners were published in Refs. [205,192]. Finally, we note that applying numerical stabilization such as SUPG method discussed in Section 5.2.3 may perturb the matrix structure in Eq. (5.38), leading to (1,2)-block not equal to the transpose of (2,1)-block; also (2,2) may become nonzero. These changes may affect algebraic properties of the matrix making them more or less favorable, depending on the stabilization method applied and algebraic solver to be used.

The algebraic system becomes even more complicated for the problem where blood flow interacts with the elastic walls of the vessel. For the semi-implicit method (Eqs. (5.30)–(5.32)), the algebraic system can be written in the block form:

$$\begin{pmatrix} E_f & 0 & 0 & I_{fs} & 0 \\ 0 & A_f & B^T & 0 & J_{fs} \\ 0 & B & 0 & 0 & 0 \\ 0 & 0 & 0 & M_s & C_s \\ 0 & J_{sf}^v & J_{sf}^p & E_s & A_s \end{pmatrix} \begin{pmatrix} u_f \\ v_f \\ p \\ u_s \\ v_s \end{pmatrix} = \text{r.h.s. vector}, \quad (5.40)$$

$v_f, p$  are the vectors of nodal values of FE fluid (blood) velocity and pressure functions,  $u_f$  is ALE displacement field in the fluid domain, and  $u_s$  and  $v_s$  are the displacement and velocity of the elastic body.

From Eq. (5.40), we see that  $u_f$  can be found separately after  $u_s$  becomes available. Other variables  $v_f, p, u_s$ , and  $v_s$ , however, cannot be decoupled. To solve for them numerically, either a preconditioner for GMRES/BiCGstab iterations has to be designed or one can use a direct solve based on exact factorization of the matrix. The latter is a feasible option only if the number of degrees of freedom is not too large. For numerical examples in Sections 5.3.3 and 5.4.4, we use multifrontal sparse direct solver MUMPS [106]. The acceptable accuracy with moderate number of degrees of freedom (not significantly exceeding  $10^5$  d.o.f.) is achieved, thanks to the higher-order FE combined with a mesh adaptation.

There exists an extensive literature on building suitable preconditioners for linear systems resulting from monolithic FSI FE formulations like Eqs. (5.30)–(5.32). Most of them exploit the block structure of the matrix in Eq. (5.40). One natural strategy would be to build a preconditioner by removing some coupling off-diagonal blocks in Eq. (5.40) so that fluid and structure problems can be solved independently, when the preconditioner is applied. Such decoupling may inherit a deficiency related to the added mass effect (see Section 5.5.2) in the sense that the convergence of the preconditioned iterations may deteriorate for the same values of physical parameters, when the splitting time-stepping method exhibits numerical instability. In Ref. [107], it was noted that the stable splitting Eqs. (5.33)–(5.36) can be translated into more robust preconditioning of the coupled system (5.40). More on preconditioning of FSI linear algebraic systems can be found, for example, in Refs. [119,125,130,160].

# Lumped parameter models

## 6.1 Introduction

### 6.1.1 General idea of the lumped models

Depending on a biomedical application, a different level of details is required from the mathematical model of the cardiovascular system. If only basic (averaged) information is required, then a common approach is to apply spatial reduction techniques. The extreme spatial reduction produces lumped parameter models (also known as zero-dimension or 0D models). In a lumped parameter model, the region of interest (whole organism or its local part) is virtually represented by a set of compartments connected to each other. Each compartment may represent an organ, a portion of a tissue, or a part of the body. For example, the 0D model presented in Ref. [211] relates average values of the flow rate, velocity, and pressure in the compartments without resolving any spatial details, whereas the 0D model from Ref. [212] takes into account some spatial elements like heart valves.

Lumped parameter models usually need a few parameters that can be measured easily for a specific patient. The 0D models have low computational cost. They allow fast hemodynamic simulations over dozens of heart cycles. The lumped parameter hemodynamic models can be classified into heart function models, vascular compartment models, and terminal resistance models. Examples of such models are the four-compartment dynamical model of the heart from Ref. [213], leading to a stiff system of ordinary differential equations (ODEs), or the model of cerebral hemodynamics from Ref. [214], resulting in the nonlinear ODE of Van der Pol–Duffing oscillator.

In this chapter, we focus on a model of the heart function. The model is simple enough and shares a lot of features with many lumped parameter models. We note that a detailed mathematical model of the heart function should account the action potential propagation, myocardium tissue mechanics, hydrodynamics of the blood in the chambers, and coronary flow with myocardium perfusion, although modeling some of these phenomena separately may have practical sense as well. Closed models of the cardiovascular system, studied in Refs. [213,216–222], describe the heart function in terms of the pressure–volume relationship and/or the cardiac output and the ejection fraction. Both statistics depend on the venous inflow to the auricles (preload conditions) and arterial outflow from the

ventricles (afterload conditions). These models operate with such parameterized statistics (called further *parameters*) as the volume of the heart chambers, the pressure, and the flow rate through chamber–chamber or chamber–vessel connections. The conservation laws and semi-empirical hydrodynamic laws help to relate these parameters together.

Another common approach relates the lumped parameters of the heart and vasculature using electromechanical analogy between the elements of electrical circuit (voltage, current, resistance, capacity, and inductance) and the mechanical variables (pressure, flow rate, hydraulic resistance due to the blood viscosity, elasticity, and blood inertia). The resulting system of ODEs has the same mathematical properties for both lumped hydrodynamic and electric circuit approaches. The number of equations depends on the compartment decomposition, which may include heart chambers, vascular regions, microcirculatory regions, aneurysms, etc. The reviews of the underlining principles and mathematical models for both the heart chambers and the vascular regions can be found in Refs. [223–226].

### ***6.1.2 The scope and limitations of lumped models***

The output of lumped models describes the dynamics of averaged flow statistics for compartments such as flow rate, pressure, and volume, without providing any spatial details. Such models may be used to describe blood flows in a segment of a large vessel [227], to simulate hemodynamics in a part of a network of large vessels [212], to account for a large region of microcirculation [215], to analyze the heart ejection dynamics [213], to set boundary conditions for terminal vessels in higher dimensional models [221,228], to perform the closure of arterial and venous network models [218,221,228] (required for drug transport simulations), and to facilitate smooth coupling for models of different dimensions [229] (we refer to Section 7.3 for details). Various aspects of the lumped parameter approach for blood flow modeling can be found in Refs. [223–225,230]. The work [231] defines heart outflow as a function of time, which correlates with the auricle pressure and provides construction of a conservative closed circulation model. Lumped models may account for several physiological effects such as vascular bed nervous control [218,225] and viscoelasticity of vascular walls [223].

Among the drawbacks of 0D models, we note the lack of spatial details and the absence of the heart rate variability accounting for dependence of the systole to diastole ratio under preload and after-load conditions and the heart rate. The heart rate variability is an important phenomenon for some clinical applications such as coronary circulation during tachycardia (Section 7.6.3) and assessment of the fractional flow reserve (Section 9.4.2).

## 6.2 Electromechanical analogy

Although the electric circuit approach is difficult to apply to the detailed compartment representation of the cardiovascular system due to the indirect analogy between electric circuits and vascular networks (so-called inexact consistency [224]), one may compare formulations of two basic 0D models of a lumped compartment with one input and one output channel. The first model uses mechanical principles and operates with averaged pressure ( $P$ ) and flow rate ( $Q$ ) through an elastic reservoir with volume ( $V$ ). The second model is the electric circuit-based analog.

The mass conservation states the balance between the change of volume and flow rate:

$$\frac{dV}{dt} = Q_{in} - Q_{out}, \quad (6.1)$$

where  $Q_{in}$  and  $Q_{out}$  are the instantaneous inflow and outflow rates. The Poiseuille's law relates pressure drop  $\Delta P_{in,out}$  and flow rate over the input or the output through

$$\Delta P_{in} = R_{in}Q_{in}, \quad \Delta P_{out} = R_{out}Q_{out} \quad (6.2)$$

where  $R_{in,out}$  is the hydraulic resistance of the input or output channel, which may be constant or may vary depending on time and flow parameters (regulation, autoregulation, non-Newtonian rheology, etc.).

For the linear elastic material of the vessel wall, we have  $V = PC$ , where  $C$  is the elasticity coefficient and  $P$  is the pressure inside the compartment. Finally, dynamics of the volume is subject to second Newton's law:

$$I \frac{d^2V}{dt^2} + R \frac{dV}{dt} + \frac{V}{C} = P^{ext}, \quad (6.3)$$

where  $I$  is the inertia parameter,  $R$  is the hydraulic resistance of the compartment, and  $P^{ext}$  is the pressure exerted by external forces. System (6.1)–(6.3) can be used alone or can be coupled with other models via input and output pressure drops  $\Delta P_{in}$  and  $\Delta P_{out}$  and flow rates  $Q_{in}$  and  $Q_{out}$ .

The standard analysis of ODEs shows that system (6.1)–(6.3) describes free or forced oscillations.

According to second Kirchhoff's law, a similar system describes oscillations of an alternating current in electric circuit that includes resistor, inductance, and capacity:

$$L_e \frac{dI_e}{dt} + R_e I_e + U_e = E_e, \quad (6.4)$$

where  $I_e$  is the current,  $L_e$  is the inductance,  $R_e$  is the electric resistance,  $U_e$  is the voltage, and  $E_e$  is the electromotance. Recalling that

$$I_e = \frac{dq_e}{dt}, \quad U_e = \frac{q_e}{C_e}, \quad (6.5)$$

where  $q_e$  is the electric charge and  $C_e$  is the capacity, one can rewrite Eq. (6.4) as

$$L_e \frac{d^2 q_e}{dt^2} + R_e \frac{dq_e}{dt} + \frac{q_e}{C_e} = E_e. \quad (6.6)$$

The obvious equivalence of Eqs. (6.3) and (6.6), as well as the equivalence of Eq. (6.1) and the first Kirchhoff law and the equivalence of Eq. (6.2) and Ohm's law for a part of circuit, allows us to postulate an analogy between the blood flow in a vascular region and a heart chamber and the electric current in an electrical circuit with parallel and sequential elements. Within this framework, the electric potential ( $U_e$ ) corresponds to the hydraulic pressure ( $P$ ), the electric charge ( $q_e$ ) corresponds to the volume of blood ( $V$ ), the electric current ( $I_e$ ) corresponds to the flow rate ( $Q$ ), the electric resistance ( $R_e$ ) corresponds to the hydraulic resistance ( $R$ ), the capacity ( $C_e$ ) corresponds to the elasticity coefficient ( $C$ ), and the inductance ( $L_e$ ) corresponds to the inertia coefficient ( $I_e$ ). Methods for electric circuit modeling are well developed; the initial value problem for the system of ODEs (6.4)–(6.6) is computationally simple.

It is proved [227] that the solution to Eqs. (6.4)–(6.6) for a single compartment is a first-order (both in space and time) approximation of solution to a linearized 1D hemodynamic system. However, inexact consistency of the electric circuit models complicates the development of complex compartment models [224].

### 6.3 Dynamical lumped model of the heart

In absence of interchamber defects, the left and right hearts can be considered separately using similar models. We consider a model for the left heart. It includes the left auricle, which receives blood from the pulmonary vein, and the left ventricle, which ejects blood to the aorta. One fundamental concept of the heart function is time-varying elastance. Periodic heart function can be analyzed by the pressure–volume trajectory (PV diagram) that represents a closed contour in  $(P, V)$  coordinates. The lumped elasticity of the heart chamber is defined as a slope of PV diagram, which is the instant ratio  $E = \frac{\Delta P}{\Delta V}$ . Here,  $\Delta V$  is volume change due to pressure change  $\Delta P$ . Details about the cardiac cycle within the scope of variable elasticity model are given in Refs. [232–235]. The cardiac cycle is driven by a periodic change of the elasticity  $E$  due to electrical stimulation of myocardium by the sinoatrial node activation. During systole, the myocardium becomes stiffer so that tension increases to its maximum value and ejection happens. During diastole,

elasticity decreases to its minimum, which promotes a faster filling of the chambers at low pressures. A detailed review in Ref. [224] covers lumped models of chamber interactions, various regulatory effects, and interaction with vascular and respiratory systems.

For the sake of brevity, we denote by  $d$  the diastolic phase,  $fr$  is the friction force,  $max$  is the maximum value,  $min$  is the minimum value,  $p$  is the pressure force,  $pb$  is the beginning of the  $P$  wave,  $pw$  is the duration of the  $P$  wave,  $r$  is the resistance force,  $s$  is the systole,  $s1$  is the peak systole, and  $s2$  is the end systole, whereas  $mi$  refers to the mitral valve,  $ao$  to the aortic valve,  $lpv$  to the input from left pulmonary veins to the left auricle, and  $sas$  to the entrance to aorta (aortic sinus). For notations, see also Fig. 6.1.

Using the concept of variable elastance, one can adopt a basic model of lumped compartment (Eqs. 6.1–6.3) for the two-chamber dynamical model of the left heart:

$$\begin{aligned} I_{lv} \frac{d^2 V_{lv}}{dt^2} + R_{lv} \frac{dV_{lv}}{dt} + E_{lv}(t)(V_{lv} - V_{lv}^0) + P_{lv}^0 &= P_{lv}, \\ I_{la} \frac{d^2 V_{la}}{dt^2} + R_{la} \frac{dV_{la}}{dt} + E_{la}(t)(V_{la} - V_{la}^0) + P_{la}^0 &= P_{la}, \end{aligned} \quad (6.7)$$

where  $lv$  refers to the left ventricle,  $la$  refers to the left auricle,  $V^0$  is the reference volume of the chamber, and  $P^0$  is the reference pressure in the chamber,

$$E(t) = E^d + \frac{E^s - E^d}{2} e(t). \quad (6.8)$$

For the left ventricle, we set

$$e_{lv}(t) = \begin{cases} 0.5 \left( 1 - \cos \frac{t}{T_{s1}} \pi \right), & 0 \leq t \leq T_{s1}, \\ 0.5 \left( 1 + \cos \frac{t - T_{s1}}{T_{s2} - T_{s1}} \pi \right), & T_{s1} < t < T_{s2}, \\ 0, & T_{s2} \leq t \leq T. \end{cases} \quad (6.9)$$

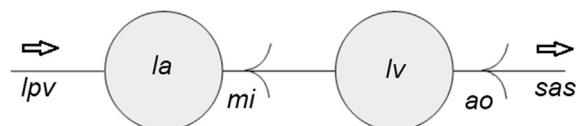


**Figure 6.1**  
Scheme of the lumped heart model.

whereas for the left auricle

$$e_{la}(t) = \begin{cases} 0, & 0 \leq t \leq T_{pb}, \\ 0.5 \left( 1 - \cos \frac{t - T_{pb}}{T_{pw}} 2\pi \right), & T_{pb} < t < T. \end{cases} \quad (6.10)$$

Flow rate through the left ventricle and auricle is given by

$$\begin{aligned} \frac{dV_{lv}}{dt} &= Q_{mi} - Q_{ao}, \\ \frac{dV_{la}}{dt} &= Q_{lpv} - Q_{mi}. \end{aligned} \quad (6.11)$$

The Poiseuille pressure drop condition (6.2) for every connecting channel is

$$\begin{aligned} Q_{ao} &= g_{ao}(\theta_{ao}) \frac{P_{lv} - P_{sas}}{R_{ao}}, \\ Q_{mi} &= g_{mi}(\theta_{mi}) \frac{P_{la} - P_{lv}}{R_{mi}}, \\ Q_{lpv} &= \frac{P_{lpv} - P_{la}}{R_{lpv}}, \end{aligned} \quad (6.12)$$

where  $g(\theta) = \{\theta^{\min} \leq \theta \leq \theta^{\max}, 0 \leq g(\theta) \leq 1\}$  is a monotone function, which models valve opening. For the closed valve, it holds  $g(\theta^{\min}) = 0$ , while for the opened valve, we have  $g(\theta^{\max}) = 1$ . For the simplest model with the instant valves closing, it is natural to define

$$\begin{aligned} g_{ao}(\theta_{ao}) &= \begin{cases} 1, & P_{lv} \geq P_{sas}, \\ 0, & P_{lv} < P_{sas}, \end{cases} \\ g_{mi}(\theta_{mi}) &= \begin{cases} 1, & P_{lpv} \geq P_{lv}, \\ 0, & P_{lpv} < P_{lv}. \end{cases} \end{aligned} \quad (6.13)$$

Parameters and coefficients of the model are given in Table 6.1 according to the study in [212].

Essential elements of the heart are the valves between the auricles and ventricles and between ventricles and aorta or pulmonary artery. Valves help to maintain the unidirectional flow from venous to arterial parts, especially during the diastole phase when the heart chambers are filled with a new portion of venous blood.

The periods of valves rapid opening and closing are rather small, but the dynamics of valves makes significant impact on the blood flow through the heart during these periods. The authors of Ref. [213] describe the valve function as an instant opening/closing of appropriate flow channels between the chambers and between the chambers and outgoing

**Table 6.1: Parameters of the model in Eqs. (6.7)–(6.13).**

Parameter	Value
$E_{lv,s}$	2.0 mm Hg/mL
$E_{lv,d}$	0.05 mm Hg/mL
$I_{lv}$	$10^{-5}$ mm Hg/mL
$R_{lv}$	$4 \cdot 10^{-5}$ mm Hg s/mL
$E_{la,s}$	0.25 mm Hg/mL
$E_{la,d}$	0.15 mm Hg/mL
$I_{la}$	$10^{-5}$ mm Hg/mL
$R_{la}$	$4 \cdot 10^{-4}$ mm Hg s/mL
$T_{pw}$	0.08 s
$K^p$	$5.5 \cdot 10^3$ rad/s <sup>2</sup> ·mm/Hg
$K^b$	2 rad/s/m
$\theta_{ao}^{min}$	0°
$\theta_{ao}^{max}$	75°
$\theta_{mi}^{min}$	0°
$\theta_{mi}^{max}$	75°
$P_{sas}$	100 mm Hg
$P_{lpv}$	37 mm Hg
$T_{s1}$	0.3 s
$T_{s2}$	0.44 s
$T_{pb}$	0.92 s
$K^f$	50 s <sup>-1</sup>
$K_{ao}^v$	7 rad/s/m
$K_{mi}^v$	3.5 rad/s/m

arteries at prescribed time moments. Also the work [222] accounts for the valve function by the sign of pressure drop (Eq. 6.13): negative sign means the closed state. Electrical analog of the heart valve is a diode combined with a resistor. In reality, valve motion depends on many flow phenomena such as the pressure gradient across the valve, vorticity generation, the shear forces acting on the valve leaflets as discussed in Ref. [224]. A mechanical lumped parameter model accounting for these phenomena is proposed in Refs. [212,236]. The model uses the angle of valve opening, which is, of course, a lumped parameter describing the valve status and motion. For a model that takes valve dynamics into account, one may consider the following valve function:

$$g_{ao}(\theta_{ao}) = \frac{(1 - \cos \theta_{ao})^2}{(1 - \cos \theta_{ao}^{max})^2}, \quad \theta_{ao}^{min} \leq \theta_{ao} \leq \theta_{ao}^{max},$$

$$g_{mi}(\theta_{mi}) = \frac{(1 - \cos \theta_{mi})^2}{(1 - \cos \theta_{mi}^{max})^2}, \quad \theta_{mi}^{min} \leq \theta_{mi} \leq \theta_{mi}^{max}, \quad (6.14)$$

$$g(\theta) = \begin{cases} 0, & \theta < \theta^{min}, \\ 1, & \theta > \theta^{max}, \end{cases}$$

where  $\theta_{ao}$  and  $\theta_{mi}$  are governed by second Newton's law:

$$\begin{aligned}\frac{d^2\theta_{ao}}{dt^2} &= -K_{ao}^f \frac{d\theta_{ao}}{dt} + (P_{lv} - P_{sas}) K_{ao}^p \cos \theta_{ao} + K_{ao}^b Q_{ao} \cos \theta_{ao} - K_{ao}^v Q_{ao} \sin 2\theta_{ao} \tilde{f}_{ao}, \\ \frac{d^2\theta_{mi}}{dt^2} &= -K_{mi}^f \frac{d\theta_{mi}}{dt} + (P_{la} - P_{lv}) K_{mi}^p \cos \theta_{mi} + K_{mi}^b Q_{mi} \cos \theta_{mi} - K_{mi}^v Q_{mi} \sin 2\theta_{mi} \tilde{f}_{mi}.\end{aligned}\quad (6.15)$$

Here, we introduced functions:

$$\begin{aligned}\tilde{f}_{ao} &= \frac{1}{2} (1 + \tanh \tilde{A}_{ao} (P_{lv} - P_{sas})), \quad \tilde{A}_{ao} = 10, \\ \tilde{f}_{mi} &= \frac{1}{2} (1 + \tanh \tilde{A}_{mi} (P_{la} - P_{lv})), \quad \tilde{A}_{mi} = 10,\end{aligned}\quad (6.16)$$

which produce smooth switching of the corresponding terms in Eq. (6.15).

## 6.4 Numerical methods

### 6.4.1 Heart model

With parameters chosen in physiological range, the system of ODEs (6.7)–(6.16) is stiff. It means that the solution includes both sharp and gradual variations, especially in the case of instant valve opening and closing. Numerical discretization of such ODEs requires special stability control, which may substantially limit the integration step. An implicit one-step A- and L-stable third-order accurate method described below provides a reasonable basic choice of a numerical solver for system (6.7)–(6.16). The idea of the method can be found in Ref. [237].

Adopting vector notations

$$\mathbf{y} = \left( V_{lv} \quad \frac{dV_{lv}}{dt} \quad V_{la} \quad \frac{dV_{la}}{dt} \quad \theta_{ao} \quad \frac{d\theta_{ao}}{dt} \quad \theta_{mi} \quad \frac{d\theta_{mi}}{dt} \right)^T, \quad (6.17)$$

we rewrite system (6.7)–(6.16) as

$$\frac{d\mathbf{y}}{dt} = \mathbf{f}(t, \mathbf{y}), \quad \frac{d\mathbf{w}}{dt} = \frac{\partial \mathbf{f}}{\partial t} + \frac{\partial \mathbf{f}}{\partial \mathbf{y}} \mathbf{f}, \quad (6.18)$$

where  $\mathbf{w} = \frac{d\mathbf{y}}{dt}$ ,  $\mathbf{f}$  is the right-hand side of Eqs. (6.7)–(6.16). The general single-step implicit Runge–Kutta method for the numerical solution of Eq. (6.18) has the form of a system of nonlinear equations:

$$\mathbf{R}(\mathbf{y}^{n+1}) = \sum_{k=0}^1 \left[ a_k \mathbf{y} - \tau b_k \mathbf{f} - \tau^2 c_k \left( \frac{\partial \mathbf{f}}{\partial t} + \frac{\partial \mathbf{f}}{\partial \mathbf{y}} \mathbf{f} \right) \right]_{t=t^{n+k}, \mathbf{y}=\mathbf{y}^{n+k}} = \mathbf{0}, \quad (6.19)$$

which can be solved by Newton's method:

$$\mathbf{y}_{s+1}^{n+1} = \mathbf{y}_s^{n+1} - \mathbf{B}^{-1}(t^{n+1}, \mathbf{y}^{n+1}) \mathbf{R}(\mathbf{y}_s^{n+1}), \quad s = 1, 2, \dots, \mathbf{y}_0^{n+1} = \mathbf{y}^n, \quad (6.20)$$

where

$$\mathbf{B} = \frac{\partial \mathbf{R}}{\partial \mathbf{y}^{n+1}} = \mathbf{E} - \tau b \frac{\partial \mathbf{f}}{\partial \mathbf{y}} - \tau^2 c \left( \frac{\partial}{\partial \mathbf{y}} \left( \frac{\partial \mathbf{f}}{\partial t} \right) + \left( \frac{\partial \mathbf{f}}{\partial \mathbf{y}} \right)^2 + \mathbf{C} \right), \quad (6.21)$$

and

$$\mathbf{C} = \left\{ \left( \frac{\partial}{\partial y_j} \left( \frac{\partial \mathbf{f}}{\partial \mathbf{y}} \right) \right) \mathbf{f} \right\}, \quad \left( \frac{\partial \mathbf{f}}{\partial \mathbf{y}} \right)_{i,j} = \frac{\partial f_i}{\partial y_j}. \quad (6.22)$$

The set of parameters

$$a_1 = 1, a_0 = -1, b_0 = \frac{1}{2} + c_0 + c_1, b_1 = \frac{1}{2} - c_0 - c_1, c_1 = c_0 - \frac{1}{6}, c_0 = 0 \quad (6.23)$$

defines a third-order numerical method, which is both A- and L-stable as shown in Ref. [238].

#### 6.4.2 Coupling with the vascular network

The model in Eqs. (6.7)–(6.16) assumes constant pressure at  $lpv$  and  $ao$ . One may use these values for coupling the model with the 1D network model of vascular hemodynamics discussed in Chapter 7. The values of pressure  $P_{lpv}$  and  $P_{ao}$  are the same as the values of pressure  $P(S)$  at the corresponding points of 1D vessels. Thus, the complete discrete system of equations includes the mass conservation Eq. (7.16), the discretized compatibility conditions (7.32), the constitutive relationship (7.44) at  $lpv$  and  $ao$ , and the numerical implementation of the model in Eqs. (6.7)–(6.16). The above system is solved after completing one time step for the 1D model in internal nodes of the vessels presented in detail in Section 7.4.2. The following iterative algorithm can be applied to solve the coupled 1D–0D system:

1. Set the initial values of pressure  $P_{lpv}$  and  $P_{ao}$  equal to the values from the previous time step or previous iteration.
2. Perform one time step using the numerical discretization of the 0D heart model according to Section 6.4.1. This step invokes embedded iterations and computes flow rates  $Q_{lpv}$  and  $Q_{ao}$ .
3. Compatibility condition (7.32) and constitutive relationship (7.44) provide the updated 1D linear velocity ( $v$ ), cross section ( $S$ ), and pressure values at  $lpv$  and at  $ao$  (refer to Section 7.4.2).

4. Compute pressure difference between the current iteration and previous time step at  $lpv$  and at  $ao$ , and check the relative error.

## 6.5 Accounting for valve pathologies

The heart valves function causes a significant impact on the cardiac output. In this section, we compare the difference between the model with instant aortic and mitral valve opening and closing and the model with dynamical valves opening and closing (Eqs. (6.14–6.16)). The narrowing of the atrioventricular lumen may cause the stenosis of mitral valve and decrease the cardiac output. It is modeled by a decrease of maximum opening angle of the mitral valve  $\theta_{mi}^{max}$ . The backward flow through the aortic valve during diastole due to aortic dilatation is known as aortic regurgitation or aortic insufficiency. It is modeled by an increase of minimum opening angle  $\theta_{ao}^{min}$ .

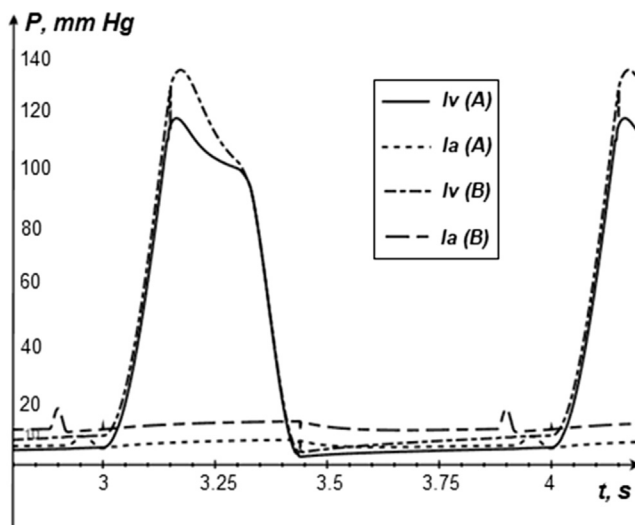
### 6.5.1 Comparison of valve closing models

Here, we compare the difference between the model with dynamical valves opening and closing (Eqs. 6.14–6.16) (model A) and the model with the instant aortic and mitral valve closing (model B). Instead of the instant valves closing controlled by the pressure drop condition across the valve (Eq. 6.13), we shall use another model with the prescribed valve function  $g(\theta)$  for the predefined time periods from Ref. [213].

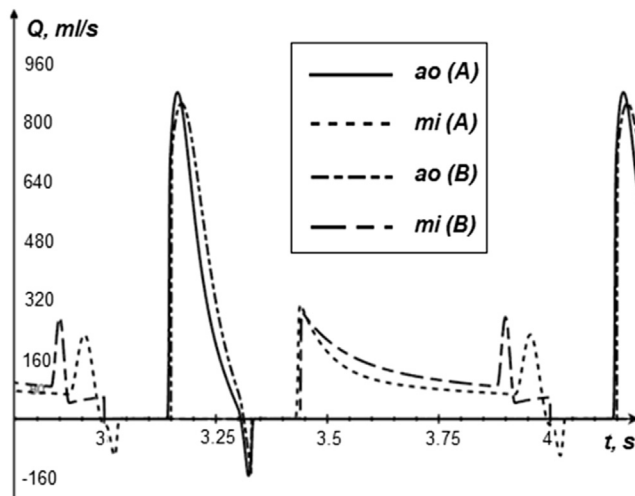
$$g(\theta) = \begin{cases} 0, & 0 \leq t < T_{open}, \\ 1, & T_{open} \leq t \leq T_{close}, \\ 0, & T_{close} < t \leq T, \end{cases} \quad (6.24)$$

where  $T_{open}^{ao} = 0.15$  s,  $T_{close}^{ao} = 0.33$  s,  $T_{open}^{mi} = 0.44$  s,  $T_{close}^{mi} = 1$  s. The results of the simulations are shown in Figs. 6.2–6.4. In all simulations, periodic solutions are observed starting from the third cardiac cycle. The time of the valves opening and closing in the dynamical model of the valves is rather short (0.05 s), but it changes the flow parameters substantially.

The results shown in Figs. 6.2–6.4 for model A are in a good agreement with the well-known physiological data presented in Refs. [239,240]. The systolic pressure in the left ventricle equals to the standard value 120 mm Hg. The maximum flow through the aortic valve equals to 900 mL/s, which is a typical value for aorta with diameter of 3 cm. The maximum flow through the mitral valve is 300 mL/s. The volume of the left ventricle changes from 50 to 120 mL, and the volume of left auricle changes from 40 to 60 mL. Thus, model A will serve as a reference model for all comparisons here and in Sections 6.5.2 and 6.5.3.

**Figure 6.2**

Pressure in the left ventricle and auricle (A: dynamical model of the valves, B: instant valves opening/closing).

**Figure 6.3**

Flow through the aortic and mitral valve (A: dynamical model of the valves, B: instant valves opening/closing).

Comparison of models A and B shows substantial differences in all computed parameters. The most pronounced is the difference of systolic pressures in the left ventricle ( $P_{Lv,syst}^A = 120 \text{ mm Hg}$ ,  $P_{Lv,syst}^B = 130 \text{ mm Hg}$ , see Fig. 6.2). The peak value of the flow rate through aortic valve is achieved 0.05 s later in model A than in model B. This causes substantial changes in the dynamics of the heart chambers volumes (see Fig. 6.4).

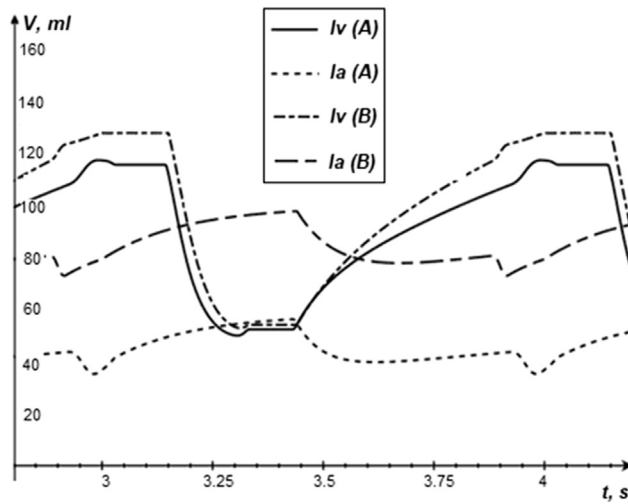


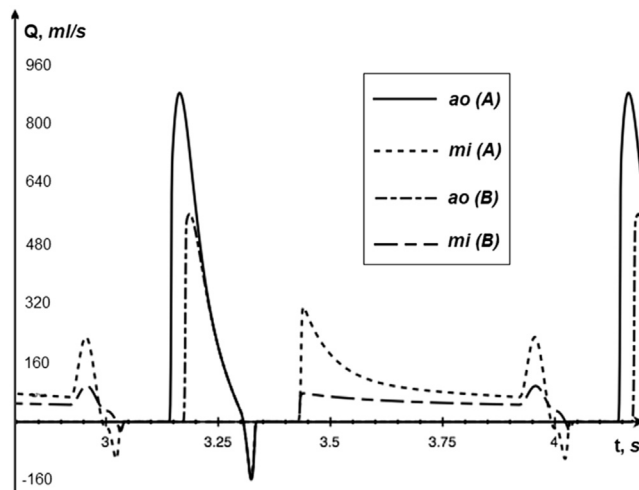
Figure 6.4

Volume of the left ventricle and auricle (A: dynamical model of the valves, B: instant valves opening/closing).

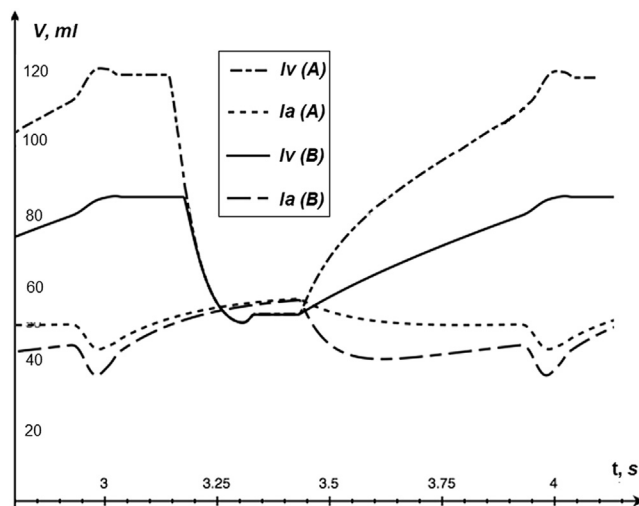
According to the physiological literature [239,240], one of the well-known effects of the dynamical closing of the valves is the backward flow from the aorta to the left ventricle during the early diastole (aortic regurgitation). This backward flow phenomenon results from the rapid decrease of pressure in the ventricle, which occurs faster than the aortic valve closing completes. Both models A and B predict backward flow showing negative flow rates at some instance (see Fig. 6.3). We note that backward flow in model B has no physiological sense because the instantly closed valve should immediately terminate the retrograde flow. The observed negative flow in model B may be explained either by the instability of the numerical solution due to the discontinuous change of parameters or by inappropriate setting of the predefined periods of opening and closing in Eq. (6.24). Model A conforms to physiological data and produces realistic dynamics for basic parameters of the cardiac cycle. Model B may be adjusted to known physiological values, but it requires manual fitting in every case. It makes model B less useful for patient-specific applications.

### 6.5.2 Stenosis of the mitral valve

Mitral valve stenosis is a pathology caused by the narrowing of the atrioventricular lumen between left auricle and left ventricle. The coalescence of mitral valve leaflets is the main reason of such narrowing. As a result, the blood flow from the auricle to the ventricle decreases and so it reduces the stroke volume and the cardiac output. In paper [212], the mitral valve stenosis is modeled by 30% decrease of the maximum opening angle  $\theta_{mi}^{max}$ . This decrease leads to the decrease of the lumen by 25%. The results of the simulations are shown in Figs. 6.5 and 6.6.

**Figure 6.5**

Flow through the aortic and mitral valve (A: normal conditions, B: mitral valve stenosis).

**Figure 6.6**

Volume of the left ventricle and auricle (A: normal conditions, B: mitral valve stenosis).

The change in dynamics of the mitral valve has impact on the dynamics of the aortic valve. The moment of aortic valve opening is delayed by 0.05 s compared with the normal reference conditions. The changes in peak pressure in the left auricle from 115 to 110 mm Hg and in the left ventricle from 8 to 10 mm Hg are not significant. A pronounced effect is observed for both the flow rate and the volume of the heart chambers. Fig. 6.5 demonstrates the decrease of the systolic blood flow through the aortic valve from 900 to 560 mL/s. The peak systole is delayed by 0.05 s compared with the reference conditions,

which conforms to late aortic valve opening. The shape of the mitral blood flow rate curve changes significantly. The first maximum at the early diastole and the negative flow at the end of the cardiac cycle disappear (see Fig. 6.5). Substantial decrease of the left ventricle volume from 120 to 85 mL is shown in Fig. 6.6. The volume of the left auricle increases from 40 up to 50 mL.

Thus, the model is able to reproduce the well-known facts that the mitral valve stenosis increases the load to the left auricle and hence may produce subsequent hypertrophy. The mitral valve stenosis also causes substantial decrease of the cardiac output, which can be evaluated on the basis of model personalization.

### 6.5.3 Aortic regurgitation

Aortic regurgitation (aortic insufficiency) is the incompetence of aortic valve that causes reverse flow from aorta into the left ventricle during diastole. The reasons of aortic insufficiency include intrinsic features, aortic root dilation, valvular degeneration, aortic root dissection, and some others. In paper [212], aortic valve insufficiency is modeled by the increase of minimum opening angle  $\theta_{ao}^{min}$  from  $0^\circ$  to  $25^\circ$ . Results of simulations are shown in Figs. 6.7 and 6.8. The change of aortic valve dynamics affects the mitral valve dynamics. The moment of mitral valve opening keeps ahead by 0.05 s compared with normal reference conditions. The pressure in the left auricle remains the same. The change of peak pressure in the left auricle from 120 to 125 mm Hg and in the left ventricle from 8 to 10 mm Hg is not significant. However, it is enough for an early opening of the aortic valve and for resulting substantial changes in cardiac output. In Fig. 6.7, one may see the

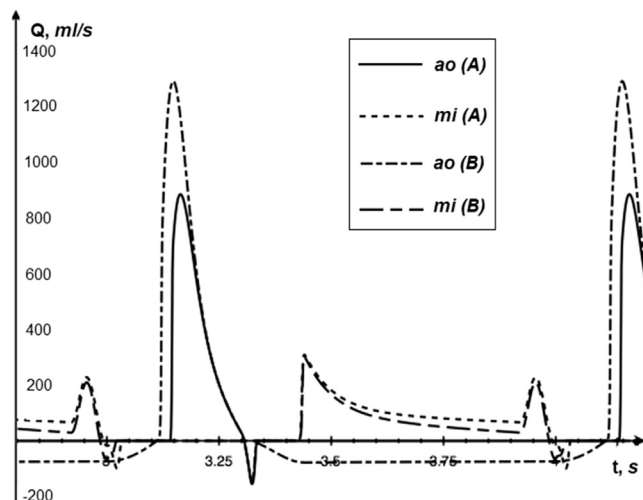


**Figure 6.7**

Flow through the aortic and mitral valve (A: normal conditions, B: aortic regurgitation).

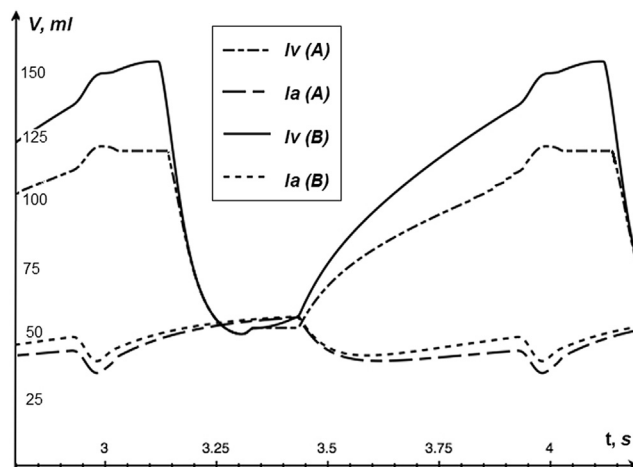


Figure 6.8

Volume of the left ventricle and auricle (A: normal conditions, B: aortic regurgitation).

substantial increase of the systolic blood flow rate through the aortic valve from 900 to 1300 mL/s. The peak systole keeps ahead by 0.05 s compared with the reference conditions, which conforms to early aortic valve opening. The increase of systolic flow is formally compensated by the reverse flow during diastole, but such regime causes substantial overload of the left ventricle and aorta. The straightforward effect of the aortic insufficiency is the negative flow of 70 mL/s during diastole (see Fig. 6.7). Systolic volumes of the chambers remain the same. Substantial increase of the left ventricle volume from 115 to 150 mL is shown in Fig. 6.8.

## Conclusions

The 0D model of the heart outflow, which accounts for heart chambers and valves dynamics, leads to physiologically correct simulations of certain heart diseases. It also provides a tool for constructing closed hemodynamic model of a vascular network. The basic feature of the cardiac cycle is the periodic alternation of sharp and smooth solution variations, which causes stability problems in numerical simulations. Higher-order implicit A- and L-stable methods are suitable for the numerical integration of the models of cardiac dynamics. Patient-specific evaluation of basic model parameters (heart rate, angles of valve opening, the volume of chambers) can be performed in a hospital through echocardiography or other conventional methods. Other model parameters (inertia coefficient, hydraulic resistance, variable elastance function) are hard to evaluate directly. They can be identified by fitting known measured and computed variables (e.g., volume dynamics, cardiac output, and ejection fraction). The obvious advantage of the lumped parameters approach is its low computational cost compared with higher-dimension models.

# 1D vascular hemodynamics

## 7.1 Introduction

The development of reduced order models that describe physiological and pathophysiological processes in the cardiovascular system is an active research area. The spatial order reduced models were proved to suit well for a number of clinical problems since they enable fast personalized simulations for planning pharmacological or surgical treatment.

Section 7.2 of this chapter introduces 1D hemodynamic equations in a single vessel and their extension to a network of vessels. This extension is done through boundary and coupling conditions of different types. Advanced approaches use 1D hemodynamic models as a part of multiscale modeling. Section 7.3 describes 0D–1D, 3D–1D, and 3D–0D–1D multiscale models. Numerical methods are discussed in Section 7.4. Modifications of reduced order models, which account for physiological conditions and some pathologies, are presented in Sections 7.5 and 7.6.

### 7.1.1 Model reduction in hemodynamics

Detailed numerical 3D modeling of blood flow in a realistic vascular network is a complicated technological and practical task. A typical network includes from dozens to hundreds of vessels. A mathematical model should account the interaction of flow with a moving viscoelastic vessel wall (fluid–structure interaction models, FSI). Furthermore, it is necessary to specify a sufficiently accurate 3D geometry of the vascular bed, elastic properties of the vessel wall material and boundary conditions, and finally to apply advanced numerical schemes (see Chapter 5). On the other end of the model complexity range, we have lumped parameter (0D) models capable to address the mean dynamics of the system but unable to describe finer effects, in particular, those related to wave propagation (see Chapter 6). Within this range, spatial order reduction (SOR) approaches provide mathematical models of various complexities.

Averaging procedures or other methods are applied to eliminate the dependency of flow variables on one or two spatial coordinates under certain assumptions regarding the flow. The limitations of these assumptions determine the scope of a given SOR model. Reduction procedures should preserve important physiological features of the problem so

that the resulting model is able to reproduce the flow and vascular dynamics with sufficient details. Since the original problem is highly nonlinear and the reduction process builds on a combination of several simplifying assumptions, the resulting models should be thoroughly validated. The SOR approach applied to the 3D FSI problem leads to a 1D reduced flow model, a compromise between the detailed 3D FSI and the rough 0D models. Mechanical interpretation of the resulting 1D flow model is the laminar flow of viscous incompressible fluid flow through a network of elastic tubes. 1D modeling is an attractive alternative to fully resolving 3D simulations thanks to much lower computational costs of studying regional, systemic, and closed (global) circulation. Primary applications of these models are the transport of blood gases, nutrients, and drugs through the whole organism, the analysis of the blood flow variations under external or internal mechanical action such as physical exercise or stimulation by medical devices, and the analysis of the effect of intravascular surgery, such as stenting or shunting. For description of the full-body hemodynamics, these models can be combined with models of the heart (see Chapter 6) and a model of microcirculation (see Chapter 8).

The computational domain of 1D models is the human vascular 1D network or its parts. A realistic network can be generated using anatomical atlases and physiological data found, for instance, in Refs. [120,239,240]. Alternative approaches use the reduction of a detailed 3D anatomical model [241] and segmentation methods of medical images obtained from MRI/CT [100,242,243]. Algorithms of processing patient MRI/CT data include 3D segmentation, centerlines identification, and construction of a graph with 1D straight segments (we refer to Chapter 3 for details). The construction of 1D models may be also based on aggregated laboratory data and experiments [244–246].

The analysis of blood flows by 1D hemodynamic models in vascular networks composed of hundreds of vascular segments can be found, for instance, in Refs. [213,247]. Extensive reviews of different aspects of 1D blood flow modeling can be found in Refs. [43,224,248–250].

### **7.1.2 *Applicability and limitations***

In the SOR approach, 1D hemodynamic equations are derived by averaging the full 3D Navier–Stokes equations in a single vessel [248,251]. 1D hemodynamic models are usually based on the following assumptions (some of them can be alleviated):

1. The ratio of vessel diameter to its length is relatively small.
2. The blood rheology corresponds to Newtonian viscous incompressible fluid.
3. The blood viscosity is constant.
4. The blood flow profile in any cross section orthogonal to the vessel centerline is radially symmetric.

5. The shape of the velocity profile in any such cross section does not vary along the vessel (e.g., it stays flat or parabolic).
6. The pressure is constant in each cross section.
7. Longitudinal stretching of the vessels is negligibly small.
8. The thickness of vessel walls is sufficiently small and constant.
9. The forces act on the wall in normal directions.
10. All cross sections of the vessel are circular.
11. Wall displacements occur only in the radial direction.
12. The deformation gradient of the vessel wall changes along the centerline continuously.
13. The material of the vessel wall is incompressible, and the deformation is linear.

Models based on (a subset of) the above assumptions are often well suited for simulating blood flow in large and medium arteries and superficial veins. In practice, they are also used for the hemodynamic simulation in deep veins, since the latter in the standing position (subject to the gravity field) have a circular cross section. The elliptic shape of the vessel cross section may be included in 1D hemodynamic models by modifying the equation describing the elasticity of the wall [252–254] or by different averaging procedure for the Navier–Stokes equations.

We note that the existence of a smooth solution for 1D hemodynamic models in a network with junctions is not known yet. For single vessel, the existence of a smooth solution to the 1D hemodynamic equations has been proven with the zero right-hand side and under certain additional assumptions in Ref. [251], whereas in Ref. [255], the existence is proven for particular boundary and initial conditions given as linear combinations of trigonometric functions. Surprisingly, smooth pulsating boundary conditions at the entrance of a *semi-infinite* compliant vessel typically lead to the formation of shock waves outside (2.8 m from the entrance) of the physiologically interesting domain [251].

For realistic cardiovascular simulations, the above assumptions may be considered somewhat restrictive and arguable. In particular, the shape of the velocity profile is not constant, and the Coriolis parameter (Boussinesq coefficient) and the friction coefficient from Eq. (7.12) are not constant either [256]. The model of thin-walled elastic cylinder is only a rough approximation of the realistic vascular material. Therefore, only extensive validation can support the practical use of the 1D hemodynamic models. Such validation includes comparisons with experimental and laboratory data, with the results of modeling using different methods, as well as with the solutions to the full 3D FSI problems. For example, studies [209,257–259] report reasonably good agreement of numerical solutions with physiological data, 3D FSI simulations, and physical experiments with the network of silicone tubes, while testing on clinical data is presented in Ref. [112]. Comparison of several 1D models on benchmark problems is given in Refs. [258,260]. Comparison of different boundary conditions for a 1D model using the Windkessel model and the

structured tree method as the truncated conditions was done in Ref. [261]. It is interesting that, despite significant differences in mathematical formulations and numerical methods used for 1D simulations, in most cases, it is possible to achieve satisfactory agreement. Moreover, 1D models may successfully incorporate important physiological conditions such as gravity force, muscles contraction force, regulation, and autoregulation (see Section 7.5). Therefore, the 1D blood flow modeling is currently accepted as the adequate approach for regional and global blood flow simulations and as a useful tool for a number of physiological and clinical problems.

## 7.2 Derivation of equations

### 7.2.1 Averaged Navier–Stokes equations in a vessel

Based on assumptions outlined in the previous section, one can derive a 1D hemodynamic model in several ways. For example, one may perform averaging and asymptotic analysis of the Navier–Stokes equations assuming small ratio  $r/L$ , where  $r$  is the radius and  $L$  is the length of a vessel [262,263], or one may integrate the 3D Navier–Stokes equations over a cross-sectional slice [248].

Let  $x$  denote the coordinate along the centerline of a vessel with circular cross section  $\Gamma_S$  orthogonal to the centerline,  $r$  be the radial coordinate in the cross section,  $t$  be the time,  $R(t, x)$  be the radius of the cross section,  $\eta(t, x)$  be a given displacement of the vascular wall in the radial direction, and let the cross-sectional velocity profile be given by  $\xi(y) = \frac{\gamma+2}{\gamma} (1 - y^\gamma)$ ,  $0 \leq y \leq 1$ . Note that  $\gamma = 2$  corresponds to the parabolic (Poiseuille) profile, and  $\gamma = 9$  corresponds to almost flat profile.<sup>1</sup>

We assume that  $v_x$  and  $v_r$  components of the velocity satisfy

$$v_x(t, r, x) = \bar{v}(t, x) \xi\left(\frac{r}{R(t, x)}\right), \quad v_r(t, R, x) = \frac{\partial \eta}{\partial t}(t, x). \quad (7.1)$$

Here  $\bar{v}$  is the average velocity in cross section  $\Gamma_S$ ,  $\bar{v} = S^{-1} \int_{\Gamma_S} v_x ds$ . The component  $v_x$  attains its maximum at the centerline ( $r = 0$ ) and vanishes at the vascular wall ( $r = R(t, x)$ ). Since  $v_x(t, R, x) = 0$ , the condition on  $v_r(t, R, x)$  represents the nonslip condition on the vessel wall.

To derive 1D hemodynamic equations, we define a vessel slice  $V$  as a neighborhood of a cross section  $\Gamma_S$  with coordinate  $x^*$ . The boundary of  $V$  is  $\partial V = \Gamma_1 \cup \Gamma_2 \cup \Gamma_W$ , and the external normal is  $\mathbf{n}$  with components  $n_x, n_r$ . The inlet and outlet cross sections at  $x^* - \Delta x/2, x^* + \Delta x/2$  are denoted by  $\Gamma_1$  and  $\Gamma_2$ , respectively;  $\Gamma_W$  is a part of the vessel wall, as shown in Fig. 7.1.

<sup>1</sup> Alternative options such as the power law profile and the Stokes layer are analyzed in [250].

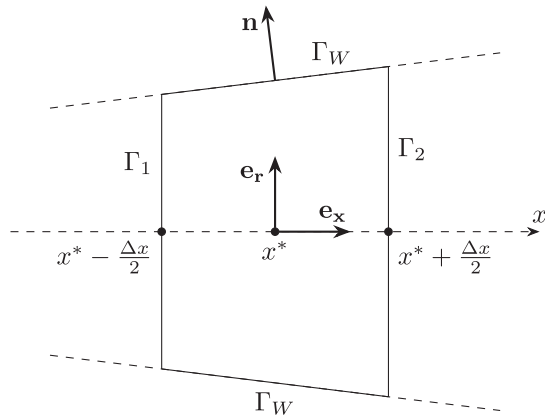


**Figure 7.1**  
Integration domain of a 3D model.

The integration of the incompressibility Eq. (4.16) over  $V$  yields

$$0 = \int_V \operatorname{div} \mathbf{v} \, d\mathbf{x} = \int_{\partial V} \mathbf{v} \cdot \mathbf{n} \, ds = \int_{\Gamma_2} v_x \, ds - \int_{\Gamma_1} v_x \, ds + \int_{\Gamma_W} v_r \, ds. \quad (7.2)$$

For the last term, we get from Eq. (7.1) the equality

$$\int_{\Gamma_W} v_r \, ds = \int_{\Gamma_W} \frac{\partial \eta}{\partial t} \, ds = \left. \frac{\partial S}{\partial t} \right|_{x=x^*} \Delta x + O(|\Delta x|^2). \quad (7.3)$$

Denoting the average flow  $\mathcal{Q}|_{\Gamma_*} = \int_{\Gamma_*} v_x \, ds$  through the cross section  $\Gamma_*$ , substituting Eq. (7.3) to Eq. (7.2), dividing by  $\Delta x$ , and taking the limit  $\Delta x \rightarrow 0$ , we obtain

$$0 = \lim_{\Delta x \rightarrow 0} \frac{\left( \int_{\Gamma_2} v_x \, ds - \int_{\Gamma_1} v_x \, ds \right)}{\Delta x} + \frac{\partial S}{\partial t} = \lim_{\Delta x \rightarrow 0} \frac{\mathcal{Q}\left(x^* + \frac{\Delta x}{2}\right) - \mathcal{Q}\left(x^* - \frac{\Delta x}{2}\right)}{\Delta x} + \frac{\partial S}{\partial t},$$

which leads to the 1D mass conservation equation:

$$\frac{\partial S}{\partial t} + \frac{\partial \mathcal{Q}}{\partial x} = 0. \quad (7.4)$$

Next, we rewrite the  $x$ -component of the Navier–Stokes equations for the incompressible Newtonian fluid (Eq. (4.18)) as follows:

$$\frac{\partial v_x}{\partial t} + \operatorname{div}(v_x \mathbf{v}) + \frac{1}{\rho} \frac{\partial p}{\partial x} - \nu \Delta v_x = 0. \quad (7.5)$$

Integrating Eq. (7.5) over the slice  $V$  leads to

$$\int_V \frac{\partial v_x}{\partial t} d\mathbf{x} + \int_V \operatorname{div}(v_x \mathbf{v}) d\mathbf{x} + \frac{1}{\rho} \int_V \frac{\partial p}{\partial x} d\mathbf{x} - \nu \int_V \Delta v_x d\mathbf{x} = 0. \quad (7.6)$$

We transform each term in Eq. (7.6) as follows:

$$\int_V \frac{\partial v_x}{\partial t} d\mathbf{x} = \frac{\partial Q}{\partial t} \Delta x + O(|\Delta x|^2); \quad (7.7)$$

$$\begin{aligned} \int_V \operatorname{div}(v_x \mathbf{v}) d\mathbf{x} &= \int_{\partial V} v_x \mathbf{v} \cdot \mathbf{n} ds = - \int_{\Gamma_1} v_x^2 ds + \int_{\Gamma_2} v_x^2 ds + \int_{\Gamma_W} v_x \mathbf{v} \cdot \mathbf{n} ds \\ &= \frac{(\alpha S \bar{v}^2)|_{\Gamma_2} - (\alpha S \bar{v}^2)|_{\Gamma_1}}{\Delta x} \Delta x = \frac{\partial}{\partial x} \frac{(\alpha Q^2)}{S} \Delta x + O(|\Delta x|^2); \end{aligned} \quad (7.8)$$

$$\int_V \frac{\partial p}{\partial x} d\mathbf{x} = \left( S \frac{\partial p}{\partial x} \right) \Big|_{x=x^*} \Delta x + O((\Delta x)^2); \quad (7.9)$$

$$\begin{aligned} \int_V \Delta v_x d\mathbf{x} &= \int_{\partial V} \nabla v_x \cdot \mathbf{n} ds = - \int_{\Gamma_1} \frac{\partial v_x}{\partial x} ds + \int_{\Gamma_2} \frac{\partial v_x}{\partial x} ds + \int_{\Gamma_W} \nabla v_x \cdot \mathbf{n} ds \\ &= \int_{\partial V} n_x \nabla v_x \cdot \mathbf{e}_x ds + \int_{\Gamma_W} n_r \nabla v_x \cdot \mathbf{e}_r ds \\ &= \int_{\Gamma_W} \frac{\bar{v}}{R} \xi'(1) n_r ds + O(|\Delta x|^2) = 2\pi \bar{v} \xi'(1) \Delta x + O(|\Delta x|^2). \end{aligned} \quad (7.10)$$

Here  $\alpha = S_i^{-1} \bar{v}^{-2} \int_{\Gamma_1} v_x^2 ds$ , and for Eq. (7.8), we used  $v_x = 0$  on  $\Gamma_W$ . In derivation of (7.10) we used  $\int_{\partial V} n_x \nabla v_x \cdot \mathbf{e}_x ds = O((\Delta x))^2$  since  $\int_{\partial V} n_x ds = 0$ .

Substituting Eqs. (7.7)–(7.10) into Eq. (7.6) and passing to the limit for  $\Delta x \rightarrow 0$  gives the 1D momentum conservation equation:

$$\frac{\partial Q}{\partial t} + \frac{\partial}{\partial x} \left( \alpha \frac{Q^2}{S} \right) + \frac{S}{\rho} \frac{\partial p}{\partial x} = K_r \bar{v}, \quad (7.11)$$

where

$$K_r = 2\pi \nu \xi'(1). \quad (7.12)$$

Note that  $K_r$  is negative since  $\xi'(1) < 0$ . Eqs. (7.4) and (7.11) constitute the hemodynamic 1D model in  $(S, v, p(S))$  variables. It can be reformulated in  $(S, Q, p(S))$  variables. Indeed, substituting  $Q = Sv$  in Eqs. (7.4) and (7.11), we arrive at

$$\frac{\partial S}{\partial t} + \frac{\partial (Sv)}{\partial x} = 0, \quad (7.13)$$

$$\frac{\partial v}{\partial t} + \frac{\partial}{\partial x} \left( \frac{v^2}{2} + \frac{P}{\rho} \right) = \psi, \quad (7.14)$$

where  $\psi = S^{-1} K_r \bar{v}$  denotes the friction force.

The  $(S, v, p(S))$  formulation is used by many researchers [248,250,252,257,264], since it can be written in the divergent form:

$$\begin{aligned} \frac{\partial \mathbf{V}}{\partial t} + \frac{\partial \mathbf{F}(\mathbf{V})}{\partial x} &= \mathbf{G}(\mathbf{V}), \\ \mathbf{V} = \begin{pmatrix} S \\ v \end{pmatrix}, \mathbf{F}(\mathbf{V}) &= \begin{pmatrix} Sv \\ v^2/2 + p(S)/\rho \end{pmatrix}, \mathbf{G}(\mathbf{V}) = \begin{pmatrix} \varphi \\ \psi \end{pmatrix}. \end{aligned} \quad (7.15)$$

The divergent form is convenient for constructing efficient numerical methods (see [Section 7.4](#)). The right-hand side depends on a particular application. For instance,  $\varphi$  may account for the loss or gain of blood inside the vessel due to a damage of vascular wall or hemotransfusion;  $\psi$  accounts for exerted forces (e.g., friction force, muscle contraction) addressed in [Section 7.5.3](#). The constitutive relationship  $p(S)$  defines elastic properties of the vessel wall (refer to [Section 7.5.1](#) for more details).

## 7.2.2 Boundary and junction conditions

Most of 1D hemodynamic models need inlet boundary conditions describing the outflow from the heart. The models also require boundary conditions at vessel's junctions and outflow boundary conditions at terminal arteries or an arteriovenous transition condition. The inlet conditions are usually given by a predefined time-dependent function. This function is defined based on one of the following statistics: the heart output profile, the aortic pressure, or a coupling condition with a 0D heart model. In the latter case, a closed 1D hemodynamic model needs a heart model, which connects the pulmonary vein and vena cava with the heart outflow conditions to the aorta and pulmonary artery through a lumped parameter 0D model as presented in Refs. [221,224,231,252,265,266].

1D hemodynamic models account for microcirculation regions through special boundary conditions. In the simplest case, the free flow or nonreflecting boundary condition can be set at terminal arteries. More accurate outflow conditions for models with truncated arterial tree are considered in Refs. [267,268]. For example, selected parts of small arteries and microcirculation are modeled as structured trees whose root impedance can be evaluated from linearization of the governing equations [268]. Alternative choices include time-domain coupling of 1D blood flow models with lumped parameter 0D models [252,269] and arteriovenous pressure gradient condition [213,221,231,250]. The authors of Ref. [259] define characteristic impedances that relate terminal arteries or veins to lumped parameter microvasculature compliances and a pressure-dependent vascular bed resistance. For further details, we refer to review papers [43,224,250].

Blood vessel junctions include bifurcations, trifurcations, anastomoses, merging, or structural one-to-one connections. A junction may have no distinct inlet and/or outlet vessels since the flow direction there may change in time. Therefore, a flow direction-independent formulation is needed at vessel junctions. It follows from hyperbolicity of 1D hemodynamic models (7.15) that at junctions one should impose so-called compatibility conditions along characteristics. As noted in Refs. [221,250,252,270], for every vessel end point, there exists one incoming and one outgoing characteristic, which implies subsonic flow regimes in almost all physiological cases. Thus, only one additional compatibility condition is required at every vessel end point (see Section 7.4.2 for further details). The second necessary condition at a junction is the mass conservation condition given by

$$\sum_{k=k_1, k_2, \dots, k_{M_l}} \varepsilon_k S_k(t, \tilde{x}_k) v_k(t, \tilde{x}_k) = 0. \quad (7.16)$$

The system of boundary conditions at junction points can be closed using one of the following options: the total or Bernoulli pressure continuity, as addressed in, e.g., Ref. [271],

$$\frac{v_k^2(t, \tilde{x}_k)}{2} + \frac{p_k(S_k(t, \tilde{x}_k))}{\rho} = I^l, \quad k = k_1, k_2, \dots, k_{M_l}, \quad (7.17)$$

the Hagen–Poiseuille pressure drop condition, as studied in Ref. [221]:

$$p_k(S_k(t, \tilde{x}_k)) - p_{node}^l = \varepsilon_k R_k^l S_k(t, \tilde{x}_k) u_k(t, \tilde{x}_k), \quad k = k_1, k_2, \dots, k_{M_l}, \quad (7.18)$$

or the pressure continuity condition:

$$p_k(S_k(t, \tilde{x}_k)) = p_{node}^l, \quad k = k_1, k_2, \dots, k_{M_l}, \quad (7.19)$$

which is mentioned in Ref. [250] as one of the possible options. Here  $l$  is the junction index,  $k_1, k_2, \dots, k_{M_l}$  are the vessels indices at the junction,  $M_l$  is the total number of the vessels in junction  $l$ ,  $p_{node}^l(t)$  is the pressure at the junction, and  $R_k^l$  is the hydraulic resistance coefficient for the vessel  $k$  in junction  $l$ . For vessels incoming into the junction  $\varepsilon_k = 1$ ,  $\tilde{x}_k = L_k$ , whereas for outgoing vessels,  $\varepsilon_k = -1$ ,  $\tilde{x}_k = 0$ . Numerical implementation of boundary and coupling conditions is addressed in Section 7.4.2.

### 7.3 Geometric multiscale methods (0D–1D–3D)

Hemodynamic 1D models reproduce averaged flow statistics on a network of vessels and cannot give detailed information about the 3D flow in any specific region of interest.

Geometric multiscale models provide such information by coupling a full 3D model based on the Navier–Stokes equations or FSI equations with a reduced 1D model in the rest of the network. Geometric multiscale modeling has become nowadays conventional approach in computational hemodynamics (see, e.g., Refs. [139,272,273]). The multiscale approach

is particularly useful for description of complex vascular networks such as the circle of Willis. We shall present two approaches for coupling the 1D hemodynamic model with the Navier–Stokes equations posed in a 3D domain with rigid walls.

### 7.3.1 The 1D–3D model: hard coupling

Assume that a 1D flow model is coupled to a part of the open boundary  $\Gamma \subset \partial\Omega_{3D}$  of the 3D domain  $\Omega_{3D}$ , see the illustration in Fig. 7.2. The continuity of the normal stress on  $\Gamma$  is imposed conventionally at the interface:

$$\left( -\nu \frac{\partial \mathbf{v}}{\partial \mathbf{n}} + p \mathbf{n} \right) \Big|_{\Gamma} = \bar{p}|_{x=b} \mathbf{n}, \quad (7.20)$$

where  $\mathbf{n}$  is an outward normal vector for  $\Omega_{3D}$ . If we assume for a moment that  $\bar{p}$  is given at the right-hand side of Eq. (7.20), then the condition (7.20) is the natural boundary condition for the weak formulation of the Navier–Stokes equations, see Eqs. (5.7) and (5.8). The continuity of the flow rate is another standard condition at the interface:

$$\int_{\Gamma} \mathbf{v} \cdot \mathbf{n} ds = -S\bar{v}|_{x=b}. \quad (7.21)$$

The coupling conditions (7.20) and (7.21) ensure the total mass conservation for the multiscale model; however, they are known to violate the energy balance of the system. To fix the energy balance, Eq. (7.21) can be combined with the continuity condition for the normal total stress as suggested in Ref. [274]. Another approach from Ref. [275] suggests to enforce continuity of a combination of the fluid flux and the energy flux:

$$\bar{p} \int_{\Gamma} \mathbf{v} \cdot \mathbf{n} ds + \frac{\rho}{2} \int_{\Gamma} |\mathbf{v}|^2 (\mathbf{v} \cdot \mathbf{n}) ds = - \left( \bar{p} S \bar{v} + \frac{\rho}{2} S \bar{v}^3 \right) \Big|_{x=b}. \quad (7.22)$$

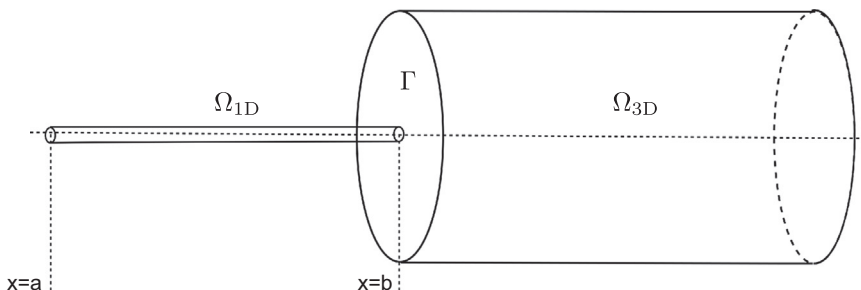


**Figure 7.2**

A simple multiscale 1D–3D model. Coupling conditions are prescribed for  $\Gamma$  and  $x = b$ . From T. Dobroserdova, M. Olshanskii, S. Simakov, Multiscale coupling of compliant and rigid walls blood flow models, Int. J. Numer. Methods Fluids 82 (12) (2016) 799–817.

Condition (7.22) together with condition (7.20) leads to the correct energy balance and hence to the fundamental energy estimate, at the expense of the exact global mass conservation.

Being sufficiently efficient as the downstream coupling condition, the hard coupling of the 1D elastic wall model and the 3D rigid wall model produces reflected spurious pressure waves, especially if the interface is located upstream. The spurious oscillations may spoil the numerical solution and make it physiologically irrelevant. To ameliorate this phenomenon, more flexible soft coupling conditions were suggested in Refs. [229,276].

### 7.3.2 The 1D–0D–3D model: soft coupling

We introduce a 0D absorber as an elastic sphere  $\Omega_{0D}$  of volume  $V = V(t)$  filled with fluid with homogeneously distributed pressure. The variable  $p_{0D}(t)$  has the meaning of the difference between fluid and external pressures and so  $p_{0D}$  may have any sign. The reference volume  $V_0$  for the sphere at rest is prescribed for  $p_{0D} = 0$ . The kinematics of the sphere under the action of the fluid pressure is described by the following ordinary differential equation (ODE) (see Chapter 6):

$$I \frac{d^2V}{dt^2} + R_0 \frac{dV}{dt} + \frac{V - V_0}{C} = p_{0D}. \quad (7.23)$$

Here, the expansibility factor  $C$  and the resistance coefficient  $R_0$  characterize the elastic properties of the sphere walls. The second-order term accounts the inertia. The coefficient  $I$  is positive, if one prescribes a nonzero mass to the elastic walls of the sphere; otherwise, one may set  $I = 0$ . The hydraulic model (7.23) can be used as a 0D mediator [276] at the interface between 1D and 3D models. The virtual absorbing device (Eq. 7.23) mimics the effect of the 3D model compliance and thus reduces pressure wave reflections and instabilities caused by the inconsistency of elastic-rigid walls coupling. Fig. 7.3 illustrates this geometric multiscale model.

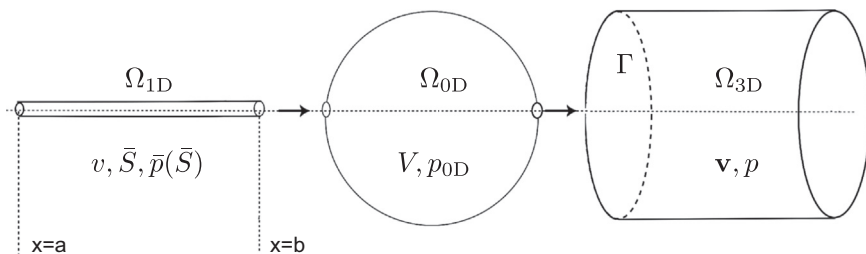


**Figure 7.3**

The schematic coupling of  $\Omega_{1D}$ ,  $\Omega_{0D}$ , and  $\Omega_{3D}$  domains. From T. Dobroserdova, M. Olshanskii, S. Simakov, Multiscale coupling of compliant and rigid walls blood flow models, Int. J. Numer. Methods Fluids 82 (12) (2016) 799–817.

It remains to couple the 0D hydraulic model to 1D and 3D blood flow models using the machinery presented in Chapter 6. The conservation of mass leads to the following equation for the rate of volume change:

$$\frac{dV}{dt} = Q_{1D} - Q_{3D}, \quad (7.24)$$

where  $Q_{1D} = S\bar{v}$  is the fluid flux at  $x = b$  and  $Q_{3D} = -\int_{\Gamma} \mathbf{v} \cdot \mathbf{n} \, ds$  is the 3D fluid flux through  $\Gamma$  from  $\Omega_{0D}$  to  $\Omega_{3D}$ . Finally, with the help of the Poiseuille law, one links the flow rate to the pressure drop:

$$\begin{aligned} \bar{p} - p_{0D} &= R_{1D0D} Q_{1D} && \text{at } x = b, \\ p_{0D} - p &= R_{0D3D} Q_{3D} && \text{on } \Gamma, \end{aligned} \quad (7.25)$$

where  $R_{1D0D}$  and  $R_{0D3D}$  are the resistance coefficients. Thus, Eqs. (7.23)–(7.25) form the complete set of coupling conditions. In Ref. [229], the authors show that positive  $R_0$ ,  $R_{1D0D}$ , and  $R_{0D3D}$  introduce additional dissipation in the cumulative energy balance of the complete 1D–0D–3D system consisting of Eqs. (7.15), (4.16), and (4.18) and coupling conditions (7.23)–(7.25).

## 7.4 Numerical methods

The computational domain of a 1D hemodynamic model for a vascular network includes vessels, junction points of vessels, and inputs and outputs of the network. In internal parts of the vessels, the hyperbolic system (Eq. 7.15) should be solved. The well-posedness of the problem in the internal regions requires the enforcement of the compatibility conditions discussed in Section 7.2.2. Boundary conditions at the input and terminal points, at the connections of the vessels of similar type (arterial and venous junctions) and the connections of different types of the vessels (arteriovenous junctions), result in a system of nonlinear algebraic equations or a mixed system of algebraic–ordinary differential equations. Thus, 1D hemodynamic models are represented by algebraic–differential system of equations. A variety of numerical methods can be applied for the numerical solution of such algebraic–differential systems: discontinuous Galerkin and Taylor-Galerkin methods [270], second-order local conservative Galerkin methods [271,277], high-order finite volume method [252], finite differences method with artificial viscosity [231], characteristic methods [213,221,270,278], and fast Fourier transform method [256,279].

### 7.4.1 The grid-characteristic method

Although blood flows are normally subsonic, external impacts or elasticity malfunction can produce transonic or even supersonic regimes. Robustness of a numerical scheme in this case requires the oscillation-free property. The first-order monotone characteristic

method and its second-order counterpart that minimizes possible oscillations can be combined with a fractional time steps explicit–implicit scheme to result in an efficient numerical procedure as demonstrated in Refs. [213,221,278]. Moreover, the scheme is easily parallelized since computations are split between independent local subproblems. In the following, we present this method.

The explicit–implicit fractional time steps algorithm splits computations into several stages. At the first explicit stage, one applies a hybrid first/second-order explicit method to solve the system (7.15) in all internal (nonboundary) nodes of the computational grid. At the second implicit stage, one solves by the Newton method nonlinear algebraic equations for boundary nodes of the grid at the network inlet, outlets, and junctions. The nonlinear systems stem from a finite difference discretization of compatibility conditions, which needs values computed in the internal grid nodes at the first explicit stage of the algorithm. The initial guess for the Newton iterations at the second stage is set to values from the previous time step. The Newton iterations converge, if the time step is sufficiently small. Practically, less than five iterations provide error reduction by a factor of  $10^5$ .

For every vessel, we introduce the numerical grid with a constant spatial step and a variable time step:

$$\left\{ (x_j, t_n) : x_j = jh, hJ = L, j = 0, \dots, J; t_n = \sum_{p=1}^n \tau_p \right\}, \quad (7.26)$$

where  $h$  is the spatial step,  $\tau_p$  is  $p$ -th time step,  $t_n$  is the time after  $n$  time steps,  $L$  is the length of the vessel, and  $J + 1$  is the number of grid nodes.

The eigenvalues  $\lambda_i$  and the left eigenvectors  $\mathbf{w}_i$  of the Jacobi matrix

$$\mathbf{A} = \left\{ \frac{\partial \mathbf{F}_i}{\partial \mathbf{V}_j} \right\}_{i,j=1,2} = \begin{pmatrix} v & S \\ \frac{1}{\rho} \frac{\partial p}{\partial S} & v \end{pmatrix} \quad (7.27)$$

for the flux  $\mathbf{F}$  from (7.15) are

$$\lambda_i = v + (-1)^i c(S), \quad \mathbf{w}_i = \left\{ S^{-1} c(S), (-1)^i \right\}, \quad i = 1, 2, \quad (7.28)$$

where

$$c(S) = \sqrt{\frac{S}{\rho} \frac{\partial p}{\partial S}}. \quad (7.29)$$

The values of the grid function  $\mathbf{V}_j^{n+1}$  in the internal nodes  $(x_j, t_{n+1}), j = 1, \dots, J - 1$ , of the grid (7.26) are calculated by the following two-step hybrid explicit conservative scheme proposed in Ref. [280]:

$$\widehat{\mathbf{V}}_j = \mathbf{V}_j^n - \tau_{n+1} \left( \mathbf{F}_{j+1}^n - \mathbf{F}_{j-1}^n \right) / 2h, \quad (7.30)$$

$$\begin{aligned} \mathbf{V}_j^{n+1} = & \widehat{\mathbf{V}}_j + (\Omega^{-1} \mathbf{B} \Omega)_{j+1/2} \left( \mathbf{V}_{j+1}^n - \mathbf{V}_j^n \right) - (\Omega^{-1} \mathbf{B} \Omega)_{j-1/2} \left( \mathbf{V}_j^n - \mathbf{V}_{j-1}^n \right) \\ & + (\Omega^{-1} D \Omega)_{j+1/2} \left( \widehat{\mathbf{V}}_{j+1} + \widehat{\mathbf{V}}_j - \mathbf{V}_{j+1}^n - \mathbf{V}_j^n \right) \\ & - (\Omega^{-1} D \Omega)_{j-1/2} \left( \widehat{\mathbf{V}}_j + \widehat{\mathbf{V}}_{j-1} - \mathbf{V}_j^n - \mathbf{V}_{j-1}^n \right) + \tau_{n+1} \mathbf{G}_j^n, \end{aligned} \quad (7.31)$$

where matrix  $\Omega$  is composed of  $\mathbf{w}_i$ ,  $\mathbf{B}_{ij} = \{\delta_{ij} b_i\}$ ,  $D_{ij} = \{\delta_{ij} d_i\}$ ,  $i = 1, 2$ ,  $b_i = |\sigma_i| [1 + 5(1 - \gamma)(1 - |\sigma_i|)/19]/2$ ,  $d_i = 6(1 - \gamma)\sigma_i(1/|\sigma_i| - 1)/19$ ,

$$\sigma_i = \frac{\tau_{n+1}}{h} (\lambda_i)_j^n, \quad 0 \leq \gamma \leq 1.$$

The stability condition  $|\sigma_i| < 1$  is used to identify the new time step. If  $\gamma = 1$ , the scheme is reduced to the first-order monotone scheme. If  $\gamma = 0$ , the scheme has the second order and may produce some oscillations on sharp and discontinuous jumps. Physiologically relevant solutions to Eq. (7.15) are smooth, and in our clinical applications, we set  $\gamma = 0$ . However, if an application suggests solution discontinuity, the choice  $\gamma = 1$  is recommended.

#### 7.4.2 Implementation of boundary conditions

All boundary conditions include compatibility conditions along outgoing characteristics of the hyperbolic system (7.15). In subsonic regimes, it holds  $v < c(S)$ ; therefore, the eigenvalues satisfy  $\lambda_1 < 0$ ,  $\lambda_2 > 0$ , and there exists one outgoing and one incoming characteristic  $dx/dt = \lambda_i$  for system (7.15). For the first node ( $x_0 = 0$ ), the outgoing characteristic corresponds to  $i = 1$ , whereas for the last node ( $x_J = L$ ), the outgoing characteristic corresponds to  $i = 2$ .

Note that the scalar product of the vector identity (7.15) with the eigenvector  $\mathbf{w}_i$  gives

$$\mathbf{w}_i \cdot \frac{\partial \mathbf{V}}{\partial t} + \lambda_i \mathbf{w}_i \cdot \frac{\partial \mathbf{V}}{\partial x} = \mathbf{w}_i \cdot \mathbf{G}, \quad i = 1, 2. \quad (7.32)$$

We derive the compatibility condition at the first node for  $x_0 = 0$ ,  $i = 1$  from the second-order discretization of Eq. (7.32) at the internal nodes. The compatibility condition at the last node for  $x_J = L$ ,  $i = 2$  is derived similarly.

Let a grid function  $\{\mathbf{V}_j^n\}_{j=0}^J$  be known after the previous time step  $n$  and a grid function  $\{\mathbf{V}_j^{n+1}\}_{j=1}^{J-1}$  be known after the explicit stage of the current step  $n + 1$ . Using the finite difference approximation

$$\left(\frac{\partial \mathbf{V}}{\partial x}\right)_0^{n+1} \approx \frac{-3\mathbf{V}_0^{n+1} + 4\mathbf{V}_1^{n+1} - \mathbf{V}_2^{n+1}}{2h}, \quad \left(\frac{\partial \mathbf{V}}{\partial t}\right)_0^{n+1} \approx \frac{\mathbf{V}_0^{n+1} - \mathbf{V}_0^n}{\tau^{n+1}}$$

and assuming smooth variations in time,

$$(\mathbf{w}_i)_j^{n+1} \approx (\mathbf{w}_i)_j^n, \quad (\lambda_i)_j^{n+1} \approx (\lambda_i)_j^n, \quad j = 0, \dots, J, n = 0, \dots, N - 1, \quad (7.33)$$

we discretize Eq. (7.32) with the second-order accuracy in space and the first-order accuracy in time [281]:

$$(\mathbf{w}_1)_0^n \cdot \left( \frac{\mathbf{V}_0^{n+1} - \mathbf{V}_0^n}{\tau} + (\lambda_i)_0^n \frac{-3\mathbf{V}_0^{n+1} + 4\mathbf{V}_1^{n+1} - \mathbf{V}_2^{n+1}}{2h} \right) = (\mathbf{w}_1)_0^n \cdot \mathbf{G}_0^{n+1}. \quad (7.34)$$

One may rewrite (7.34) as

$$\begin{aligned} & \omega_0^n \left[ S_0^{n+1} - S_0^n + \sigma_0^n \left( -\frac{3}{2}S_0^{n+1} + 2S_1^{n+1} - \frac{1}{2}S_2^{n+1} \right) \right] \\ & - \left[ v_0^{n+1} - v_0^n + \sigma_0^n \left( -\frac{3}{2}v_0^{n+1} + 2v_1^{n+1} - \frac{1}{2}v_2^{n+1} \right) \right] = \tau^{n+1} (\omega_0^n \phi_0^{n+1} - \psi_0^{n+1}) \end{aligned}$$

and obtain

$$v_0^{n+1} = \alpha_0^{n+1} S_0^{n+1} + \beta_0^{n+1}, \quad (7.35)$$

where

$$\begin{aligned} \alpha_0^{n+1} &= \omega_0^n, \\ \beta_0^{n+1} &= \left[ \omega_0^n \left( \sigma_0^n \left( 2S_1^{n+1} - \frac{1}{2}S_2^{n+1} \right) - S_0^n \right) - \left( \sigma_0^n \left( 2v_1^{n+1} - \frac{1}{2}v_2^{n+1} \right) - v_0^n \right) \right. \\ &\quad \left. - \tau^{n+1} (\omega_0^n \phi_0^{n+1} - \psi_0^{n+1}) \right] \left( 1 - \frac{3}{2} \sigma_0^n \right)^{-1}. \end{aligned} \quad (7.36)$$

To use Eq. (7.35) for both endpoints  $x_0, x_J$ , we rewrite the compatibility condition in a general form:

$$v_k = \alpha_k S_k + \beta_k, \quad (7.37)$$

where  $k$  is the index of the vessel and other indices are suppressed assuming appropriate choice of  $(0, n + 1)$  or  $(J, n + 1)$  for the first and last node.

The full system of boundary conditions at a junction with index  $l$  of  $M_l$  vessels is represented by conditions (7.32) and (7.16) and one of Eqs. (7.17)–(7.19). Formally, it is the mixed system of algebraic and differential equations with  $2M_l + 1$  unknown parameters. The system can be reduced to a system of  $M_l$  nonlinear algebraic equations with unknown vector  $\mathbf{S} = \{S_{k_m}\}_{m=1}^{M_l}$ , where  $k_m$  is the index of a vessel at the junction  $l$ :

$$\mathbf{Q}(\mathbf{S}) = \mathbf{A}\mathbf{S}^{\text{II}} + \mathbf{B}\mathbf{S} + \mathbf{R}\mathbf{P}(\mathbf{S}) + \mathbf{D} = 0, \quad (7.38)$$

where

$$\mathbf{S}^{\text{II}} = \left\{ S_{k_m}^2 \right\}_{m=1}^{M_l}, \mathbf{P}(\mathbf{S}) = \{p_{k_m}(S_{k_m})\}_{m=1}^{M_l}.$$

In case of the total pressure continuity (7.17), the matrices and vectors in Eqs. (7.38) are

$$\begin{aligned} A_{mm} &= \delta \alpha_{k_m}, A_{mn} = 0, \quad m \neq n, \\ B_{mm} &= \frac{\beta_{k_m}}{2\alpha_{k_m}} \left( \delta - \frac{\varepsilon_{k_m}}{2\alpha_{k_m}} \right), B_{mn} = -\varepsilon_{k_n} \beta_{k_n}, \quad m \neq n, \\ R_{mm} &= 2 \left( \delta - \frac{1}{\alpha_{k_m}} \right), R_{mn} = -\frac{2}{\alpha_{k_m}}, \quad m \neq n, \\ D_m &= \beta_{k_m}^2 \left( \delta - \frac{\varepsilon_{k_m}}{\alpha_{k_m}} \right), \delta = \sum_{m=1}^{M_l} \frac{\varepsilon_{k_m}}{\alpha_{k_m}}, \quad m, n = 1, \dots, M_l. \end{aligned} \quad (7.39)$$

In case of the Hagen–Poiseuille pressure drop condition (7.18), the matrices and vectors in (7.38) are given by

$$\begin{aligned} A_{mm} &= \Delta \varepsilon_{k_m} \alpha_{k_m}, A_{mn} = 0, m \neq n, \\ B_{mm} &= \Delta \varepsilon_{k_m} \beta_{k_m}, B_{mn} = 0, m \neq n, \\ R_{mm} &= - \sum_{n=1}^{M_l} \prod_{\substack{p=1 \\ p \neq m}}^{M_l} R_{k_p}^l, R_{mn} = \prod_{\substack{p=1 \\ p \neq m \\ p \neq n}}^{M_l} R_{k_p}^l, \\ D_m &= 0, \Delta = \sum_{i=1}^{M_l} \prod_{\substack{j=1 \\ j \neq i}}^{M_l} R_{k_j}^l, m, n = 1, \dots, M_l. \end{aligned} \quad (7.40)$$

$$D_m = 0, \Delta = \sum_{i=1}^{M_l} \prod_{\substack{j=1 \\ j \neq i}}^{M_l} R_{k_j}^l, m, n = 1, \dots, M_l.$$

In case of the pressure continuity (7.19), the system (7.38) can be reduced to single equation as follows. As stated in Section 7.5.1,  $p(S)$  is a monotone function, and thus, Eq. (7.19) can be uniquely resolved:

$$S_{k_m} = \tilde{p}_{k_m}(p_{node}^l), \quad (7.41)$$

where  $\tilde{p}(p)$  is the inverse function for  $p(S)$ . Substituting Eqs. (7.41) and (7.37) into Eq. (7.16), one derives the nonlinear equation with variable  $p_{node}^l$ :

$$\sum_{k=k_1, k_2, \dots, k_{M_l}} \varepsilon_k \left( \alpha_k \tilde{p}_k^2(p_{node}^l) + \beta_k \tilde{p}_k(p_{node}^l) \right) = 0. \quad (7.42)$$

The system of Eqs. (7.38) and (7.42) can be solved by Newton's method. For Eq. (7.38), one iteration of the Newton method reads as follows:

$$\mathbf{S}^{r+1} = \mathbf{S}^r - \mathbf{J}(\mathbf{S}^r)^{-1} \mathbf{Q}(\mathbf{S}^r), \quad \mathbf{J} = \left\{ \frac{\partial \mathbf{Q}_i}{\partial S_j} \right\}. \quad (7.43)$$

## 7.5 Accounting for physiological phenomena

Blood flow in a vascular network is a physiological process with some unique features. The vascular wall is a living tissue with a complex structure. The active smooth muscle contractions are governed by physiological factors such as physical activity and regulatory signals from baroreceptors and chemoreceptors. These signals are response of the body to changes of internal and external parameters (temperature, oxygen and carbon dioxide concentration in blood, average pressure, etc.) and electrical stimulation. Mechanical properties of the wall may vary depending on the average flow. Some vessels have valves, which allow unidirectional flow. Surrounding muscles or artificial devices may exert external forces on blood vessels. Moreover, the gravity field affects the blood flow, depending on the body position. This section discusses the above physiological conditions and their mathematical formulations.

### 7.5.1 Vessel wall elasticity

The nonlinear mechanical response of a vessel wall is included in 1D hemodynamic models through the constitutive equation. In general form, the constitutive equation relates the energy of deformation to the principal stretches, invariants of Cauchy–Green strain tensor, and other material parameters. The development of adequate constitutive equations for living tissues is the topic of an active ongoing research. In 1D hemodynamic models, the reduced constitutive equation relates the transmural pressure  $p$  and the cross-section  $S$

through a given function  $p(S)$ . The extended reviews of various constitutive equations can be found in Refs. [254,282,283].

In principle, the reduced constitutive equation  $p(S)$  can be derived for each vessel from its energy of wall deformation and any knowledge about the vessel wall composition.

Function  $p(S)$  can be determined *in vivo* by direct measurements of  $p$  and  $S$  in laboratories, as shown in Refs. [23,24,284]. However, this approach is hardly feasible in clinical practice due to limitations of current diagnostic tools.

In the majority of studies,  $p(S)$  is obtained empirically or by simplifying elastic models of the vessel wall. In most cases, it can be written as

$$p(S) = p_0 + f(\eta(S)), \quad (7.44)$$

where  $p_0 = \text{const}$  and  $\eta(S) = S/S_0$ . [Table 7.1](#) summarizes the most common expressions for function  $f(\eta)$ . The values  $p_0$  and  $S_0$  should be specified for each vessel either from experimental data (such as the canine common femoral vein [23,284]), fitting procedures (such as fitting medical data for human common carotid and common femoral arteries [24,288]), or other models. Qualitative analysis of physical experiments on oscillating flows in collapsible tubes with passive elastic response confirms that  $p(S)$  function should be a monotone  $S$ -like curve, which can describe both circular and elliptic shapes of vessel cross sections [120,252,285,289]. It is easy to see that different formulations of  $p(S)$  are almost identical for  $\eta \approx 1$  after appropriate choice of parameters, although they may deviate outside a vicinity of  $\eta = 1$ , for too high or too low transmural pressure. Moreover, even for  $\eta = 1$ , the difference becomes significant if we compare the pulse wave velocity  $c(\eta)$  (7.29) for different formulations from [Table 7.1](#) (refer to Ref. [254] for the detailed comparison).

Elastic vessel wall model can be generalized to viscoelastic wall models [257,290,291],

which assume dependence  $p(S) = F\left(S, \frac{\partial S}{\partial t}\right)$ , e.g.,

$$p(S) = p_0 + \beta(\sqrt{\eta} - 1) + \frac{\Gamma}{\sqrt{S_0\eta}} \frac{\partial\eta}{\partial t}, \quad (7.45)$$

where  $\beta = \frac{4}{3}\sqrt{\pi Eh}$ ,  $\Gamma = \frac{2}{3}\sqrt{\pi\varphi h}$ ,  $E$  is the Young's modulus,  $h$  is the vessel wall thickness, and  $\varphi$  is the viscosity of the wall material (for details, we refer to Ref. [257]). Accounting for vessel bending stiffness requires more arguments in function  $F$ ,

$p(S) = F\left(S, \frac{\partial S}{\partial t}, \frac{\partial^2 S}{\partial t^2}, \frac{\partial^2 S}{\partial x^2}\right)$ , e.g.,

$$p(S) = p_0 + f(S) + \varepsilon^2 \left( \frac{\partial^2 S}{\partial t^2} - c_0^2 \frac{\partial^2 S}{\partial x^2} \right) + 2\beta\varepsilon \frac{\partial S}{\partial t}, \quad (7.46)$$

**Table 7.1: Artery models:** 1—Refs. [231,285], 2—Ref. [268], 3—Refs. [248,266,269,270], 4—Refs. [213,221,286];  
**vein models:** 1—Ref. [285], 2—Ref. [287], 3—Ref. [252], 4—Refs. [213,221,286].

Human common carotid artery			Canine common femoral vein	
	$f(\eta)$ , kPa	$c^2(\eta)$ , kPa	$f(\eta)$ , kPa	$c^2(\eta)$ , kPa
1	$25.80(\eta - 1)$	$25.80\eta$	$7.21\left(1 - \frac{1}{\eta^{\frac{3}{2}}}\right)$	$\frac{10.815}{\eta^{\frac{3}{2}}}$
2	$70.32\left(1 - \frac{1}{\sqrt{\eta}}\right)$	$\frac{70.32}{2\sqrt{\eta}}$	$-22.09\eta^3 + 53.02\eta^2 - 31.17\eta$	$-66.27\eta^3 + 106.04\eta^2 - 31.17\eta$
3	$57.42(\sqrt{\eta} - 1)$	$\frac{57.42\sqrt{\eta}}{2}$	$1.5\left(\eta^{10} - \frac{1}{\eta^{\frac{3}{2}}}\right)$	$1.5\left(10\eta^{10} + \frac{3}{2\eta^{\frac{3}{2}}}\right)$
4	$19.89(\exp(\eta - 1) - 1)$	$19.89\eta \exp(\eta - 1)$	$11.72 \ln \eta$	11.72

where  $f(S)$  is an  $S$ -like function,  $\varepsilon$  is a small parameter,  $\beta$  is a material constant, and  $c_0$  is the dimensionless velocity of the shear wave in the empty vessel. The work [289] used this function and explained for the first time the origin of Korotkoff sounds (heard in a tonometer) and shock waves.

### 7.5.2 Regulation and autoregulation

Physical conditions and physiological reactions play a key role in cardiovascular system functionality. They make the cardiovascular system substantially different from a purely mechanical system. A change of external conditions results in a new state of blood circulation with new flow rates and pressures. During a transient regime between the states, which take a few minutes, blood vessels adapt to new conditions. Autoregulation is the tendency of blood flow to sustain itself despite the changes of external conditions. It is realized via the vessel wall adaptation to blood flow changes in this vessel. Even isolated vessels exhibit this phenomenon *in vitro*. Regulation is the vessel wall adaptation to changes in remote parts of the organism (far from the considered vessel). Main mechanisms of autoregulation are summarized in Ref. [32]: myogenic, metabolic, tissue pressure, tubuloglomerular feedback, and local neural control.

The laboratory study in Ref. [292] addresses the pressure-driven mechanism of autoregulation, when stepwise pressure elevation causes initial expanding (passive phase) and subsequent gradual contraction (active phase), as illustrated in Fig. 7.4.

According to the myogenic hypothesis, smooth vascular muscles respond to the changes of the mean pressure. An increase of the mean pressure results in smooth vascular muscle contraction and vessel wall stiffening, and vice versa. Vascular smooth muscle cells site in

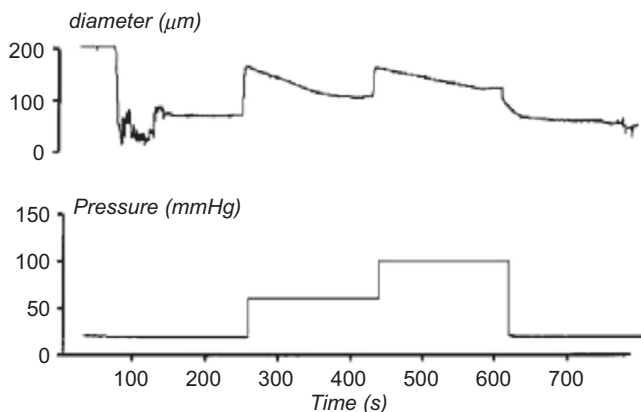


**Figure 7.4**

The effect of stepwise pressure elevation on diameter of a rat artery [292].

tunica media, a wall layer that is thick in arteries and relatively thin or absent in veins. As a result, myogenic autoregulation in veins provides no effect on the blood flow. The myogenic mechanism relates wall stiffening and timings, which are well described by 1D hemodynamic models. Regulation and autoregulation processes have been addressed in such models by several authors [224,244,246]. We follow a model of myogenic autoregulation from Ref. [293] where mean pressure variation causes flow rate variation and wall shear stress change, which affects the permeability of vessel wall for the nitric oxide. The latter causes a variation of  $\text{Ca}^{2+}$  and phosphorylated myosin, which may stiffen or relax the vessel wall. The model is self-adaptive to the flow so that it recovers the initial average shear stress.

We consider a particular version of constitutive equation (7.44) proposed in Refs. [221,286]:

$$p(S) = p_0 + \rho c_0^2 f(S). \quad (7.47)$$

Here,  $\rho$  is the wall density,  $c_0$  is the pulse wave velocity, and function  $f(S)$  (characterizing elastic properties of the wall) is assumed to be intact during the transient regime of autoregulation. Therefore,

$$\frac{\bar{p} - \bar{p}_0}{\rho c_0^2} = \bar{f}(S) = \text{const}, \quad (7.48)$$

where bar means the averaging over time period and length of the vessel. Assuming  $\bar{p}_0 = 0$  and  $\rho = \text{const}$ , we obtain

$$\frac{\bar{p}}{c_0^2} = \text{const}. \quad (7.49)$$

Consider three subsequent averaging time intervals  $[T_1, T_2]$ ,  $[T_2, T_3]$ , and  $[T_3, T_4]$  and set the new value  $c_0^{\text{new}}$  for  $t \in [T_3, T_4]$  by

$$\frac{c_0^{\text{new}}}{c_0^{\text{old}}} = \sqrt{\frac{\bar{p}_{\text{new}}}{\bar{p}_{\text{old}}}}, \quad (7.50)$$

where

$$\begin{aligned} \bar{p}_{\text{old}} &= \frac{1}{(T_2 - T_1)L} \int_{T_1}^{T_2} \int_0^L p(x, t) dx dt, \\ \bar{p}_{\text{new}} &= \frac{1}{(T_3 - T_2)L} \int_{T_2}^{T_3} \int_0^L p(x, t) dx dt. \end{aligned} \quad (7.51)$$

Each time interval is bounded from below by the cardiac cycle  $T_{\text{card}}$  and from above by the characteristic time of autoregulation (a few minutes). The study [253] shows that the

choice  $T_2 - T_1 = T_3 - T_2 = T_4 - T_3 = 4T_{card}$  provides stable reversible solutions. Of course, the autoregulatory response is not instant; therefore, the pulse wave velocity  $c_0(t)$  should be a continuous function of time. The simplest linear approximation gives

$$c_0(t) = c_0^{\text{old}} + \gamma \frac{t - T_3}{T_4 - T_3} (c_0^{\text{new}} - c_0^{\text{old}}), \quad T_3 \leq t \leq T_4, \quad (7.52)$$

where  $0 \leq \gamma \leq 1$  is the parameter controlling the actual autoregulation response. The value  $\gamma = 1$  corresponds to the normal case, and  $\gamma = 0.1$  can be related to some autoregulatory pathway malfunction, e.g., the effect of a vasodilator administration.

### 7.5.3 Internal and external forces

Various internal and external forces influence the blood flow. The internal shear forces produce friction which depends on flow conditions and blood composition. The venous valves ensure unidirectional flow toward the heart: being closed, venous valves serve as flow barriers. The gravity field and other inertial forces produce hydrostatic pressure gradient, which pushes the blood in the direction of gradient. External forces deform the vessel wall and, therefore, exert additional external pressure to blood. These forces result from the periodic contraction of myocardium or respiratory muscles as well as contraction of other muscles during physical activity, external cuff or socks compression, etc.

#### 7.5.3.1 Blood viscosity and friction

The viscosity of blood depends on rheological properties of plasma, cellular components (RBCs), and volume fraction of RBCs (hematocrit). An apparent blood dynamic viscosity ( $\mu_{app}$ ) is given by

$$\mu_{app} = \mu_{rel}\mu, \quad (7.53)$$

where  $\mu$  is the dynamic viscosity of plasma and  $\mu_{rel}$  is the relative viscosity that depends on hematocrit (see Chapter 8 for more details). In Refs. [294,295], the blood is assumed to be Newtonian fluid with linear rheological relationship (4.17). This assumption works well for modeling blood flows in large vessels at high and medium shear stress under nonpathological conditions. Non-Newtonian effects in blood flows become significant at shear stress smaller than  $100 \text{ s}^{-1}$  [295]. Such nonlinear rheological effects are more likely to occur in veins, small arteries, and capillaries.

The following expression gives the general form of the viscous friction in Eq. (7.15):

$$\psi_{fr} = -\frac{2\tau}{\rho R}, \quad (7.54)$$

where  $\tau$  is the shear stress and  $\tilde{R}$  is the vessel radius. Given the axial velocity component  $v(x, r, t)$ , the viscous friction term reduces to

$$\psi_{fr} = -2\pi\gamma\nu\bar{v}, \quad \gamma = \frac{\tilde{R}}{\bar{v}} \left| \frac{\partial v}{\partial r} \right|_{r=\tilde{R}},$$

where  $\nu$  is the kinematic viscosity of blood ( $\nu = \frac{\mu}{\rho}$ ). For derivation, we refer to, e.g., Refs. [139,256].

For parabolic profile,  $\psi_{fr} = -8\pi\mu\nu$ ; a good agreement with experimental data was observed in Ref. [269] for  $\psi_{fr} = -22\pi\mu\nu$ . We remind that  $\bar{v}$  is the axial velocity averaged over the cross section. The viscous friction that is invariant to vessel contraction or dilation was proposed in Refs. [213,221]:

$$\psi_{fr} = -\frac{4\pi\nu\bar{v}}{S^2} fr(\eta), \quad (7.55)$$

where  $\eta = S/S_0$ ,

$$fr(\eta) = \begin{cases} 2, & \eta \geq 1 \\ (\eta + \eta^{-1}), & \eta < 1. \end{cases} \quad (7.56)$$

Many non-Newtonian rheology models for blood flows consider the dynamic viscosity dependent on the shear stress  $\tau$ . For instance, Carreau–Yasuda model states

$$\mu = \mu_\infty + (\mu_0 + \mu_\infty)[1 + (\lambda\tau)^p]^{(n-1)/p}, \quad (7.57)$$

where  $\lambda = 0.438s$ ,  $n = 0.191$ ,  $p = 0.409$ ,  $\mu_0 = 51.9$  mPas, and  $\mu_\infty = 4.76$  mPas [296]. We refer to Refs. [41,43,297] for a review of more than 30 models of shear-dependent viscosity.

### 7.5.3.2 Venous valves function

The venous valves consist of a pair of thin leaflets attached to the vessel walls and oriented toward the heart. When the pressure difference across the valve drives anterograde flow, the leaflets are pushed apart allowing free flow. A reversed pressure difference pushes the leaflets together, and flowback toward the microcirculation region is impeded. Thus, in the veins, the valves maintain the unidirectional flow (see Fig. 7.5).

Within 1D hemodynamic modeling, the simplest way to account for a venous valve is to modify the friction force as proposed in Ref. [253]:

$$\psi_{vl} = \begin{cases} \psi_{fr}, & v > 0 \\ \psi_{fr}^\infty, & v < 0 \end{cases} \quad (7.58)$$

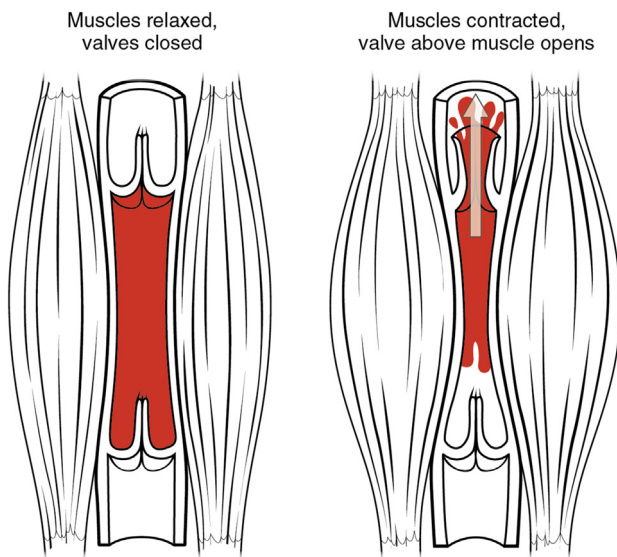


**Figure 7.5**

Venous valves. *Image source: OpenStax, Anatomy and Physiology. OpenStax CNX. Available at: <http://cnx.org/content/col11496/>.*

where  $\psi_{fr}^\infty \approx 100\psi_{fr}$  is the “infinite” resistance prohibiting backward flows. Similar approach was applied in Ref. [298] by setting small effective cross-sectional area ( $A_{eff}$ ) in the Poiseuille resistance  $R = \frac{8\pi\eta l_{eff}}{A_{eff}^2}$  in the case of closed valves, which also causes almost “infinite” resistance for retrograde flows. More advanced models proposed in Refs. [299,300] consider venous valve as a 0D lumped compartment generating a pressure drop across the valve that controls the effective cross-sectional area. Actually, the set of venous valve models ranges from 0D lumped parameters models (e.g., Ref. [301]) to 3D models (e.g., Ref. [302]).

#### 7.5.3.3 Gravity force

According to physiological data from Refs. [239,240], the gravity force increases the hydrostatic pressure in a column of blood by about 0.77 mmHg per 1 cm of height. The change of the body position in the gravity field, the G (acceleration) force, and microgravity conditions of space flights influence the systemic blood flow distribution, cerebral circulation, venous filling, and pulmonary circulation. The gravity force and G force cause passive mechanical displacements and regulatory/compensatory responses in cardiovascular system. The arterial system responds to the orthostasis by gradually reducing its capacity and the blood flow velocity. The most pronounced effect is observed for the lower extremities. In the upright position, the resulting hydrostatic pressure difference is up to 100 mmHg between the ankle and the right atrium. This additional

pressure should be compensated for successful blood return to the heart auricles through veins. Several mechanisms provide this compensation: venous valves, peripheral resistance regulation, heart suction pump, and muscle pump. In upright position, the hemodynamic effect of the calf muscle pump is greater than in supine position.

To account for gravity force, one sets in Eq. (7.15) the right-hand side equal to

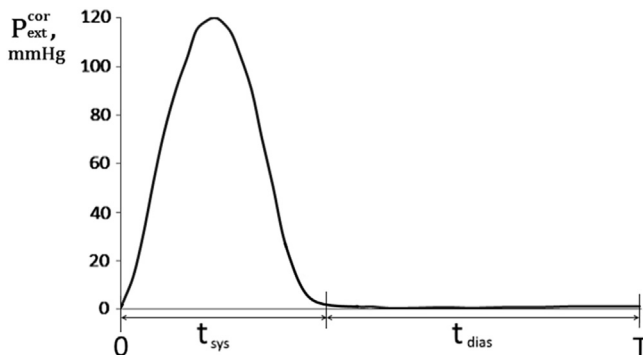
$$\psi_{grav} = g \sin \theta, \quad (7.59)$$

where  $g$  is the gravity constant and  $\theta$  is the angle between the vessel centerline and the gravity field. This model was used in Ref. [298] for modeling venous hemodynamics with muscle pump function and in Ref. [300] for simulating gravitational impact on global hemodynamics in different postures. The authors of Ref. [246] account for the G force by additional modifications of the 1D hemodynamic model (7.15) in the heart outflow model and the constitutive relationship  $p(S)$ .

#### 7.5.3.4 Muscle pump and external compression

Various external forces exert pressure to deformable vascular walls and change the blood flow pressure. External forces may be periodic (contraction of myocardium and respiratory muscles, other muscle activation) or irregular (intentional muscle activation or cuff compression during an enhanced external counterpulsation [291,328] procedure or venous reflux probe). All these forces may change regional and/or systemic circulation via imposing blood pressure gradient and triggering regulatory mechanisms (autoregulatory adaptation and systemic oxygen and carbon dioxide–based regulators, metaboreflex, mechanoreflex, and baroreflex controls). For simulations of physical activity, the modeling of external forces is accompanied by the modeling of gravity and venous valves effects. If we assume that a compressing force has normal direction to the surface of vessel, then the external pressure  $p_0$  in Eq. (7.44) may account for the effect of muscle pumping. A general approach to external pressure modeling consists of a modification of the term  $p_0$  as appropriate for a given application.

For instance, the important feature of the coronary circulation is the periodic compression of a part of coronary arteries by myocardium during systole and their relaxation during diastole when major coronary flow and myocardial perfusion occur, as stated in physiology textbooks [239,240]. This feature may be taken into account as follows [264]. Myocardium compression can be taken into account by scaling the heart outflow time profile to fit physiological data and defining the external pressure  $p_0 = P_{ext}^{cor}(t)$ . The maximum value of  $P_{ext}^{cor}(t)$  should be set to the ventricular pressures, i.e., 120 mmHg for the terminal branches of the left coronary artery (see Fig. 7.6) and 30 mmHg for the terminal branches of the right coronary artery. Moreover, according to Ref. [304], the myocardium contraction causes the threefold increase of the terminal resistance  $R$  of peripheral circulation in Eq. (7.18) during the systole compared with the diastolic resistance.

**Figure 7.6**

External pressure applied to the branches of the left coronary artery. From T.M. Gamilov, F. Liang, S.S. Simakov, *Mathematical modeling of the coronary circulation during cardiac pacing and tachycardia*, Lobachevskii J. Math. 40 (4) (2019), 448–458.

If we address muscle contractions during physical activity, the induced external pressure compresses deep veins rather than arteries and superficial veins. There are two reasons for this: both arteries and superficial veins are less exposed to the compression, as they have a lot of collagen fibers in their walls, and the superficial veins are located near the surface of the body. As an example, we consider a periodic contraction of powerful muscles of the thigh and the shin during walking or running. The period  $T$  is the time for two strides. A cylindrical muscle holding the weight  $m$  of a human body generates the pressure:

$$p_0^{max} = \frac{mg}{S} \frac{\sigma}{1 - \sigma}, \quad (7.60)$$

where  $S$  is the average cross-section of the muscle and  $\sigma$  is its Poisson ratio. Setting  $m \approx 60$  kg,  $\sigma = 0.49$ , and  $S \approx 600$  cm $^2$ , we obtain  $p_0^{max} \approx 10$  kPa. The extravascular pressure in lower extremities during walking/running is proposed in Refs. [253,305] to be a periodic function:

$$p_0 = \frac{p_0^{max}}{2} \left( 1 + \sin \left( \frac{2\pi t}{T} + \Phi \right) \right), \quad (7.61)$$

where  $\Phi$  is the phase distinguishing the contractions of muscles of the left leg ( $\Phi_{left} = 0$ ) and the right leg ( $\Phi_{right} = \frac{\pi}{2}$ ). The extravascular pressure may account for spatial inhomogeneity of muscles distribution [298].

Some medical procedures exploit compression of cuffs for external mechanical stimulations of the blood flow. The reflux-provoking maneuvers help to assess severity of chronic venous disease. A three-step graded sequential compression procedure (EECP) is the mean of cardiac assist for patients suffering from cardiogenic shock, acute myocardial

infarction, and as a treatment for cardiac ischemia and angina. In these procedures, the external pressure is applied to both legs simultaneously. The issues of EECP modeling will be addressed in [Section 7.6.4](#).

## 7.6 Accounting for pathologies

Normal blood flow is vitally important for the human body since vascular and circulation pathologies result in disability or death. Numerical simulation on the basis of 1D hemodynamic models gives additional insight in several important vascular diseases. In this section, we address blood flow models for stenosis of arteries, pathological tortuosity (PT) of cerebral vessels, coronary circulation during cardiac pacing and tachycardia, as well as for analysis of EECP.

### 7.6.1 Models of the blood flow across stenosis

Atherosclerosis is a chronic inflammatory process in artery walls, leading to their thickening and plaque formation. The atherosclerotic plaque is composed of a lipid pool and a fibrous cap embedded to the diseased vascular wall. As a consequence of plaque formation, the vascular lumen narrows and produces a stenosis. The latter may cause an acute decrease of the blood flow in a downstream part of the vascular network either due to a significant occlusion or due to a plaque rupture and associated clot formation and embolization. Thrombi produced in cerebral circulation may provoke stroke.

Atherosclerosis of the coronary arteries causes the lack of oxygen in the cardiac tissue followed by ischemia, myocardial infarction, arrhythmia, and fibrillation. It is one of the leading causes of mortality and morbidity.

Atherosclerosis is a complex disease involving different cell processes, hemodynamic effects, and biomechanics of the vessel wall. Reduced-order models can simulate disturbed circulation caused by a vascular stenosis. For a review of lumped compartment (0D) models of flow-through stenosis, we refer to Ref. [306]. A 0D model is a system of ODEs stemming from a model of an elastic reservoir with blood or from its electric circuit analogs discussed in Chapter 6. An example from Ref. [269] of such ODE system for flow in a vascular compartment is the following system:

$$C_e \frac{d\hat{p}}{dt} = q_{in} - q_{out}, \quad (7.62)$$

$$L_e \frac{d\hat{q}}{dt} + R_e \hat{q} = p_{in} - p_{out}, \quad (7.63)$$

where  $C_e$ ,  $L_e$ , and  $R_e$  are the capacity, the inductance, and the resistance of the electric circuit compartment;  $q_{in}$ ,  $q_{out}$ ,  $p_{in}$ , and  $p_{out}$  are the flow rates and pressures at the input and output of the lumped element; and  $\hat{p}$ ,  $\hat{q}$  are the averaged pressure and flow rate in the

lumped element. If  $A_0$ ,  $A_s$ ,  $l_0$ , and  $l_s$  denote cross-sectional areas and lengths of nonstenotic and stenotic vessels, respectively, then parameters of the stenosed region with degree  $\alpha = A_s/A_0$  should be updated:

$$R_s = R_e \alpha^{-2}, C_s = C_e \alpha^{3/2}, L_s = L_e \alpha^{-1}.$$

The physiological impact of the stenosis is the pressure drop  $\Delta p$  across the stenosed region, resulting in the reduction of flow rate  $Q$ . Empirical dependencies of  $\Delta p$  on  $Q$  may be diverse:

$$\Delta p = \frac{288\rho}{2ReA_s^2} Q^2, \quad [310]$$

$$\Delta p = (R_1 + R_2)Q + (K_1 + K_2)Q^2, \quad [312]$$

$$\Delta p = \frac{K_v\mu}{2\pi R^3} Q + \frac{K_t\rho}{2A_0^2} \left( \frac{A_0}{A_s} - 1 \right)^2 Q|Q| + \frac{K_u\mu l_s}{A_0} \frac{dQ}{dt}, \quad [222, 311]$$

$$\frac{dp}{dx} = \left( \frac{8\rho Q^2 B_1 B_2}{\pi^2 R^5} \right) \frac{dR}{dx} - \frac{60\mu Q B_3}{\pi R^4}, \quad [313]$$

where  $Re$  is the Reynolds number,  $R_1$ ,  $R_2$ ,  $K_1$ ,  $K_2$ ,  $B_1$ ,  $B_2$ ,  $B_3$ ,  $K_v$ ,  $K_t$ , and  $K_u$  are constants, and  $R$  is the diameter of the vessel. The pressure drop across a stenosis with irregular geometric structure requires more detailed two-scale 1D–3D models such as models presented in Refs. [271,311], although asymmetric lumen produces no appreciable difference in the pressure drop as stated in Refs. [312,313]. If the stenosis is considered as a node of a 1D vascular graph, these relations for  $\Delta p$  can be used as a part of the boundary conditions in a 1D hemodynamic model instead of Eqs. (7.17), (7.18), or (7.19).

Stenoses may be taken into account by a 1D hemodynamic model directly in two ways. First, a stenosis with degree  $\alpha$  may be incorporated into a healthy vascular network as a tubular segment with modified cross-sectional area  $A_s = \alpha A_0$  and length  $L_s$ . At the inlet and outlet of this segment, one adds to the boundary conditions the Poiseuille pressure drop condition  $\Delta p = R_s Q$  with hydraulic resistance  $R_s \sim \alpha^{-2}$  as was done in Refs. [242,314,315]. Second, the presence of a stenosis may modify the constitutive relation (7.44) for a healthy vessel by locally increasing the vessel wall stiffness.

A more advanced approach is to recover function  $f$  from Eq. (7.44) for the healthy and stenosed vessels as proposed in Refs. [316,317]. Recovery of function  $f$  is based on representation of the vessel wall by concentric elastic shells. It is assumed that the vessel is cylindrical and the plaque is axisymmetric, uniform, and lengthy; hence, the strain in the axial direction is negligible. Inhomogeneous distribution of collagen and elastin fibers in the healthy vessel wall (see Chapter 2) produces nonlinear (e.g., neo-Hookean) elastic

response to blood pressure load. The equilibrium state for such thin wall (with middle radius  $R$  and thickness  $H$ ) composed of a neo-Hookean material with a material constant  $\mu$  and inflated by internal pressure  $p_0$  gives the nonlinear equation on the principal radial stretch  $\lambda_r$  derived in Ref. [317]:

$$\mu(\lambda_r^{-2} - \lambda_r^2) = p_0 / (\lambda_r H)(R / \lambda_r - \lambda_r H / 2).$$

This equation defines implicitly function  $f$  since it relates the pressure and the lumen area.

As an atherosclerotic wall contains three layers, it can be represented by a three-layer circular cylindrical shell inflated by internal pressure  $p_0$ . The internal (vessel wall) and external layers (fibrous cap) are represented by thin-walled cylindrical shells. The middle layer is a thick-walled cylinder that represents the lipid pool. The static equilibrium conditions allow the authors of [316,317] to compute the lumen area under given blood pressure  $p_0$  for isotropic incompressible linear elastic (Hookean) [316] or incompressible nonlinear materials [317] of vessel wall, lipid pool, and fibrous cap. In Fig. 7.7, we compare functions  $p_0(S/S_0)$  for an atherosclerotic vessel with a lengthy axisymmetric plaque and lumen 10%. Since  $S_0$  denotes the lumen area of the healthy artery, zero transmural pressure corresponds to  $S/S_0 = 0.1$ . Parameters for the static equilibrium problem are set according to the properties of the common carotid artery. The substantial difference in pressures is observed at transmural pressures over 4 kPa as well as for negative transmural pressures. The nonlinear materials demonstrate higher sensitivity to inflating transmural pressure and higher resistivity to deflating transmural pressure.

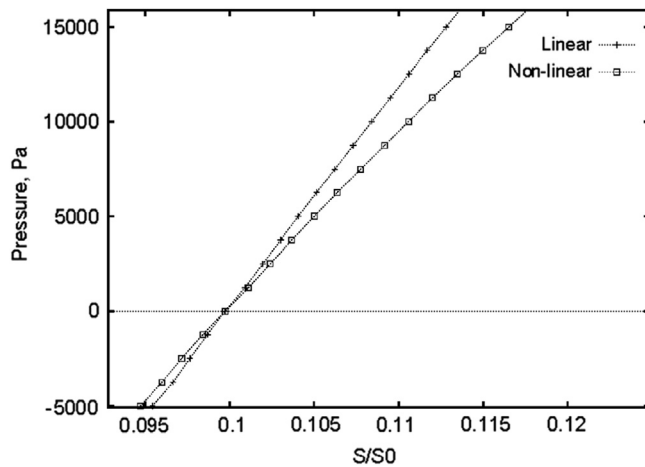


Figure 7.7

Comparison of the constitutive relations for Hookean and neo-Hookean materials for an atherosclerotic common carotid artery. From Y. Vassilevskii, S. Simakov, V. Salamatova, Y. Ivanov, T. Dobroserdova, *Vessel wall models for simulation of atherosclerotic vascular networks*, *Math. Model. Nat. Phenom.* 6 (7) (2011), 82–99.

Derivation of the constitutive relation in case of asymmetry of the vessel and the plaque is based on numerical methods. For instance, following Ref. [318], the elastic response of a tube wall may be computed from its representation by sets of axial fibers, ring fibers, and helical fibers and computation of the response of the fibers collection to a deformation.

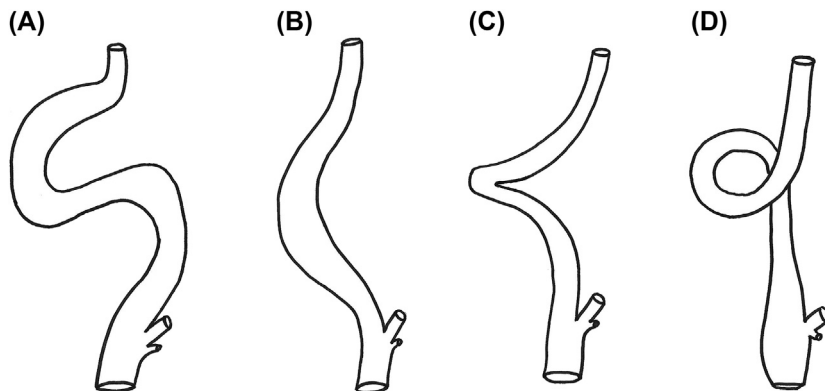
The response of an atherosclerotic vessel to inflation may be computed from representation of the fibrous cap and the arterial wall by sets of linear elastic rings and the lipid pool by a set of radial springs. The response of the springs is derived from analytically known radial displacements of an incompressible linear isotropic cylindrical shell with exerted external and internal pressures. Two concentric grids of ring fibers represent the external (artery) and internal (fibrous cap) layers. These layers and balancing forces applied on these layers at each grid point lead to a system of discrete nonlinear equations to be solved by the Newton method. For all possible pressures and plaques observed in the common carotid artery, such numerical model is shown in Ref. [316] to provide the error for displacements less than 2% compared with the semi-analytic solution known for axisymmetric geometries as demonstrated.

The case of several sequential stenoses is less studied. The circulation disturbance caused by sequential stenoses is addressed in Refs. [319–322].

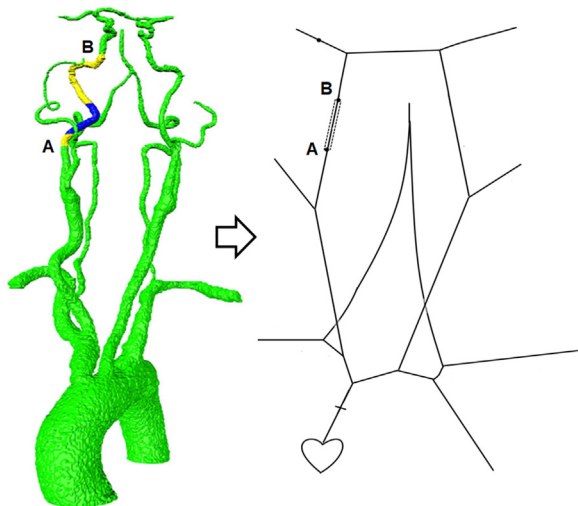
### **7.6.2 Blood flow in tortuous vessels**

PT of the carotid and vertebral arteries (CVAs) is the major pathological factor in the development of insufficiency in the cerebral circulation. PT takes the second place after the atherosclerosis disease and often develops without symptoms. PT is observed in 30% cases of the deaths from stroke. The ancestral features and hypertension are the major reasons of PT. The possible side effect of the PT is the blood flow decrease in CVA. The PT under low-flow conditions (e.g., hypotension) produces the most pronounced effect to the patient. PT has one of four general types: C-like (see Fig. 7.8B), S-like PT (see Fig. 7.8A), kinking (artery bending) (see Fig. 7.8C), and coiling (see Fig. 7.8D). The less threatening C and S types may transform to the more significant cases (kinking and coiling). A variety of PTs and their complicated geometry require patient-specific analysis and treatment that suggest the use of simulation tools.

The blood flow with high Reynolds numbers ( $Re > 10^3$ ) in PT regions has a complex 3D structure exhibiting turbulence and backward flows. High curvature may produce total occlusion and blood flow termination. Internal viscous friction in PT produces energy losses, increase of the hydraulic resistance, and decrease of the downstream pressure and velocity. The pressure loss takes place at every bend. The hydraulic resistance of every bend is proportional to the velocity. The latter may increase in the bend and decrease after the bend. Thus, the total effective resistance of a PT is not equal to the sum of the resistances of its every bend. Patient-specific numerical simulations are needed to assess

**Figure 7.8**

Types of pathological deformation of the internal carotid artery. (A) S-like tortuosity, (B) C-like tortuosity, (C) kinking, and (D) coiling. *Image from I.P. Dudanov, S.V. Ordynets, I.A. Lukinskiy, B.C. Abuazab, V.V. Akhmetov, A.A. Shabonov, O.P. Verbitskiy, Extracranial nonatherosclerotic pathology of the carotid artery in the causes of acute ischemic stroke, Res. Pract. Med. J. 4 (4) (2017), 35–49.*

**Figure 7.9**

Patient-specific 3D and 1D segmentation. AB is a region with pathological tortuosity.

the effective resistance of the whole PT region. 1D hemodynamic models have insufficient accuracy for the detailed simulations of the blood flow in the PT regions. Nevertheless, they may help to make fast assessment of the disease stage. For the algorithms of identification of PT and the generation of 1D vascular structure with PT (see Fig. 7.9), we refer to Chapter 3. The PT region can be treated in detail using a more complex mathematical model.

The pressure drop in relatively smooth C-like and S-like regions is proportional to the friction along the route and to the length of the route. One may account for the PT in such regions via the modification of the friction force:

$$f_{fr}^{PT} = f_{fr}(1 + \alpha_{fr}\kappa(x_k)), \quad \kappa = \left| \frac{d^2\mathbf{r}(s)}{ds^2} \right|, \quad (7.64)$$

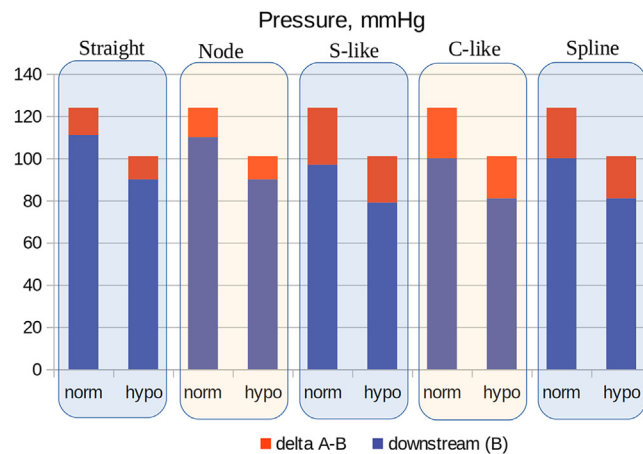
where  $\kappa$  is the local curvature of the vessel centerline,  $\mathbf{r}(s)$  is a 3D curve parameterization provided by the segmentation of the patient-specific medical images,  $0 \leq s \leq 1$  is the parameter along the curve, and  $\alpha_{fr}$  is a factor that may be set according to lab experiments presented in Ref. [324]. For reference cases, one may use  $\mathbf{r}(s) = (1 - \cos(2\pi\nu s), 0, 0)$  and set  $\nu = 1$  for a C-like PT and  $\nu = \frac{3}{2}$  for an S-like PT.

In the complex cases of kinking and coiling, one may introduce a node with a lumped compartment providing the pressure drop conditions:

$$\Delta p = k_b \frac{v^2}{2}, \quad (7.65)$$

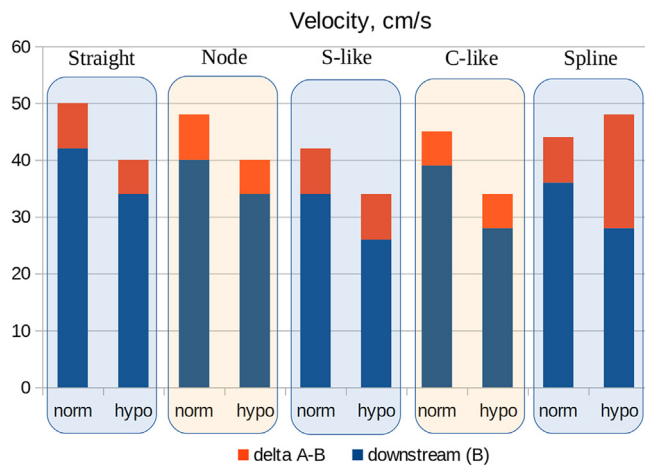
where  $v$  is the upstream velocity, and  $k_b$  is the energy loss coefficient estimated in rigid tube experiments presented in Ref. [325].

Comparisons of the pressure drop and velocity decrease over PT under normal and hypotension conditions are shown in Figs. 7.10 and 7.11. Hypotension conditions were simulated by the decrease of the stroke volume (SV) from 55 to 45 mL. The segment of the right internal carotid artery AB (see Fig. 7.9) was simulated by different geometrical models of the PT: straight line, node with lumped parameters with the pressure drop model (7.65), S-like and C-like shapes with friction (7.64), and spline approximation of patient-specific centerlines.



**Figure 7.10**

Comparison of the pressure drop over pathological tortuosity (PT) region in normal and hypotensive conditions with the different models of PT geometry.

**Figure 7.11**

Comparison of the velocity decrease over pathological tortuosity (PT) region in normal and hypotensive conditions with the different models of PT geometry.

The presence of PT produces almost the same velocity decrease and substantially greater pressure drop compared with the straight case. The larger pressure drop results in the blood flow redistribution: flow increases in the collateral path (left internal carotid artery), whereas the flow through the right internal carotid artery decreases. This effect is more pronounced under the hypotension condition.

### **7.6.3 Coronary circulation during cardiac pacing and tachycardia**

Sinoatrial node (SA) initiates the myocardium contraction. Activity of the SA is modified by signals from the sympathetic and the parasympathetic nervous system and humoral factors. Pathological processes (e.g., tachycardia) and external stimulation of the myocardium (e.g., cardiac pacing) modify the myocardium contractions and change the coronary blood flow decreasing nutrients delivery to the myocardium and provoking ischemic events in the heart. The impact of cardiac pacing and tachycardia to the coronary circulation may be assessed by patient-specific 1D hemodynamic models based on clinical data collected by noninvasive procedures (see, e.g., Refs. [17,264]). The remainder of this section is based on the work [303]; the reader is referred to it for details.

#### *7.6.3.1 Effect of asynchronous myocardial stimulation*

Cardiac pacing is performed by a pacemaker, which produces electrical pulses to prompt the heart to beat at the normal rate. Improper placement or synchronization of the pacemakers may lead to abnormalities in ventricle contractions and violation of the normal coronary flow in right (RCA) and left (LCA) coronary arteries and their branches.

**Table 7.2: Simulated systolic blood flow through right coronary artery (RCA) and left coronary artery (LCA) in the case of the delayed contractions in left ventricle (LV) and right ventricle (RV).**

	Blood flow, mL/s	
	RCA	LCA
No pacing	1.68	2.60
RV delay	1.49	3.04
LV delay	1.75	3.33

From T.M. Gamilov, F. Liang, S.S. Simakov, Mathematical modeling of the coronary circulation during cardiac pacing and tachycardia, Lobachevskii J. Math. 40 (4) (2019), 448–458.

Modeling of the coronary circulation during pacing is based on modifications of the external pressure and the terminal hydraulic resistance for coronary vessels according to their proximity to the pacemaker. We compare two opposite cases. First, we assume that a pacemaker is placed in the left ventricle (LV) and produces 0.03 s delay in the increase of pressure and peripheral resistance in RCA branches. Second, we assume that a pacemaker is placed in the right ventricle (RV) and causes 0.03 s delay in the increase of pressure and peripheral resistance in LCA branches. Results of simulations are shown in [Table 7.2](#).

Comparative simulation results shown in [Table 7.2](#) demonstrate small variations of the systolic flow in the RCA compared with the normal case without pacing. However, the systolic flow in the LCA is increased both for the right delay with LV stimulation and for the left delay with RV stimulation. Moreover, the delayed activation of the RV in the case of the LV pacing may cause decreased blood supply of the RCA, the known fact from common clinical practice.

#### 7.6.3.2 Effect of pacemaker position

Pacemaker position may produce asynchronous contractions in both LV and RV. We examine three options of the pacemaker position: LV base, RV apex, and RV base. The impact of the position is accounted by scaling the amplitude of the coronary blood pressure and peripheral resistance proportional to the myocardial tension, which depends on the distance from the pacemaker. The work [326] provides necessary clinical data for these simulations.

The simulation results collected in [Table 7.3](#) show distinctive decrease of the systolic flow in RCA for RV apex and LV pacing compared with the normal case without pacing. We also observe considerable increase of the systolic flow in LCA for all positions of the pacemaker compared with the normal case. The computed blood flows support the common opinion that the optimal pacemaker position is in the RV base.

**Table 7.3: Blood flow through right coronary artery (RCA) and left coronary artery (LCA) for the different pacemaker positions.**

Pacemaker position	Blood flow, mL/s	
	RCA	LCA
No pacing	1.68	2.6
RV apex	1.53	3.16
RV base	1.67	3.05
LV	1.44	3.17

*LV*, left ventricle; *RV*, right ventricle.

From T.M. Gamilov, F. Liang, S.S. Simakov, *Mathematical modeling of the coronary circulation during cardiac pacing and tachycardia*, *Lobachevskii J. Math.* 40 (4) (2019), 448–458.

### 7.6.3.3 Tachycardia

Stable permanent increase of the heart rate (HR) of an adult at rest above 100 beats per minute is associated with a pathological type of tachycardia. Tachycardia can be induced by cardiac pacing or caused by various cardiovascular disorders. For elderly people, the tachycardia may be a consequence of excessive emotional and/or physical stress or myocardial infarction. Tachycardia contributes to morbidity and mortality of patients with the ischemic heart disease.

The impact of tachycardia on the coronary circulation can be simulated by the increase of the HR and the fraction of systole, decrease of the SV, modifications of the external pressure, and the terminal hydraulic resistances. In normal (healthy) case, the fraction of systole is 40%. According to the clinical data [327], for the tachycardia conditions, the fraction can be set to 56%. The SV decreases from 60 mL in healthy case to 35 mL in case of tachycardia. The increase of the coronary vessels elasticity by 20% reproduces conditions in pediatric patients with supraventricular tachycardia.

We compare three models of tachycardia designated as A, B, and C. All models use increased HR, but only model C accounts the increased systolic fraction. Models B and C take into account the decreased SV.

The simulation results shown in [Table 7.4](#) prove that the blood flow through the coronary arteries increases during tachycardia. However, the fraction of the coronary flow in the cardiac output  $\delta_* = 60 \cdot Q_*/(\text{HR} \cdot \text{SV})$  is different (\* denotes LCA or RCA). The increase of the systolic fraction (case C) leads to the decrease of relative blood supply  $\delta_*$  in RCA and LCA.

Simulations of coronary circulation in pediatric patients with supraventricular tachycardia ([Table 7.5](#)) show that for model C the blood flow through RCA and LCA as well as the fraction of the coronary flow in the cardiac output becomes smaller than for the healthy heart, which can induce the development of ischemia.

**Table 7.4: Blood flow through right coronary artery and left coronary artery for models A, B, and C.**

	Healthy heart	Case A	Case B	Case C
HR, bpm	60	120	120	120
SV, mL	60	60	35	35
$Q_{RCA}$ , mL/s	0.9	2.1	1.2	1.0
$Q_{LCA}$ , mL/s	2.8	6.5	3.8	3.05
$\delta_{RCA}$ , %	1.5	1.7	1.7	1.4
$\delta_{LCA}$ , %	4.7	5.4	5.4	4.3

HR, heart rate; SV, stroke volume.

From T.M. Gamilov, F. Liang, S.S. Simakov, Mathematical modeling of the coronary circulation during cardiac pacing and tachycardia, Lobachevskii J. Math. 40 (4) (2019), 448–458.

**Table 7.5: Blood flow through right coronary artery and left coronary artery for pediatric patients (healthy heart and tachycardia).**

	Healthy heart	Case B	Case C
HR, bpm	98	207	207
SV, mL	55	28	28
$Q_{RCA}$ , mL/s	1.5	1.8	1.4
$Q_{LCA}$ , mL/s	4.7	5.6	4.4
$\delta_{RCA}$ , %	1.7	1.9	1.4
$\delta_{LCA}$ , %	5.2	5.8	4.5

HR, heart rate; SV, stroke volume.

From T.M. Gamilov, F. Liang, S.S. Simakov, Mathematical modeling of the coronary circulation during cardiac pacing and tachycardia, Lobachevskii J. Math. 40 (4) (2019), 448–458.

We should note that HR increase leads to the increase of the mechanical work performed by the myocardium and, thus, to the increase of the oxygen and nutrients consumption. Thus, formally normal blood flow through LCA and RCA in cases B and C in [Table 7.4](#) and in case B in [Table 7.5](#) may be insufficient and can induce the development of ischemia.

#### 7.6.4 Enhanced external counterpulsation

EECP is a noninvasive method of stretching blood vessels and blood flow recovery. The EECP procedure initiates reverse blood flow in arteries during aortic valve closing (diastole) by a three-step sequential cuff compression (see [Fig. 7.12](#)). EECP pressurizes during systole and depressurizes during diastole the inflatable cuffs surrounding the legs and the lower abdomen of a patient (see Refs. [291,328] for the description of EECP procedure). EECP increases diastolic pressure and stretches coronary arteries and improves the blood supply of the myocardium, as significant coronary flow occurs during diastole

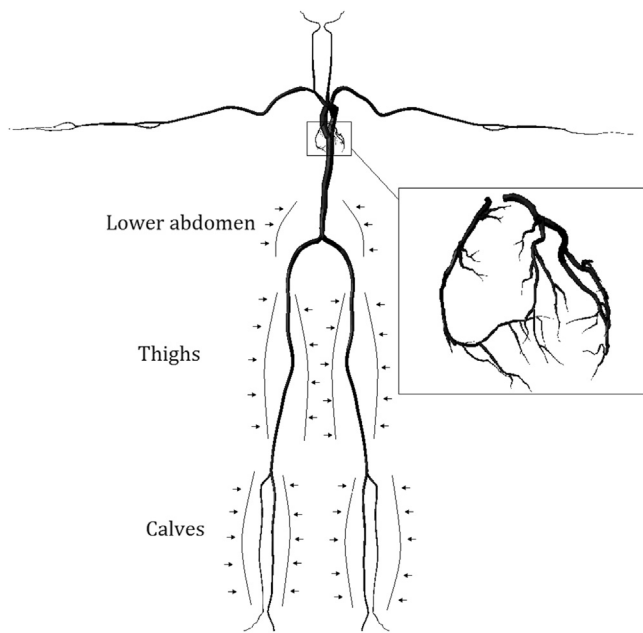


**Figure 7.12**  
External compression scheme.

(see [Section 7.5.3](#)). The primary application of EECP is a noninvasive treatment of cardiac ischemia and angina. Different studies indicate its positive effect on blood pressure, cardiac index (e.g., see Ref. [328]), pulse waves (e.g., see Ref. [329]), and endothelial function (e.g., see Ref. [330]).

Possible side effects of the increased pressure in systemic arteries may include aneurysm formation and rupture, atherosclerotic plaques rupture, etc. Therefore, EECP procedure should be analyzed to keep patient in safe conditions. The 1D hemodynamic model can be used for such analysis. Cuffs performance is simulated as external pressure (see [Section 7.5.3](#)) applied to the lower abdomen, thigh, and calf arteries according to the schedule shown in [Table 7.6](#). Here, the cardiac cycle is 1 s,  $T_s$  is the time of the compression initiation, and  $T_f$  is the time of the compression termination. The values of the standard times and pressure amplitude are taken from Ref. [291].

**Table 7.6: Pressure and time synchronization for enhanced external counterpulsation.**

	<b>External pressure</b> $P_{ext}$ , mmHg	<b>Standard time</b>		<b>Delayed time</b>	
		$T_s$ , s	$T_f$ , s	$T_s^*$ , s	$T_f^*$ , s
Calves	200	0.24	0.8	0.35	0.95
Thighs	150	0.25	0.8	0.6	0.95
Lower abdomen	100	0.26	0.8	0.75	0.95

**Table 7.7: Relative change of averaged coronary flow and pressure for different enhanced external counterpulsation schedules.**

<i>m/n</i>	Coronary flow, %	Coronary pressure, %
1/0	50	82
1/1	26	15
10/10	39	43
10/100	44	57
1/0*	-10	-5
1/1*	18	-1
10/10*	34	22
10/100*	57	48

\* Means delayed schedule.

**Table 7.8: Relative change of averaged systolic aortic pressure in working and resting phases for different enhanced external counterpulsation schedules.**

<i>m/n</i>	Working phase, %	Resting phase, %
1/0	54	0
1/1	54	7
10/10	31	16
10/100	35	15

We examine numerically several EECP regimes. Each regime is denoted by a pair *m/n*, where *m* is the number of the cardiac cycles with applied external pressure (so-called working phase) and *n* is the number of the cycles without the external pressure (resting phase). Regime 1/0 represents the standard protocol. The following cases were considered: 1/0, 1/1, 10/10, and 10/100. Simulations were performed for both standard and delayed time synchronization (see [Table 7.6](#)). The duration of EECP treatment in each simulation was 1 h.

Relative changes in averaged coronary flow and pressure for different EECP schedules are shown in [Table 7.7](#). All values are normalized to the reference values without EECP. Simulations show that the standard EECP procedure 1/0 results in the largest averaged pressure and blood flow in the coronary vessels. Such schedule also produces the largest averaged systolic aortic pressure (see [Table 7.8](#)), affecting the cerebral circulation and other regional circulations through the baroreflex regulation. The advantage of other schedules is the decrease of the averaged systolic pressure in the aorta. Results for schedules with time delay (marked by \* in [Table 7.7](#)) show that synchronization with the cardiac cycle influences EECP performance as well, and optimization of synchronization time may give substantial improvement of EECP efficiency.

# ***Hemodynamics in normal and angiogenic capillary networks***

## ***8.1 Introduction***

One of the main purposes of microcirculation network is supplying cells with nutrients. A microcirculation network can adjust itself according to the metabolic needs of a perfused tissue. For instance, formation of new microvessels, i.e., angiogenesis, takes place during wound healing, embryonic development, and growth of muscle or adipose tissue as well as other processes. However, the most prominent example is probably the growth of a malignant tumor, which is accompanied by intense reorganization of microcirculatory network. From the very beginning of tumor growth, blood capillaries are partially pushed away from the actively proliferating tumor mass and partially destroyed inside it due to growth-induced pressure [331] as well as various chemical factors, including increased acidity and alterations in expression of vascular growth factors, called angiopoietins, in tumor microenvironment [332]. These processes, along with the inability of the microcirculatory system to meet the increased metabolic needs of neoplastic cells, limits the rate of tumor growth and ultimately leads to metabolic stress in the tumor core and the subsequent formation of necrosis within it. Tumor cells respond to nutritional deficiencies by stimulating angiogenesis, which is widely recognized as one of the main hallmarks of cancer [54,333]. In a healthy body, angiogenesis is well organized by a balanced action of pro- and antiangiogenic factors, which results in fine-tuned, well-functioning vascular system. However, the unceasing overproduction of proangiogenic factors by tumor, the main of which is vascular endothelial growth factor (VEGF), leads to the formation of an anomalous microcirculatory network with rather chaotic structure. The capillaries of tumor microvasculature network are characterized by abnormal morphology of endothelial cells, lack of supporting pericytes, and the resulting changes in shape and functionality—these capillaries are enlarged, curved, and much more permeable to substances dissolved in blood plasma, than ordinary continuous capillaries, which are the predominant type of capillaries in the body [334,335]. Moreover, the structure of preexisting microvessels also changes in a similar way in the presence of VEGF, which in particular results in a rapid increase in their permeability [336].

Most clinically approved antiangiogenic drugs are aimed at blocking the action of VEGF. Such treatment ultimately leads to the restriction of nutrients inflow to the tumor, because it stops the formation of new capillaries, while the existing ones continue to degrade with the tumor growth. Also, anti-VEGF therapy results in normalization of the structures of single capillaries, bringing the microcirculatory network of the tumor to a more physiologically normal state [337,338].

The structure of a real microcirculatory network is quite complex and is characterized by an extremely high density of microvessels. Due to this fact, accurate experimental studies of the structure of microvasculature network under natural conditions are associated with certain difficulties and became available only in the past decade by virtue of microcomputed tomography. This modern method allows to restore the structure of objects with a characteristic size of the order of microns. Such resolution is sufficient to study the morphology of the capillary bed, including the case of a tumor [339]. Herein, a novel approach to mathematical modeling of microcirculation is presented. This approach is based on the idea of generating networks, having similar structural and functional characteristics to the ones of a real microcirculatory network. At first, an algorithm of the realistic microcirculatory network structure reconstruction is discussed. Then, the models of the blood flow in the capillary network are considered accounting for nonlinear features. One of the models is applied to the simulation of the microcirculatory flow in generic networks.

Since capillaries are the sites of substances exchange between blood and tissue, one of the main requirements for the modeled networks is obviously a uniform distribution of capillaries in three-dimensional space, which in particular ensures the supply of all cells with metabolites. The influx of nutrients from larger vessels with a thicker wall containing muscular layer is negligible; however, for the well-posedness of the considered task, it is also necessary to generate microvessels that bring blood to the capillaries. Of particular interest is the fact that the influx of two most essential nutrients, i.e., oxygen and glucose, depends on different properties of capillary bed [49]. The transfer of glucose relies on its passive diffusion through the pores in the walls of capillaries and glucose inflow rate is small enough so that its concentration decreases only slightly during the flow of blood through the capillary bed even in tumors, which consume it excessively (see, for example, Ref. [340]). This implies that local glucose inflow is—at least at a first approximation—proportional to the density of capillaries surface area. Contrarily, oxygen, as a lipid-soluble substance with low molecular weight, penetrates directly through the walls of capillaries, and permeability for it is at least four orders of magnitude greater than that for glucose. Oxygen levels in arterial and venous blood even under normal conditions differs more than twice, which means that its influx is defined mainly by the value of local blood flow. These facts mean that in the microcirculatory network model both the density

of the capillaries surface area and the density of blood flow through them should be evenly distributed. The corresponding statistical studies are presented in this chapter.

The following applications of the microcirculatory network model are discussed below: the dependence of blood flow on capillary network density; an algorithm of coupling this model with a model of tumor growth in tissue. We also investigate a clinically observed phenomenon of tumor blood flow increase induced by antiangiogenic therapy.

## **8.2 Structure of microcirculatory network**

### **8.2.1 Review of structure generation methods**

The angioarchitecture is a necessary ingredient for modeling microcirculation at macroscale. The structure of the microcirculatory network is quite complex. It includes a large number of small vessels (arterioles, venules and capillaries), which are surrounded by the tissues. Observations of such structures are difficult. Topological (connectivity of the network), morphological (length and diameter), and hemodynamic parameters (flow rate and hematocrit) were studied in Ref. [341] by means of intravital microscopy in the rat mesentery, which is rather flat. In that study, networks consisted of several thousands elements were considered. Correlations between morphological and hemodynamic parameters were observed. Classification of the elements of the microvascular network was proposed, which is based on the following three ordering parameters: segment diameter, generation, and pressure.

The 3D region of a whole microcirculation was studied in Ref. [339] by *ex vivo* high-resolution microcomputed tomography imaging method. The authors reconstructed the vasculature structure of a human breast cancer of the volume approximately equal to 280 mm<sup>3</sup>. Similar direct observations are rarely performed nowadays. Different methods of microvascular structure simulation are used instead. They are aimed to reproduce physiological function of the microvascular network rather than its exact structure. One of the most popular is the concept of dichotomous branching tree. Basing on the idea of minimization of work for transport and upkeep, Murray derived the relationship of the radii in the lumen-based network system [342]:

$$r^n = r_1^n + r_2^n, \quad (8.1)$$

where  $n = 3$ ,  $r$  is the radius of the parent vessel,  $r_1, r_2$  are radii of the daughter vessels. The Eq. (8.1) for  $n = 3$  is well known as Murray's law. In Refs. [343–345,347,369], microvasculature is approximated as a fractal branching self-similar tree-like structure. It was shown that similarity dimension of the blood vessel tree should be greater than the embedding space dimension and should be equal to 3.4 [371]. This value ensures homogeneous blood supply of the tissue. The numerically found values of pressure and

velocity were compared for different values of bifurcation exponent  $n = 2.5, 2.7, 3$  in Ref. [343]. The general case  $r^n$  and relationship of the fractal similarity dimension and the value of bifurcation exponent have been systematically studied in Ref. [346]. It was reported that the value  $n = 2.85$  ensures the best fitting with experimental data in the case of retinal microvasculature. A method for constructing randomized fractal-tree structure similar to the kidney microvasculature was presented in Ref. [345].

A realistic microvascular network without assumption of tree-like self-similarity was proposed in Ref. [348]. In this paper, the network is uniformly distributed in space using direct force repulsion–attraction nonlinear model.

The structural adaptation due to physiological and pathophysiological factors was considered in Refs. [347–353]. According to the [351], the main factors of the morphological angioadaptation (change of the diameters and area of the microvessels) are wall shear stress, intravascular pressure, local metabolic stimulus, information transfer via convection and conduction from upstream and downstream parts of the network, circumferential wall tension, and wall mass. The model for the change of the resistance, pressure, and blood flow due to morphological angioadaptation was presented in Ref. [349]. The topological angioadaptation (change of the network structure due to collapse, degradation, or growth) in normal and pathological (tumor angiogenesis) conditions was considered in Refs. [347,348,352,353].

At the scale of a whole organ, continuum mechanics approaches have been developed. In Ref. [215], microcirculation in a large region of tissue was simulated in 2D as a set of three porous domains. These domains correspond to the arterioles, capillaries, and venules. A filtration process is considered in every 2D domain according to the Darcy's law. They connected each other by a Poiseuille pressure drop condition. This model was combined with a 1D model of closed circulation [354]. In Ref. [355], the model of the perfusion of myocardium tissue is composed by 31 layers, which are described by the lumped parameters model.

Another multiscale model of cerebral microcirculation was proposed in Ref. [356]. Four levels of spatial scale were highlighted in this model. The capillary bed was simulated as a homogeneous space-filling medium, whereas arteriolar and venular trees were simulated using the network approach. Similar idea has been used in the context of cardiac [357] and tumor [358] microcirculation.

### **8.2.2 Algorithm for generating microcirculatory network structure**

Here, we describe an algorithm of a realistic microvascular network generation without assumption of tree-like fractal self-similarity. It can be applied to a tissue region of about  $1 \text{ cm}^3$ . The algorithm of the generic microcirculatory network generation consists of two

stages. At the first stage, arteriole and venule tree-like structures are generated. For this purpose, the considered three-dimensional space is divided into equal cubic cells. In each cell, two nodes of the zero level and one node of the first level are placed using a random uniform distribution by coordinates. The first level nodes are connected with the zero level nodes by the zero-level edges, which represent precapillary arterioles/postcapillary venule. Then, the set of cells is divided into pairs of neighboring cells. Two nodes of the first level of each pair are connected with a new node of the second level, which is located outside the both cells as shown in Fig. 8.1. At every subsequent step, the two nodes of the highest possible level are connected with a new node of the next level. One repeats these steps until only one node remains at the new level. In the case of an odd number of cells, one of the new nodes is connected to only one node of the previous level. The exact spatial positions of the edges above the first level are not significant, since these vessels provide no nutrient exchange, and their length is used as a parameter.

At the second stage, generated capillary tree-like structures are attached to the zero-level edges of the arterial and venous trees. The positions of the capillaries in space are assigned iteratively in order: (1) to minimize the variation of the distances between the

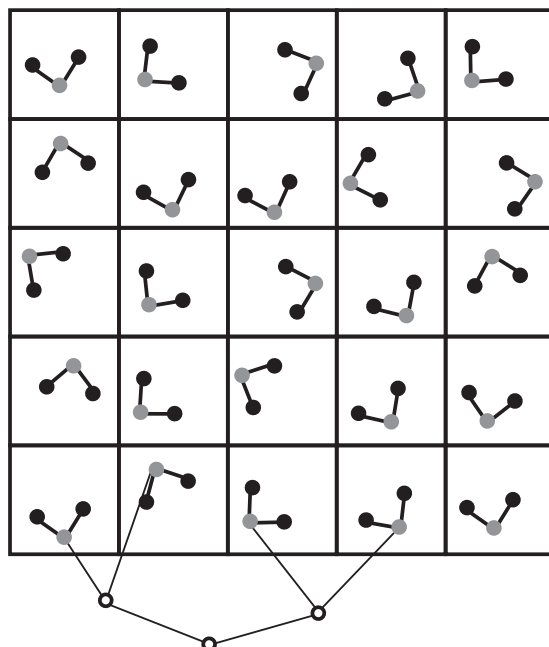


**Figure 8.1**

Illustration for the first stage of the microcirculatory network generation algorithm. *Black points* are nodes of the zero level, *gray points* are nodes of the first level, and white points are nodes of higher levels.

nearest initial nodes of the capillary trees, which should be in the range of 50–200  $\mu\text{m}$ ; (2) to minimize variation of the distances between the centers of the nearest capillaries; (3) to fit the distributions of the lengths and the diameters obtained in the experimental work on the reconstruction of the microcirculatory network [339]; (4) to match each free edge of the arteriole capillary trees with some free edge of a venule capillary tree.

Comparison of the generic distribution of the microvessel lengths in one random run of the algorithm with experimental data is shown in Fig. 8.2. The variation among different runs is not significant. The total number of capillaries is set as an input parameter for the network generation algorithm. It determines the depth of the capillary trees.

### 8.2.3 Study of statistical properties of the algorithm for generating microcirculatory network structure

The microcirculatory network generation algorithm is based on the use of random values; therefore, a new network is formed upon each implementation of it. To use such an algorithm for research purposes, it is necessary to study the statistical properties of the structures of the generated networks. The main statistical property, as was stated in Section 8.1, is the uniformity of distribution of capillaries surface area in space, which results in the uniform supply of cells with glucose and other crucial nutrients.

To study the statistical properties of the considered algorithm, microcirculatory networks were generated in a spherical region with a diameter of 1 cm, which contains  $M = 5 \cdot 10^4, 10^5$ , and  $2 \cdot 10^5$  capillaries. These microvessel densities correspond by the order of magnitude to microvascular network of human breast cancer [339]. The modeling area was divided into  $N = 25$  concentric spherical layers. Such segmentation has been chosen to ease the subsequent integration of this model with the 1D model of tumor growth, which is discussed further in Section 8.4.3. The following values were used for analysis:

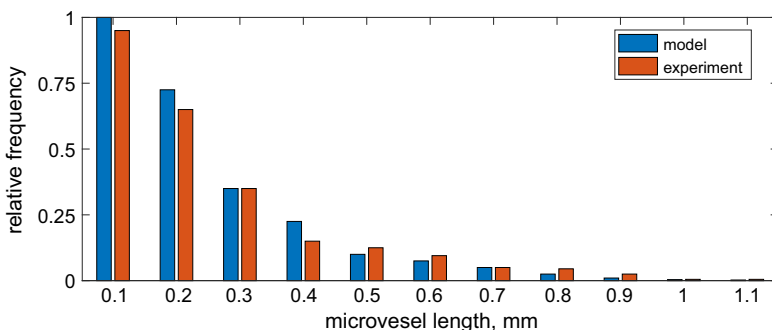


Figure 8.2

Distribution of the length of microvessels: comparison of the model and experimental data [339].

- the average, over the algorithm implementations under given  $M$ , of the relative standard deviation of the average density of the capillary surface area in  $N$  layers from its mean value over all layers in an implementation:

$$\Delta_1 s = \frac{1}{L} \sum_{j=1}^L \frac{1}{\bar{s}^j} \sqrt{\frac{1}{N} \sum_{i=1}^N \left( s_i^j - \bar{s}^j \right)^2},$$

where  $s_i^j = \frac{1}{V_i} \sum_{n=1}^{K_i^j} S_n$  is the average capillary surface area density in the  $i$ -th layer for the  $j$ -th implementation;  $S_n$  is the surface area of  $n$ -th capillary or capillary part in the considered layer;  $K_i^j$  is the number of capillaries or their parts in the  $i$ -th layer for the  $j$ -th implementation (for the capillaries, which cross the boundary between two layers, for both layers, only the fraction of their surface area, lying in it, was accounted for),  $\bar{s}^j = \frac{1}{N} \sum_i^N s_i^j$  is the mean value of average surface area densities throughout all the layers for the  $j$ -th implementation;

- relative standard deviation of the mean value of average surface area densities in a single layer throughout a single implementation from its average throughout all algorithm implementations under given  $M$ :

$$\Delta_2 s = \frac{1}{\bar{s}} \sqrt{\frac{1}{L} \sum_{j=1}^L \left( \bar{s}^j - \bar{s} \right)^2},$$

where  $\bar{s} = \frac{1}{L} \sum_{j=1}^L \bar{s}^j$  is the mean value of capillary surface area density throughout the implementations under given  $M$ .

For each number of capillaries  $M$ , several generated networks, which did not match to the following condition, were discarded:

$$\frac{\max_{i \in [1, N]} |s_i^j - \bar{s}^j|}{\bar{s}} < 20\%.$$

This allowed us to eliminate the cases containing the statistical outliers of regions with very dense capillary clusters. The results of the statistical analysis for remaining networks,  $L = 50$  items per each  $M$ , are presented in [Table 8.1](#). Statistical analysis demonstrates that, with an increase in the capillary density, the irregularity of spatial distribution of capillaries decreases, indicating the adequacy of the model.

**Table 8.1: The results of statistical analysis of the structures of microcirculatory networks.**

$M$	$\Delta_1 s, \%$	$\Delta_2 s, \%$	$\bar{s}, \text{cm}^{-1}$
$5 \cdot 10^4$	6.7	2.9	12
$1 \cdot 10^5$	5.9	2.3	25
$2 \cdot 10^5$	4.8	2.0	49

## 8.3 Hydraulic equations

### 8.3.1 Review of microcirculatory flow models

In the microvascular networks, the size of the red blood cells (RBCs) is comparable with the diameters of the microvessels. The average velocity of the blood flow is about a thousandth of that in the large arteries. The hydrodynamics of such creeping flows is quite different from the hydrodynamics of the flows in the aorta and other large vessels. The physical *in vitro* studies of capillary flows are presented in Refs. [359–361], which also include experiments on capillary resistance to the flow and measurements of the pressure required to force mammalian erythrocytes through pores having a diameter less than the cells.

Microcirculatory flows are characterized by the small Reynolds numbers in the approximate range from  $10^{-3}$  to 1. The inertial effects in these flows are negligible, and viscous effects dominate. The linear Stokes approximation for incompressible fluid dynamics and the lubrication theory are commonly applied to model such flows.

In the smallest capillaries, only one red cell may enter a microvessel at a time. RBCs travel in a single line surrounded by a thin lubricating layer of plasma. In a medium-sized vessels, which contain up to 20 erythrocytes across the diameter, the traditional continuum mechanics approach is hardly applicable. It was observed that RBCs do not touch the endothelial wall [362]. Several physiological phenomena are responsible for the formation of a cell-depleted or even a cell-free layer near the vascular wall. The RBCs migrate toward the center line of the vessel due to their deformability, nonuniformity across the radial Poiseuille-like velocity profile, and gel-like deformable endothelial glycocalyx layer. The cell–cell interactions with the neighboring RBCs, leukocytes, thrombocytes and less deformable molecules with similar size, in particular chylomicrons, result in the reverse migration to the wall. But this effect is less pronounced. A review on cell–cell and cell–glycocalyx interactions can be found in Ref. [363]. The presence of the cell-free layer reduces the effective hydraulic resistance to the flow. This phenomenon is responsible for the well-known Fåhraeus–Lindqvist effect. An extensive detailed review of the most important physiological factors affecting the hydrodynamics in microcirculatory network can be found in Refs. [42,363,364].

A group of mathematical models considers the capillary blood flow as a flow of fluid (plasma) with suspended flexible solid objects (RBCs) in a tubes of different dimensions

(capillaries, arterioles, venules) [43,365–372]. A particle method for the computer simulation of blood flow was proposed to analyze the motion of a deformable RBC in flowing blood plasma. An RBC is modeled as a portion of an incompressible viscous fluid bounded by elastic membrane. Plasma is considered as a viscous fluid. The membrane particles were connected to their neighboring membrane particles by springs, and the motion of the particles was determined on the basis of the minimum energy principle.

Particle methods are still computationally expensive for blood flow simulations in a microcirculatory network at macroscopic scale. The low Reynolds numbers of the flow regimes allow to apply well-known Poiseuille pressure-drop condition for steady laminar flow of a Newtonian fluid in a single vessel [42,339,345,349,364,373]:

$$\Delta P = RQ, R = \frac{128L\mu}{\pi D^4} \quad (8.2)$$

where  $\Delta P$  is pressure drop over the vessel's terminal points,  $Q$  is flow rate,  $R$  is hydraulic resistance,  $L$  and  $D$  are the length and diameter of the vessel, and  $\mu$  is viscosity. The length of the vessel is obviously constant. Thus, the relationship between the pressure drop over the vessel and the flow through it is characterized by the vessel diameter and viscosity. The diameter variations are associated with the growth, regulatory modulation, metabolic demands, and diseases [352]. The viscosity is, probably, the most uncertain parameter, which depends on various factors including vessel's diameter, blood temperature and composition, in particular, RBCs volume fraction  $H$  (hematocrit), flow rate, pathological change of the elastic properties of the RBC membranes due to sickle cell anemia, diabetes, etc. All these and other factors are modeled within the considered approach as some effective (apparent) viscosity, which can be a nonlinear function of various parameters  $\mu = \mu_{app}(Q, D, H, \dots)$ . In different cases, this function can be derived from fundamental principles of continuum mechanics, from simulations by some particle method or from experimental observations. Thus, the study of non-Newtonian rheological properties of blood in microvessels is the central problem of modeling blood flow in microcirculatory network.

In vitro analysis of the flow of RBC suspension in glass tubes allows to derive the following empirical relationship [374,375]:

$$\frac{\mu_{app}}{\mu_p} = 1 + \left( \frac{\tilde{\mu}}{\mu_p} - 1 \right) \frac{(1 - H_D)^C - 1}{(1 - \tilde{H}_D)^C - 1}, \quad (8.3)$$

where  $\mu_p$  is the viscosity of plasma,  $H_D$  is the ratio of the volume flux of RBCs to the total volume flux of blood (discharge hematocrit),  $\tilde{\mu}$  is the apparent viscosity of blood for a discharge hematocrit  $\tilde{H}_D = 0.45$ ,  $\tilde{\mu}(D)$ ,  $C(D)$  are functions of the vessel diameter  $D$ . See

Refs. [364,374] for more details on this model. *In vivo* analysis of living microvessels results in much higher values, which are determined by the following empirical relationship [364,373,376]:

$$\frac{\mu_{app}}{\mu_p} = \left[ 1 + \left( \frac{\tilde{\mu}}{\mu_p} - 1 \right) \frac{(1 - H_D)^C - 1}{(1 - \tilde{H}_D)^C - 1} \left( \frac{D}{D - D_0} \right)^2 \right] \left( \frac{D}{D - D_0} \right)^2. \quad (8.4)$$

The reason for the difference  $D - D_0$  is the presence of the glycocalyx layer on the inner surface of endothelial layer of the microvessels ( $D_0 = 1.1$  microns), which slows down the plasma flow in the cell-free layer.

The flow in macroscopic regions of microvascular network (several cubic centimeters) can be simulated by applying the mass conservation condition to vascular junctions [339,348,373,377]:

$$\sum_i Q_i = 0 \quad (8.5)$$

and solving the set of nonlinear algebraic Eqs. (8.2) and (8.5). Conservation of the total number of RBCs also can be used [345]:

$$\sum_i Q_i H_{D,i} = 0. \quad (8.6)$$

Specific attention should be paid to the assessment of incomplete boundary conditions [377]. It should be mentioned that relationship between flow rates and distribution of RBCs and, thus, hematocrit between the connected vessels at junction has a complicated nonlinear form. This dependency is associated with the presence of a cell-free layer. The vessels with lower flow rate attract more flow from a cell-free layer (plasma component), and thus, the vessels with greater flow receive more RBCs [373]:

$$\text{logit } FQ_{RBC} = A + B \text{logit} \left( \frac{FQ_{total} - X_0}{1 - X_0} \right), \quad (8.7)$$

where  $\text{logit } x := \ln \frac{x}{1-x}$  and

$$A = -13.29 \frac{(1 - H_D)}{D_p} \frac{d_{\alpha,\beta}^2 - 1}{d_{\alpha,\beta}^2 + 1}, d_{\alpha,\beta} = \frac{D_\alpha}{D_\beta}, \quad (8.8)$$

$$B = 1 + 6.98 \frac{(1 - H_D)}{D_p}, X_0 = 0.964 \frac{(1 - H_D)}{D_p}, \quad (8.9)$$

$FQ_{RBC}$  is a fractional flow of RBCs to some daughter vessel in junction,  $FQ_{total}$  is a total fractional flow of blood to the same vessel in junction,  $D_p$  is a diameter of the parent vessel supplying the daughter vessels  $\alpha$  and  $\beta$ ,  $D_\alpha, D_\beta$  are diameters of the daughter vessels. See Refs. [364,373,375,378] for more details on this model.

### 8.3.2 Mathematical model of microvascular network flow

There exists a lot of complicated approaches to the modeling of blood flow in microcirculatory networks. Numerical simulations with these nonlinear models face significant computational expenses. Thus, most of them are suitable only for small networks. Such approaches will lead to absolutely enormous calculations for macroscopic networks, substantially limiting any statistical analysis and obtaining physiologically correct results. Therefore, it is practical to use a phenomenological model, which provides physiologically reasonable approximation of blood flow behavior with the change in parameters of microvessels.

A typical microcirculatory network, which perfuses the tissue of about  $1 \text{ cm}^3$ , contains hundreds of thousands of elements. Here, we describe a model, which is suitable for simulations of a macroregion of microcirculatory network containing up to  $2 \cdot 10^5$  of elements. We consider a flow in the network, which is generated by the stochastic algorithm, described in [Section 8.2.2](#). Let  $V$  be a set of nodes of the network and  $E$  be a set of edges, which corresponds to the microvessels. Every edge is specified as a pair of nodes  $(u, v)$ :  $u, v \in V$ . Thus, a particular network can be specified as a set  $(V, E)$ , which is also definition of a graph in graph theory. The blood flow in the microcirculatory network is calculated on the basis of the Poiseuille pressure drop and the mass conservation condition in the nodes representing microvessel's joints,

$$Q_{uv} = G_{uv}(P_v - P_u), \quad \sum_{uv \in \mathcal{P}_u} Q_{uv} = 0, \quad (8.10)$$

where  $Q_{uv}$  is the flow rate between the nodes  $u$  and  $v$  if the corresponding edge  $(u, v)$  exists,  $P_u$  is the pressure in the node  $u$ ,  $G_{uv}$  is the conductivity coefficient of the edge  $(u, v)$ , which equals to the reversed hydraulic resistance,  $\mathcal{P}_u$  is the set of edges with the node  $u$ . The Newtonian fluid approximation for the small Reynolds numbers results in the constant value of  $G_{uv}$ :

$$G_{uv} = \frac{8\mu l_{uv}}{\pi k_{uv} r_{uv}^4}, \quad (8.11)$$

where  $l_{uv}$  is the length of the edge,  $\mu$  is the blood viscosity,  $r_{uv}$  is the radius of the edge,  $k_{uv}$  is the variable parameter for the resistance of tumor angiogenic capillaries. Parameter  $k_{uv}$  is equal to unity by default (in the normal network) and considered in more details in [Sections 8.4.2](#) and [8.4.3](#). The nonlinear effects are simulated by the following relationship:

$$G_{uv} = \frac{8\mu l_{uv}}{\pi k_{uv} r_{uv}^4} (1 + \alpha Q_{uv}^2)^{-1}, \quad (8.12)$$

which helps to account for the nonlinear behavior of the blood flow in the capillary bed by a relatively simple but physiologically reasonable way. For the slow flows (small values of  $Q_{uv}$ ),

$G_{uv}$  equals some constant value. For faster flows (relatively big values of  $Q_{uv}$ ),  $G_{uv}$  decreases. It should be mentioned that, in the nonlinear case (Eq. (8.12)),  $\mu$  and  $\alpha$  are just parameters defining nonlinear blood rheology.  $\alpha$  is the coefficient, which determines the effect of the blood flow on the microvessel resistance. In this work, we set  $\alpha = 0.4$ .

At the input and output nodes of the network, we set  $P_{in} = 35$  mm Hg,  $P_{out} = 15$  mm Hg. The first value slightly overestimates and the second one slightly underestimates common physiological hydrostatic pressures at arterial and venous ends of a capillary bed [379].

The Newton method is used for the numerical solution of the set of equations with nonlinear term for conductivity (Eqs. (8.10) and (8.12)). As a starting point for solving a nonlinear problem, a linear model solution is taken (Eqs. (8.10) and (8.11)), which is sufficient for the convergence in this case.

### 8.3.3 Study of statistical properties of capillary blood flow model

To use the model for research purposes, it is necessary to conduct a study, similar to the one made in Section 8.2.3. In particular we need to examine statistical properties of the blood flow in the generated microcirculatory networks. Namely, it is necessary to estimate the uniformity of blood flow in the capillaries throughout space, which determines the uniformity of oxygen supply to the cells, as it was explained in Section 8.1. In turn, only the flow in the capillaries emanating from the arterioles matters (which are hereafter referred to as “first capillaries”). The later is due to assumption that the free oxygen concentration in blood comes to an equilibrium with the one in tissue already when blood flows through them, due to the extremely high permeability of the capillary walls for oxygen. In this regard, to estimate the correctness of the mathematical model, the parameter of density of blood flow in first capillaries is chosen, which will be further occasionally referred to as just blood flow for short. Note that total blood flow for all first capillaries is equal to blood flow in the input arteriole.

We use here the same microcirculatory networks, which were used for statistical analysis of network structure and contain  $M = 5 \cdot 10^4$ ,  $10^5$ , and  $2 \cdot 10^5$  capillaries and  $L = 50$  networks for each of the number. In addition, the simulation area is divided into  $N = 25$  concentric spherical layers, and the average density of blood flow in first capillaries in the  $i$ -th spherical layer for the  $j$ -th implementation is calculated as:

$$q_i^j = \frac{1}{V_i} \sum_{n=1}^{K_i^j} Q_n.$$

Here,  $V_i$  is the volume of the  $i$ -th spherical layer;  $K_i^j$  is the number of first capillaries in the  $i$ -th layer for the  $j$ -th implementation (for our purposes a capillary is assumed to be in

the same layer with its arterial end);  $Q_n$  is the blood flow in  $n$ -th first capillary in  $i$ -th layer for the  $j$ -th implementation.

The analysis is performed using the average of the relative standard deviation of the mean density of blood flow in first capillaries in  $N$  layers. The average is computed over all implementations for given  $M$ :

$$\Delta_1 q = \frac{1}{L} \sum_{j=1}^L \frac{1}{\bar{q}^j} \sqrt{\frac{1}{N} \sum_{i=1}^N \left( q_i^j - \bar{q}^j \right)^2},$$

where  $q_i^j$  is the average density of blood flow in first capillaries in the  $i$ -th layer for the  $j$ -th implementation;  $\bar{q}^j$  is the mean value of the average density of blood flow in first capillaries over all layers for the  $j$ -th implementation.

We also consider the relative standard deviation of the mean value of the averaged density of blood flow in first capillaries throughout all the layers in a single implementation:

$$\Delta_2 q = \frac{1}{\bar{q}} \sqrt{\frac{1}{L} \sum_{j=1}^L \left( \bar{q}^j - \bar{q} \right)^2},$$

where  $\bar{q} = \frac{1}{L} \sum_{j=1}^L \bar{q}^j$  is the average density of blood flow in first capillaries in all

implementations with a given number of capillaries. The results of analysis are presented in [Table 8.2](#). They show that  $\Delta_1 q$  decreases within a considered sample of generated networks with increase in number of capillaries; however,  $\Delta_2 q$  does not. This may be just the statistical effect for the given sample, which would smooth out with its further increase, but also this may be a peculiarity of the considered approach; thus, this question requires further investigation. Nevertheless, since the deviations of the blood flow are rather moderate, it was decided to use the model for now in its actual state.

**Table 8.2: The results of statistical analysis of density of blood flow in first capillaries of generated microcirculatory networks.**

$M$	$\Delta_1 q, \%$	$\Delta_2 q, \%$	$\bar{q}, 10^{-2} \text{ s}^{-1}$
$5 \cdot 10^4$	14.5	6.3	0.78
$1 \cdot 10^5$	12.2	6.8	1.24
$2 \cdot 10^5$	10.2	6.6	2.21

## 8.4 Capillary blood flow and tumor growth

### 8.4.1 Investigation of dependence of blood flow on capillary network density in normal networks

The dependence of blood flow on capillary network density is an interesting and practically significant question, since it, in particular, defines how the oxygen supply grows under angiogenesis and to what extent it can be increased. Some values of blood flow for different numbers of capillaries are already given in Table 8.2. Fig. 8.3 provides more complete data obtained by the model simulations using microcirculatory networks, which were all generated in a spherical region of diameter 1 cm. Unfortunately, with the growth in number of microvessels, model simulations require more and more computing resources and simulations become extremely difficult already under  $5 \cdot 10^5$  capillaries, which explains the absence of data for this and larger numbers of vessels. Moreover, statistical errors also grow with increase in microcirculatory density, since less and less networks were created.

Nevertheless, the obtained data still allow to draw an important conclusion that, while microcirculatory network becomes denser, the rate of increase in blood flow slows down. The results also suggest that there may be a limit of blood flow growth. This result correlates well with the common physiological reasoning. To clarify this, consider a small capillary tree linking arterious and venous parts, so that the resistance of this capillary tree is much greater than that of other part of circulatory network and so blood flow rate through it is close to zero. The addition of another identical capillary tree parallel to the first one will halve their total resistance and increase blood flow rate through them almost twice. So, under sufficiently low microcirculatory density, blood flow should grow linearly

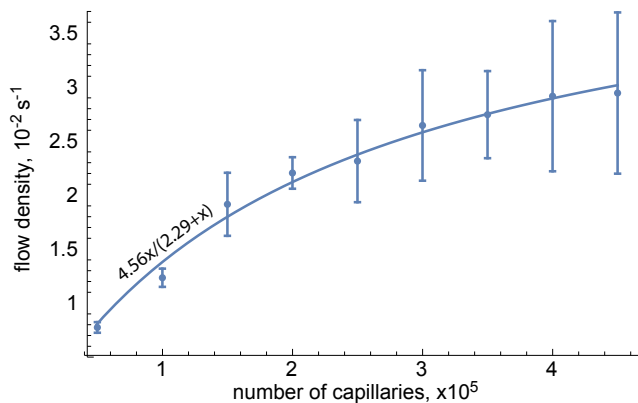


Figure 8.3

The dependence of the blood flow density through the microcirculatory network on the number of capillaries in it.

with density increase. However, under sufficiently larger amount of such capillary trees, so that their overall resistance is much less than that of other part of circulatory network, adding any amount of new capillaries would result in almost no increase in blood flow, since it is determined by resistance of other vessels in this case.

This reasoning leads to an important physiological conclusion that changes in microvessel density during angiogenesis and antiangiogenic therapy should serve only as a preliminary indicator of changes in oxygen supply. Although these changes should have the same sign, their values are not necessarily proportional, especially in very dense capillary networks. Thus, several-fold increase in capillary density leads to the only conclusion that the increase in oxygen supply is less. Note that sufficiently active proangiogenic activity also results in considerable increase in interstitial pressure, which leads to compression of capillaries and thus slows down the blood flow in them. This effect is considered further in [Section 8.4.2](#). However, it should be noted that, for other major metabolites, the situation should be more straightforward. As we discussed in [Section 8.1](#), this happens because metabolites local inflow, which is diffusion limited rather than flow limited, is almost proportional to the capillaries surface area density.

Such kind of investigation makes it possible to obtain a fitting function, which provides a link between local capillary network density and local oxygen inflow. This result can be useful for spatially distributed mathematical models of complex physiological processes, e.g., tumor growth in tissue, an example of which is presented in Chapter 10. At the moment, a common approach in such models is the description of the microcirculatory network via spatially distributed variables. This approach is fairly coarse but unavoidable simplification when dealing with equations of reaction-diffusion type. Inability of such models to adequately—from a physiological point of view—describe inflow of oxygen in the tissue is one of the major drawbacks of such approach. In the work [380], a new approach to modeling of oxygen inflow has been presented, which relies on the preliminary results, obtained in such investigation. It also relies on some other general physiological assumptions, discussed in detail further in [Section 8.4.3](#). The results from [401] will be further discussed in [Section 8.4.2](#).

#### ***8.4.2 Investigation of increase in tumor blood flow induced by antiangiogenic therapy***

As discussed in the introduction to this chapter, an excessive production of proangiogenic factors by tumor leads to the formation of new capillaries with altered properties including increased permeability, which leads to an increased influx of nutrients and blood plasma into the tissue and a subsequent local increase in interstitial pressure (further IP for short), and a lack of supporting cells, in particular pericytes, which reduces elasticity of capillary wall. As a result of this alteration, due to an increased IP, the lumina of capillary wall may

decrease, leading to the increase in their resistance and the reduction in blood flow volume through them [381]. Also, under the influence of proangiogenic factors, the properties of preexisting capillaries change in a similar way.

Experiments on murine tumor models demonstrate that administration of antiangiogenic therapy (further AAT for short) can lead to temporal change in tumor perfusion, both to its increase [383,503] and decrease [384,385] in different cases. This is not surprising, since AAT triggers a variety of physiological processes, and each process has a different effect on the overall resistance of the microcirculatory network. Some of the processes reduce the resistance of microvessels, the most important of which, apparently, is the reduction of interstitial pressure. On the contrary, a decrease in the diameters of capillaries, caused by the normalization of their structure, leads to an increase in their resistance, and the subsequent degradation of capillaries leads to an increase in the total resistance of the microcirculatory network.

Cases of increased tumor blood flow during AAT are of considerable clinical interest, as this results in increase of oxygen flow to the tumor. This is currently considered to be the main cause for the temporary alleviation of intratumoral hypoxia, which makes it possible to increase the effectiveness of subsequent tumor irradiation, which depends on the concentration of oxygen as a potent radiosensitizer. Direct measurement of changes in blood flow in result of AAT are impossible, and so various indirect methods are used for this purpose. They allowed to estimate that the maximum relative increase in perfusion is not more than by 50% [386,503]. We further present a theoretical investigation of blood flow behavior in a tumor microcirculatory network under AAT. We shall use the set of microcirculatory networks generated according to the approach described in [Section 8.2.2](#). One of the questions that this study addresses is what values can be achieved by the relative increase of blood flow through the tumor during such treatment.

In our model, the angiogenic properties of the capillaries are taken into account in a phenomenological way by setting the value of  $k_{uv}$  (it is normally equal to 1 (see [Eqs. \(8.11\)](#) and [\(8.12\)](#))), to some varying value  $k_{AC} > 1$  for a given number of capillaries, located in the central part of a microcirculatory network. The parameter  $k_{AC}$  should strongly depend on IP, which, in turn, is tumor- and patient specific and can vary in a wide range. The choice of central capillaries is dictated by the fact that, as a rule, cells in the center of solid tumors are the first to experience metabolic stress and to produce angiogenic factors; in addition, the IP has maximum values in the center of the tumor. Degradation of capillaries is neglected here, since from the point of view of the considered problem, the formation of angiogenic capillaries in the tumor core is effectively equivalent to removing capillaries from the central region along with formation of equivalent capillaries in adjacent area (see [Fig. 8.6](#)). Note that exact position of microvessels in physical space does not play a role for the considered task. For simplicity, the parameter

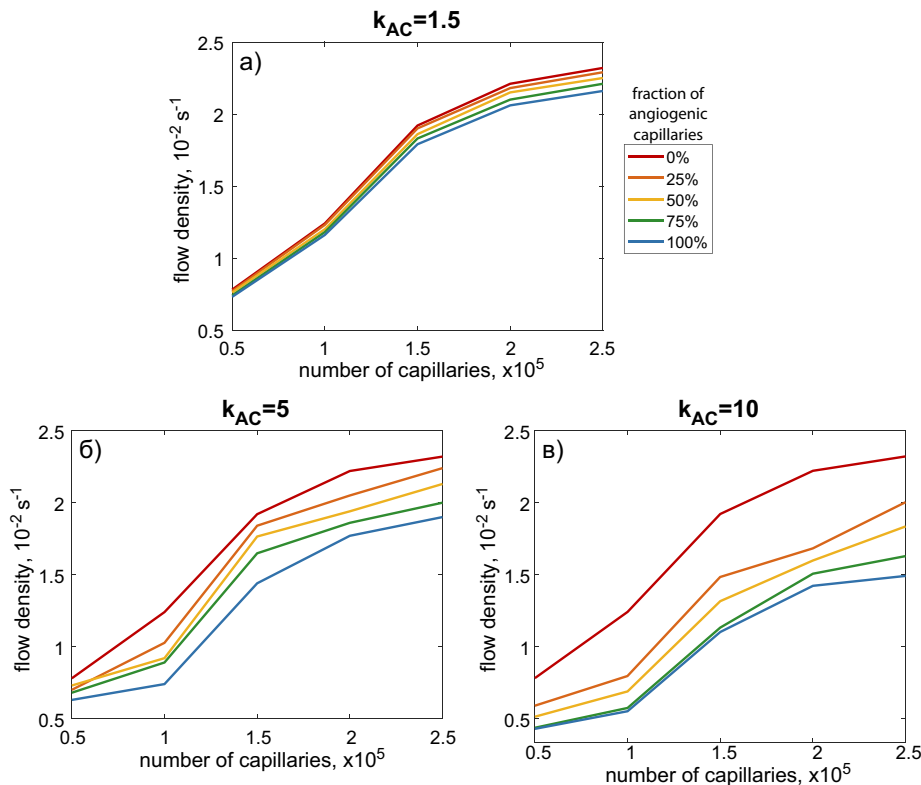
$k_{AC}$  in each case has the same value for all capillaries with angiogenic properties. This is justified by the fact that the pressure gradient in a tumor is usually small [387]. At the same time, alterations in the resistances of arterioles and venules are not taken into account, since it is known that in response to changes in transmural pressure (i.e., the pressure difference between the inner and outer side of the microvessel), they are able to actively change the size of their lumina. This size adjustment is possible due to the presence of smooth muscle layer in their walls. It helps to maintain constancy of blood flow in the capillary network and so to meet the metabolic needs of the perfused tissue. This phenomenon is well studied and is called autoregulation of blood flow [32]. Due to this reason, the input and output pressures are also considered to be unchanged during AAT, which typically does not affect blood pressure in practice. However, it should be noted that according to clinical studies, the chance of hypertension due to VEGF inhibitors is approximately 20% [388].

Of course, a sufficiently large increase in IP will result in compression of the microvessels, but this does not occur within the range of typical values of IP in tumors, which does not rise higher than the average pressure in the capillaries [389]. Moreover, such values of pressure do not lead to the collapse of capillaries (not to mention larger vessels), which can happen inside a tumor for another reason, i.e., due to the pressure caused by proliferation of cells [390].

The graphs in Fig. 8.4 show the values of blood flow density in the simulation domain, depending on the number of capillaries in the network and the fraction of angiogenic capillaries for three values of  $k_{AC}$ . The choice of the maximum value of  $k_{AC} = 10$  is suggested by the results of work [381], in which a detailed bioengineering analysis demonstrated that the resistance of a single capillary can grow by almost an order of magnitude due to an increase in IP up to the average value of hydrostatic pressure in the capillary (compared with capillary resistance at normal IP, which is near 0 mm Hg). Each value in the graphs is the average of the values obtained via 10 different implementations of the microcirculatory network generation algorithm, whereas the same networks were used for the same number of capillaries. Thus, the upward movement within the figure means the gradual normalization of the microcirculatory network and the relief of tumor-associated edema. The results show that, under  $k_{AC} = 1.5$ , these processes only slightly increase the intratumoral blood flow, whereas, under  $k_{AC} = 5$ , the blood flow increases 1.2 times, and, under  $k_{AC} = 10$ , it increases 1.8 times, which agrees well with experimental estimations [386,503].

#### 8.4.3 Coupling with the model of tumor growth

The potential of coupling between the microvasculature model and a spatially distributed model of tumor growth is surely not limited to including a physiologically justified term of

**Figure 8.4**

The dependence of the blood flow density through the microcirculatory network on the number of capillaries in the network, the fraction of angiogenic capillaries, and the ratio of the resistance of angiogenic capillaries to the resistance of normal ones,  $k_{AC}$ . Error bars are not shown for the sake of clear presentation.

local oxygen inflow depending on the density of capillaries as discussed in [Section 8.4.1](#). Firstly, such local coupling obviously disregards that a change in the structure of microcirculatory network at a single point in space can significantly affect the blood flow, and therefore, the oxygen supply at another point. For example, in case of degradation of a capillary branching off from arterioles, blood flow stops in all the capillary tree that it feeds, and in case of shunting between arterial and venous ends, the overall blood flow in the network may even increase but in some areas will significantly drop. Secondly, the specific properties of angiogenic capillaries, mentioned in [Section 8.1](#), also alter the local inflow of substances, so the accounting for the functional state of capillaries throughout space is also significant.

The further path of development in this area is a complete spatiotemporal integration of the models, which would allow to simulate simultaneously the tumor growth and tumor-induced

microvascular network remodeling. A completely integrated model may become an extremely valuable tool for research and development strategies for antiangiogenic therapy. The steps made in this direction and the prototype of the coupled model are discussed further.

Note that simultaneous simulations of microvasculature network remodeling along with tumor growth become a rather popular field of mathematical modeling. Early modeling setups included a consideration of tumor growth with fixed capillary network [391,392] and, vice versa, evolving vasculature with unchangeable tumor which play a role of a source of proangiogenic factors [393,394]. The majority of papers accounting for the dynamics of both tumor and microvasculature network are based on discrete methods, such as cellular automata approach, where capillaries are built from a portion lattice elements, while other elements represent tumor cells [394,395]. For other approaches see [396,397]. These models produce fascinating illustrative results but, due to heavy computational cost, may be suitable only for simulation of the initial stage of tumor growth. In the work [347], an approach is presented, similar to the one presented here in the sense that tumor is modeled via continuum variable, which allows to run simulations for a tumor up to 5 mm in diameter. However, on a more detailed level, the methods discussed here differ from those in [365] in many aspects, including algorithms of generation of microvasculature.

In our coupled multiscale model, the submodel of microcirculation determines the quasi-stationary blood flow along the microcirculatory bed and provides data on the inflow of oxygen and glucose to the submodel of tumor growth, which, in turn, determines the transformation of the capillary network. The transformation happens as a result of factors that stimulate both angiogenesis and degradation of existing capillary network (such factors were discussed in [Section 8.1](#)). The model of tumor growth used herein is a variation of the model presented in Chapter 10, and except for small alterations in specific form of terms and parameter values, insufficient for presentation of qualitative results, this model differs from it in two major aspects: interstitial fluid is not considered here, but oxygen is taken into account. Model description of its inflow will be provided further. For explanation of other features of the model of tumor growth, the reader is referred to Chapter 10. Currently, data exchange protocols between submodels have been developed, integration of models being carried out as follows.

The reference point of the coordinate system of a microcirculatory model coincides with the center of tumor. Tumor growth is considered to be spherically symmetric, which allows us to significantly simplify calculations without distorting qualitative results. Also, to allow the consideration of a huge number of capillaries, the space step used in the microcirculatory network model, i.e., the width of the calculated spherical layer, is chosen to be larger than the space step in the tumor growth model. Data exchange between

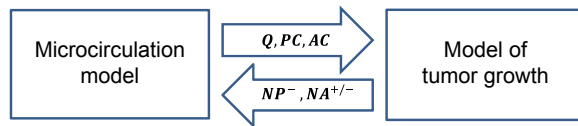


Figure 8.5

Block scheme of coupling of models.  $NA^+$  is the number of capillaries appeared in process of angiogenesis;  $NP^-$ ,  $NA^-$  are the numbers of degraded normal and angiogenic capillaries;  $PC$ ,  $AC$  are the surface densities of normal and angiogenic capillaries,  $Q$  is the blood flow density.

submodels occurs at a constant time interval determined by the rate of microcirculatory network restructuring. This interval is chosen in such a way that, in each calculated layer of the microcirculatory network model, the number of capillaries that appear or degrade during this interval is no more than a hundred. This condition ensures a smooth change in the structure of the capillary network and thus a smooth change in the inflow of nutrients. The basic scheme of interactions between submodels is shown in Fig. 8.5.

The submodel of tumor growth provides information on the number and location in space of new angiogenic capillaries  $NA^+$  that arise in the submodel of the microcirculatory network. The tumor submodel also informs the whole model about degraded preexisting and angiogenic capillaries  $NP^-$  and  $NA^-$ , these capillaries are removed from the graphs. Since we do not consider antiangiogenic therapy yet, there is no term  $NP^+$  corresponding to the process of capillary normalization. Information about new capillaries is determined by the distribution of VEGF, denoted by variable  $V$  in tumor model; information about destroyed ones is determined by the interaction of the tumor (fraction of cells along with necrosis in tissue is denoted by variable  $n_t$ ), with the microcirculatory network, which is described in the tumor growth model by two variables of normal and angiogenic capillary surface density  $PC$  and  $AC$ . Each transferred value refers to a specific  $i$ -th spherical layer and  $j$ -th time interval of the microcirculatory network model. The corresponding equations are as follows:

$$\begin{aligned}
 NA_{i,j}^+ &= 4\pi \int_{t_{j-1}}^{t_j} \int_{r_{i-1}}^{r_i} \left[ R \frac{V(r,t)}{V(r,t) + V^*} (PC_j(r) + AC_j(r)) \times \left( 1 - \frac{PC_j(r) + AC_j(r)}{C_{max}} \right) \right] r^2 dr dt, \\
 NP_{i,j}^- &= 4\pi \int_{t_{j-1}}^{t_j} \int_{r_{i-1}}^{r_i} [\kappa n_t(r,t) PC_j(r)] r^2 dr dt, \\
 NA_{i,j}^- &= 4\pi \int_{t_{j-1}}^{t_j} \int_{r_{i-1}}^{r_i} [\kappa n_t(r,t) AC_j(r)] r^2 dr dt,
 \end{aligned} \tag{8.13}$$

where  $R$  is the maximum rate of tumor angiogenesis, which is achieved under levels of VEGF, sufficiently greater than  $V^*$ ;  $C_{max}$  is the maximum possible capillary surface density; and  $\kappa$  determines the rate of capillary degradation under the influence of

malignant cells and necrotic tissue. Note that the influence of VEGF on the structure and functionality of normal capillaries is yet not accounted for.

At each moment of the data exchange  $t_j$ , on the basis of this data, the structure of the microvascular network is updated. Angiogenic capillaries are formed as bridges between two already existing vascular elements. The distance between these elements does not exceed 1 mm. The lengths and diameters of angiogenic capillaries are assigned to correspond the known experimental statistical distribution, discussed in [Section 8.2.2](#).

Parameter  $k_{uv} > 1$  is assigned to angiogenic capillaries. It influences their resistance and allows to account for their tortuosity and compression (see [Eqs. 8.11 and 8.12](#)). If a degraded capillary is the only one that supplies a set of other capillaries, they are destroyed as well. However, the number of these secondary degraded capillaries is not accounted in  $NP_{i,j}^-$  and  $NA_{i,j}^-$ . Therefore, this approach allows to reproduce a spontaneous nature of capillary degradation. Then, the microcirculatory network model provides new data on the surface density of normal and angiogenic capillaries,  $PC$  and  $AC$ , and the density of blood flow  $Q$ :

$$PC_{i,j} = \left( \sum_{\substack{k_{norm}, \\ r_{i-1} < r_k < r_i}} \pi d_k l_{k,i} \right) / \left( \frac{4}{3} \pi [r_i^3 - r_{i-1}^3] \right),$$

$$AC_{i,j} = \left( \sum_{\substack{k_{ang}, \\ r_{i-1} < r_k < r_i}} \pi d_k l_{k,i} \right) / \left( \frac{4}{3} \pi [r_i^3 - r_{i-1}^3] \right), \quad (8.14)$$

$$Q_{i,j} = \left( \sum_{\substack{k_{first}, \\ r_{i-1} < r_k < r_i}} q_k \frac{l_{k,i}}{l_k} \right) / \left( \frac{4}{3} \pi [r_i^3 - r_{i-1}^3] \right),$$

where  $k_{norm}$  and  $k_{ang}$  are normal and angiogenic capillaries,  $k_{first}$  are capillaries that branch off from arterioles (as discussed in [Section 8.3.3](#), we assume that all oxygen goes into the tissue through them),  $d_k$  and  $l_k$  are the diameter and length of the  $k$ -th capillary,  $l_{k,i}$  is the length of the part of the  $k$ -th capillary located in the  $i$ -th layer. The resulting data arrays are then interpolated by cubic splines, i.e., piecewise smooth cubic polynomials  $PC_j(r)$ ,  $AC_j(r)$ ,  $Q_j(r)$ , which are then used in the model of tumor growth (see Ref. [398] for algorithm of cubic spline interpolation).

Using the obtained information, the inflows of oxygen and glucose  $Q_{O_2}$  and  $Q_S$  are calculated in the tumor growth model. The local inflow of glucose is proportional to the diffusive permeability of capillaries, which is different for normal and angiogenic capillaries, and also to the difference in its concentrations in blood and in tissue. The inflow of oxygen is calculated under the assumptions that (1) oxygen transvascular transport is fast enough for values of oxygen pressure in capillary and in tissue to become equal along one capillary length (which has already been discussed) and (2) the rate of binding to and unbinding from hemoglobin is sufficiently fast for oxygen so that use of quasi-stationary approximation is legitimate. Together with more general model assumption that microvasculature volume is negligible compared with tissue volume, this approach results in term for oxygen inflow proportional to the difference between hemoglobin saturation under two values of unbound oxygen concentration—the one in arterial blood, which enters the capillaries, and the one in tissue. The form of the function of oxyhemoglobin fraction depending on oxygen pressure, or oxygen–hemoglobin dissociation curve, is well known for already about a century [399]. Thus, the inflow of nutrients for the time interval  $[t_j, t_{j+1}]$  is calculated according to the following equations:

$$\begin{aligned} Q_S(r, t) &= [P_{PC}PC_j(r) + P_{AC}AC_j(r)][S_{blood} - S(r, t)], \\ Q_{O_2}(r, t) &= Q_{O_2}^{norm}Q_j(r)[HS(O_2^{art}) - HS(O_2(r, t))], \\ HS(O_2(r, t)) &= \left( O_2(r, t)/\widetilde{O}_2 \right)^{hill} / \left[ 1 + \left( O_2(r, t)/\widetilde{O}_2 \right)^{hill} \right], \end{aligned} \quad (8.15)$$

where  $P_{PC}$  and  $P_{AC}$  are the permeability values of normal and angiogenic capillaries for glucose;  $S_{blood}$  is the level of glucose in blood;  $Q_{O_2}^{norm}$  is the normalization constant for the oxygen inflow selected so that, in the absence of tumor cells, the oxygen level is equal to its predetermined normal physiological level in tissue;  $O_2^{art}$  is oxygen concentration in artery;  $\widetilde{O}_2$  and  $hill$  are coefficients that fit the oxygen–hemoglobin dissociation curve  $HS(O_2)$ .

The resulting inflows of nutrients are substituted into the equations of tumor growth submodel. These equations include terms describing nutrients inflow, diffusion and consumption by cells. Altogether this defines nutrients dynamics. Next, the tumor growth model is simulated until the next moment of the models conjugation is reached. After that, the above algorithm is repeated.

At the initial moment of time  $t = 0$  in the submodel of tumor growth, the distributions of surface densities of capillaries  $PC_0(r)$  and  $AC_0(r)$  are determined on the basis of the normal microcirculatory network according to the algorithm described above. Other initial conditions correspond to normal tissue with a small population of tumor cells in the center of the computational domain.

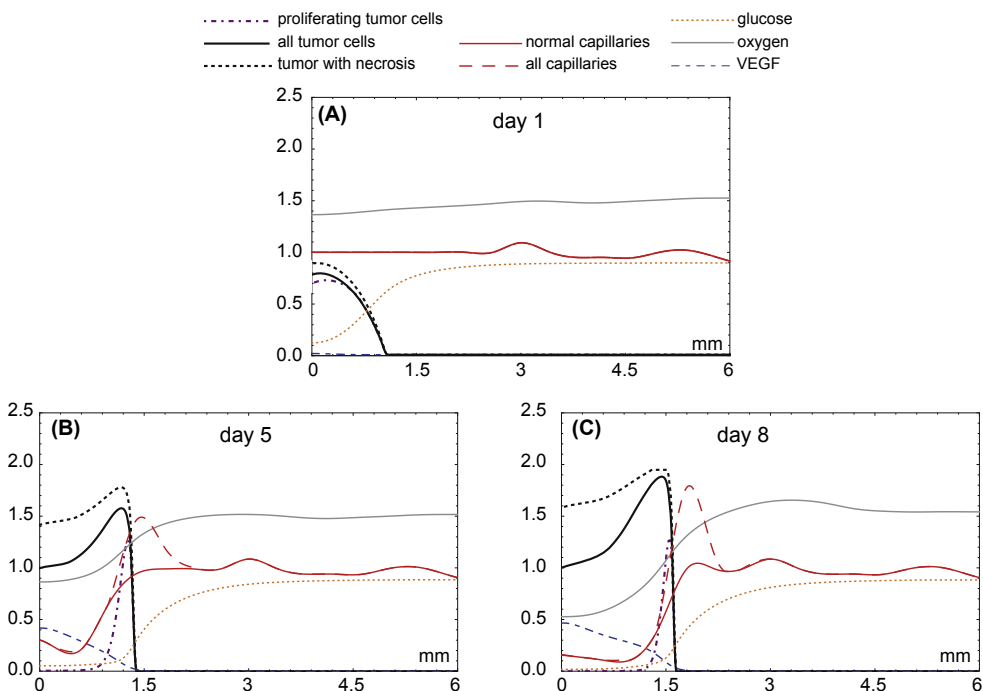


**Figure 8.6**  
Distribution of variables of coupled model of tumor growth in tissue that account for microcirculatory network remodeling, during several days of tumor growth.

Fig. 8.6 demonstrates examples of distributions of model variables during first days of tumor growth. It is seen that the resulting model is able to adequately reproduce known physiological features at the beginning of tumor growth. Capillaries degrade inside the tumor core, leading to reduction in inflow of nutrients and subsequent formation of necrosis, while proliferating tumor cells are located at the tumor rim. Angiogenic capillaries are formed mainly in the peritumoral region, providing an increased supply of metabolites in this area, noticed by a slight increase in oxygen concentration there.

Unfortunately, the practical implementation of the presented model meets restrictions, already discussed in Section 8.4.1, i.e., enormous computational costs. Utilizing such approach for the investigation of tumor growth larger than 1 cm in diameter obviously requires utilization of a supercomputer. Obtaining qualitative physiologically meaningful results requires a considerable variation of model parameters. This also increases the computational burden.

## Conclusions

In this study, a novel modeling approach was presented, which allows to generate microcirculatory networks, possessing similar geometric and functional characteristics to the ones of a real microcirculatory network. In program implementation of the method, the generation of the network structure obeys a number of requirements. One requirement is matching the distributions of microvessels' lengths and diameters obtained in experimental work on the microcirculatory network of breast cancer [339]. Blood flow calculations in the generated microcirculatory networks are based on the Poiseuille law with nonlinear conductivity term and the law of mass conservation. The adequacy of the model prediction, i.e., the ability of the generated microcirculatory network to virtually supply all cells in tissue with key metabolites, was checked by statistical analyses. This analysis confirmed the space-uniformity of distributions of capillaries surface area and blood flow in capillaries emanating from the arterioles. The homogeneous surface area distribution is crucial for glucose and most other nutrients supply, while the uniform blood flow is important for oxygen delivery. The investigations of the model showed that, as the number of microvessels in the network increases, the total blood flow at first increases and then approaches the saturation threshold, what is in a good agreement with common physiological sense. This implies that increase in oxygen supply is always less than corresponding increase in microvascular density, which should be accounted for in experiments. This result served as the basis for the introduction of a new physiologically motivated term of oxygen inflow in the model of tumor growth. We may conclude that the oxygen supply is flow limited rather than diffusion limited, overcoming a common fallacy in the models of tumor growth (see, e.g., Refs. [400,401]). This already led to a separate fruitful investigation [380], the results of which are mentioned further. An attempt for complete coupling of microvasculature and tumor models was performed and resulted in a working and physiologically adequate prototype. However, its further development is constrained by serious computational limitations.

A significant result obtained here is the model prediction that the normalization of structure of tumor microvessels and the concomitant decrease in tumor-associated edema as a result of antiangiogenic therapy should lead to less than twofold local increase in tumor perfusion within the range of standard observed values of tumor interstitial pressure before therapeutic intervention. This result agrees well with the experimental data [386,503]. It should be emphasized that the experimental measurements, made together with the measurements of tumor perfusion in the work [503], indicate a simultaneous almost fourfold increase in the oxygen pressure within the tumor, whereas two- to threefold growths in intratumoral oxygen pressure in different corresponding experiments have been reported in work [383]. These facts lead to doubts that an increase in tumor blood flow is the only—or even the main—cause for transient alleviation of tumor

hypoxia. In the work [380], it was demonstrated that this phenomenon may also result from changes in tumor metabolism and in the rates of inflow of key nutrients in the tissue, caused by the therapy. Thus, the results of the present study support this hypothesis.

Of course, the real tumor angiogenic capillary network differs from the simulated one in that it does not constitute a tree structure, since the sprouting angiogenic capillaries connect with each other and with the existing capillaries rather chaotically; moreover, tumor angiogenesis results in a large number of blind ends of capillaries. Nevertheless, preliminary estimates show that deviations from the tree structure (i.e., adding bridges of capillaries) do not affect the obtained result, and further research is planned in this direction.

# ***Computational hemodynamics in vascular surgery***

## ***9.1 Introduction***

In this chapter, we address several clinical applications of regional patient-specific hemodynamic models. Clinical practice imposes rather demanding requirements on a mathematical model and numerical methods used for predictive simulations. An ideal model must take into account all patients' data available in routinely clinical diagnosis and may not require additional costly or time-consuming measurements. The model should minimize the number of parameters to be identified, and the remaining parameters should have clear physiological meaning. It should be feasible to run simulations in a conventional clinical environment, which means only a few minutes or even seconds of simulation time on a personal computer or a workstation. The model should produce a result demanded by clinicians, which often comes down to one or few statistics related to several scenarios of an endovascular intervention.

The one-dimensional hemodynamic model of regional blood circulation introduced in Chapter 7 meets these requirements to a large extent. Although the considered clinical applications address different regional vasculatures, including leg arteries [242,253], coronary arteries [17,260,264,320,402–406], and cerebral arteries [281,314,407,408], the corresponding regional hemodynamic models have many common features: they are based on the same methods of 3D image segmentation, they account for autoregulation, they are not closed and use inlet boundary condition from the heart or the aorta, they use aggregated or virtual venous system, and they use the same method of parameters identification and microcirculation resistance.

## ***9.2 Identification of parameters***

Clinical applications of hemodynamic models require personalized simulations. The geometry of the vascular bed can be recovered by methods discussed in Chapter 3. Apart from the geometry, hemodynamic models operate with other functional parameters that have to be patient specific such as stroke volume, peripheral resistance, and vessel wall stiffness. For some applications, systolic/diastolic pressure and flow rate waveforms (if available) may help to fit better the model to the patient circulation. General information

such as height, weight, age, smoking status, and clinical records can be accounted in model parameters as well.

The stroke volume is the integral of flow rate at the entrance to the aorta within one cardiac cycle. If known, the flow rate profile can be used in patient-specific simulations. Usually, such information is not available in a clinic due to the extreme precision required by such measurement. By default, the averaged physiological flow rate profile  $Q_{heart}(t)$  (Fig. 9.1) is scaled in accordance with the measured stroke volume and the heart rate. For any patient, the heart rate at rest is available, and the argument  $t$  of function  $Q_{heart}(t)$  can be scaled to match the cardiac cycle. The magnitude of the stroke volume can also be adjusted by multiplying the function  $Q_{heart}(t)$  by a weight factor:  $\alpha_{in}Q_{heart}(t)$ . The value  $\alpha_{in} = 1$  corresponds to a stroke volume of 62 mL. In the absence of data on the stroke volume,  $\alpha_{in}$  is selected to fit the simulated and measured blood flow rates at the points close to the aortic arch. By default, the central venous pressure  $p_v$  is assumed to be equal to 8 mm Hg. This value can be changed to patient's pressure if available.

For each terminal artery, it is necessary to select the hydraulic resistance  $R$  of the regional microcirculation. The initial values of  $R$  are chosen so that the simulated velocities and pressures correspond to the physiological norm [239,240]. For instance, for brachiocephalic arteries (Fig. 9.2), the following resistances result in blood flow rates close to physiological flow rates: for the aortic arch passing into the thoracic aorta  $R = 250 \text{ dyn s/cm}^5$ , for the subclavian arteries (LSA and RSA)  $R = 4 \text{ kdyn s/cm}^5$ , for the

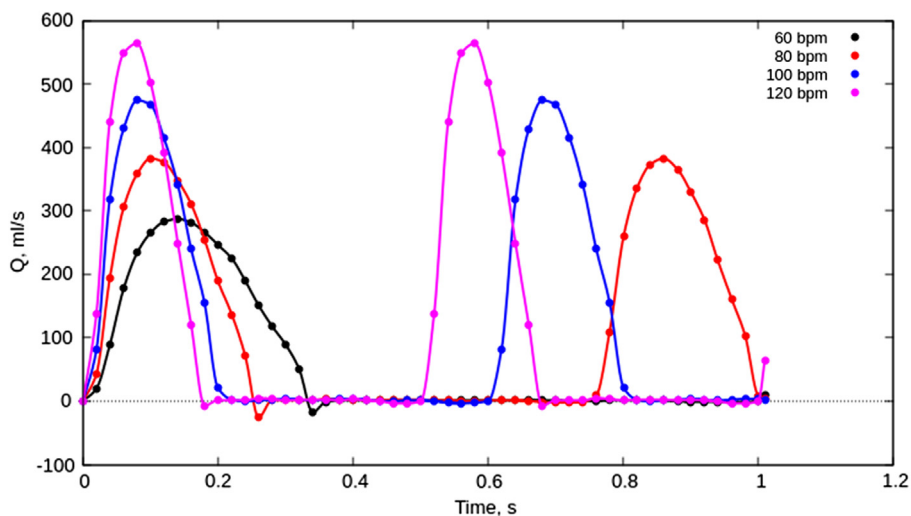


**Figure 9.1**

Scaling of the heart outflow condition. Four curves correspond to different heart rates and to the same stroke volume 62 mL: 60 bpm (beats per minute) (black), 80 bpm (red [dark gray in print version]), 100 bpm (blue [gray in print version]), and 120 bpm (pink [light gray in print version]).

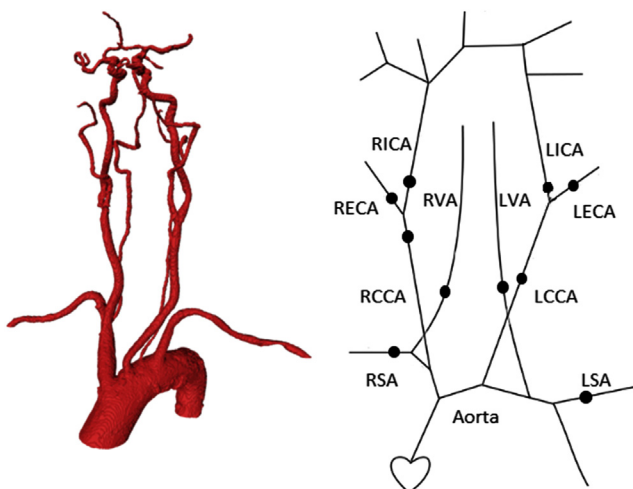


**Figure 9.2**

3D and 1D structures of the vasculature. Points indicate positions of ultrasound measurements of blood flow velocity. The designations: right (R), left (L), carotid artery (CA), common carotid artery (CCA), internal carotid artery (ICA), external carotid artery (ECA), vertebral artery (VA), subclavian artery (SA).

external carotid arteries (left external carotid artery and posterior external carotid artery)  $R = 40 \text{ kdyn s/cm}^5$ , and for remaining terminal arteries  $R = 400 \text{ kdyn s/cm}^5$ .

When modeling the blood flow of a particular patient, the resistances need to be changed to fit the measured blood flow velocity. For instance, in case of brachiocephalic arteries, the measurement points are shown in the right picture of Fig. 9.2. With a significant deviation (more than 20%) of the measured velocity from the calculated one, the resistance of microvasculature lying downstream of the measurement site has to be corrected as follows: in the case of overestimated velocities,  $R$  should be increased and vice versa. The increment should not exceed 10% of the original resistance value  $R$ . Larger deviations may be out of physiological range. If the velocities do not match at several points of measurement, the resistance should be modified first in the terminal vessels located closer to the aortic arch. In all considered cases, such procedure allows to achieve deviation of measured velocities from calculated ones with the error less than 20%. To fit the model better, one needs to adjust wall elasticity (stiffness) parameters.

The vessel wall stiffness can be interpreted as the velocity of small disturbance propagation  $c_k$  (pulse wave propagation) along the vessel  $k$  under zero transmural pressure (7.47). Higher velocity corresponds to a relatively stiff wall, and lower velocity indicates more flexible and compliant wall. The pulse wave velocity is related to vessel compliance [409] and elastic modulus [410]. This velocity can be measured in arteries directly [411,412]; however, necessary equipment may not be available in a hospital and, moreover, the measurement gives only averaged characteristics for the whole body.

On the other hand, the pulse wave velocity in different arteries is available in the literature [413,414]. These data can be adapted to physiological status and lifestyle conditions of the patient. Such approach gives a good initial approximation of the pulse wave velocity if we are given basic characteristics of the patient and his or her clinical record. Further refinement of the parameter  $c_k$  for each individual vessel is possible if ultrasound measurement is available in it: if the simulated velocity deviates from the measured one by more than 5%, then  $c_k$  in the selected vessel  $k$  is adjusted, whereas in the neighboring vessels, the parameter is adjusted only partly (one half of the adjustment). Pulse wave velocities may vary considerably from one vessel to another one, so the adjustment may change the velocity up to 50% of the initial value, which is within the range of  $c_k$  variability as shown in the following.

Morphological changes due to aging result in vessel stiffness changes: arteries become less compliant and more stiff with age. The simplest formula accounting for this phenomenon is given by:

$$c_0(y) = \begin{cases} c_a, & y < y_a \\ c_a + (y - y_a) \frac{c_b - c_a}{y_b - y_a}, & y_a \leq y \leq y_b \\ c_b, & y > y_b \end{cases} \quad (9.1)$$

where  $y$  is the age of a patient and  $c_a$  and  $c_b$  are the pulse wave velocity for a young man ( $y_a = 20$  years) and an old man ( $y_b = 80$  years), respectively. Clinical studies [415,416] provide the parameters  $c_a = 500$  cm/s and  $c_b = 650$  cm/s.

We note that Eq. (9.1) may need parameter adjustment depending of patient's gender. For instance, according to Fig. 9.3, the left and right coronary arteries of women lose much of flexibility 10 years later than for men (compare groups V and VI).

Apart from age, the pulse wave velocity is affected by other factors, which can be accounted by formula.

$$c = c_0 \alpha_{hyper} \alpha_{smoke} \alpha_{sport}. \quad (9.2)$$

Factor  $\alpha_{hyper}$  introduces dependence on patient's blood pressure [417]. It is set to 1 for the normal systolic pressure  $p_{norm} = 120$  mm Hg and increases linearly to 1.5 for patients with strong hypertension  $p_{hyper} = 220$  mm Hg:

$$\alpha_{hyper} = 1 + \frac{p_{syst} - p_{norm}}{2(p_{hyper} - p_{norm})}, \quad (9.3)$$

where  $p_{syst}$  is patient's systolic pressure.

Factor  $\alpha_{smoke}$  accounts vessel stiffening for smokers [418]. Table 9.1 presents dependence of factor  $\alpha_{smoke}$  on smoking status.

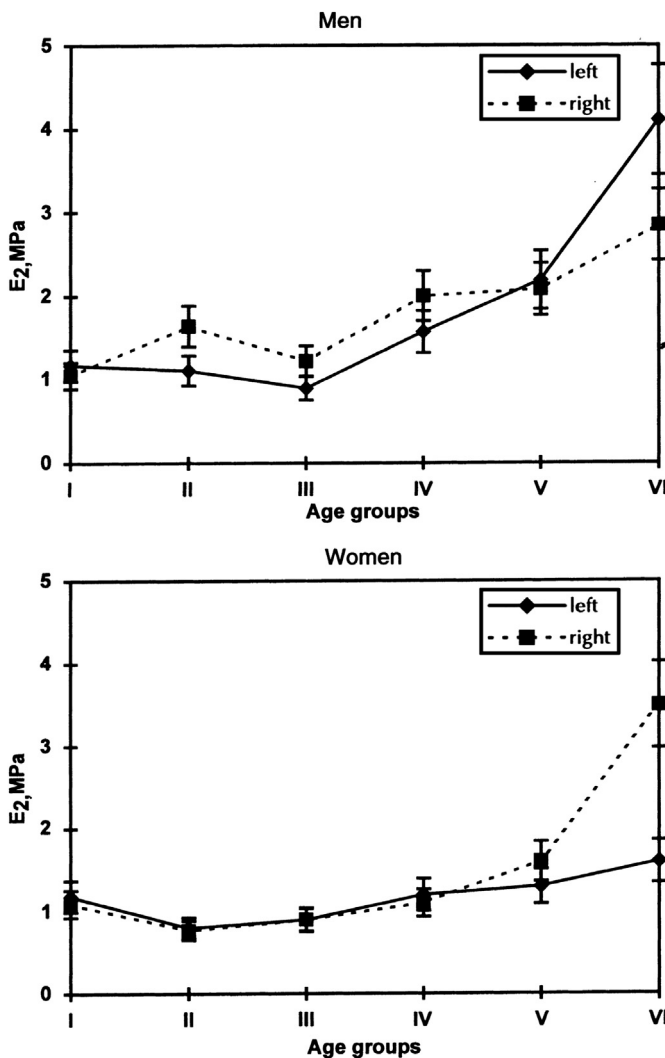


Figure 9.3

Circumferential Young's modulus of left and right coronary arteries for different ages and genders. Age groups: I 0–1 years; II 1–7 years; III 8–19 years; IV 20–39 years; V 40–59 years; VI 60–80 years. *Image from I. Ozolanta, et al., Changes in the mechanical properties, biochemical contents and wall structure of the human coronary arteries with age and sex, Med. Eng. Phys. 20 (7) (1998) 523–533.*

Table 9.1: Factor  $\alpha_{\text{smoke}}$  for smoking status.

	Non-smoker	Modest smoker	Chronical smoker
$\alpha_{\text{smoke}}$	1.0	1.2	1.5

"Modest smoker" means that a person smokes less than 10 years and in average consumes less than 10 cigarettes per day. "Chronical smoker" means that a person smokes more than 10 years and in average consumes more than 20 cigarettes per day.

**Table 9.2: Factor  $\alpha_{sport}$  dependence on athletic status.**

Sport	Nonsportsmen	Long-distance running	Weightlifting	Swimming
$\alpha_{sport}$	1.0	0.6	1.5	0.9

Factor  $\alpha_{sport}$  accounts changes of vessel elasticity for sportsmen [413,416]. Sport activity may both increase and decrease the pulse wave velocity ([Table 9.2](#)).

Various diseases have a significant impact on the elastic properties of blood vessels. They can be taken into account by introducing additional factors in [Eq. \(9.2\)](#). We discuss briefly some factors that can be determined through noninvasive examination of the patient.

Although we are not aware of any studies that address explicitly the dependence of the elastic properties of arteries on body mass index or overweight, a relationship between the volume of pericardial fat and calcification of coronary vessels is statistically proved. Moreover, it is shown in Ref. [419] that the pericardial fat volume correlates with the body mass index. Thus, the body mass index and the volume of pericardial fat volume may be accounted in [Eq. \(9.2\)](#).

The study of the impact of diabetes on the stiffness of the carotid artery and the abdominal aorta [420] showed that in this case the stiffness of the arteries strongly depends on gender. Gender correlates with the elastic properties of all arteries in patients with diabetes. For men, there is no statistical difference between the stiffness of the artery walls for healthy and diabetics. For women with diabetes, the arterial walls are stiffer than for healthy women.

Hyperglycemic patients have stiffer coronary vessels than people without hyperglycemia [421]. In particular, the compliance for people without hyperglycemia is  $(10.6 \pm 4.4) \cdot 10^3 \text{ kPa}^{-1}$  (40–52 years) and  $(7.0 \pm 2.5) \cdot 10^3 \text{ kPa}^{-1}$  (52–75 years); for hyperglycemic people, it is  $(7.9 \pm 5.8) \cdot 10^3 \text{ kPa}^{-1}$  (40–49 years) and  $(7.2 \pm 3.4) \cdot 10^3 \text{ kPa}^{-1}$  (49–75 years). The large variation (over 70%) in the results for hyperglycemic patients may be explained by nondistinguishing between men and women in the hyperglycemic group.

Identification of the functional parameters of the model is performed in several stages. At the first stage, we select the cardiac flow rate profile and the venous pressure, we set the default values for the resistances of microcirculation and define the pulse wave velocities by [Eqs. \(9.1\) and \(9.2\)](#). At the next stage, the resistances are corrected to minimize deviations of the measured and calculated blood flow rates. At the final stage, the pulse wave velocity (vascular stiffness) is adjusted to achieve a better fit between the calculated and measured blood flow rates. This procedure can be made in the black-box manner if a method identifying arteries is given (for the example of such, we refer to Chapter 3).

The described three-stage procedure of parameters identification allows us to achieve an average deviation of 4% of the calculated flow rates from the measured ones. The alternative method of parameters identification [209,422] is based on the Kalman filter, a recursive algorithm that optimizes the system state vector using a number of noisy measurements. In theory, the Kalman filter provides a fully automated selection of parameters. However, in practice, its use is associated with certain difficulties. In case of nonlinear models, the numerical implementation of the algorithm is rather cumbersome, and iterations of parameter sets may not converge. If many model parameters are to be determined, extra computational resources are required, which makes it difficult to run the model on personal computers. Finally, the Kalman filter does not solve the problem of arteries identification, since it requires explicit localization of velocity measurements.

The hemodynamic model is written in terms of time-dependent differential equations, which describe a quasi-periodic solution. Suitable initial conditions can be chosen from a sufficiently large range of physiologically correct values (positivity of the cross section  $S$ , continuity of the velocity  $v$ , etc.). For instance, one can set  $S_k(0, x) = S_k^0, v_k(0, x) = 0$ , where  $S_k^0$  corresponds to the unstressed vessel  $k$  as it can be directly determined from anatomical atlases, morphometric data, MRI data, etc. Any choice of initial conditions requires computation of several cardiac cycles to attain the quasi-periodic state. The number of cycles depends on the number of vessels in the considered network, their size, network topology, and proximity of the initial conditions to the quasi-stationary state. In case of networks consisting of arteries only, one needs five to six cardiac cycles, and addition of venous system increases the number of cycles to 10–12.

### **9.3 Stenting of leg artery**

We start with occlusion treatment in the femoral artery, which was addressed in detail in Ref. [242]. The objective of the application is to predict presurgically changes of regional hemodynamics in thigh vasculature and compare these changes with postsurgical ones. Segmentation and skeletonization of patient-specific MRI data result in the arterial network shown in Fig. 9.4.

The region of the thigh vasculature is distanced from the heart in the following sense: the entry point of the regional network coincides with the beginning of common iliac artery (vessel 1 in Fig. 9.4). The blood flow inlet profile is obtained by the scaling of the heart ejection profile  $Q(t)$  from Fig. 9.1 with coefficient  $\alpha = 0.21$ , which provides the best fit between calculated and measured presurgical velocity maximum in the femoral artery. This value is in a good agreement with the value computed in the model of the global systemic circulation. Moreover, according to Ref. [423], for heart rate 60 beats/min and stroke volume 60 mL, the blood flow through the femoral artery is 635 mL/min; therefore,

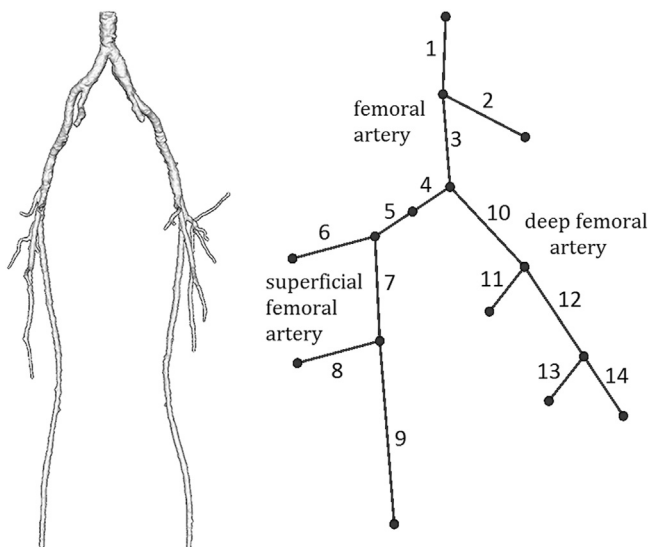


Figure 9.4

The large arteries of two legs and the arterial network of the left thigh. From T. Gamilov, Y. Ivanov, P. Kopylov, S. Simakov, Y. Vassilevski, *Patient specific haemodynamic modeling after occlusion treatment in leg*, *Math. Model. Nat. Phenom.* 9 (6) (2014) 85–97.

Table 9.3: Comparison of calculated and measured systolic blood velocities.

Measurement at	Artery	Maximum velocity (cm/s)			
		Presurgical	Postsurgical	Presurgical	Postsurgical
Index	Index	Patient	Model	Patient	Model
Common femoral	3	148	149	150	155
Superficial femoral proximal	4	48	54	65	70
Occlusion	5	>300	340	—	71
Superficial femoral distal	7	—	67	98	86
Popliteal	9	52	56	72	72
Deep femoral	12	103	93	69	83

Index denotes the vessel index from Fig. 9.4.

From T. Gamilov, Y. Ivanov, P. Kopylov, S. Simakov, Y. Vassilevski, *Patient specific haemodynamic modeling after occlusion treatment in leg*, *Math. Model. Nat. Phenom.* 9 (6) (2014) 85–97.

$$\alpha > \frac{635 \text{ mL/min}}{60 \text{ min}^{-1} \cdot 60 \text{ mL}} \approx \frac{1}{6}, \quad (9.4)$$

which is in a good agreement with  $\alpha = 0.21$  as well. Since the surgery is applied far downstream from the beginning of common iliac artery, we apply the same inlet velocity profile for both presurgical and postsurgical states.

Other parameters are fitted to match the available presurgical Doppler ultrasound measurements at several points of the vasculature located proximal and distal to the occlusion (see the column *presurgical* in Table 9.3). These parameters are assumed to

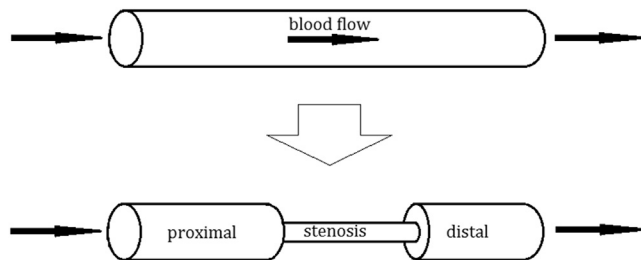


**Figure 9.5**  
Model of stenosis in a 1D vessel.

remain intact after the occlusion treatment. The only exception is vessel 5, which is a fragment of the femoral artery where the occlusion is located. Thus, the diseased artery is split into the stenosed part and healthy proximal and distal parts (Fig. 9.5).

Presurgical parameters of vessel 5 are the modifications of parameters of healthy vessel 4: the hydraulic resistance is increased by factor of 3, the diameter and the artery lumen are decreased by 60% and 84%, respectively (see Section 7.6.1 for this and other options of the stenosis models). Postsurgical parameters of vessel 5 are assumed to coincide with the parameters for the healthy vessel 4. Although vessels with atherosclerotic occlusion are characterized by the increased stiffness, variations of the pulse wave velocity in vessel 5 within a physiologically reasonable range do not influence the computational results essentially.

The column *postsurgical* in Table 9.3 presents the simulated and measured postsurgical velocities. Locations of measurements refer to Fig. 9.4. The flow rates are different before and after the treatment. Both show a reasonably good coincidence between modeled and measured values (the maximum relative error does not exceed 20%). The 20% error in the distal part of the superficial femoral artery is caused by the insufficient MRI resolution. According to general anatomy, the deep femoral artery branch is connected with the popliteal artery providing an alternative pass in the case of femoral artery occlusion. The segmentation of the patient MRI data failed to detect this connection. Introducing the alternative pass decreases the systolic velocity and the error in the deep femoral artery due to the collateral flow. This example demonstrates importance of the correct segmentation of the regional vasculature.

## 9.4 Stenting of coronary arteries and fractional flow reserve

### 9.4.1 Model of coronary hemodynamics

The model of coronary hemodynamics inherits some basic features of other models for regional circulation. However, certain features distinguish it from the others. One difference is the compression of some coronary arteries, veins, and microvasculature by myocardium

during systole (see Section 7.5.3 for details). Furthermore, one may adopt Windkessel models at terminal arteries or generate an artificial venous vasculature to mimic the performance of the coronary veins. In the latter case, in addition to the venous vasculature that mirrors the arterial counterpart, virtual vessels with Poiseuille pressure drop (Eq. (7.18)) are introduced between terminal arteries and terminal veins. The total pressure is assumed to be continuous (Eq. (7.17)) at bifurcations of the arteries and veins, to mimic the microvasculature resistance. Following Ref. [264], we take into account compression of vessels by myocardial tissues during the systole phase by the threefold increase of the virtual vessel resistance  $R$  and the increase of the external pressure  $P_{ext}^{cor}(t)$  (see Section 7.5.3).

Personalization of the model implies fitting the virtual vessel resistances  $R$ , the pulse wave velocities  $c$ , and boundary conditions at the heart. The coronary vessels lie deep inside the human body, so it is not possible to measure the velocity or pressure using inexpensive noninvasive methods. Fitting functional parameters is based on available information about the patient. The patient information is represented by CT scans of his chest area and general characteristics: height, weight, lifestyle, clinical records, etc.

If the patient's cardiac output is known, the averaged flow rate profile at the aorta entrance is corrected. The cardiac output is given to us in the form of the heart rate and, more seldom, in the form of the stroke volume. These two characteristics allow us to choose an appropriate boundary condition by scaling the function  $Q_{heart}(t)$  (see Section 9.2). If no data on cardiac output is available, the default heart rate 60 beats per minute and a stroke volume 62 mL are fitted to patient's age and clinical record. The pressure at the outlet of the vein network by default is taken to be 8 mm Hg. Of course, these values can be changed to known values.

Selecting parameters  $c$  and  $R$  is based on the separation of arteries in two parts: the branches of the right coronary artery (RCA) and the branches of the left coronary artery (LCA). For the aortic arch passing into the thoracic aorta,  $R = 20 \text{ dyn s/cm}^5$ ; for the branches of the right coronary artery,  $R = 7200 \text{ dyn s/cm}^5$ ; and for the branches of the left coronary artery,  $R = 720 \text{ dyn s/cm}^5$ . The coronary arteries have more rigid walls than other vessels, as they are strongly affected by the myocardium. The base value of the stiffness parameter  $c$  is taken to be 1200 cm/s for RCA branches and 950 cm/s for LCA branches in accordance with Ref. [414]. If additional patient information is available, the base value is modified following Eq. (9.2). The artificial network of coronary veins has the identical structure, but the veins have doubled diameters  $d$  and stiffness parameter  $c$  reduced by 20%.

The virtual vessels connecting terminal arteries and veins have the following parameters: length 20 cm, diameter 3 cm,  $c = 300 \text{ cm/s}$ , and resistance  $R = 6 \text{ kdyn s/cm}^5$ . These parameters are chosen to yield the known pressure drop and flow deceleration between arteries and veins.

Typical personalized coronary vasculature shown in Fig. 9.6 has parameters  $l$ ,  $d$ ,  $c$ , and  $R$  presented in Table 9.4.

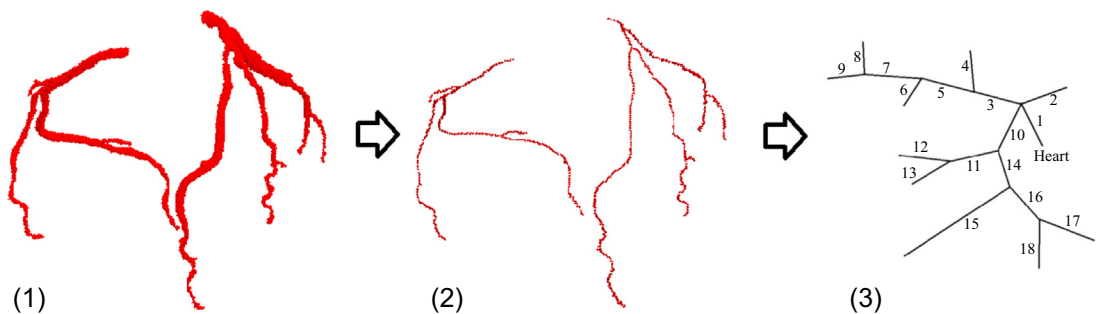


Figure 9.6

Typical coronary vasculature. (1) segmentation of CT image, (2) skeletonization, and (3) 1D network. From S.S. Simakov, T.M. Gamilov, F.Y. Kopylov, Y.V. Vasilevskii, Evaluation of hemodynamic significance of stenosis in multiple involvement of the coronary vessels by mathematical simulation, Bull. Exp. Biol. Med. 162 (1) (2016) 111–114.

**Table 9.4: Default parameters for coronary arteries:**  $k$  is the vessel index according to Fig. 9.6,  $l_k$  (cm) is the length,  $d_k$  (mm) is the diameter,  $c_k$  (cm/s) is the pulse wave velocity, and  $R_k$  ( $\text{dyn s/cm}^5$ ) is the resistance.

$k$	$l_k$	$d_k$	$c_k$	$R_k$	$k$	$l_k$	$d_k$	$c_k$	$R_k$
1	5.28	21.7	1050	20	10	0.59	3.6	950	720
2	60.0	25.1	840	20	11	6.1	3.0	950	720
3	2.72	3.1	1200	7200	12	2.05	1.17	950	720
4	1.44	1.31	1200	7200	13	1.75	1.21	950	720
5	1.40	2.73	1200	7200	14	1.39	3.8	950	720
6	6.75	1.52	1200	7200	15	12.1	2.05	950	720
7	5.01	2.50	1200	7200	16	5.4	1.91	950	720
8	1.27	1.19	1200	7200	17	0.38	1.01	950	720
9	5.65	0.157	1200	7200	18	2.62	1.19	950	720

From Y. Vassilevski, T. Gamilov, P. Kopylov, Personalized computation of fractional flow reserve in case of two consecutive stenoses, in: Proceedings of the VII European Congress on Computational Methods in Applied Sciences and Engineering, ECCOMAS Congress 2016, Crete, Greece, 5–10 June, vol. 1, 2016, pp. 90–97.

#### 9.4.2 Fractional flow reserve

One important clinical task is to estimate the hemodynamic significance of the stenosis as a decision indicator for a surgical treatment. The vascular occlusion factor (VOF, the relative lesion cross-sectional area  $\lambda = (1 - S_{st}S^{-1}) 100\%$  or relative diameter decrease  $\lambda_d = (1 - d_{st}d^{-1}) 100\%$ , where  $S_{st}$ ,  $d_{st}$  are the vascular lumen area and diameter at the narrowest place) has been used as the conventional significance index for decades. The VOF cross section-based value  $\lambda > 75\%$  and the VOF diameter-based value  $\lambda_d > 50\%$  were assumed to be hemodynamically significant [425]. Hemodynamic significance of a stenosis, however, is also affected by collateral flows development, hemostasis, autoregulation, etc. Recently, the fractional flow reserve (FFR) has become the golden

standard for the evaluation of stenosed coronary arteries [426,427]. Clinical decisions based on FFR have reduced the number of expensive high-risk surgical interventions and improved the statistics of incidences caused disability or death [428].

FFR is the ratio between the maximum achievable blood flow in a diseased coronary artery and the theoretical maximum flow in a normal coronary artery. In practice, FFR is computed as the ratio of the mean distal to the stenosis pressure ( $P_{mean,d}$ ) to the mean aortic pressure ( $P_{mean,a}$ ) under maximal hyperemia conditions (see Fig. 2.9):

$$\text{FFR} = P_{mean,d}/P_{mean,a}. \quad (9.5)$$

The hyperemic conditions are achieved using vasodilator (e.g., adenosine or papaverine) administration [428,429]. FFR close to 1.0 is considered as the normal value. FFR values less than 0.75–0.80 are associated with myocardial ischemia and possible need for surgical intervention.

Initially, FFR was measured invasively in clinics through coronary catheterization by a single-use transducer [427]. The procedure is rather expensive. The recent trend is the development of noninvasive methods for personalized estimate  $\text{FFR}_{CT}$  on the basis of personalized mathematical models of the blood flow in atherosclerotic coronary vasculature. Usually, the input of these noninvasive methods consists of CT scans, blood pressure, and heart rate.

Evaluation of FFR using three-dimensional models of coronary blood flow is the most popular approach [430–433] although it raises doubts and criticism of experts [434].

Among the problems of  $\text{FFR}_{CT}$ , we mention the impossibility of setting patient-specific boundary conditions, rigid wall assumption, restrictions to the computational domain, difficulty in selecting and fitting model parameters, and high demands on computing resources, which limit the applicability of models in clinical practice. A remedy for the latter problem can be the use of machine learning tools that compute  $\text{FFR}_{CT}$  within seconds instead of lengthy 3D simulations [435].

1D hemodynamic models offer a feasible alternative for computation of  $\text{FFR}_{CT}$  [17,260,264,312,436]. The associated low computational cost is appealing for clinical use, where the 1D simulations can be performed on-site and faster than the full 3D analog. The 1D approach proposed in Ref. [264] also features user independence since it is fully automated provided a sufficient quality of CT images, as discussed in Ref. [100].

In [Fig. 9.7](#), we compare invasively measured FFR and  $\text{FFR}_{CT}$  computed by HeartFlow software [433] and the 1D hemodynamic model for several dozens of anonymized patient-specific data. Both techniques demonstrate similar quality of FFR estimation. Importantly, false indications for surgery are rare that makes both methodologies appealing in clinics.

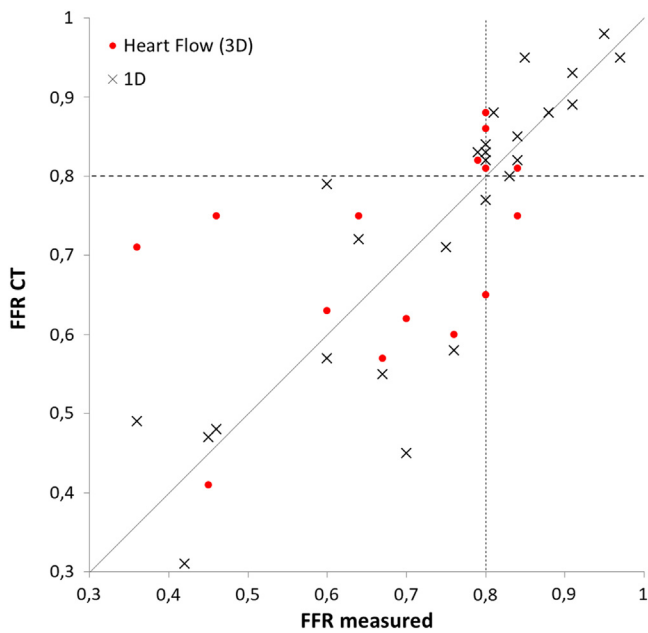


**Figure 9.7**

Comparison of invasively measured FFR and  $\text{FFR}_{CT}$  computed by HeartFlow software and 1D hemodynamic model.

The importance of transition from the use of VOF to estimating FFR can be demonstrated by the following example. Consider the coronary vasculature shown in Fig. 9.6 and assume that the left anterior descending (LAD) artery has a stenosis with  $\lambda$  ranging from 50% to 99%. The diameter  $d$  of the LAD artery may be 2 or 3 mm; both values are anatomically acceptable.

Fig. 9.8 shows  $\text{FFR}_{CT}$  for varying  $\lambda$  and two cases of  $d$ . We observe that the same VOF may give different  $\text{FFR}_{CT}$  for different diameters  $d$ . If one assesses the hemodynamic significance of the stenosis with the help of VOF, stenting should be performed for  $\lambda > 70\%$ . If one assesses the hemodynamic significance of the stenosis basing on  $\text{FFR}_{CT}$ , stenting should be performed for  $\text{FFR}_{CT} < 0,75$ , and the case  $0,75 < \text{FFR}_{CT} < 0,8$  has no clear indication for surgical intervention. These thresholds for  $\lambda$  and  $\text{FFR}_{CT}$  are marked by horizontal and vertical lines in Fig. 9.8. The lines define domains with conflicting indications for stenting. In the case of narrow LAD artery ( $d = 2$  mm), surgical intervention is necessary or possible ( $\text{FFR}_{CT} < 0,8$ ) even if the degree of stenosis is within  $57\% < \lambda < 70\%$  (curve 2 from  $a$  to  $b$ ). Vice versa, in case of thick LAD artery ( $d = 3$  mm), surgical intervention is not required or is likely not required ( $\text{FFR}_{CT} > 0,75$ ) even if the degree of stenosis is in the range of  $70\% < \lambda < 83\%$  (curve 1 from  $b$  to  $c$ ).

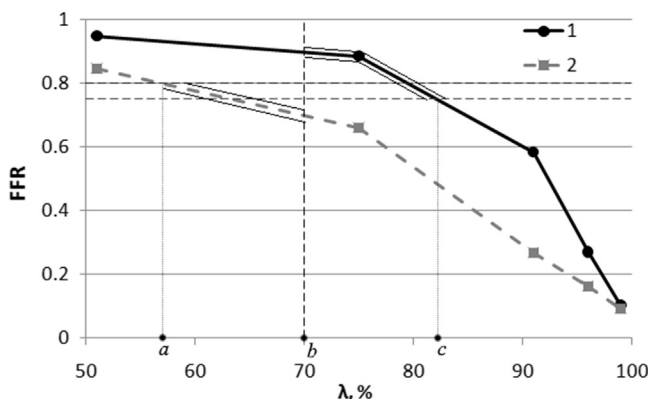


Figure 9.8

Comparison of  $FFR_{CT}$  for stenoses with the same VOF of LAD artery with diameter 2 mm (curve 1) or 3 mm (curve 2). FFR, fractional flow reserve; LAD, left anterior descending; VOF, vascular occlusion factor. From S.S. Simakov, T.M. Gamilov, F.Y. Kopylov, Y.V. Vasilevskii, Evaluation of hemodynamic significance of stenosis in multiple involvement of the coronary vessels by mathematical simulation, Bull. Exp. Biol. Med. 162 (1) (2016) 111–114.

Therefore, VOF is not a reliable indicator for assessing the hemodynamic significance of coronary artery stenosis. The use of this indicator in some cases may lead to both substantial underestimation and substantial overestimation of the hemodynamic significance of stenosis.

The hemodynamic significance of stenoses may vary depending on the physiological state. The common reason of changes in the state is physical activity. Conditions of physical activity are impossible or difficult to reproduce in a clinical examination of a particular patient. However, to some extent, they can be taken into account in numerical simulation. Physical exercise causes intensification of cardiac activity, which is modeled by scaling the heart outflow condition as shown in Ref. [17] (see also Fig. 9.1).

To study the impact of the cardiac output on  $FFR_{CT}$ , we consider two anonymized patient cases with multiple stenoses of coronary arteries. Patient 1 has stenoses in the proximal part (one-third) of the left main coronary artery (LCA-1,  $\lambda = 55\%$ ), the middle one-third of the left circumflex artery (LCX-1,  $\lambda = 80\%$ ), and the middle one-third of the left anterior descending artery (LAD-1,  $\lambda = 50\%$ ). Patient 2 has stenoses in the proximal part (2 mm length) of the right main coronary artery (RCA-2,  $\lambda = 55\%$ ) and the middle one-third (2 cm length) of the left circumflex artery (LAD-2,  $\lambda = 80\%$ ). The stenoses are marked by letters A, B, C, D, and E in Fig. 9.9.

The value of  $FFR_{CT}$  was measured in every case for every stenosis. The computational 1D network of coronary vessels and functional parameters (stiffness and resistance) was personalized using the techniques from Sections 3.4.2 and 9.2, respectively, and  $FFR_{CT}$  was computed for every stenosis with acceptable errors. For details, we refer to Ref. [264].

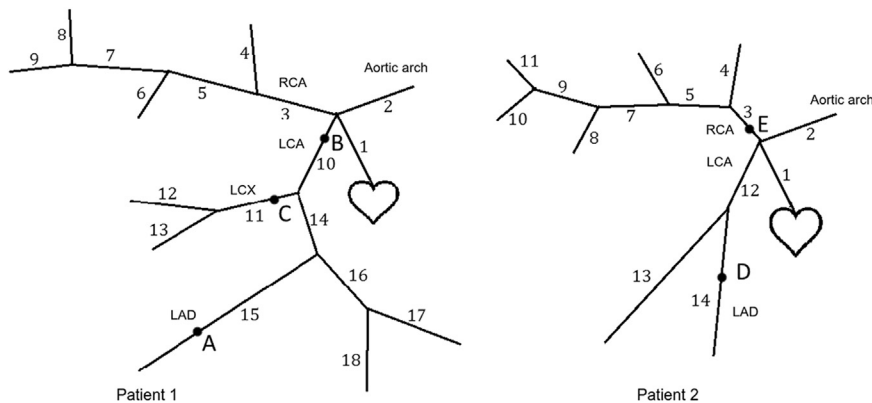


Figure 9.9

1D arterial networks for two patients. A, B, C, D, and E are labels of stenoses.

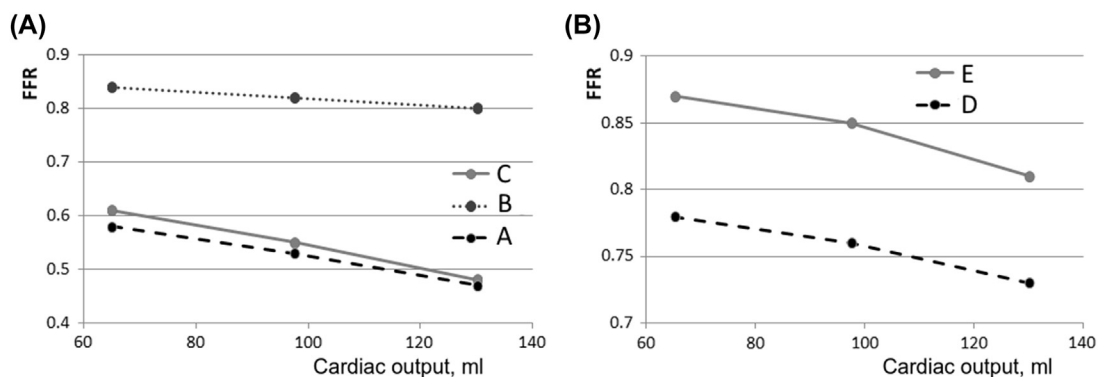


Figure 9.10

FFR<sub>CT</sub> for different stroke volumes. Patient 1, plot (A); patient 2, plot (B). Labels of stenoses are shown in Fig. 9.9.

First, we fix the heart rate to 60 bpm and vary the stroke volume (65, 97.5, and 135 mL) by scaling the heart outflow function  $\alpha_{in}Q_{heart}(t)$ . The values of FFR<sub>CT</sub> are presented in Fig. 9.10.

Alternatively, we fix the stroke volume to 65 mL and vary the heart rate (see Fig. 9.1). The values of FFR<sub>CT</sub> for stenosis D are shown in Fig. 9.11 for different values of VOF.

The results show that, with the increase of cardiac output, the FFR<sub>CT</sub> values decrease. As a result, hemodynamically insignificant stenoses at rest may fall during exercise in the category of hemodynamically significant. This observation is especially important in the case of diagnosing stenosis for athletes and physically active people.

The pulse wave propagation velocity  $c$  from Eqs. (9.2) and (7.47) and the autoregulation parameter  $\gamma$  from Eq. (7.52) affect FFR<sub>CT</sub> since elastic properties of coronary arteries

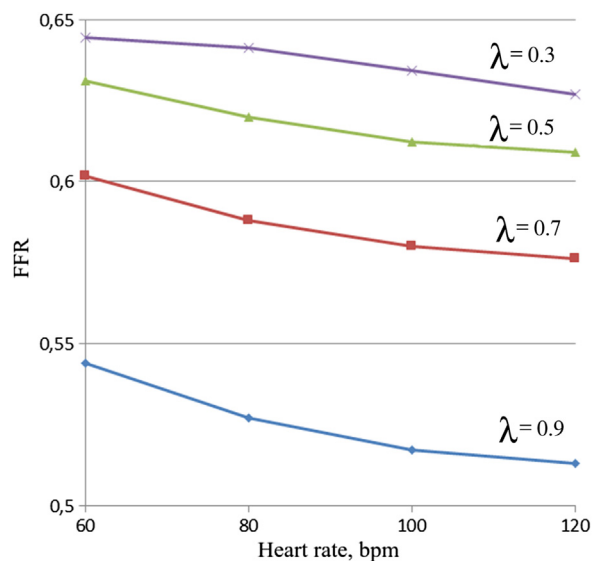


Figure 9.11

$\text{FFR}_{\text{CT}}$  for different heart rates and VOF of stenosis D in Fig. 9.9.

control the degree of vessel compliance. The value of  $c$  varies in a wide range depending on age, training status, etc. Sensitivity of  $\text{FFR}_{\text{CT}}$  to vessel wall elasticity indicates the accuracy for identification of  $c$ , which is sufficient for computation of  $\text{FFR}_{\text{CT}}$ .

We return to patient 1 (Fig. 9.9) with three stenoses. First, we vary values of  $c$  multiplying them by factor  $\varepsilon \in [0.4; 2.0]$ . The choice  $\varepsilon < 1$  increases the compliance; the choice  $\varepsilon > 1$  corresponds to a higher stiffness. The left part of Fig. 9.12 demonstrates the computed  $\text{FFR}_{\text{CT}}$  for the patient-specific stenoses A ( $\lambda = 55\%$ ), B ( $\lambda = 80\%$ ), and C ( $\lambda = 50\%$ ), whereas the right part shows  $\text{FFR}_{\text{CT}}$  for the increased degree of stenosis A (VOF 95%). The reason for the latter increase is twofold: we wanted to cover a wider range of stenoses

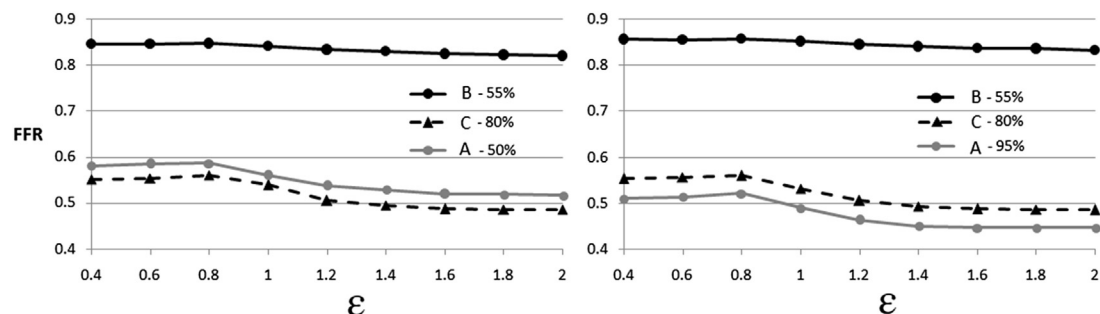


Figure 9.12

$\text{FFR}_{\text{CT}}$  for stenoses A, B, and C of patient 1 for different pulse wave velocities  $\varepsilon c_k$ . Left: patient-specific stenoses, right: stenosis A is increased to  $\lambda = 95\%$ .

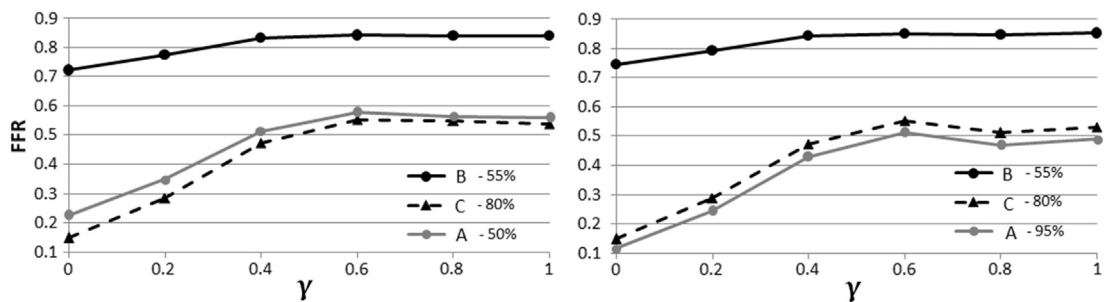


Figure 9.13

FFR<sub>CT</sub> for stenoses A, B, and C of patient 1 for different degrees of autoregulation depending on autoregulation parameter  $\gamma$ . Left: patient-specific stenoses, right: stenosis A is increased to  $\lambda = 95\%$ .

and to show the impact of stenosis A on stenoses B and C. The increase in vessel stiffness makes the stenoses more significant hemodynamically, although the impact is not considerable: 50% variations of  $c$  produce  $\sim 5\%$  variations of FFR<sub>CT</sub>. This implies that one can roughly assess the pulse wave velocity by assigning the patient to a group from a predefined population cohort.

Fig. 9.13 shows the sensitivity of FFR<sub>CT</sub> to the degree of autoregulation. We fix  $c_k$  in each vessel of patient 1 and vary autoregulation parameter  $\gamma$  (7.52) from 0 (no autoregulation) to 1 (normal autoregulation). It is clear that patients with impaired autoregulation may exhibit a distorted FFR<sub>CT</sub> value.

The value of FFR is a good measure of hemodynamic significance of an isolated stenosis. In the above examples, we considered all stenoses as isolated and used the FFR definition (9.5). In case of a multivessel stenotic lesion of the coronary bed, stenoses may be arranged in a chain and thus influence each other (see Fig. 9.14). In this case, an estimation of hemodynamic significance of each stenosis should be done on the basis of virtual stenting and comparison of presurgical and postsurgical flow rates.

For two consecutive stenoses A and B, however, one can derive an analog [437] of Eq. (9.5):

$$\text{FFR}_A = \frac{P_d - (P_m/P_a)P_v}{P_a - P_m + P_d - P_v}, \quad \text{FFR}_B = 1 - \frac{(P_a - P_v)(P_m - P_d)}{P_a(P_m - P_v)}, \quad (9.6)$$

where  $P_a, P_d, P_m, P_v$  are mean pressures at locations shown in Fig. 9.15. These formulas allow us to evaluate the individual hemodynamic significance of each of the stenoses, as if there was no the other stenosis.

We analyze Eq. (9.6) for the case of two consecutive stenoses in the anterior descending artery marked by index 15 in Fig. 9.6. The parameters of the coronary network are given in Table 9.4. The degree  $\lambda_A$  of stenosis A is 96%. The degree  $\lambda_B$  of stenosis B varies in



**Figure 9.14**  
CT angiography of multistenotic lesion of the coronary bed.

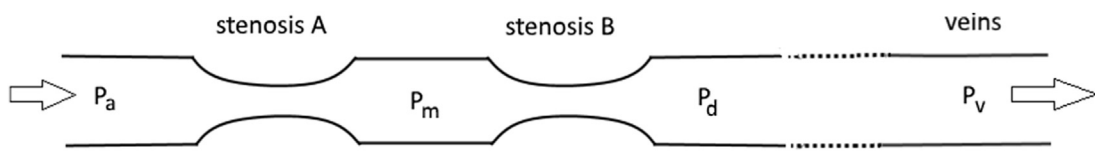


**Figure 9.15**  
Notations for FFR definition in case of two consecutive stenoses.

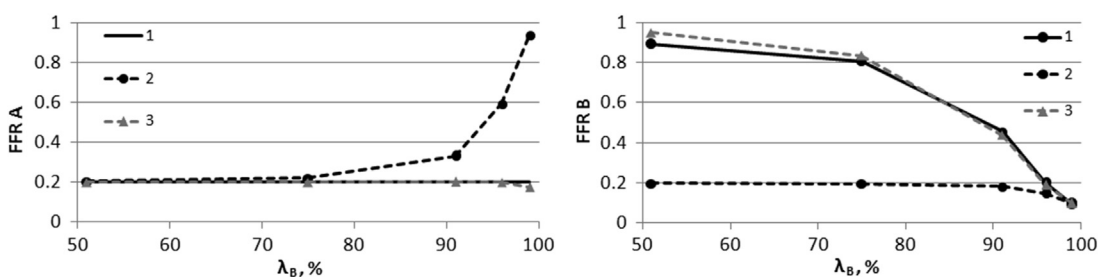


**Figure 9.16**  
FFR<sub>CT</sub> values for each of two consecutive stenoses computed by Eqs. (9.5) and (9.6) under varying  $\lambda_B$ . FFR<sub>CT,A</sub> is shown on the left: 1—FFR<sub>CT,A</sub> for  $\lambda_B = 0\%$ , 2—FFR<sub>CT,A</sub> is computed by Eq. (9.5), 3—FFR<sub>CT,A</sub> is computed by Eq. (9.6); FFR<sub>CT,B</sub> is shown on the right: 1—FFR<sub>CT,B</sub> for  $\lambda_A = 0\%$ , 2—FFR<sub>CT,B</sub> is computed by Eq. (9.5), 3—FFR<sub>CT,B</sub> is computed by Eq. (9.6).

the range from 50% to 99%. The values of FFR<sub>CT,A</sub> and FFR<sub>CT,B</sub> calculated using Eqs. (9.5) and (9.6), and using Eq. (9.5) for the case when only one of the stenoses A or B is present, are shown in Fig. 9.16. FFR<sub>CT</sub> values calculated by Eq. (9.6) for both stenoses almost coincide with FFR<sub>CT</sub> values calculated by Eq. (9.5) when other stenosis is

removed. Thus, Eq. (9.6) allows us to evaluate the hemodynamic significance of each stenosis separately, even in the case of a multivessel stenotic lesion. Moreover, using Eq. (9.5) in configuration shown in Fig. 9.15 may give incorrect FFR values. The left plot in Fig. 9.16 demonstrates that using Eq. (9.5) results in hemodynamic insignificance of stenosis A with an increase of  $\lambda_B$ , since the difference between  $P_a$  and  $P_m$  becomes smaller. The right plot in Fig. 9.16 indicates hemodynamics significance of stenosis B even for small values of  $\lambda_B$ , due to the significant pressure drop at stenosis A, which is not taken into account by Eq. (9.5) in configuration of Fig. 9.15.

## 9.5 Stenting of cerebral arteries

The hemodynamic model of cerebral vasculature inherits the basic features of the coronary flow model with a few exceptions. It postulates the total pressure continuity at vessels junctions, aggregates the venous network, sets different boundary conditions at microcirculation regions, and does not account for systolic contractions of the vasculature by the myocardium. The total pressure continuity (Eq. (7.17)) is posed at vessels junctions since the cerebral arteries are lengthy ( $d_k / L_k \leq 1$ ) and feature laminar blood flows. At the outlet of a terminal cerebral artery with index  $k$ , we set the following boundary condition:

$$R_k Q_k = p_k - p_v, \quad (9.7)$$

where  $p_v = 8$  mm Hg is the central venous pressure (common to all veins),  $p_k = p_k(S_k)$  is the pressure at the outlet of the terminal artery,  $Q_k = S_k v_k$  is the flow rate through the terminal artery, and  $R_k$  is the resistance of a microcirculation region neighboring to the  $k$ -th vessel. To be more precise,  $R_k$  represents resistance of the patch of the microvasculature and a part of the venous system draining the patch.

The reason for the aggregation of veins into a lumped structure instead of their reconstruction or mirroring the arterial network is twofold: (1) the cerebral veins are not seen well under conventional 3D image modalities, and the structure of the venous network deviates considerably from that of the arterial network; (2) brachiocephalic venous system contains a large number of lengthy vessels, and model reduction (9.7) allows us to halve the simulation time and avoid selection of the length, diameter, and elasticity of the virtual vessels.

Of course, for a complete representation of the patient-specific cerebral blood flow, the structure of the venous network must be taken into account (refer, for instance, to Ref. [252]). Such detailization gives a chance to assess risks of many diseases and malformations. However, generation of the patient-specific venous structure would increase the cost of diagnosis and restrict the applicability of our approach to technologically advanced hospitals only. That is why we address cerebral hemodynamics only in arteries and, moreover, only in large arteries.

The boundary condition (9.7) is incorporated into the numerical scheme through the iterative process:

1. Set terminal pressure  $p_k$  to the terminal pressure from the previous time step.
2. Compute the flow rate  $Q_k$  using Eq. (9.7).
3. Compute the cross-sectional area  $S_k$  from  $Q_k = S_k v_k$  and the compatibility condition (7.37).
4. Using the wall state Eq. (7.44), compute  $p_k^{new} = p(S_k)$ .
5. If  $|p_k - p_k^{new}| > 0.01p_k$ , set  $p_k = p_k^{new}$  and go to step 2.

The iterative process needs black-box functions  $p_k(S_k)$ ,  $\frac{\partial p_k}{\partial S_k}(S_k)$ , which return the pressure and its derivative for given  $S_k$ .

In the current clinical practice, hemodynamic significance of stenosis in a cerebral artery is the VOF determined from angiography or CT scans. This parameter is fairly simple to estimate but is rather rough as was demonstrated in the previous section. In case of coronary arteries, the good index of stenosis significance is the FFR (Eq. (9.5)). In the neck and head arteries, this parameter works poorly for two reasons. The first reason is a large number of regulatory mechanisms that maintain the pressure in the cerebral arteries at a constant level as stated in Ref. [240]. The second reason is the presence of a large number of collateral arteries (see, e.g., Fig. 9.2). Moreover, the *a priori* assessment of the hemodynamic significance of a stenosis is very difficult in the case of multistenotic vasculature. Any index for a stenosis is affected by the presence of other stenoses. The most adequate approach in this case is the personalized numerical simulation, which provides an estimate for various surgical intervention strategies without a risk to the patient. We illustrate such strategy by the following study [314].

Endovascular interventions (carotid endarterectomy or stenting) in carotid arteries affect the blood flow and may cause perioperative strokes. Personalized evaluation of cerebral hemodynamics is the most promising method for the prognosis of such complications. We analyzed presurgically hemodynamic changes in extracranial parts of brachiocephalic arteries due to the carotid endarterectomy. For the study, seven patients were randomly selected from a large set of patients with carotid stenosis. Two patients were excluded from the study as changes in their heart function had a significant impact on cerebral hemodynamics. Data of remaining five anonymized patients (two men and three women of age from 61 to 82 years old) were used for the numerical simulations. Doppler ultrasound measurement of blood flow rates at several points (see Fig. 9.2) before and after surgery was performed in each patient. Arterial networks (Fig. 9.17) were recovered from the contrast-enhanced CT data, and identification of the model functional parameters was performed. The fitted parameters for patient 1 are shown in Table 9.5.

Presurgical blood flow rates measured in each patient in different locations are presented in Tables 9.6 and 9.7. The notations of the arteries are introduced in Fig. 9.2: right (R),

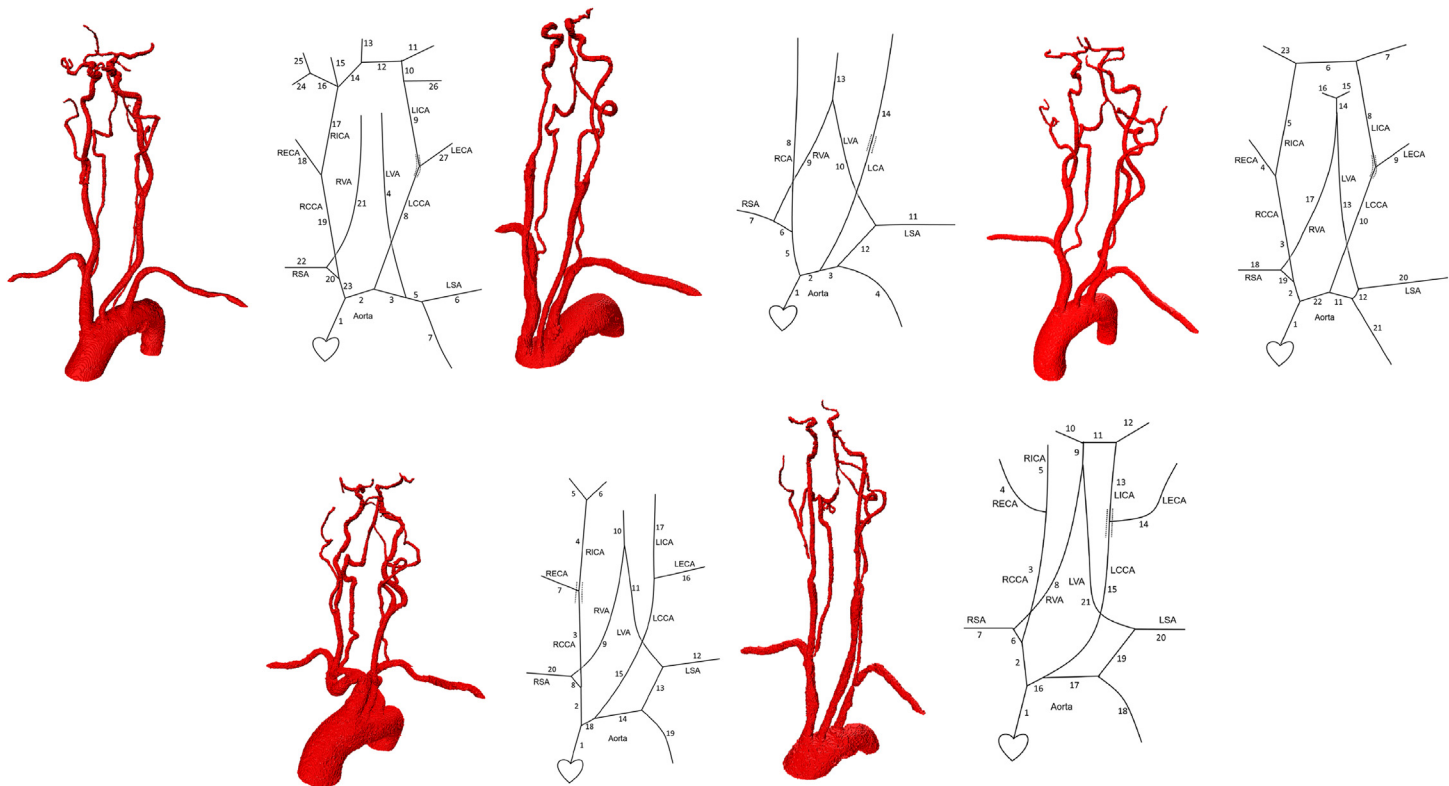


**Figure 9.17**

Networks of cerebral arteries of five patients with carotid stenosis. Dotted lines indicate stenosis. From D.V. Burenchev, K.F. Yu, A.A. Bykova, et al., Mathematical modelling of circulation in extracranial brachiocephalic arteries at pre-operation stage in carotid endarterectomy, Russ. J. Cardiol. 144 (4) (2017) 88–92.

**Table 9.5: Functional parameters for patient 1:  $k$  is the vessel index,  $l$  is the length,  $d$  is the diameter,  $c$  is the stiffness, and  $R$  (kdyn s/cm<sup>5</sup>) is the resistance for terminal arteries in Eq. (9.7).**

$k$	$l, \text{ cm}$	$d, \text{ cm}$	$c, \text{ cm/s}$	$R$	$k$	$l, \text{ cm}$	$d, \text{ cm}$	$c, \text{ cm/s}$	$R$
1	0.83	3.29	600		15	3.72	0.20	600	400
2	1.99	3.15	600		16	1.72	0.26	600	
3	1.31	2.84	600		17	16.3	0.46	600	
4	26.4	0.28	600	400	18	12.3	0.27	600	40
5	0.16	2.82	600		19	10.8	0.69	300	
6	15.6	0.60	600	4	20	1.25	0.92	600	
7	7.03	2.45	600	0.24	21	27.0	0.28	600	400
8	14.7	0.74	600		22	11.0	0.54	600	4.4
9	16.2	0.50	600		23	5.28	1.68	600	
10	0.41	0.32	600		24	0.46	0.17	600	400
11	4.82	0.27	600	400	25	5.34	0.21	600	400
12	1.96	0.20	600		26	3.86	0.19	600	400
13	2.79	0.17	600	400	27	12.2	0.27	600	40
14	1.79	0.19	600						

**Table 9.6: Presurgical blood velocities in nonstenosed cerebral arteries.**

Artery	Velocity (mean $\pm$ deviation), cm/s	#Patients
RCCA	51 $\pm$ 6	5
LCCA	31 $\pm$ 5	5
RICA	60 $\pm$ 5	4
LICA	60 $\pm$ 2	2
RECA	47 $\pm$ 5	3
LECA	54 $\pm$ 14	4
RVA	36 $\pm$ 1	3
LVA	32 $\pm$ 9	3
RSA	74 $\pm$ 15	3
LSA	68 $\pm$ 19	3

#Patients denotes the number of patients with measurements in the artery without stenosis. LCCA, left common carotid artery; LECA, left external carotid artery; LICA, left internal carotid artery; LSA, left subclavian artery; LVA, left vertebral artery; RCCA, right common carotid artery; RECA, right external carotid artery; RICA, right internal carotid artery; RSA, right subclavian artery; RVA, right vertebral artery.

From D.V. Burenchev, K.F. Yu, A.A. Bykova, et al., Mathematical modelling of circulation in extracranial brachiocephalic arteries at pre-operation stage in carotid endarterectomy, Russ. J. Cardiol. 144 (4) (2017) 88–92.

**Table 9.7: Characteristics of stenoses and presurgical blood flow velocities there.**

Patient	Localization	Velocity, cm/s	Occlusion factor, %	Length, cm
1	RCCA–RICA	152	80	4
2	LCCA–LICA	159	72	4
3	LICA	156	75	2
4	RCCA–RICA	155	75	3
5	RCCA–RICA	302	92	4

LCCA, left common carotid artery; LICA, left internal carotid artery; RCCA, right common carotid artery; RICA, right internal carotid artery.

From D.V. Burenchev, K.F. Yu, A.A. Bykova, et al., Mathematical modelling of circulation in extracranial brachiocephalic arteries at pre-operation stage in carotid endarterectomy, Russ. J. Cardiol. 144 (4) (2017) 88–92.

**Table 9.8: Postsurgical blood velocities.**

Artery	Velocity (mean $\pm$ deviation), cm/s	#Patients
RCCA	50 $\pm$ 4	5
LCCA	53 $\pm$ 2	5
RICA	59 $\pm$ 6	5
LICA	59 $\pm$ 3	5
RECA	47 $\pm$ 1	4
LECA	53 $\pm$ 10	5
RVA	32 $\pm$ 2	4
LVA	33 $\pm$ 10	4
RSA	75 $\pm$ 8	5
LSA	71 $\pm$ 19	5

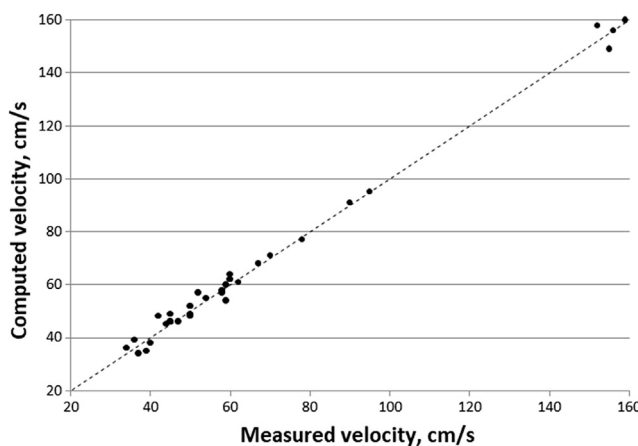
#Patients denotes the number of patients with measurements in the artery; *LCCA*, left common carotid artery; *LECA*, left external carotid artery; *LICA*, left internal carotid artery; *LSA*, left subclavian artery; *LVA*, left vertebral artery; *RCCA*, right common carotid artery; *RECA*, right external carotid artery; *RICA*, right internal carotid artery; *RSA*, right subclavian artery; *RVA*, right vertebral artery.

From D.V. Burenchev, K.F. Yu, A.A. Bykova, et al., Mathematical modelling of circulation in extracranial brachiocephalic arteries at pre-operation stage in carotid endarterectomy, Russ. J. Cardiol. 144 (4) (2017) 88–92.

left (L), carotid artery (CA), common carotid artery (CCA), internal carotid artery (ICA), external carotid artery (ECA), vertebral artery (VA), and subclavian artery (SA).

Characteristics of stenoses are presented in Table 9.7. Stenosis is modeled as a separate vessel with a given length and reduced diameter, as shown in Fig. 9.5. These data were used to develop the patient-specific regional hemodynamic models.

Table 9.8 collects postsurgical flow velocities measured after the treatment. These values are used for the comparison with the prediction of the mathematical model. Fig. 9.18 compares the calculated blood velocities with those measured before the surgical

**Figure 9.18**

Comparison of measured and calculated blood velocities before the surgical treatment. From D.V. Burenchev, K.F. Yu, A.A. Bykova, et al., Mathematical modelling of circulation in extracranial brachiocephalic arteries at pre-operation stage in carotid endarterectomy, Russ. J. Cardiol. 144 (4) (2017) 88–92.

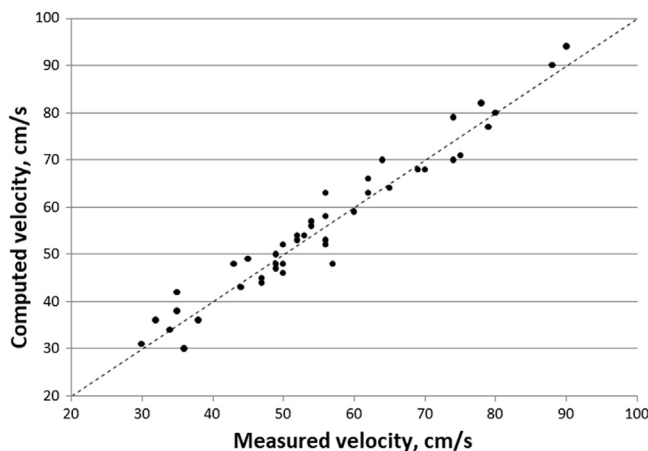


**Figure 9.19**

Comparison of measured and calculated blood velocities after the surgical treatment. From D.V. Burenchev, K.F. Yu, A.A. Bykova, et al., Mathematical modelling of circulation in extracranial brachiocephalic arteries at pre-operation stage in carotid endarterectomy, Russ. J. Cardiol. 144 (4) (2017) 88–92.

treatment. The functional parameters of the model were adjusted to these data. The model parameters were selected so that the differences between the measured and calculated blood flow rates did not exceed 5–6 cm/s. This tolerance was chosen on the basis of analysis of flow measurements before and after the surgery in regions far from the stenosis. The average absolute deviation was 2.2 cm/s, and the maximum deviation was 6 cm/s. The plot does not show a point corresponding to the velocity in the stenosis of patient 5: it was measured 302 cm/s and calculated 295 cm/s.

To predict the postsurgical blood velocities, we replaced the stenotic part of the artery with a healthy vessel whose lumen was taken to be the average of lumens of the neighboring vessels. Comparison of measured and calculated velocities is shown in Fig. 9.19. The average absolute deviation was 3 cm/s, and the maximum deviation was 9 cm/s. This demonstrates good predictability of postsurgical blood velocities after removing stenosis in the carotid arteries.

In conclusion, we note the importance of correct segmentation of the Circle of Willis for successful modeling of the cerebral blood flow. In the work [281], six different structures of the Circle of Willis were considered (see Fig. 9.20):

- closed Circle of Willis,
- absence of the anterior communicating artery (ACoA),
- absence of the right posterior communicating artery (RPCoA),
- absence of the RPCoA and left posterior communicating arteries (LPCoA),
- absence of RPCoA and ACoA,
- absence of RPCoA, LPCoA, and ACoA.

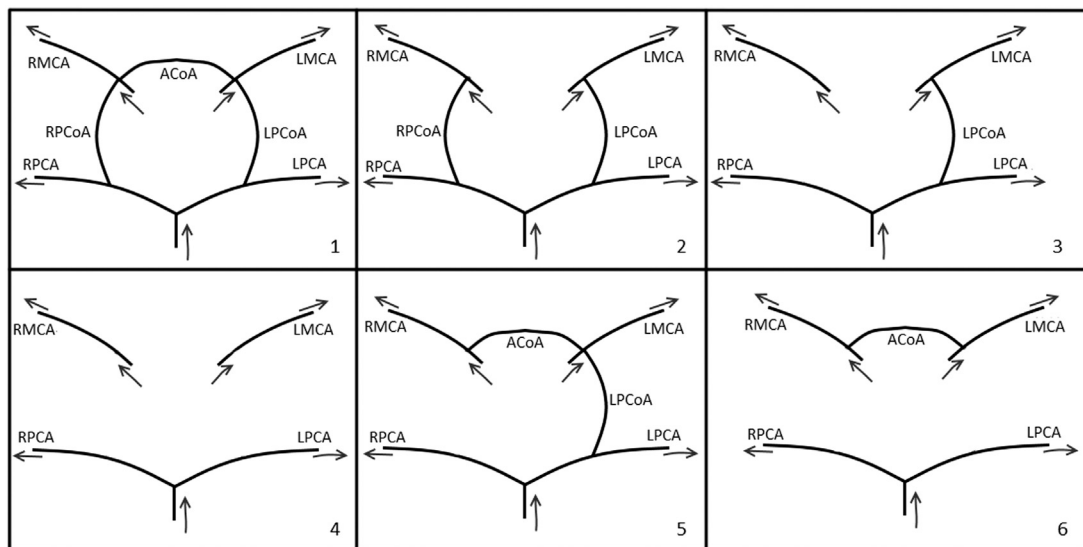


**Figure 9.20**

Structures of Circle of Willis: full Circle of Willis (1), ACoA is missing (2), ACoA and RPCoA are missing (3), ACoA, RPCoA, and LPCoA are missing (4), RPCoA is missing (5), RPCoA and LPCoA are missing (6). ACoA, anterior communicating artery; LPCoA, left posterior communicating artery; RPCoA, right posterior communicating artery. From S. Simakov, T. Gamilov, *Computational study of the cerebral circulation accounting for the patient-specific anatomical features*, in: *Smart Innovation, Systems and Technologies*, vol. 133, 2019, pp. 309–330.

The absence of the anterior and posterior communicating arteries in the Circle of Willis is a common case, whereas underdevelopment or absence of ACoA is observed in 20%–40% of cases [438].

For each structure, the impact on blood flow through the middle and posterior brain arteries from one to four stenoses located in the right and left internal carotid arteries and right and left vertebral arteries was examined. The results of the numerical study can be summarized as follows. The full Circle of Willis provides sufficient blood supply to the cerebral arteries even with significant stenoses of the carotid or vertebral arteries. However, less than 50% of population has the full Circle of Willis. In other cases, even a single stenosis may lead to a significant reduction in blood flow in one of the cerebral arteries, whereas the elimination of stenosis may improve blood flow in one region but worsen it in another region causing stealing phenomena in certain part of the vascular bed. Therefore, the accurate identification of the Willis Circle structure is crucial for the patient-specific simulation of cerebral hemodynamics. If such identification is not possible, the worst-case scenario should be considered for the sake of reliability of the prediction. The simulation results suggest the following rules for choosing a treatment strategy for stenotic lesion of the brachiocephalic arteries: in the presence of the full

Circle of Willis clearly visible on CT images, the elimination of all stenoses in the collateral arteries (left internal carotid artery, right internal carotid artery, left vertebral artery, right vertebral artery) is not necessary; in the absence of both posterior communicating arteries, compression of the vertebral arteries (for example, in case of cervical osteochondrosis) is a life threatening condition, and elimination of a stenosis may lead to stealing blood supply in a remote region.

## 9.6 Decision support software

Proprietary software MultiVox is a compelling picture archiving and communication software system developed at Moscow State University [439]. We integrated software complex implementing algorithms and methods from Chapters 3, 7 and 9 into MultiVox to create a useful tool for FFR<sub>CT</sub> assessment. Algorithms from Chapter 3 process DICOM images and extract the 3D and 1D structure of the aorta and coronary vessels. Several parameters can be adjusted by the user, such as a vesselness threshold and a stenosis position. The vesselness threshold is a parameter that restricts the probability of vessel growing in the Frangi filter discussed in Section 3.4.2. Large values lead to a lot of noise. Small values reduce the noise but cut off small vessels as well. The default value is estimated automatically, but the user can change it to obtain a clear structure of coronary vessels (see Fig. 9.21).

Various types of postprocessing, including shaded surface display, maximum intensity projection, and multiplanar reconstruction, help to identify the presence of stenoses and occlusions in the coronary arteries. Multiplanar reconstruction involves the process of converting data from an imaging modality acquired in an axial plane into another plane.

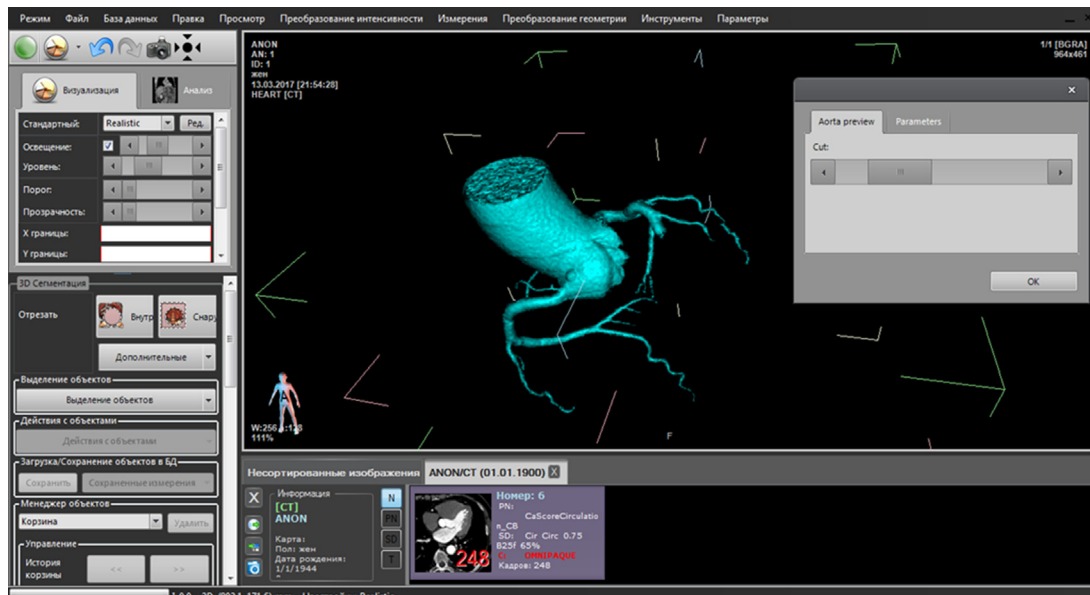


**Figure 9.21**  
3D voxel structure of aorta. Vesselness threshold.

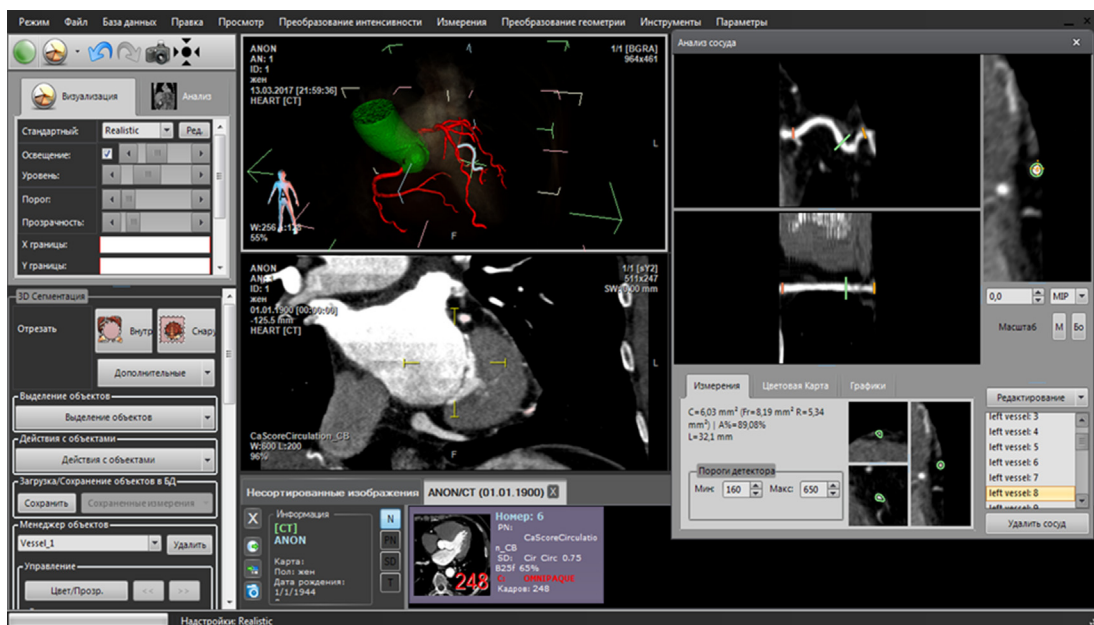


**Figure 9.22**  
Extracted coronary vessels. Multiplanar reconstruction of a coronary artery.

It is commonly performed with the thin-slice data from volumetric CT scanning in the axial plane. It also can be accomplished with scanning in any plane and any modality, which is capable of cross-sectional imaging.

The acquired data from the axial plane can be converted to nonaxial planes such as coronal, sagittal, or oblique. The MultiVox package provides additional functionality to work with the data. One of these additional tools, curved planar reformation, involves tracing a blood vessel and generating a 2D planar image, which transects the structure along its short axis. Multiplanar reconstruction is a built-in feature of the MultiVox package. We utilize it to visualize the result of segmentation and simplify stenosis detection (see Fig. 9.22).

Position and length of the stenosis can be manually adjusted by moving bars along the vessel as shown in Fig. 9.22. An automated procedure provides black-box calculation of the degree of the stenosis, although the user can reset the value. It is possible to insert a stent or additional stenoses to the virtual model as well as remove them. This helps to compare different treatment strategies or estimate possible risks.

After positioning of the stenoses, the simulations with the 1D hemodynamic model are performed. The results of the computational processing include the set of  $\text{FFR}_{CT}$  values for the designated stenoses. It takes 10–25 min to perform segmentation, arterial structure extraction, and 1D simulations on a laptop. The actual time depends on the complexity of the arterial structure. In any case, a conventional PC is enough to perform all preprocessing procedures and simulations that are appealing in clinical practice.

# *Applications in antitumor therapy*

## **10.1 Introduction**

Following cardiovascular diseases, cancer is the second leading cause of death in developed countries. Despite the fact that the risk of cancer increases with age, oncological diseases are not uncommon in all age groups. It is believed that cancer, or malignant tumor, is not a single disease, but rather a number of interrelated pathological processes triggered by the growth of cells undergoing malignant transformation. In 2000, Douglas Hanahan and Robert Weinberg [333] identified six hallmarks, i.e., common alterations in cell physiology that collectively dictate malignant growth: (1) self-sufficiency in growth signals; (2) insensitivity to antigrowth signals; (3) evasion of programmed cell death (apoptosis); (4) limitless replicative potential; (5) sustained angiogenesis; (6) tissue invasion and metastasis. In their later work of 2011, they added four more typical traits of cancer: (7) deregulated metabolism; (8) evading the immune system; (9) genome instability; (10) induction of inflammation.

Although the discussion concerning the significance of this way of cancer description is ongoing [440,441], the approach is generally accepted. As an example of criticism, we may point to Ref. [441], where the author suggests that cancer is rather a tissue-level disease and its description via cell-level hallmarks is misleading.

From mathematical point of view, the first four hallmarks can be combined into one concept that can be formulated as follows: cancer cells proliferate unlimitedly under sufficient level of nutrients. This concept is clearly supported by *in vitro* experiments with cultures of tumor cells, where the law of exponential growth of cell number is manifested at the initial stage [442]. Subsequently, as nutrients become depleted, growth rate slows down, since some cells stop proliferating and pass to a quiescent state, which requires less nutrients [443]. The dependence of tumor proliferation rate on the availability of nutrients can be seen even more clearly from results of *in vitro* experiments with multicellular tumor spheroids (MCTS), i.e., three-dimensional aggregates of malignant cells growing in nutrient solution. After a short initial growth phase, the radius of MCTS increases linearly with time, whereas the spheroid acquires rigid structure consisting of central necrotic zone and a thin outer rim of living cells, which

thickness remains constant over time. The thickness of this layer is determined by diffusion of nutrients from the solution surrounding MCTS [444]. Of course, the viable rim does not consist of only proliferating cells—a significant fraction of it consists of quiescent cells. With increase in concentrations of key metabolites, oxygen, and glucose, in the medium, the living rim enlarges and the MCTS growth rate increases proportionally.

The structure of solid tumors in tissue can both match the structure of MCTS and significantly differ from it (see Fig. 10.1). Solid tumors, which have different structures, experience different patterns of nutrient inflow. Encapsulated tumors and minimally invasive tumors, transplanted under the skin of an animal (usually rat or mouse), grow as separate compact objects. The inflow of nutrients to such tumors occurs via capillaries located in the peritumoral region, i.e., the tissue that surrounds the tumor, so their structure is similar to the one of MCTS [445]. On contrary, tumors of invasive type grow by infiltrating surrounding tissues, so there may be no clear border between a tumor and a normal tissue [446]. Inflow of nutrients to these tumors is not that much compromised, since there are microvessels inside the tumor. However, in this case gradual destruction of capillaries takes place due to various factors (as discussed in detail in Chapter 8). The absence of microvessels inside low-invasive tumors and the destruction of capillaries inside high-invasive ones both contribute to nutrient deficiency and necrosis formation in internal tumor regions. Note that, even under substantial microvasculature density, tumor growth in tissue is limited since proliferating tumor cells consume much more nutrients than normal cells. Lowering of nutrient levels inside the tumor leads to the phenomenon that a sufficiently large fraction of tumor cells experiences lack of nutrients even if their supply is adequate for surrounding healthy tissues. In the state of metabolic stress, tumor cells produce various signaling molecules that stimulate the growth of new capillaries, i.e., we have the process of angiogenesis [447]. The most universal and widespread mediator

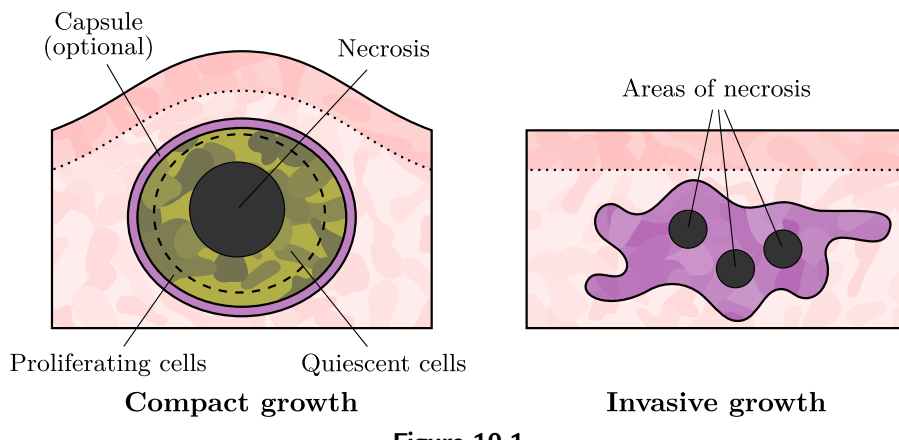


**Figure 10.1**  
Types of tumor growth.

of angiogenesis is the vascular endothelial growth factor, or VEGF, which is also known as vascular permeability factor (VPF), since it causes the increase in permeability of capillary walls.

Angiogenesis has been marked by Douglas Hanahan and Robert Weinberg as one of the hallmarks of cancer. Via stimulating of new microvessels formation, tumors obtain more nutrients and speed up their growth. In 1971, Judah Folkman suggested a new type of anticancer therapy, i.e., antiangiogenic therapy (AAT), aimed at cessation of angiogenesis, which should lead to a complete stop or at least to a significant slowdown in tumor growth [448]. The first antiangiogenic drug bevacizumab, which irreversibly binds to VEGF, rendering it inactive, was approved for medical use in 2004 and is widely used nowadays. AAT by bevacizumab not only prevents the formation of new capillaries but also leads to the normalization of tumor capillaries, i.e., brings them to a more physiologically normal state with normalized permeability of the walls, both actions limiting the supply of nutrients to the tumor. Compared with traditional radio- and chemotherapy (CT), AAT has moderate side effects but, as it was repeatedly shown in clinics, by itself cannot completely destroy the tumor and therefore has limited effectiveness [449]. Currently, almost all approved protocols that include bevacizumab combine it with various chemotherapeutic agents [450], which aim to destroy actively proliferating cells via various mechanisms. However, since they are not tumor specific and affect all proliferating tissues, their action is associated with significant side effects, such as anemia, hair loss, immunosuppression, rheumatoid arthritis, and others, which limit the use of these drugs.

Two different types of drugs administered simultaneously inevitably interact with each other. Of a special importance is the fact that AAT often ultimately leads to the decrease in the inflow of chemotherapeutic drug into tumor, which has been observed experimentally [451,452]. Therefore, a major challenge associated with the use of CT in combination with AAT is the optimal scheduling of drug administration to maximize antitumor effect and minimize side effects. Currently, this is a topic of an active research, and mathematical modeling aims to facilitate progress in this direction.

Historically, first mathematical models in oncology tried to address only tumor growth. The scope of such studies was to adequately describe the experimentally observed change of the number of cells in experiments with malignant cultures *in vitro* or to model the change in tumor volume in experiments with MCTS or transplanted tumors *in vivo* [453,454]. A common trait of such models is small number of parameters, usually two or three, which allows the authors to successfully fit the experimental data. Although the progress in this direction continues [455], such models do not take into account the structure of the tumor and basic processes that determine its development in tissue. For the first time, the importance of nutrient inflow into the tumor as a key factor for its development was demonstrated in papers by Burton [456] and Greenspan [457], where the

MCTS structure was considered. Later, as the models became more and more complicated in addressing the spatial dynamics of tumor growth, it became feasible to predict the changes in the tumor structure due to cellular motility [458,459], convective flows in the tissue [460,461] and angiogenesis [462,463]. Recently, mathematical modeling in oncology has been increasingly focusing on the description of anticancer therapy. However, most of the work in this area is devoted to classical antitumor radio- or chemotherapy alone [464–466]. In contrast to clinical practice, mathematical models that combine CT and AAT were introduced only recently [467,468]. The existing works on this topic are still built on purely phenomenological description of the effect of antiangiogenic drugs, which makes it impossible to account for the interaction of different types of therapies. Moreover, all works of this type do not consider the spatial structure of tumor, which indicates that they may be suitable only for modeling of postoperative (adjuvant) therapy. At the same time, there are many reliable studies that simulate classical monochemotherapy [469–471] and AAT by bevacizumab, considering its pharmacokinetics in blood and tissue [472,473].

Further in this chapter, using a spatially distributed model of the tumor growth and combined therapy, we compare the efficiencies of different schemes of palliative and neoadjuvant combined chemotherapy with bevacizumab, as well as monochemotherapy. Palliative therapy is administered when surgical intervention is not possible, and the drug treatment continues until tumor regrowth or lethal outcome. Neoadjuvant therapy is held before surgery to reduce the tumor volume. For the modeling of neoadjuvant therapy, it is necessary to take into account the formation of necrosis during the therapy and the mechanisms of its elimination from tissue. In the presented approach, this problem is solved by explicit consideration of dynamics of interstitial fluid (IF), which is the main constituent of necrosis.

## **10.2 Mathematical model of antitumor combined chemo- and antiangiogenic therapy**

### **10.2.1 Governing equations**

To visualize the role of different factors during the chemo- and antiangiogenic therapy, we start with [Fig. 10.2](#), which shows a block scheme of the model we are interested in. We consider a monoclonal tumor and rely on the accepted principle of migration/proliferation dichotomy of tumor cells [474]. Thus, the model tumor comprises a heterogeneous colony of malignant cells, described in terms of the normalized densities of proliferating cells,  $n_1(r, t)$ , where  $r$  and  $t$  are space and time coordinates, and quiescent cells,  $n_2(r, t)$ , which are able to migrate into surrounding tissue. Cells can change their state depending on the concentration of glucose  $G(r, t)$ , which is chosen as a key metabolite, since it is both a crucial precursor for organic synthesis and the most important energetic substrate for tumor cells. Under insufficient levels of glucose, proliferating cells pass to the quiescent

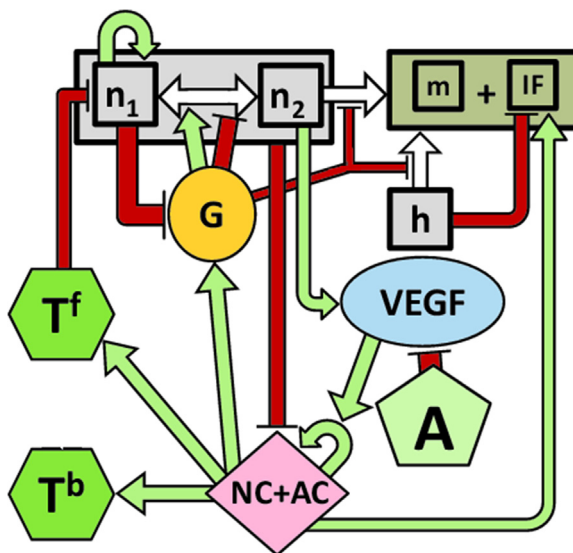


Figure 10.2

Block scheme of the model of tumor growth and combined chemotherapy with bevacizumab:  $n_1$  and  $n_2$  are proliferating and migrating tumor cells, respectively,  $h$  is normal cells,  $m$  is cell remnants,  $IF$  is interstitial fluid,  $G$  is glucose, VEGF stands for vascular endothelial growth factor,  $NC$  and  $AC$  are normal and angiogenic part of microcirculatory network, respectively,  $A$  is bevacizumab,  $T^f$  and  $T^b$  are free and protein-bound forms of cisplatin, respectively. Green arrows (gray arrows in print version) indicate stimulating links, red lines (black lines in print version) denote inhibiting actions, and white arrows correspond to cell transitions.

state. If the level of glucose is sufficient, then the reverse process takes place. The surrounding tissue consists of normal cells characterized by density  $h(r, t)$  and  $IF$ . We denote by  $IF(r, t)$  the fraction of the  $IF$ . Tumor cells and normal cells can die due to lack of glucose, while tumor cells may also die from action of chemotherapeutic agent, for which only cycle-specific action is considered. Dead cells form necrosis, which consists of nonutilized cell remnants and  $IF$ . The fraction of cell remnants in the tissue is denoted by  $m(r, t)$ . The healthy tissue contains a normal capillary network; the bulk density of its surface is  $NC(r, t)$ . As the result of the tumor angiogenesis, the normal capillary network expands by angiogenic capillaries. The bulk density of angiogenic capillaries surface is denoted by  $AC(r, t)$ . The angiogenic capillaries network is introduced in the model to account for the enhanced permeability (for various substances) of tumor angiogenic microvasculature. Besides  $IF$  formed in result of cell death, more  $IF$  enters the tissue from the microvasculature. Its influx similarly depends on the type of microvessels. The model assumes that active outflow of  $IF$  occurs only through the lymphatic system. We assume that the amount of lymphatic capillaries is proportional to the density of normal cells. Thus, the rate of outflow of  $IF$  depends on the fraction of normal cells. The model also

takes into account the concentrations of VEGF, bevacizumab, and cytotoxic drug. We denote by  $V(r, t)$  and  $A(r, t)$  the concentrations of VEGF and bevacizumab, respectively. To account for the role of the cytotoxic drug, we use the parameters of cisplatin, which is one of the chemotherapeutic agents used in the clinical practice in combination with bevacizumab [450]. Since it has a high affinity for plasma proteins, we take into account two forms of cisplatin, using the variables of concentrations of its free and protein-bound forms,  $T^f(r, t)$  and  $T^b(r, t)$ , respectively.

Summarizing, the dynamics of cells and necrosis is governed by the following system of equations:

$$\begin{aligned}
 \frac{\partial n_1}{\partial t} &= \overbrace{Bn_1}^{\text{proliferation}} - \overbrace{P_1(G)n_1 + P_2(G)n_2}^{\text{cell transitions}} - \overbrace{k_T T_n T n_1}^{\text{death from CT}} - \overbrace{\nabla(\mathbf{v} n_1)}^{\text{convection}}, \\
 \frac{\partial n_2}{\partial t} &= \overbrace{P_1(G)n_1 - P_2(G)n_2}^{\text{cell transitions}} - \overbrace{d_h(G)n_2}^{\text{death}} - \overbrace{\nabla(\mathbf{v} n_2)}^{\text{convection}} + \overbrace{D_h \Delta n_2}^{\text{migration}} \\
 \frac{\partial h}{\partial t} &= \overbrace{-d_h(G)h}^{\text{death}} - \overbrace{\nabla(\mathbf{v} h)}^{\text{convection}} \\
 \frac{\partial IF}{\partial t} &= \underbrace{\beta(d_n(G)n_2 + d_h(G)h + k_T T_n T n_1)}_{\text{cell death}} - \underbrace{v_{dr}(IF - IF_{\min})}_{\text{outflow}} \frac{h}{h + h^*} \\
 &\quad + \underbrace{[P_{IF,NC}NC + P_{IF,AC}AC](IF_{ic} - IF)}_{\text{inflow}} + \underbrace{D_{IF} \Delta IF}_{\text{diffusion}} - \overbrace{\nabla(\mathbf{v} IF)}^{\text{convection}}, \\
 \frac{\partial m}{\partial t} &= \underbrace{[1 - \beta](d_n(G)n_2 + d_h(G)h + k_T T_n T n_1)}_{\text{cell death}} - \overbrace{\nabla(\mathbf{v} m)}^{\text{convection}} \\
 n_1 + n_2 + IF + m + h &= 1,
 \end{aligned} \tag{10.1}$$

where  $P_1(G) = k_1 \exp(-k_2 G)$ ,  $P_2(G) = \frac{1}{2} k_3 (1 - \tanh[\epsilon_{tr}(G_{tr} - G)])$ ,  $d_i(G) = \frac{1}{2} d_i^{\max} (1 + \tanh[\epsilon_d(G_d - G)])$ ,  $i = n, h$ .

In Section 10.2.2, we set up all parameters and discuss how one can estimate their values. Since the model is one-dimensional, the gradient in the convection operator is a scalar function. We remark that the form of the cell transition term from proliferation to rest  $P_1(G)$  in the first equation is taken from Ref. [475], where it was successfully used for fitting experimental data. The reverse transition,  $P_2(G)$ , is important in simulating possible tumor regrowth, but its form does not affect the result qualitatively; therefore, we use a smoothed step function for it. Diffusion approximation is used to describe the transport of IF throughout the tissue.

In this model, we consider simultaneously two types of growth of solid tumor discussed in [Section 10.1](#), i.e., the dense growth as a compact object and infiltrative growth. This is a rare approach in mathematical modeling. However, it is physiologically grounded, since the growth of real tumor often represents a combination of these two types. Consideration of infiltrative growth is realized herein in a traditional way, i.e., through the term of migration of tumor cells. For description of compact growth, we use the following approach, which represents a special case of a more general method, utilized, e.g., by Ref. [476]. That method converges to the one presented herein under the assumption that values of interstitial pressure, arising due to cell dynamics, are infinitesimal, so they do not hinder the cell proliferation.

Let us consider an incompressible dense tissue in which spatial distribution of components is affected by their local kinetics, e.g., proliferating tumor cells push out surrounding tissues, providing an increase in tumor size. In mathematical form, the condition of incompressible dense tissue means the constancy of all tissue constituents, which is included in [Eq. \(10.1\)](#). To account for such phenomena, we introduce a convective velocity field  $\mathbf{v}(r, t)$ .

Convective velocity field  $\mathbf{v}(r, t)$  can be obtained by summing up the equations for all tissue constituents. During this procedure, left sides of equations produce the derivative of a constant value, i.e., zero; the transition terms of cell death are canceled out; and the sum of convection terms provides the gradient of velocity field, which can be expressed via remaining terms in the following way:

$$\nabla \mathbf{v} = Bn_1 + [P_{IF,NC}NC + P_{IF,AC}AC](IF_{ic} - IF) \\ - v_{dr}(IF - IF_{\min}) \frac{h}{h + h^*} + D_n \Delta n_2.$$

The final expression for  $\mathbf{v}$  obtains different forms depending on space dimensions and boundary conditions.

As already mentioned, the model uses two variables to describe the microcirculatory network, namely, its normal and angiogenic parts,  $NC$  and  $AC$ . The angiogenic part has significantly higher wall permeability. With the growth of tumor, the microcirculatory network is locally destroyed under the influence of increased local pressure due to proliferation and migration of tumor cells, as well as various chemical factors. These factors are implicitly taken into account by setting the rate of microvessel destruction nonzero inside necrosis and lower than in the presence of tumor cells. Under sufficient amount of VEGF, new angiogenic capillaries formation takes place along with denormalization (i.e., transformation to angiogenic) of previously existing normal ones. This is introduced in the model to reflect the increase in permeability of the capillary walls under the action of VEGF and is described by the transition from  $NC$  to  $AC$ . At low

concentrations of VEGF, capillary normalization and reverse transition occur. The rate of angiogenesis decreases in the presence of cisplatin, which also kills dividing endothelial cells. A special term is introduced to account for microcirculatory network tendency to return to a constant physiologically reasonable density under the cessation of tumor angiogenesis. This term includes the Heaviside function  $\Theta$ , since it differs from zero only when the total density of normal and angiogenic capillaries exceeds unity. Capillaries also move owing to convective flows, but more slowly than cells, due to their connectivity in network. The ability of angiogenic capillaries to grow into the tissue is accounted for by the diffusion term.

The equations describing the dynamics of capillary network read as follows:

$$\begin{aligned} \frac{\partial NC}{\partial t} &= \underbrace{-[l(n_1 + n_2) + l_m m]NC}_{\text{degradation}} + \underbrace{\frac{v_{mat}V^*}{V + V^*}AC}_{\text{normalization}} - \underbrace{\frac{v_{dem}V}{V + V^*}NC}_{\text{denormalization}} \\ &\quad \underbrace{-\mu(NC + AC - 1)NC\Theta(NC + AC - 1)}_{\text{density normalization}} \underbrace{-\nabla(\gamma v NC)}_{\text{convection}}, \\ \frac{\partial AC}{\partial t} &= \underbrace{Re^{-k_f^2 T} \frac{V}{V + V^*} (NC + AC) \left[ 1 - \frac{(NC + AC)}{C_{\max}} \right]}_{\text{angiogenesis}} \\ &\quad \underbrace{-[l(n_1 + n_2) + l_m m]AC}_{\text{degradation}} + \underbrace{\frac{v_{mat}V^*}{V + V^*}AC}_{\text{normalization}} + \underbrace{\frac{v_{dem}V}{V + V^*}NC}_{\text{denormalization}} \\ &\quad \underbrace{-\mu(NC + AC - 1)AC\Theta(NC + AC - 1)}_{\text{density normalization}} \\ &\quad \underbrace{+D_{AC}\Delta AC}_{\text{migration}} \underbrace{-\nabla(\gamma v AC)}_{\text{convection}}. \end{aligned} \tag{10.2}$$

Glucose enters the tissue from the capillary network, and its inflow is regulated by diffusion through the pores in the capillary walls, where various capillaries have different permeabilities. The level of glucose in the blood is assumed to be constant. All cells consume glucose, and the level of consumption of proliferating tumor cells is much higher due to the specific features of the tumor metabolism [477]. Glucose diffuses throughout the tissue, and its local diffusion coefficient decreases with the concentration of cells [478]. For this model, it can be formulated in terms of the fraction of IF. It is known that the coefficient of diffusion of all substances increases in necrosis (the diffusion MRI principle is based on this observation [479]). We introduce the dependence of the diffusion coefficient on the fraction of IF for all substances in the model using the linear relation:

$$D_i(IF) = D_i^0(1 + \alpha IF), \quad i = G, V, A, T^f, T^b.$$

Thus, the change of glucose concentration is determined by the equation:

$$\frac{\partial G}{\partial t} = \underbrace{[P_{G,NC}NC + P_{G,AC}AC]}_{\text{inflow}} (G_{bl} - G) - \underbrace{[q_{n_1}n_1 + q_{n_2}n_2 + q_h h]}_{\text{consumption}} \frac{G}{G + G^*} + \underbrace{D_G(IF)\Delta G}_{\text{diffusion}}. \quad (10.3)$$

Proangiogenic factor VEGF is produced by malignant cells. Since metabolic stress significantly increases its production [480], its secretion only by quiescent cells is considered. We do not consider VEGF interactions with receptors of endothelial cells and tissue elements in all their complexity. We rather use the simplest form of the term to describe VEGF internalization by endothelial cells, since it does not affect the simulation results. We also take into account diffusion of VEGF in tissue, its degradation, and outflow from tissue, the latter being explicitly included in the model under the assumption that concentration of free VEGF in the blood is negligible.

Bevacizumab is administered intravenously, which is reflected by the ordinary differential equation for its blood concentration. It contains a term representing its administration, which leads to the abrupt increase of the concentration of bevacizumab in blood after moment of its injection. The equation also contains the reaction term representing the blood clearance. Bevacizumab comes from the blood into tissue, where it diffuses and irreversibly binds to VEGF. The difference in permeabilities of walls of various capillaries is significant for bevacizumab, as its size is comparable with the pore sizes of normal body capillaries. Since bevacizumab is a macromolecule specifically designed to inhibit VEGF, its interaction with tissue elements is neglected.

$$\begin{aligned} \frac{\partial V}{\partial t} &= \underbrace{pn_2}_{\text{secretion}} - \underbrace{\omega V(NC + AC)}_{\text{internalization}} - \underbrace{[P_{V,NC}NC + P_{V,AC}AC]V}_{\text{outflow}} \\ &\quad - \underbrace{d_V V}_{\text{degradation}} - \underbrace{(k_A A_n)AV}_{\text{neutralization}} + \underbrace{D_V(IF)\Delta V}_{\text{diffusion}}, \quad (10.4) \\ \frac{\partial A}{\partial t} &= \underbrace{[P_{A,NC}NC + P_{A,AC}AC]}_{\text{inflow}} (A_{bl} - A) - \underbrace{(k_A V_n)AV}_{\text{binding with VEGF}} + \underbrace{D_A(IF)\Delta A}_{\text{diffusion}}, \\ \frac{\partial A_{bl}}{\partial t} &= \underbrace{F_A^{iv}}_{\text{administration}} - \underbrace{d_A A_{bl}}_{\text{blood clearance}}. \end{aligned}$$

Cisplatin also enters the circulatory system through intravenous injection. The model reflects this with a sharp increase in the cisplatin concentration at the moments of injection. Cisplatin has the molecular weight of only 300 Da. It actively binds to blood proteins and as a result exists in blood and tissue in two forms—in the form of free small molecules of active drug and a large inactive protein-bound complex. Their concentrations in tissue are denoted as  $T^f$  and  $T^b$ , respectively. Both forms of the drug come from blood into tissue, where they diffuse and continue to transit from one form to another. The rate of cisplatin binding to the protein should depend on the concentration of proteins, which is usually much higher in blood than in normal tissue. However, since we consider a tumor tissue, by the time of therapy, blood proteins should accumulate inside it to a level comparable with the blood level due to increased permeability of angiogenic capillaries and the impaired drainage of IF through the lymphatic system. Hence, we take the coefficient of cisplatin binding to blood proteins inside the tissue equal to the corresponding value in blood. We also neglect the blood clearance of protein-bound drug, as well as its binding to tissue elements because they are small comparing with these parameters for the free agent.

$$\begin{aligned}
 \frac{\partial T^f}{\partial t} &= \underbrace{[P_{NC,Tf}NC + P_{AC,Tf}AC]}_{\text{inflow}} \left( T_{bl}^f - T^f \right) - \underbrace{d_T T^f}_{\text{non-specific binding}} \\
 &\quad \underbrace{-k_{on}T^f + k_{off}T^b}_{\text{interaction with proteins}} \underbrace{+D_{Tf}(IF)\Delta T^f}_{\text{diffusion}}, \\
 \frac{\partial T^b}{\partial t} &= \underbrace{[P_{NC,Tb}NC + P_{AC,Tb}AC]}_{\text{inflow}} \left( T_{bl}^b - T^b \right) \\
 &\quad \underbrace{+k_{on}T^f - k_{off}T^b}_{\text{interaction with proteins}} \underbrace{+D_{Tb}(IF)\Delta T^b}_{\text{diffusion}}, \\
 \frac{\partial T_{bl}^f}{\partial t} &= \underbrace{F_T^{iv}}_{\text{administration}} \underbrace{-k_{on}T_{bl}^f + k_{off}T_{bl}^b}_{\text{interaction with proteins}} \underbrace{-d_{T,bl}T_{bl}^f}_{\text{blood clearance}}, \\
 \frac{\partial T_{bl}^b}{\partial t} &= \underbrace{k_{on}T_{bl}^f - k_{off}T_{bl}^b}_{\text{interaction with proteins}}
 \end{aligned} \tag{10.5}$$

Here, we neglect convective transport of all the substances across the capillary walls. As discussed above, this assumption is clearly justified for small molecules such as glucose. Inclusion of this type of transport for bevacizumab and VEGF would not affect the tumor growth qualitatively due to specific features of their action and dynamics in tissue. The

justifications of this approach for consideration of cisplatin transport and its impact on obtained results are discussed in [Section 10.4](#).

### 10.2.2 Model parameters

The model contains several dozens of parameters. When available, the values are taken from various experiments. Otherwise, they are evaluated to ensure that the tumor growth reflects some of its known characteristics. The basic set of parameters is given in [Table 10.1](#), where the following normalization parameters are used to obtain their model values:  $t_n = 1$  h for time,  $L_n = 10^{-2}$  cm for length, and  $G_n = 1$  mM for glucose concentration. The normalization parameters for VEGF, bevacizumab, and cisplatin are used in the corresponding terms describing the effects of the therapies and are chosen to be  $V_n = 10^{-11}$  mole/mL,  $A_n = 1.6 \cdot 10^{-9}$  mole/mL, and  $T_n = 5 \cdot 10^{-8}$  mole/mL. The last two values are estimated from the concentrations of the corresponding drugs in the blood

**Table 10.1: Model parameters.**

Parameter	Description	Value	Model	References
Value estimations based on tumor cells				
$B$	Proliferation rate	$0.02 \text{ h}^{-1}$	0.02	[481]; see text
$k_1$	Maximum transition rate into rest	$0.4 \text{ h}^{-1}$	0.4	[475]
$k_2$	Sensitivity of transition into rest to glucose	$19.8 \left( \frac{\text{mL}}{\text{mg}} \right)$	3.6	[475]
$k_3$	Maximum rate of transition into proliferative state	$0.16 \text{ h}^{-1}$	0.4	See <a href="#">Section 10.2.1</a>
$\varepsilon_{tr}$	Sensitivity of transition into proliferative state	1.8	1.8	See <a href="#">Section 10.2.1</a>
$G_{tr}$	Threshold concentration of glucose for transition into proliferative state	1.7 mM	1.7	See <a href="#">Section 10.2.1</a>
$k_T$	Sensitivity to cisplatin	$3 \cdot 10^9$	$3 \cdot 10^9$	Varies, see text
$d_n^{\max}$	Maximum rate of death	$10^{-3} \text{ h}^{-1}$	$10^{-4}$	[482]
$\varepsilon_d$	Sensitivity of death rate to glucose	5	5	See text
$G_d$	Threshold concentration of glucose for death		0.55	See text
$D_n$	Migration coefficient	$10^{-12} \text{ cm}^2/\text{s}$	$3.6 \cdot 10^{-5}$	See text
Normal cells				
$d_h^{\max}$	Maximum rate of death	$5 \cdot 10^{-3} \text{ h}^{-1}$	$5 \cdot 10^{-3}$	[482]

*Continued*

Table 10.1: Model parameters.—cont'd

Parameter	Description	Value	Model	References
Interstitial fluid				
$\beta$ $P_{IF,NC}$	Fraction in dead cells Coefficient of inflow through normal capillaries	0.8 $1.1 \cdot 10^{-4}$	0.8 $1.1 \cdot 10^{-4}$	See text See Section 10.2.4
$P_{IF,AC}$	Coefficient of inflow through angiogenic capillaries	$5.5 \cdot 10^{-4}$	$5.5 \cdot 10^{-4}$	See Section 10.2.4
$IF_c$ $IF_{\min}$	Inflow parameter Minimum fraction in tissue	0.5 0.15	0.5 0.15	See text See text
$v_{dr}$ $h^*$	Rate of drainage Michaelis constant for outflow	0.01 0.425	0.01 0.425	See text See Section 10.2.1
$D_{IF}$	Rate of transport in tissue	$10^{-9}$	0.036	See text
$\alpha$	Coefficient of increase in diffusion rate of substances in necrosis	0.3	0.3	See Section 10.2.1
Capillaries				
$l$	Degradation rate in alive region	$1.7 \cdot 10^{-10} \left( \frac{\text{cells}}{\text{mL}} \right)^{-1} \text{s}^{-1}$	0.05	See text
$l_m$	Degradation rate in necrosis	$5.1 \cdot 10^{-10} \left( \frac{\text{cells}}{\text{mL}} \right)^{-1} \text{s}^{-1}$	0.15	See text
$v_{mat}$ $V^*$	Normalization rate Michaelis constant for angiogenesis rate	$0.05 \text{ h}^{-1}$ $10^{-14} \text{ mole/mL}$	0.05 $10^{-3}$	See text See text
$v_{dem}$ $\mu$	Denormalization rate Density normalization rate	$0.05 \text{ h}^{-1}$ $10^{-5} \left( \frac{\text{cm}^2}{\text{cm}^3} \right)^{-1} \text{s}^{-1}$	0.05 $10^{-3}$	See text See text
$\gamma$ $R$	Network elasticity Maximum angiogenesis rate	0.75 $5 \cdot 10^{-3} \text{ h}^{-1}$	0.75 $5 \cdot 10^{-3}$	See text See Section 10.2.1
$C_{\max}$	Maximum surface density	$500 \frac{\text{cm}^2}{\text{cm}^3}$	5	See text
$k_T^A$	Sensitivity of angiogenesis to cisplatin	$0.35 \cdot 10^{-8} \text{ mole/mL}$	10	See text
$D_{AC}$	Migration coefficient	$10^{-11} \frac{\text{cm}^2}{\text{s}}$	$3.6 \cdot 10^{-4}$	See text
Glucose				
$P_{G,NC}$	Permeability of continuous capillaries	$1.1 \cdot 10^{-5} \frac{\text{cm}}{\text{s}}$	4	See Section 10.2.3
$P_{G,AC}$	Permeability of angiogenic capillaries	$2.8 \cdot 10^{-5} \frac{\text{cm}}{\text{s}}$	10	See Section 10.2.3
$G_{bl}$	Glucose blood level	$5.56 \frac{\text{mmol}}{\text{l}}$	5.56	[483]

Continued

**Table 10.1: Model parameters.—cont'd**

Parameter	Description	Value	Model	References
$q_{n_1}$	Proliferating tumor cells consumption rate	$6.5 \cdot 10^{-17} \frac{\text{mol}}{\text{cell} \cdot \text{s}}$	70	[481]; see text
$q_{n_2}$	Quiescent tumor cells consumption rate	$2.3 \cdot 10^{-18} \frac{\text{mol}}{\text{cell} \cdot \text{s}}$	2	See text
$q_h$	Normal cells consumption rate	$0.49 \frac{\text{mg}}{\text{min} \cdot 100 \text{ mL}}$	1.6	[484]
$G^*$	Michaelis constant for consumption rate	0.04 mM	0.04	[485]
$D_G^0$	Diffusion coefficient	$2.6 \cdot 10^{-6} \text{cm}^2/\text{s}$	94	[486]
VEGF				
$p$	Secretion rate	$0.4 \frac{\text{fg}}{\text{h} \cdot \text{cells}}$	0.2	[487]
$\omega$	Internalization rate	$2.8 \cdot 10^{-4} \text{s}^{-1}$	1	[488]
$P_{NC,V}$	Permeability of continuous capillaries	$6.4 \cdot 10^{-8} \frac{\text{cm}}{\text{s}}$	0.023	See Section 10.2.3
$P_{AC,V}$	Permeability of angiogenic capillaries	$7.8 \cdot 10^{-7} \frac{\text{cm}}{\text{s}}$	0.28	See Section 10.2.3
$d_V$	Degradation rate	$0.01 \text{ h}^{-1}$	0.01	[489]
$k_A$	Constant of binding to bevacizumab	$5.3 \cdot 10^5 \text{M}^{-1} \text{s}^{-1}$	$1.9 \cdot 10^{12}$	[490]
$D_V^0$	Diffusion coefficient	$5.9 \cdot 10^{-7} \text{cm}^2/\text{s}$	21.2	[489]
Bevacizumab				
$P_{NC,A}$	Permeability of continuous capillaries	$1.6 \cdot 10^{-9} \frac{\text{cm}}{\text{s}}$	$6 \cdot 10^{-4}$	See Section 10.2.3
$P_{AC,A}$	Permeability of angiogenic capillaries	$1.2 \cdot 10^{-7} \frac{\text{cm}}{\text{s}}$	0.044	See Section 10.2.3
$D_A^0$	Diffusion coefficient	$4 \cdot 10^{-7} \text{cm}^2/\text{s}$	14.3	See text
$d_A$	Blood clearance rate	$0.035 \text{ day}^{-1}$	$1.4 \cdot 10^{-3}$	[450]
Free cisplatin				
$P_{NC,Tf}$	Permeability of continuous capillaries	$8 \cdot 10^{-6} \frac{\text{cm}}{\text{s}}$	3	See Section 10.2.3
$P_{AC,Tf}$	Permeability of angiogenic capillaries	$2.2 \cdot 10^{-5} \frac{\text{cm}}{\text{s}}$	7.9	See Section 10.2.3
$k_{on}$	Protein-binding rate	$0.46 \text{ h}^{-1}$	0.46	[491]
$k_{off}$	Protein-unbinding rate	$0.04 \text{ h}^{-1}$	0.04	[491]
$d_T$	Rate of nonspecific binding with tissue elements	$3 \text{ h}^{-1}$	3	Varies, see text
$D_T^0$	Diffusion coefficient	$2.1 \cdot 10^{-6} \text{cm}^2/\text{s}$	77.2	See text
$d_{T,bl}$	Blood clearance rate	$0.13 \text{ h}^{-1}$	0.13	[492] "obtains different form"
Protein-bound form of cisplatin				
$P_{NC,Tb}$	Permeability of continuous capillaries	$2.8 \cdot 10^{-8} \frac{\text{cm}}{\text{s}}$	0.01	See text
$P_{AC,Tb}$	Permeability of angiogenic capillaries	$4.5 \cdot 10^{-7} \frac{\text{cm}}{\text{s}}$	0.16	See text
$D_{Tb}^0$	Diffusion coefficient	$5.8 \cdot 10^{-7} \text{cm}^2/\text{s}$	20.9	See text

in an average person shortly after the administration. The maximum density of tumor cells is  $3 \cdot 10^8$  cells/mL [481]. The normal density of capillary surface is assumed to be  $NC_n = 100 \text{ cm}^2/\text{cm}^3$  based on its average value for human muscle [49].

Estimating for the tumor cells proliferation rate and the rate of glucose consumption by proliferating cells, we rely on the data obtained in experiments studying the growth of tumor spheroids in suspension. However, we assume that these values proportionally decrease, when the tumor grows in tissue, due to such factors as mechanical pressure and increased acidity. The estimate of the glucose consumption rate by quiescent tumor cells is based on the observation made in Ref. [475] that it should be more than 40 times lower than the rate of glucose consumption by proliferating cells. The maximum rates of death of normal and tumor cells are estimated on the basis of experimental data about the behavior of cells under extreme nutrient deprivation. The parameters of sensitivity of cell death rate to the concentration of glucose are chosen so that the rate of cell death becomes significant only if glucose level decreases drastically. The migration coefficient of tumor cells corresponds to a noninvasive tumor. We assume that 80% of cell mass is a liquid that turns into IF when the cell dies. The minimum and initial levels of IF in the tissue are in physiologically justified range. The parameters of microcirculatory network are estimated so that its behavior adequately approximates the general features of structure and the dynamics of functional tumor capillary network [339,383,493], see also Chapter 8. Diffusion coefficients for bevacizumab and two forms of cisplatin are estimated based on already defined values for glucose and VEGF and molecule radii of all substances, where the radius of albumin is used for protein-bound cisplatin.

The parameter of nonspecific binding of cisplatin with tissue elements is varied in significant range to account for patient-specific effects of the therapy. We also vary the sensitivity of tumor cells for cisplatin during simulations to study the relative efficacy of different schemes of drugs administration under various conditions.

### **10.2.3 Estimate of permeability**

Increased permeability is the crucial feature of tumor pathologic microvasculature, which determines enhanced inflow of metabolites to the tumor, thus leading to its accelerated growth. It also results in formation of edema. Given the importance of increased permeability for the results of simulations, we discuss in detail how we obtained parameters of the microvasculature permeability for all the modeled substances.

The exchange of small lipid-insoluble substances between blood and tissue happens mainly due to passive diffusion through capillary pores, which can be described by Fick's law. For a single pore, which is assumed to be cylindrical and perpendicular to capillary surface, we thus can write:

$$Q = D'A \frac{C_{cap} - C_{tis}}{h},$$

where  $Q$  is the inflow of substance,  $D'$  is its intrapore diffusion coefficient,  $C_{cap}$  and  $C_{tis}$  are the concentrations of substance in capillary blood and IF,  $h$  is the length of a pore, and  $A$  is the part of pore surface area, available for movement of molecules across it. A molecule experiences an effect known as the steric exclusion, which means that the molecule cannot get closer to the pore rim than the length of its hydrodynamic radius. Hence, it holds

$$A = A(a, r) = \pi(r - a)^2,$$

where  $a$  is the hydrodynamic radius of a substance molecule and  $r$  is the radius of a pore. For the study of a capillary system, it is convenient to introduce the physically measurable parameter of its permeability  $P$ . It is defined as follows:

$$P = \frac{D' A_p}{Sh},$$

where  $A_p$  is the sum of pores areas available for the molecules movement across the microvessel wall and  $S$  is the surface area of capillaries. This definition leads to the type of equation, used herein to describe the inflow of all substances in tissue:

$$Q = PS(C_{cap} - C_{tis}).$$

We regard preexisting microvasculature as consisting of continuous capillaries. The transfer of blood solutes happens mainly through relatively small pores. At the same time, capillaries formed as a result of the tumor angiogenesis possess much larger holes called “fenestrations”, see Fig. 2.8. The diffusion of substances is restricted by pores due to additional hydrodynamic resistance, which may be quantified using the following empirically obtained Renkin equation [494]:

$$D' = D'(D, a, r) = D \cdot \left( 1 - 2.1 \frac{a}{r} + 2.09 \left( \frac{a}{r} \right)^3 - 0.95 \left( \frac{a}{r} \right)^5 \right),$$

where  $D$  is the free diffusion coefficient of the substance. The original Renkin equation also includes steric exclusion, which has already been written out in explicit form.

Although real pores are not ideal cylinders, it has been estimated that pores in skeletal and cardiac muscle restrict diffusion to the same degree as it would have been restricted by cylindrical pores of radius 4–5 nm [48], so we take 5 nm to be the pores radius of preexisting capillaries  $NC$ . For the modeling purposes, we assume that during normalization and denormalization of capillaries, i.e., transition from  $NC$  to  $AC$  and vice versa, their surface area, width of their walls, and the number of pores remain the same, whereas radii of all pores change identically. For the known value of permeability  $P_1$  in

case of free diffusion  $D_1$ , pores radius  $r_1$ , and molecules radius  $a_1$ , this approach allows us to obtain the value of permeability  $P_2$  under parameters  $D_2, r_2, a_2$ :

$$\frac{P_2(D_2, a_2, r_2)}{P_1(D_1, a_1, r_1)} = \frac{D'_2(D_2, a_2, r_2)A(a_2, r_2)}{D'_1(D_1, a_1, r_1)A(a_1, r_1)}.$$

The permeability of continuous capillaries for glucose has been estimated in experiments and is set to be  $P_{NC,G} = 1.1 \cdot 10^{-5}$  cm/s [495]. The hydrodynamic radius of glucose is 0.36 nm [496], and the one of bevacizumab is estimated to be 4.58 nm [497]. Diffusion coefficient of bevacizumab is estimated under assumption of inverse proportionality between diffusion coefficient and molecule radius, using the relevant values for VEGF as reference ones. This leads to the value of permeability of preexisting capillaries to bevacizumab  $P_{NC,A} = 1.6 \cdot 10^{-9}$  cm/s. Hydrodynamic radii of VEGF and free cisplatin are assessed to be 3 and 0.44 nm. For this prediction, one can use the formula  $r = 0.0483 \cdot M^{0.386}$  [498], where  $M$  is their molecular mass, expressed in daltons. The molecular mass is approximately  $4.5 \cdot 10^4$  for VEGF [499] and 300 for free cisplatin [500], so the value of permeability of normal capillaries for VEGF is  $P_{NC,V} = 6.4 \cdot 10^{-8}$  cm/s and for free cisplatin is  $P_{NC,Tf} = 8 \cdot 10^{-6}$  cm/s. Hydrodynamic radius of protein-bound cisplatin is assumed to be equal to the one of albumin, which is 3.5 nm [49]; permeability of normal capillaries for cisplatin is  $P_{NC,Tb} = 2.8 \cdot 10^{-8}$  cm/s. To obtain the value of permeability of angiogenic capillaries to all substances, we need to select the value of radius of their pores. We choose it to be equal to 7.5 nm. This yields

$$P_{AC,A} = 1.2 \cdot 10^{-7} \text{ cm/s}, P_{AC,V} = 7.8 \cdot 10^{-7} \text{ cm/s}, P_{AC,G} = 2.8 \cdot 10^{-5} \text{ cm/s}, \\ P_{AC,Tf} = 2.2 \cdot 10^{-5} \text{ cm/s}, \text{ and } P_{AC,Tb} = 4.5 \cdot 10^{-7} \text{ cm/s}.$$

#### 10.2.4 Initial and boundary conditions, numerical scheme

The system of Eqs. (10.1)–(10.5) is solved in one-dimensional domain of 1.5 cm diameter. Plane geometry is used for computational simplicity, since it does not affect the qualitative results compared with spherically symmetrical case. The initial and boundary conditions for all variables are defined to be:

$n_1(x, 0) = \max(0, 0.25[1 - (x/10)^2])$	$\frac{\partial n_1}{\partial x}(0, t) = 0$	$n_1(L, t) = 0$
$n_2(x, 0) = 0$	$\frac{\partial n_2}{\partial x}(0, t) = 0$	$n_2(L, t) = 0$
$h(x, 0) = 1 - n_1(x, 0) - IF(x, 0)$	$\frac{\partial h}{\partial x}(0, t) = 0$	$h(L, t) = 1 - IF(L, t)$
$IF(x, 0) = 0.2$	$\frac{\partial IF}{\partial x}(0, t) = 0$	$IF(L, t) = 0.2$
$m(x, 0) = 0$	$\frac{\partial m}{\partial x}(0, t) = 0$	$m(L, t) = 0$
$NC(x, 0) = 1$	$\frac{\partial NC}{\partial x}(0, t) = 0$	$NC(L, t) = 1$
$AC(x, 0) = 0$	$\frac{\partial AC}{\partial x}(0, t) = 0$	$AC(L, t) = 0$

---

$G(x, 0) \approx 5.24$	$\frac{\partial G}{\partial x}(0, t) = 0$	$\frac{\partial G}{\partial x}(L, t) = 0$
$V(x, 0) = 0$	$\frac{\partial V}{\partial x}(0, t) = 0$	$\frac{\partial V}{\partial x}(L, t) = 0$
$A(x, 0) = 0$	$\frac{\partial A}{\partial x}(0, t) = 0$	$\frac{\partial A}{\partial x}(L, t) = 0$
$T^f(x, 0) = 0$	$\frac{\partial T^f}{\partial x}(0, t) = 0$	$\frac{\partial T^f}{\partial x}(L, t) = 0$
$T^b(x, 0) = 0$	$\frac{\partial T^b}{\partial x}(0, t) = 0$	$\frac{\partial T^b}{\partial x}(L, t) = 0$
$\mathbf{v}(x, 0) = \mathbf{0}$	$\mathbf{v}(0, t) = \mathbf{0}$	

---

The initial conditions correspond to the normal tissue with a small colony of tumor cells located on the left border. The initial distribution of glucose is calculated assuming the steady-state concentration in a normal tissue. The initial distribution of IF is uniform. Its value is within physiologically justified range. IF inflow into tissue through normal capillaries is normalized in such a way that its distribution is stationary. Inflow of IF through angiogenic capillaries is taken to be five times greater. The values of variables of cells, necrosis, and microvasculature network on the right boundary correspond to the normal tissue.

To speed up the calculations, the equations for VEGF and glucose are solved in the quasi-stationary approximation. This is justified since these reactions have much higher rates compared with the rates for other variables. Quasi-stationary approximation leads to a system of algebraic equations with a tridiagonal matrix. Such matrices are easy to factorize and invert. For other variables, the splitting with respect to physical processes is used. Kinetic equations are solved via the fourth-order Runge–Kutta method, the Crank–Nicolson scheme is used for the diffusion equations, and convective equations are solved using flux-corrected transport scheme with explicit antidiffusion stage [501].

### 10.3 Optimization of protocol for combined antitumor chemo- and antiangiogenic therapy

#### 10.3.1 Simulation using the basic model parameters

We open this section by Fig. 10.3, which shows the distribution of model variables during CT by cisplatin combined with AAT by bevacizumab. Two schemes of drug administration are simulated. In both of them, a dose of cisplatin is injected every 3 weeks, and six injections are made. In scheme 1, injections of bevacizumab take place simultaneously with the ones of cisplatin, and its administration continues after the end of CT with the same periodicity. This scheme corresponds to the standard clinic protocol. In scheme 2, suggested herein, AAT begins with the last injection of cisplatin and continues as one injection in every 3 weeks. Fig. 10.3A refers to the day just before the start of therapy, and thus, it shows the structure of untreated tumor and its microenvironment, which adequately

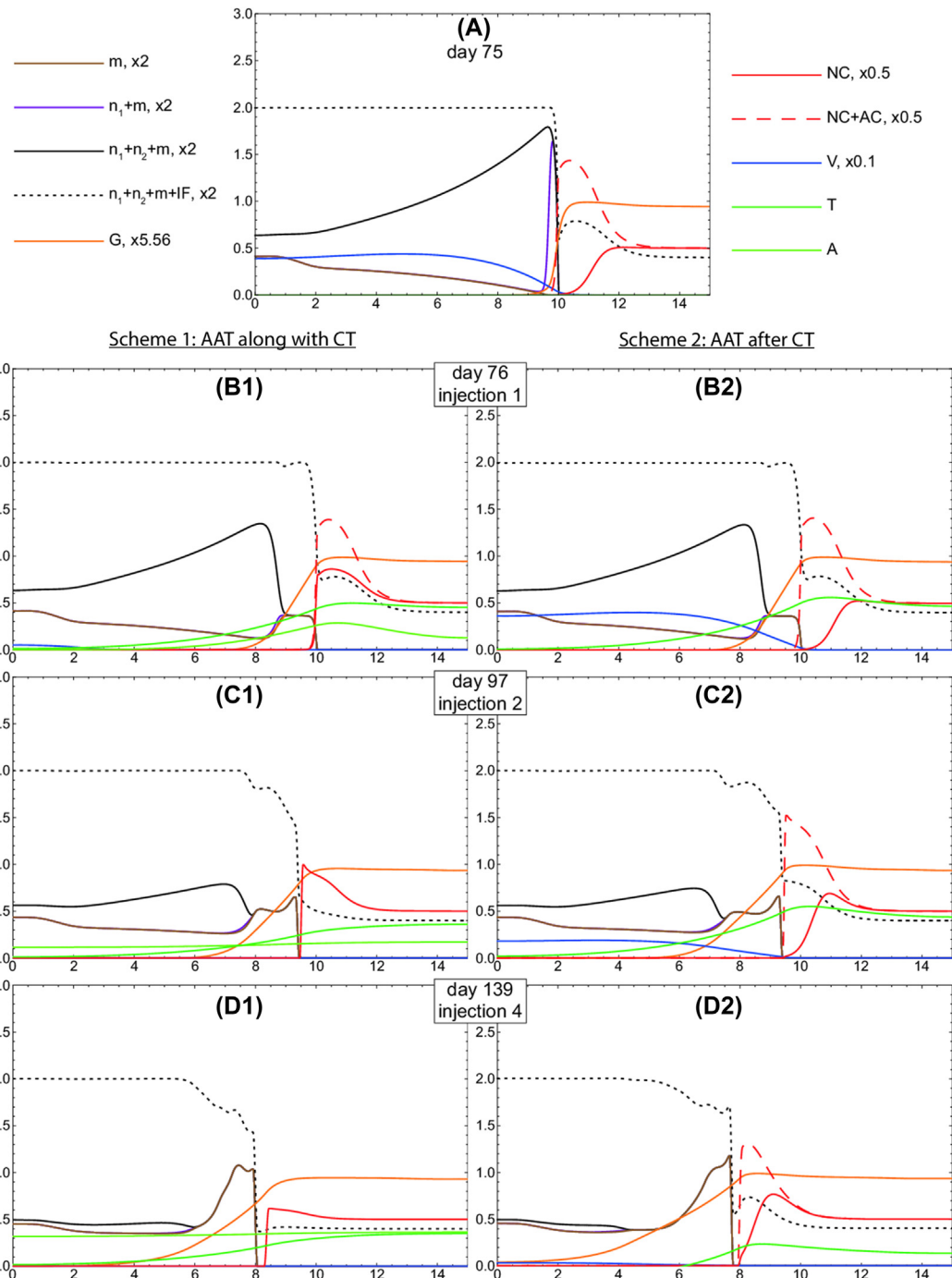


**Figure 10.3**

Profiles of proliferating tumor cells density  $n_1$ , quiescent tumor cells density  $n_2$ , fraction of cell remnants  $m$ , fraction of interstitial fluid  $IF$ , concentration of glucose  $G$ , normal microcirculatory network surface density  $NC$ , angiogenic microcirculatory network surface density  $AC$ , concentration of VEGF  $V$ , cisplatin  $T$ , and bevacizumab  $A$  under basic set of model parameters under different schemes of combined therapy: (A) on the day before therapy, (B1–E2) on the days of first, second, fourth, and sixth injections of drugs, and (F1–H2) after the end of chemotherapy.

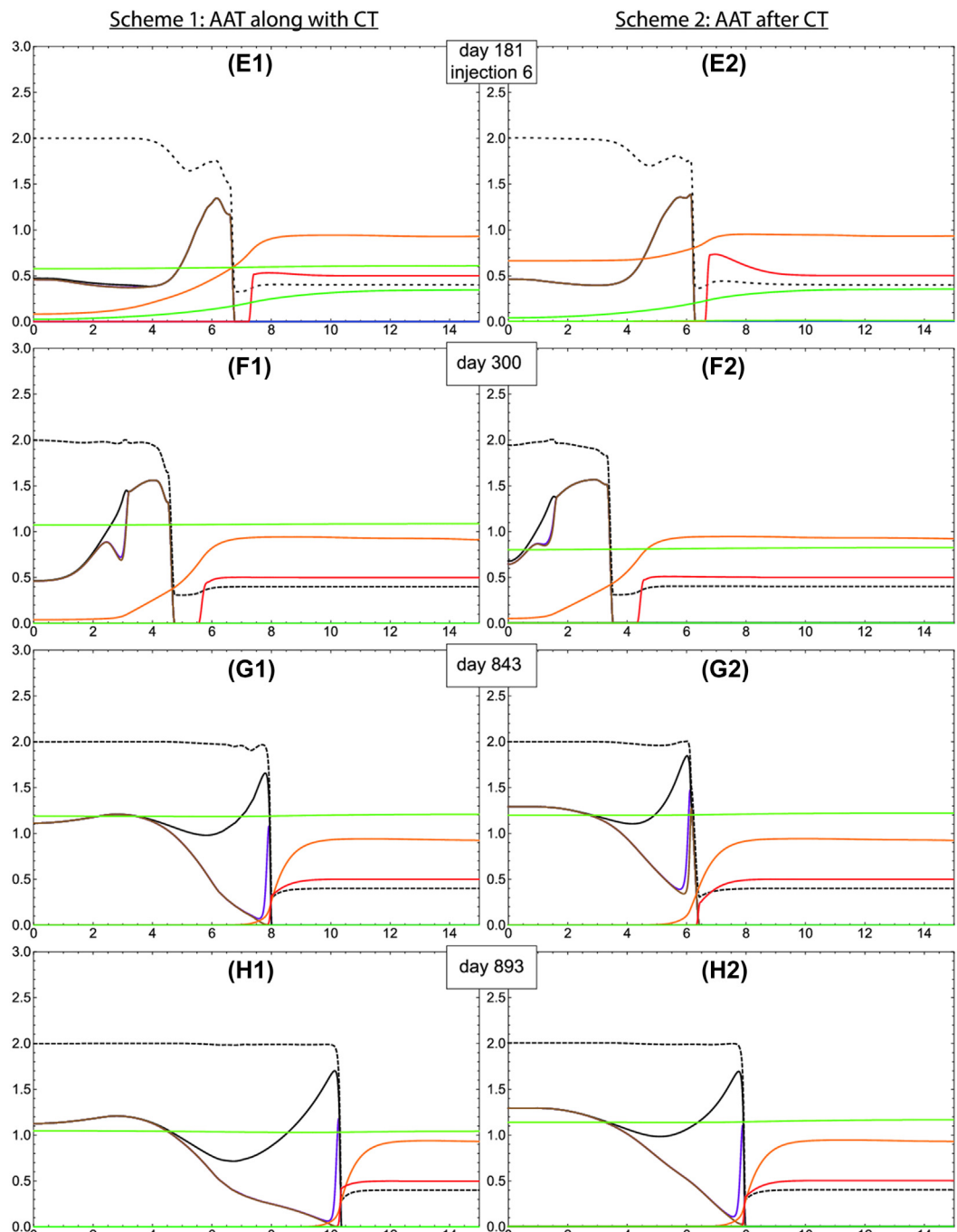


Figure 10.3

Cont'd.

resembles experimental observations. The tumor mass consists mainly of quiescent cells  $n_2$  and necrosis, which is formed from cell debris  $m$  and interstitial fluid  $IF$ . Inside the tumor, there are few capillaries, while the angiogenic part of the microvasculature network  $AC$  is situated mainly in the peritumoral area, where edema has been formed in result of increase in the inflow of  $IF$  due to the elevated capillary density and increased permeability of the walls of angiogenic capillaries. For the same reasons, this region provides increased inflow of glucose  $G$  to tumor cells, which governs the localization of proliferating cells  $n_1$  near the tumor boundary. However, this proximity of the proliferating cells to the capillaries makes them vulnerable to the action of cisplatin. The inflow of cisplatin into the tissue also depends on the number and state of the capillaries. Moreover, this dependence on the permeability of capillary network for cisplatin is more significant than for glucose, since a significant part of the drug enters the tissue in heavy protein-bound complex. For this complex, the ratio of permeability of capillaries of two types is significantly larger than for small molecules such as glucose or free cisplatin (i.e., 16 against about 2.5 for both, as follows from [Table 10.1](#)).

The day of the first injection of cisplatin is depicted in [Fig. 10.3B1,B2](#), where  $T = T^f + T^b$ . Here and further, number 1 denotes that the figure corresponds to the first scheme of simultaneous drug administration, and number 2 refers to the second scheme. The depth of glucose penetration into the tumor increases in result of death of proliferating cells, which are its main consumers. This leads to active transition of quiescent cells into the proliferative state, in which they also die under the action of a chemotherapeutic drug. Injection of bevacizumab (see [Fig. 10.3B1](#)) leads to rapid elimination of almost all free VEGF from tissue already on the first day of AAT. In turn, this provokes the cessation of angiogenesis and subsequent normalization of capillaries, described by the transition from  $AC$  to  $NC$ .

Only a fraction of tumor cells die due to the first injection of cisplatin, while the rest remain intact in depth of the tumor, where a sufficient amount of cisplatin does not penetrate. Subsequent injections of cisplatin, depicted in [Fig. 10.3C–E](#), lead to death of more and more deeply situated cells. However, in case of scheme 1, inflow of cisplatin decreases due to normalization of capillaries followed by normalization of microvasculature density that reduces efficiency of cisplatin action compared with ongoing scheme 2. On the other hand, the normalization of microvasculature also leads to the decrease in glucose inflow. This process is the main objective in prescribing AAT. Therefore, the tumor that undergoes the treatment by scheme 2 obtains more glucose, which allows it to partly recover between the injections. The degree of recovery is higher for scheme 2 than for scheme 1. However, greater inflow of glucose also facilitates the advantage of scheme 2 since cisplatin kills only proliferating cells. Thus, greater fraction of them, developed as a result of higher glucose inflow, promotes enhanced effective outcome of the following injection of cisplatin. Some alive cells in the center of the tumor

are distinguishable in Fig. 10.3E1, but not in Fig. 10.3E2. As both figures correspond to the day of the last injection of cisplatin, this confirms increased efficiency of scheme 2.

The prominent feature of AAT is the fact that its administration leads to the alleviation of peritumoral edema [502]. As it is shown in Fig. 10.3B1,C1,D1, the model adequately reproduces this effect. The normalization of the microvasculature structure and density leads to the decrease in inflow of IF from the capillaries into the tissue, and subsequent decrease in the level of IF near the tumor, while the outflow of IF remains almost unaltered (it even slightly increases since it depends on fraction of normal cells, which grows with the decline of IF fraction). Thus, as variables in peritumoral region return to the values, corresponding to normal tissue, the equilibrium of IF also returns to the healthy level. This leads to the increase in outflow of IF from interior of the tumor, which depends on the difference in fractions of IF inside and outside the tumor. This more intensive outflow yields some reduction of tumor volume. However, as it is seen in

Fig. 10.3C2,D2,E2, simulated CT turns out to be effective enough to kill sufficient amount of tumor cells to significantly decrease VEGF level. Thus, this treatment in the absence of AAT also leads to the cessation of angiogenesis, normalization of microvasculature, and eventually the alleviation of peritumoral edema and tumor shrinkage. Therefore, sufficiently strong CT reproduces qualitatively this feature of AAT but takes longer time for it. Moreover, as it is seen from the comparison of tumors radii in Fig. 10.3E1,E2, in case of mono-CT, the tumor volume decreases even faster.

An ultimately successful therapy would lead to the elimination of all tumor cells. However, if some cells remain alive deep inside the necrotic mass (in the mathematical model there is always a small nonzero cells density), this leads to slow tumor regrowth, which is seen in Fig. 10.3F–H. The rate of this regrowth depends on the amount of glucose that proliferating cells obtain. Thus, it is clear that continuous administration of antiangiogenic drug after the end of CT will restrain the tumor regrowth, which is the standard clinical practice [450]. However, in scheme 2 there are fewer cells left inside the necrosis after CT and they are located deeper. Hence, it takes longer time for the tumor to regrow. In Fig. 10.3G1,H2, where two tumors have grown to the same radius of 8 mm, scheme 2 provides additional delay of 50 days in tumor regrowth compared with scheme 1. Thus, the suggested scheme of subsequent administration of CT and AAT turns out to be more effective not only in terms of killed cells and degree of tumor shrinkage (both factors are important for neoadjuvant, or preoperative, therapy) but also in terms of time of tumor regrowth (a factor significant for palliative therapy). Note that although it is not clear from Fig. 10.3E2, the first injection of bevacizumab in scheme 2 takes place on the day of the last injection of cisplatin. However, bevacizumab concentration in tissue rises slowly due to the lower permeability of walls of continuous capillaries.

### 10.3.2 Variation of parameters

Figs. 10.4 and 10.5 demonstrate, respectively, the number of living tumor cells and tumor radius over time under three types of treatment: (1) combined CT+AAT, in which bevacizumab is administered simultaneously with cisplatin and AAT is continued after CT with the same interval between injections (widely used clinical scheme, denoted as scheme 1 in Section 10.3.1, red line); (2) combined CT+AAT, in which bevacizumab administration starts with the last injection of cisplatin and continues with 3 weeks' intervals (the scheme, suggested herein and denoted as scheme 2 in Section 10.3.1, green line); (3) mono-CT, consisting of six cisplatin injections with intervals of 3 weeks (black line). The figures are obtained for different values of parameters of tumor cells sensitivity to cisplatin  $k_T$ , which is both drug- and tumor-related parameter, and the rate of nonspecific binding of cisplatin to tissue elements  $d_T$ , which is a patient-related parameter. Cisplatin actively binds to collagen, so its concentration in tissue largely affects the latter parameter. The lower the value of  $d_T$ , the deeper the cisplatin penetrates inside the tumor. The central Figs. 10.4E and 10.5E correspond to the model simulation considered in detail in Section 10.3.1.

These figures demonstrate that the efficiency of any chosen type of treatment—measured in minimum number of living cells, degree of tumor shrinkage, and delay in tumor regrowth—expectedly increases with increase in  $k_T$  and decrease in  $d_T$ . Note that the tumor regrowth rate after treatment is lower than before therapy. This occurs due to the fact that, during regrowth, tumor cells are situated deep inside the tumor on significant distance from the capillaries. When living tumor cells reach the vascular areas, the rate of tumor growth increases. In the case of mono-CT, it reaches its pretreatment level, whereas AAT slows down the rate of recurrent tumor growth about three times. This delay results from the decrease in fraction of proliferating tumor cells caused by glucose shortage.

The relative gain in the efficiency of schemes depends on the values of varied parameters. Scheme 2 remains more efficient under any combination of them for both neoadjuvant and palliative therapy except the long-term palliative therapy under highest  $k_T$  and lowest  $d_T$  depicted in Figs. 10.4G and 10.5G. This is explained by the fact that at the end of mono-CT conducted in scheme 2, microvasculature is located closer to the remaining tumor cells than in scheme 1. The latter happens, since tumor volume is reduced more in this case, as it was noted in Section 10.3.1, which partly fosters the rate of tumor regrowth and may alter the result of relative efficiency of two considered schemes in the long run. However, in this case all the tumor cells are already killed during CT. Thus, no optimization of the treatment is required.

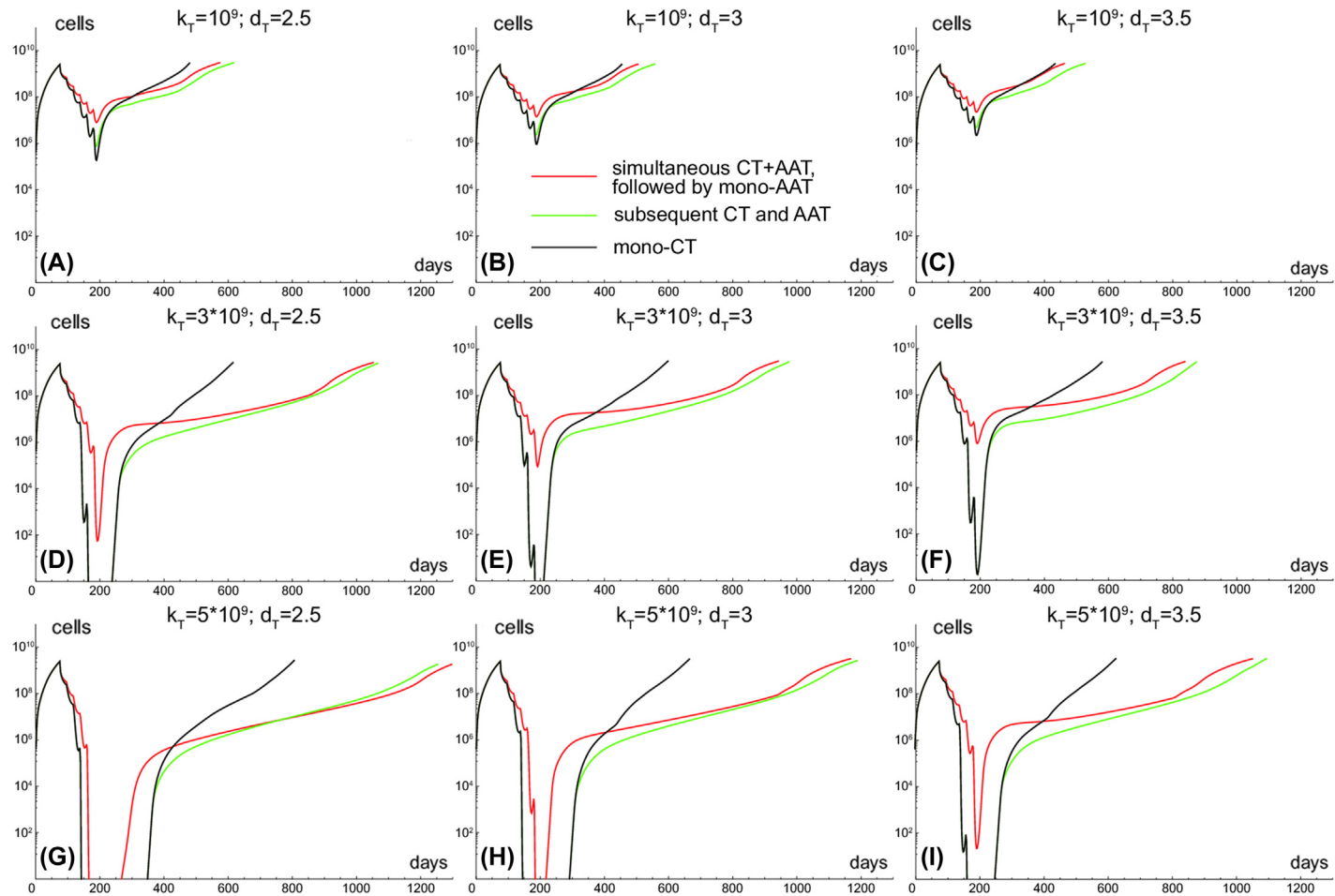


Figure 10.4

The number of living tumor cells over time for nine (A-I) pairs of parameters: tumor cell sensitivity to cisplatin  $k_T = 10^9$ ;  $3 \cdot 10^9$ ;  $5 \cdot 10^9$  and nonspecific binding of cisplatin  $d_T = 2.5$ ; 3; 3.5. There are three types of treatment at each graph: (1) simultaneous combined CT+AAT, followed by mono-AAT (red line[gray line in print version]); (2) subsequent CT and AAT (green line[light gray line in print version]); (3) mono-CT (black line). Every CT includes six cisplatin injections; drugs are administered with intervals of 3 weeks. AAT, antiangiogenic therapy; CT, chemotherapy.

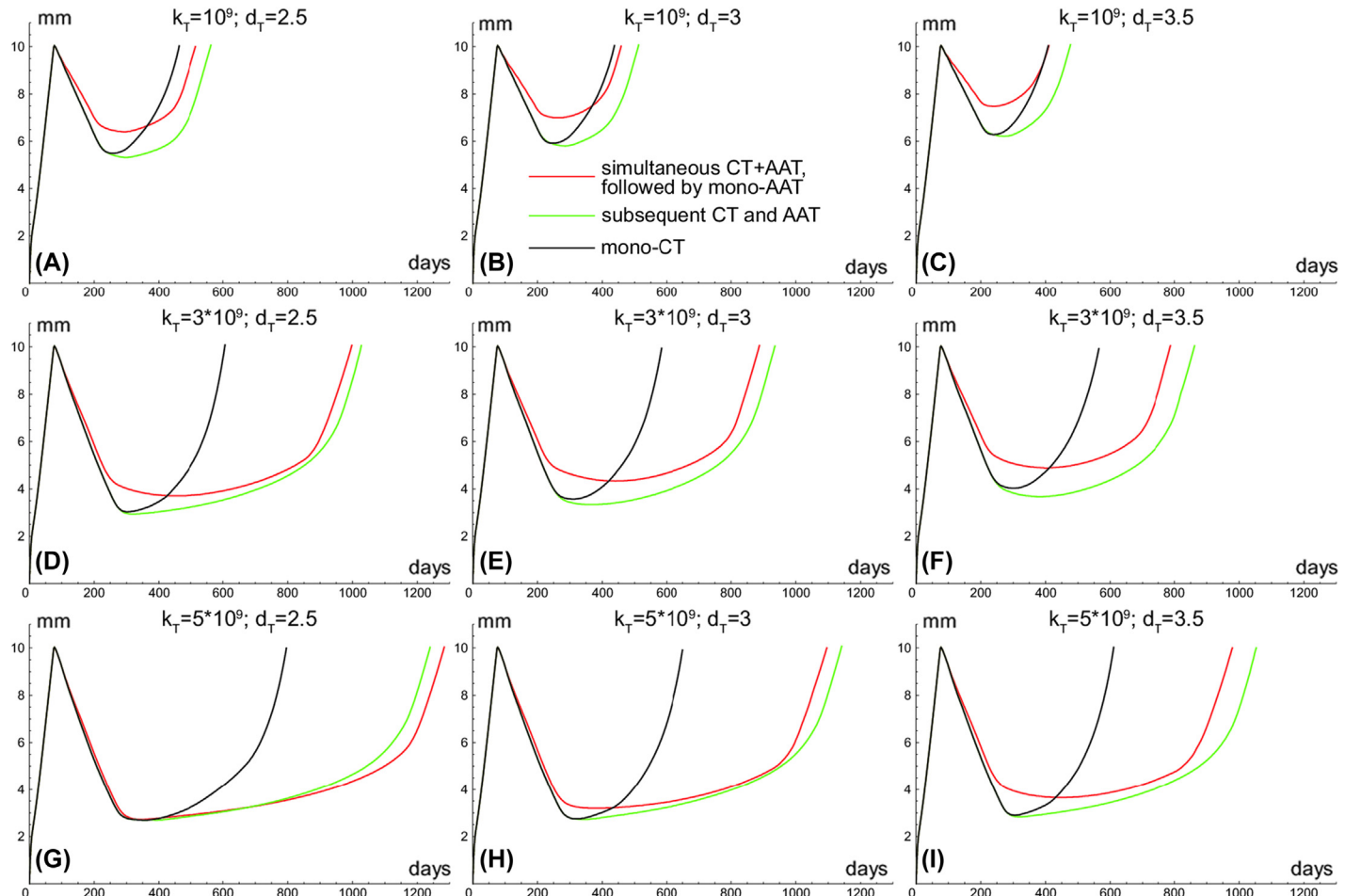


Figure 10.5

Tumor radius over time for nine (A-I) pairs of parameters: tumor cell sensitivity to cisplatin  $k_T = 10^9; 3 \cdot 10^9; 5 \cdot 10^9$  and nonspecific binding of cisplatin  $d_T = 2.5; 3; 3.5$ . There are three types of treatment at each graph: (1) simultaneous combined CT+AAT, followed by mono-AAT (red line[gray line in print version]); (2) subsequent CT and AAT (green line[light gray line in print version]); (3) mono-CT (black line). Every CT includes six cisplatin injections; drugs are administered with intervals of 3 weeks. AAT, antiangiogenic therapy; CT, chemotherapy.

Note that Fig. 10.4D–I suggests that there exists a region in the parameter space, where the usage of scheme 2 leads to the death of virtually all tumor cells, which means a complete recovery of the patient. Moreover, the simulations predict that starting AAT at the very beginning of medical treatment hinders the penetration of cisplatin inside the tumor so that some tumor cells still remain alive by the end of therapy. Of course, as already noted, increase in  $k_T$  and decrease in  $d_T$  lead to death of all tumor cells even under using of scheme 1. However, this implies the increased damage to the whole organism. The ability of scheme 2 to reach the same antitumor effect with reduced side effects is of particular importance.

## Conclusions

In this chapter, we introduced and studied a spatially distributed model of tumor growth and combined chemo- and antiangiogenic therapy. The distinctive features of this model are (1) the ability to account for convective flows emerging in tumor and surrounding tissue during its growth; (2) the explicit consideration of increased permeability of tumor capillaries; and (3) the inclusion of dynamics of IFs. The description of IF dynamics is rather schematic, but even on this stage of development, it successfully allows us to reproduce the tumor shrinkage during neoadjuvant therapy and to obtain the main result of this investigation, i.e., to suggest an optimization of the administration scheme of combined CT and AAT. It was proposed that the administration of AAT after CT results in a better total efficiency in both neoadjuvant (preoperative) and palliative settings compared with widely used simultaneous drug administration. The idea of the proposed scheme is to take an advantage of increased permeability of tumor capillaries, due to which an increased amount of chemotherapeutic drug would flow into the tumor tissue.

Although the detailed study was performed here only with two particular drugs, i.e., bevacizumab and cisplatin, the results may be projected to therapy with other agents and should be checked by in vitro experiments. Of course, individual properties of specific agents may alter the final results. For instance, experiments on mice models with combined administration of cyclophosphamide and bevacizumab [503] demonstrated the best antitumor effect when cyclophosphamide was administered 2 days after bevacizumab. However, it is well known that the cyclophosphamide action is mediated through its toxic metabolites, which production is impaired in actively proliferating tissues [504]. Hence, the slow down of tumor tissue proliferation rate during antiangiogenic therapy leads to increased efficiency of cyclophosphamide and can be the reason of observed experimental results. Although the peculiarities of the action of a cytotoxic agent can affect the effectiveness of various schemes of its administration, for most phase-specific cytotoxic antitumor drugs similar to cisplatin (carboplatin, paclitaxel, topotecan, etc.), the considered model is adequate. Therefore, the proposed new scheme of combined CT and AAT

administration is not only interesting from a theoretical point of view but is also promising for clinical research.

As a model assumption, we neglected the convective part of substances transvascular transport. The justification of such approach for glucose, VEGF, and bevacizumab was given in [Section 10.2](#). At the same time, the antiangiogenic drug therapy often leads to the interstitial pressure drop. Therefore, AAT may temporarily increase the rate of substances transvascular convection, and this fosters the inflow of chemotherapeutic agent into the tumor. However, this possible improvement is only short-term, since the rapid decrease of capillaries permeability in the absence of free VEGF ultimately leads to the diminished diffusive and convective inflow of the drug. Thus, this effect, if manifested, may support only the first injection of chemotherapeutic drug, while the other injections would be compromised by the normalization of microvasculature. Note that in corresponding experimental settings, often only one dose of antiangiogenic and chemotherapeutic drugs is given, without considering the whole course (see, e.g., Ref. [493]). Moreover, our study demonstrates that, under sufficiently strong CT, the normalization of microvasculature also takes place due to the fact that VEGF level falls drastically under the decreased number of tumor cells. We may conclude that the drop of the interstitial pressure, although delayed, would also take place in this case and promote the chemotherapeutic agent inflow the same way. Nevertheless, we believe that this effect should be studied separately by the means of mathematical modeling. It is also of interest to investigate the present model coupled with the model of microvasculature. This study would allow to identify the parameter range where such “normalization window” may affect the obtained result. To describe this effect in a general model, it is necessary to explicitly introduce the pressure of the IF. In turn, the pressure would define fluxes in the tissue through the Darcy law. An important personalized parameter of the model in this case would be the value of dynamic viscosity, which depends not only on the density of malignant and normal cells but also on the amount of the extracellular matrix compounds. We also recall that the extracellular matrix is largely responsible for the nonspecific binding of low-molecular-weight antitumor drugs that reduces the efficacy. One further research direction is the development of a more detailed and physiologically reasonable description of IF dynamics and to consider extracellular matrix as independent factor that dictates a need for personalized approach in clinic.

# Bibliography

- [1] P.C. Franzzone, L.F. Pavarino, S. Scacchi, Mathematical Cardiac Electrophysiology, vol. 13, Springer, 2014.
- [2] G. Kassab, Coronary Circulation, Springer International Publishing, 2019.
- [3] M.R. Labrosse (Ed.), Cardiovascular Mechanics, Taylor & Francis Group, LLC, 2019.
- [4] A. Quarteroni, L. Dede', A. Manzoni, C. Vergara, Mathematical Modelling of the Human Cardiovascular System: Data, Numerical Approximation, Clinical Applications, Cambridge University Press, 2019.
- [5] J. Tu, K. Inthavong, K.K.L. Wong, Computational Hemodynamics – Theory, Modelling and Applications, Springer Netherlands, 2015.
- [6] N. Westerhof, N. Stergiopoulos, M.I.M. Noble, Snapshots of Hemodynamics, 2 edition, vol. 5, Springer, 2010.
- [7] J. Bayer, R. Blake, G. Plank, N. Trayanova, A novel rule-based algorithm for assigning myocardial fiber orientation to computational heart models, *Ann. Biomed. Eng.* 40 (10) (2012) 2243–2254.
- [8] F. Pashakhanloo, D. Herzka, H. Ashikaga, S. Mori, N. Gai, D. Bluemke, N. Trayanova, E. McVeigh, Myofiber architecture of the human atria as revealed by submillimeter diffusion tensor imaging, *Circulation* 9 (4) (2016) e004133.
- [9] M. Sulkin, F. Yang, K. Holzem, C. Van Leer, B. Bugge, J. Laughner, K. Green, I. Efimov, Nanoscale three-dimensional imaging of the human myocyte, *J. Struct. Biol.* 188 (1) (2014) 55–60.
- [10] R. Clayton, A. Panfilov, A guide to modelling cardiac electrical activity in anatomically detailed ventricles, *Prog. Biophys. Mol. Biol.* 96 (1–3) (2007) 19–43.
- [11] K.H. Tusscher, A.V. Panfilov, Modelling of the ventricular conduction system, *Prog. Biophys. Mol. Biol.* 96 (2008) 152–170.
- [12] R. Aliev, A. Panfilov, A simple two-variable model of cardiac excitation, *Chaos Solit. Fractals* 7 (3) (1996) 293–301.
- [13] R. Aliev, A. Panfilov, Modeling of heart excitation patterns caused by a local inhomogeneity, *J. Theor. Biol.* 181 (1) (1996) 33–40.
- [14] I. Efimov, V. Sidorov, Y. Cheng, B. Wollenzien, Evidence of three-dimensional scroll waves with ribbon-shaped filament as a mechanism of ventricular tachycardia in the isolated rabbit heart, *J. Cardiovasc. Electrophysiol.* 10 (11) (1995) 1452–1462.
- [15] D. Nickerson, N. Smith, P. Hunter, A model of cardiac cellular electromechanics, *Philos. Trans. R. Soc. Lond. A* 359 (1783) (2001) 1159–1172.
- [16] H.-T. Shih, Anatomy of the action potential in the heart, *Mol. Cell. Cardiol.* 21 (1) (1994) 30–41.
- [17] Y. Vassilevski, A. Danilov, T. Gamilov, Y. Ivanov, R. Pryamonosov, S. Simakov, Patient-specific anatomical models in human physiology, *Russ. J. Numer. Anal. Math. Model.* 30 (3) (2015) 185–201.
- [18] S. Sovilj, R. Magjarevi, A. Al Abed, N. Lovell, S. Dokos, Simplified 2D bidomain model of whole heart electrical activity and ECG generation, *Meas. Sci. Rev.* 14 (3) (2014) 136–143.
- [19] H. Parlakpinar, M. Orum, M. Sagir, Pathophysiology of myocardial ischemia reperfusion injury: a review, *Med. Sci.* 2 (4) (2013) 935–954.
- [20] J. Anderson, D. Morrow, Acute myocardial infarction, *N. Engl. J. Med.* 376 (2017).
- [21] H. Shimokawa, S. Yasuda, Myocardial ischemia: current concepts and future perspectives, *J. Cardiol.* 52 (2) (2008) 67–78.
- [22] C. Katikireddy, N. Mann, D. Brown, A. Van Tosh, K. Stergiopoulos, Evaluation of myocardial ischemia and viability by noninvasive cardiac imaging, *Expert Rev. Cardiovasc. Ther.* 10 (1) (2012) 55–73.
- [23] P. Dobrin, Mechanics of normal and diseased blood vessels, *Ann. Vasc. Surg.* 2 (3) (1988) 283–294.

- [24] R. Armentano, J. Megnien, A. Simon, F. Bellenfant, J. Barra, J. Levenson, Effect of hypertension on viscoelasticity of carotid and femoral arteries in humans, *Hypertension* 26 (1) (1995) 48–54.
- [25] J. Cameron, Estimation of arterial mechanics in clinical practice and as a research technique, *Clin. Exp. Pharmacol. Physiol.* 26 (4) (1999) 285–294.
- [26] S. Greenwald, C. Berry, Improving vascular grafts: the importance of mechanical and haemodynamic properties, *J. Pathol.* 190 (3) (2000) 292–299.
- [27] B. Levy, Mechanics of the large artery vascular wall, *Pathol. Biol.* 47 (6) (1999) 634–640.
- [28] G. McVeigh, P. Hamilton, D. Morgan, Evaluation of mechanical arterial properties: clinical, experimental and therapeutic aspects, *Clin. Sci.* 102 (1) (2002) 51–67.
- [29] R. Vito, S. Dixon, Blood vessel constitutive models—1995–2002, *Annu. Rev. Biomed. Eng.* 5 (2003).
- [30] S. Balocco, O. Basset, G. Courbebaisse, E. Boni, A. Frangi, P. Tortoli, C. Cachard, Estimation of the viscoelastic properties of vessel walls using a computational model and Doppler ultrasound, *Phys. Med. Biol.* 55 (12) (2010) 3557–3575.
- [31] M. Orosz, G. Molnárka, G. Ndasy, G. Raffai, G. Kozmann, E. Monos, Validity of viscoelastic models of blood vessel wall, *Acta Physiol. Hung.* 86 (3–4) (1999) 265–271.
- [32] P. Johnson, Autoregulation of blood flow, *Circ. Res.* 59 (5) (1986) 483–495.
- [33] B. Blackman, G. García-Cardeña, M. Gimbrone, A new in vitro model to evaluate differential responses of endothelial cells to simulated arterial shear stress waveforms, *J. Biomech. Eng.* 124 (4) (2002) 397–407.
- [34] O. Traub, B. Berk, Laminar shear stress: mechanisms by which endothelial cells transduce an atheroprotective force, *Arterioscler. Thromb. Vasc. Biol.* 18 (5) (1998) 677–685.
- [35] B. Carlson, J. Arciero, T. Secomb, Theoretical model of blood flow autoregulation: roles of myogenic, shear-dependent, and metabolic responses, *Am. J. Physiol. Heart Circ. Physiol.* 295 (4) (2008) H1572–H1579.
- [36] M. O'Rourke, A. Pauca, X.-J. Jiang, Pulse wave analysis, *J. Clin. Pharmacol.* 51 (6) (2001) 507–522.
- [37] I. Sazonov, A. Khir, W. Hacham, E. Boileau, J. Carson, R. van Loon, C. Ferguson, P. Nithiarasu, A novel method for non-invasively detecting the severity and location of aortic aneurysms, *Biomech. Model. Mechanobiol.* 16 (4) (2017) 1225–1242.
- [38] T. Du, D. Hu, D. Cai, A fast algorithm for the simulation of arterial pulse waves, *J. Comput. Phys.* 314 (2016).
- [39] N. de Moura, I. Cordovil, A. de S Ferreira, Traditional Chinese medicine wrist pulse-taking is associated with pulse waveform analysis and hemodynamics in hypertension, *J. Integr. Med.* 14 (2) (2016) 100–113.
- [40] A. Baskurt, H. Meiselman, Blood rheology and hemodynamics, *Semin. Thromb. Hemost.* 29 (5) (2003) 435–450.
- [41] F. Yilmaz, M. Gundogdu, A critical review on blood flow in large arteries; relevance to blood rheology, viscosity models, and physiologic conditions, *Korea Aust. Rheol. J.* 20 (4) (2008) 197–211.
- [42] A.S. Popel, P.C. Johnson, Microcirculation and hemorheology, *Annu. Rev. Fluid Mech.* 37 (2005) 43–69.
- [43] N. Bessonov, A. Sequeira, S. Simakov, Y. Vassilevski, V. Volpert, Methods of blood flow modelling, *Math. Model. Nat. Phenom.* 11 (1) (2016) 1–25.
- [44] G. Zvodszyk, B. van Rooij, V. Azizi, A. Hoekstra, Cellular level in-silico modeling of blood rheology with an improved material model for red blood cells, *Front. Physiol.* 8 (563) (2017) 1–14.
- [45] G. Clough, C. Michel, The role of vesicles in the transport of ferritin through frog endothelium, *J. Physiol.* 315 (1) (1981) 127–142.
- [46] M. Intaglietta, P.C. Johnson, R.M. Winslow, Microvascular and tissue oxygen distribution, *Cardiovasc. Res.* 32 (4) (1996) 632–643.
- [47] M. Bundgaard, The three-dimensional organization of tight junctions in a capillary endothelium revealed by serial-section electron microscopy, *J. Ultrastruct. Res.* 88 (1) (1984) 1–17.
- [48] J. Pappenheimer, E. Renkin, L. Borrero, Filtration, diffusion and molecular sieving through peripheral capillary membranes, *Am. J. Physiol. Legacy Content* 167 (1) (1951) 13–46.

- [49] J.R. Levick, An Introduction to Cardiovascular Physiology, Butterworth-Heinemann, 2013.
- [50] A. Carreau, B.E. Hafny-Rahbi, A. Matejuk, C. Grillon, C. Kieda, Why is the partial oxygen pressure of human tissues a crucial parameter? Small molecules and hypoxia, *J. Cell Mol. Med.* 15 (6) (2011) 1239–1253.
- [51] M.A. Febbraio, A. Steensberg, R.L. Starkie, G.K. McConell, B.A. Kingwell, Skeletal muscle interleukin-6 and tumor necrosis factor- $\alpha$  release in healthy subjects and patients with type 2 diabetes at rest and during exercise, *Metab. Clin. Exp.* 52 (7) (2003) 939–944.
- [52] J.R. Levick, C.C. Michel, Microvascular fluid exchange and the revised Starling principle, *Cardiovasc. Res.* 87 (2) (2010) 198–210.
- [53] W. Risau, Mechanisms of angiogenesis, *Nature* 386 (6626) (1997) 671.
- [54] D. Hanahan, R.A. Weinberg, Hallmarks of cancer: the next generation, *Cell* 144 (5) (2011) 646–674.
- [55] J.C. Lasheras, The biomechanics of arterial aneurysms, *Annu. Rev. Fluid Mech.* 39 (2007) 293–319.
- [56] D. Sforza, C. Putman, J. Cebral, Hemodynamics of cerebral aneurysms, *Annu. Rev. Fluid Mech.* 41 (2007) 91–107.
- [57] E. Fries, Hemodynamic changes in hypertension, *Med. Clin. North. Am.* 45 (2) (1961) 239–245.
- [58] A. Wassef, W. Lim, C. Wu, Indications, complications and outcomes of inferior vena cava filters: a retrospective study, *Thromb. Res.* 153 (2017).
- [59] Y. Vassilevski, S. Kapranov, Parallel modeling of blood flow peculiarities in the vicinity of cava filter with captured clot, *Math. Model.* 17 (11) (2005) 3–15 (in Russian).
- [60] Y. Vassilevski, S. Simakov, S. Kapranov, A multi-model approach to intravenous filter optimization, *Numer. Methods Biomed. Eng.* 26 (7) (2010) 915–925.
- [61] X. Xu, K. Eckerman (Eds.), *Handbook of Anatomical Models for Radiation Dosimetry*, Taylor & Francis, 2009.
- [62] M. Cristy, Development of mathematical pediatric phantoms for internal dose calculations: successes, limitations, and prospects, *Int. J. Nucl. Med. Biol.* 10 (1) (1983) 54.
- [63] M. Caon, Voxel-based computational models of real human anatomy: a review, *Radiat. Environ. Biophys.* 42 (4) (2004) 229–235.
- [64] F. Dazzo, B. Niccum, Use of CMEIAS image analysis software to accurately compute attributes of cell size, morphology, spatial aggregation and color segmentation that signify *in situ* ecophysiological adaptations in microbial biofilm communities, *Computation* 3 (1) (2015) 72–98.
- [65] A. Kislytsyn, R. Savinkov, M. Novkovic, L. Onder, G. Bocharov, Computational approach to 3D modeling of the lymph node geometry, *Computation* 3 (2) (2015) 222–234.
- [66] I. Sazonov, S.Y. Yeo, R.L.T. Bevan, X. Xie, R. van Loon, P. Nithiarasu, Modelling pipeline for subject-specific arterial blood flow – A review, *Int. J. Numer. Methods Biomed. Eng.* 27 (12) (2011) 1868–1910.
- [67] A. Quarteroni, M. Tuveri, A. Veneziani, Computational vascular fluid dynamics: problems, models and methods, *Comput. Visual. Sci.* 2 (4) (2000) 163–197.
- [68] J.-F. Gerbeau, M. Vidrascu, P. Frey, Fluid–structure interaction in blood flows on geometries based on medical imaging, *Comput. Struct.* 83 (2–3) (2005) 155–165.
- [69] M. Holtzman-Gazit, R. Kimmel, N. Peled, D. Goldsher, Segmentation of thin structures in volumetric medical images, *IEEE Trans. Image Process.* 15 (2) (2006) 354–363.
- [70] A.G. Radaelli, J. Peiró, On the segmentation of vascular geometries from medical images, *Int. J. Numer. Methods Biomed. Eng.* 26 (1) (2010) 3–34.
- [71] S.Y. Yeo, X. Xie, I. Sazonov, P. Nithiarasu, Segmentation of biomedical images using active contour model with robust image feature and shape prior, *Int. J. Numer. Methods Biomed. Eng.* 30 (2) (2014) 232–248.
- [72] T. Rohlfing, R. Brandt, R. Menzel, D.B. Russakoff, C.R. Maurer, Quo vadis, atlas-based segmentation? in: *Topics in Biomedical Engineering International Book Series* Springer US, 2005, pp. 435–486.
- [73] I. Isgum, M. Staring, A. Rutten, M. Prokop, M. Viergever, B. van Ginneken, Multi-atlas-based segmentation with local decision fusion – application to cardiac and aortic segmentation in CT scans, *IEEE Trans. Med. Imaging* 28 (7) (2009) 1000–1010.

- [74] H. Wang, J.W. Suh, S.R. Das, J.B. Pluta, C. Craige, P.A. Yushkevich, Multi-atlas segmentation with joint label fusion, *IEEE Trans. Pattern Anal. Mach. Intell.* 35 (3) (2013) 611–623.
- [75] R.M. Haralick, L.G. Shapiro, *Computer and Robot Vision*, first ed., Addison-Wesley Longman Publishing Co., Inc., Boston, MA, USA, 1992.
- [76] S. Golomb, Run-length encodings (corresp.), *IEEE Trans. Inf. Theory* 12 (3) (1966) 399–401.
- [77] N. Nikopoulos, I. Pitas, An efficient algorithm for 3D binary morphological transformations with 3D structuring elements of arbitrary size and shape, in: *Proceedings of 1997 IEEE Workshop on Nonlinear Signal and Image Processing (NSIP'97)*, 1997.
- [78] L. Vincent, Morphological transformations of binary images with arbitrary structuring elements, *Signal Process.* 22 (1) (1991) 3–23.
- [79] P.A. Yushkevich, Y. Gao, G. Gerig, ITK-SNAP: An interactive tool for semi-automatic segmentation of multi-modality biomedical images, in: *2016 38th Annual International Conference of the IEEE Engineering in Medicine and Biology Society (EMBC)*, IEEE, 2016.
- [80] A. Buades, B. Coll, J.M. Morel, A review of image denoising algorithms, with a new one, *Multiscale Model. Simul.* 4 (2) (2005) 490–530.
- [81] P.A. Yushkevich, J. Piven, H.C. Hazlett, R.G. Smith, S. Ho, J.C. Gee, G. Gerig, User-guided 3D active contour segmentation of anatomical structures: significantly improved efficiency and reliability, *Neuroimage* 31 (3) (2006) 1116–1128.
- [82] K. Pearson, On lines and planes of closest fit to systems of points in space, *Philos. Mag.* 2 (11) (1901) 559–572.
- [83] H. Tek, M.A. Gulsun, S. Laguitton, L. Grady, D. Lesage, G. Funka-Lea, Automatic coronary tree modeling, in: *The Midas Journal – 2008 MICCAI Workshop Grand Challenge Coronary Artery Tracking*, 2008. URL, <http://hdl.handle.net/10380/1426>.
- [84] L. Grady, Fast, quality, segmentation of large volumes – Isoperimetric distance trees, in: A. Leonardis, H. Bischof, A. Pinz (Eds.), *Computer Vision – ECCV 2006*, Vol. 3953 of *Lecture Notes in Computer Science*, Springer Berlin Heidelberg, 2006, pp. 449–462.
- [85] R.O. Duda, P.E. Hart, Use of the Hough transformation to detect lines and curves in pictures, *Commun. ACM* 15 (1) (1972) 11–15.
- [86] A.F. Frangi, W.J. Niessen, K.L. Vincken, M.A. Viergever, Multiscale vessel enhancement filtering, in: *Medical Image Computing and Computer-Assisted Intervention — MICCAI'98*, Springer Berlin Heidelberg, 1998, pp. 130–137.
- [87] L.M. Florack, B.M. ter Haar Romeny, J.J. Koenderink, M.A. Viergever, Scale and the differential structure of images, *Image Vis. Comput.* 10 (1992) 376–388.
- [88] T. Lindeberg, Edge detection and ridge detection with automatic scale selection, in: *Computer Vision and Pattern Recognition, 1996. Proceedings CVPR '96, 1996 IEEE Computer Society Conference on*, 1996, pp. 465–470.
- [89] G. Yang, P. Kitslaar, M. Frenay, A. Broersen, M.J. Boogers, J.J. Bax, J.H.C. Reiber, J. Dijkstra, Automatic centerline extraction of coronary arteries in coronary computed tomographic angiography, *Int. J. Cardiovasc. Imaging* 28 (2012) 921–933.
- [90] H.A.F. Gratama van Andel, H.W. Venema, G.J. Streekstra, M. van Straten, C.B. Majoe, G.J. den Heeten, C.A. Grimbergen, Removal of bone in CT angiography by multiscale matched mask bone elimination, *Med. Phys.* 34 (10) (2007) 3711–3723.
- [91] Z. Wu, J.M. Sullivan, Multiple material marching cubes algorithm, *Int. J. Numer. Methods Eng.* 58 (2) (2003) 189–207.
- [92] G. Taubin, A signal processing approach to fair surface design, in: *Proceedings of the 22nd Annual Conference on Computer Graphics and Interactive Techniques — SIGGRAPH 95*, ACM Press, 1995, pp. 351–358.
- [93] P.J. Frey, P.-L. George, *Mesh Generation: Application to Finite Elements*, ISTE, 2008.
- [94] A.A. Danilov, Unstructured tetrahedral mesh generation technology, *Comput. Math. Math. Phys.* 50 (1) (2010) 139–156.

- [95] L. Rineau, M. Yvinec, A generic software design for Delaunay refinement meshing, *Comput. Geom.* 38 (1–2) (2007) 100–110.
- [96] J. Escobar, E. Rodríguez, R. Montenegro, G. Montero, J. González-Yuste, Simultaneous untangling and smoothing of tetrahedral meshes, *Comput. Methods Appl. Mech. Eng.* 192 (25) (2003) 2775–2787.
- [97] C. Pudney, Distance-ordered homotopic thinning: a skeletonization algorithm for 3D digital images, *Comput. Vis. Image Understand.* 72 (3) (1998) 404–413.
- [98] G. Bertrand, G. Malandain, A new characterization of three-dimensional simple points, *Pattern Recognit. Lett.* 15 (1994) 169–175.
- [99] G. Borgefors, Distance transformations in arbitrary dimensions, *Comput. Vis. Graph. Image Process.* 27 (1984) 321–345.
- [100] A. Danilov, Y. Ivanov, R. Pryammonosov, Y. Vassilevski, Methods of graph network reconstruction in personalized medicine, *Int. J. Numer. Methods Biomed. Eng.* 32 (8) (2015) e02754.
- [101] P. Dierckx, *Curve and Surface Fitting with Splines*, Oxford University Press, Inc., New York, NY, USA, 1993.
- [102] S. Lee, G. Wolberg, S. Shin, Scattered data interpolation with multilevel B-splines, *IEEE Trans. Vis. Comput. Graph.* 3 (3) (1997) 228–244.
- [103] A. Kanitsar, D. Fleischmann, R. Wegenkittl, P. Felkel, E. Groller, CPR – curved planar reformation, in: *IEEE Visualization, VIS 2002*, IEEE, 2002.
- [104] H.A. Marquering, J. Dijkstra, P.J.H. de Koning, B.C. Stoel, J.H.C. Reiber, Towards quantitative analysis of coronary CTA, *Int. J. Cardiovasc. Imaging* 21 (1) (2005) 73–84.
- [105] N. Ahmed, T. Chacón Rebollo, V. John, S. Rubino, A review of variational multiscale methods for the simulation of turbulent incompressible flows, *Arch. Comput. Methods Eng.* 24 (1) (2017) 115–164.
- [106] P. R Amestoy, I.S. Duff, J.-Y. L'Excellent, J. Koster, A fully asynchronous multifrontal solver using distributed dynamic scheduling, *SIAM J. Matrix Anal. Appl.* 23 (1) (2001) 15–41.
- [107] S. Badia, A. Quaini, A. Quarteroni, Modular vs. non-modular preconditioned for fluid-structure systems with large added-mass effect, *Comput. Methods Appl. Mech. Eng.* 197 (49) (2008) 4216–4232.
- [108] Y. Bazilevs, V.M. Calo, T.J.R. Hughes, Y. Zhang, Isogeometric fluid-structure interaction: theory, algorithms and computations, *Comput. Mech.* 43 (2008) 3–37.
- [109] M. Benzi, G.H. Golub, J. Liesen, Numerical solution of saddle point problems, *Acta Numerica*. 14 (2005) 1–137.
- [110] C. Bertoglio, A. Caiazzo, A Stokes-residual backflow stabilization method applied to physiological flows, *J. Comput. Phys.* 313 (2016) 260–278.
- [111] D. Boffi, B. Franco, M. Fortin, et al., *Mixed Finite Element Methods and Applications*, vol. 44, Springer, 2013.
- [112] E. Boileau, P. Nithiarasu, P.J. Blanco, L.O. Müller, F.E. Fossan, L.R. Hellevik, W.P. Donders, W. Huberts, M. Willemet, J. Alastrauey, A benchmark study of numerical schemes for one-dimensional arterial blood flow modelling, *Int. J. Numer. Method. Biomed. Eng.* 31 (10) (2015) e02732, 1–33.
- [113] J. Bonet, R.D. Wood, *Nonlinear Continuum Mechanics for Finite Element Analysis*, Cambridge university press, 1997.
- [114] M. Braack, P.B. Mucha, W.M. Zajączkowski, Directional do-nothing condition for the Navier-Stokes equations, *J. Comput. Math.* 32 (5) (2014) 507–521.
- [115] S. Brenner, R. Scott, *The Mathematical Theory of Finite Element Methods*, vol. 15, Springer Science & Business Media, 2007.
- [116] W.L. Briggs, S.F. McCormick, et al., *A Multigrid Tutorial*, vol. 72, SIAM, 2000.
- [117] A.N. Brooks, T.J.R. Hughes, Streamline Upwind/Petrov-Galerkin formulations for convection dominated flows with particular emphasis on the incompressible Navier-Stokes equations, *Comput. Methods Appl. Mech. Eng.* 32 (1–3) (1982) 199–259.

- [118] C.-H. Bruneau, P. Fabrie, New efficient boundary conditions for incompressible Navier-Stokes equations: a well-posedness result, *ESAIM Math. Model. Numer. Anal.* 30 (7) (1996) 815–840.
- [119] X.-C. Cai, M. Sarkis, A restricted additive Schwarz pre-conditioner for general sparse linear systems, *SIAM J. Sci. Comput.* 21 (2) (1999) 792–797.
- [120] C.G. Caro, T.J. Pedley, R.C. Schroter, W.A. Seed, *The Mechanics of the Circulation*, second ed., Cambridge University Press, 2012.
- [121] P. Causin, J.-F. Gerbeau, F. Nobile, Added-mass effect in the design of partitioned algorithms for fluid-structure problems, *Comput. Methods Appl. Mech. Eng.* 194 (42-44) (2005) 4506–4527.
- [122] G. Chagnon, M. Rebouah, D. Favier, Hyperelastic energy densities for soft biological tissues: a review, *J. Elast.* 120 (2) (2015) 129–160.
- [123] C. Chnafa, S. Mendez, F. Nicoud, Image-based large-eddy simulation in a realistic left heart, *Comput. Fluid* 94 (2014) 173187.
- [124] P.G. Ciarlet, Mathematical elasticity: three dimensional elasticity, in: *Studies in Mathematics and its Applications*, vol. 1, Elsevier Science Publishers BV, Amsterdam, 1988.
- [125] P. Crosetto, S. Deparis, G. Fourestey, A. Quarteroni, Parallel algorithms for fluid-structure interaction problems in haemodynamics, *SIAM J. Sci. Comput.* 33 (4) (2011) 1598–1622.
- [126] O. Dahl, S.Ø. Wille, An ILU preconditioner with coupled node fill-in for iterative solution of the mixed finite element formulation of the 2D and 3D Navier-Stokes equations, *Int. J. Numer. Methods Fluids* 15 (5) (1992) 525–544.
- [127] A. Danilov, A. Lozovskiy, M. Olshanskii, Y. Vassilevski, A finite element method for the Navier-Stokes equations in moving domain with application to hemodynamics of the left ventricle, *Russ. J. Numer. Anal. Math. Model.* 32 (4) (2017) 225–236.
- [128] J. Degroote, R. Haelterman, S. Anerel, P. Bruggeman, J. Vierendeels, Performance of partitioned procedures in fluid-structure interaction, *Comput. Struct.* 88 (7–8) (2010) 446–457.
- [129] R.S. Dembo, S.C. Eisenstat, T. Steihaug, Inexact Newton methods, *SIAM J. Numer. Anal.* 19 (2) (1982) 400–408.
- [130] S. Deparis, D. Forti, G. Grandperrin, A. Quarteroni, FaCSI: a block parallel preconditioner for fluid-structure interaction in hemodynamics, *J. Comput. Phys.* 327 (2016) 700–718.
- [131] S. Deparis, G. Grandperrin, A. Quarteroni, Parallel preconditioners for the unsteady Navier-Stokes equations and applications to hemodynamics simulations, *Comput. Fluid* 92 (2014) 253–273.
- [132] T. Dobroserdova, F. Liang, G. Panasenko, Y. Vassilevski, Multiscale models of blood flow in the compliant aortic bifurcation, *Appl. Math. Lett.* 93 (2019) 98–104.
- [133] Y. Dubief, F. Delcayre, On coherent-vortex identification in turbulence, *J. Turbul.* 1 (1) (2000), 011–011.
- [134] A. Eken, M. Sahin, A parallel monolithic algorithm for the numerical simulation of large-scale fluid structure interaction problems, *Int. J. Numer. Methods Fluids* 80 (12) (2016) 687–714.
- [135] H.C. Elman, D.J. Silvester, A.J. Wathen, *Finite Elements and Fast Iterative Solvers: With Applications in Incompressible Fluid Dynamics*, 2 ed., Oxford Univ. Press, 2014.
- [136] A. Falahatpisheh, A. Kheradvar, High-speed particle image velocimetry to assess cardiac fluid dynamics *in vitro*: from performance to validation, *Eur. J. Mech. B Fluid* 35 (2–8) (2012).
- [137] C.L. Fefferman, Existence and smoothness of the Navier-Stokes equation, *Millenn. Prize Probl.* (2006) 57–67.
- [138] M.A. Fernandez, J.-F. Gerbeau, C.A. Grandmont, A projection semi-implicit scheme for the coupling of an elastic structure with an incompressible fluid, *Int. J. Numer. Methods Eng.* 69 (4) (2007) 794–821.
- [139] L. Formaggia, J.-F. Gerbeau, F. Nobile, A. Quarteroni, On the coupling of 3D and 1D Navier-Stokes equations for flow problems in compliant vessels, *Comput. Methods Appl. Mech. Eng.* 191 (6–7) (2001) 561–582.
- [140] L. Formaggia, J.-F. Gerbeau, F. Nobile, A. Quarteroni, Numerical treatment of defective boundary conditions for the Navier-Stokes equations, *SIAM J. Numer. Anal.* 40 (1) (2002) 376–401.
- [141] L.P. Franca, S.L. Frey, Stabilized finite element methods: II. the incompressible Navier-Stokes equations, *Comput. Methods Appl. Mech. Eng.* 99 (2–3) (1992) 209–233.

- [142] M.W. Gee, U. Küttler, W.A. Wall, Truly monolithic algebraic multigrid for fluid-structure interaction, *Int. J. Numer. Methods Eng.* 85 (8) (2011) 987–1016.
- [143] J.-F. Gerbeau, M. Vidrascu, A quasi-Newton algorithm based on a reduced model for fluid-structure interaction problems in blood flows, *ESAIM Math. Model. Numer. Anal.* 37 (4) (2003) 631–647.
- [144] V. Girault, P.-A. Raviart, *Finite Element Methods for Navier-Stokes Equations: Theory and Algorithms*, vol. 5, Springer Science & Business Media, 2012.
- [145] R. Glowinski, Finite element methods for incompressible viscous flow, *Handb. Numer. Anal.* 9 (2003) 3–1176.
- [146] J.-L. Guermond, P. Minev, J. Shen, An overview of projection methods for incompressible flows, *Comput. Methods Appl. Mech. Eng.* 195 (44–47) (2006) 6011–6045.
- [147] M.D. Gunzburger, *Finite Element Methods for Viscous Incompressible Flows: A Guide to Theory, Practice, and Algorithms*, Elsevier, 2012.
- [148] X. He, D.N. Ku, J.E. Moore, Simple calculation of the velocity profiles for pulsatile flow in a blood vessel using mathematica, *Ann. Biomed. Eng.* 21 (1) (1993) 45–49.
- [149] A. Hessenthaler, N.R. Gaddum, O. Holub, R. Sinkus, O. Rihrle, D. Nordsletten, Experiment for validation of fluid-structure interaction models and algorithms, *Int. J. Numer. Method. Biomed. Eng.* 33 (9) (2017).
- [150] A. Hessenthaler, O. Röhrle, D. Nordsletten, Validation of a non-conforming monolithic fluid-structure interaction method using phase-contrast MRI, *Int. J. Numer. Method. Biomed. Eng.* 33 (8) (2017).
- [151] J.G. Heywood, R. Rannacher, S. Turek, Artificial boundaries and flux and pressure conditions for the incompressible Navier-Stokes equations, *Int. J. Numer. Methods Fluids* 22 (5) (1996) 325–352.
- [152] G.A. Holzapfel, Biomechanics of soft tissue, in: *The Handbook of Materials Behavior Models*, 3, 2001, pp. 1057–1071.
- [153] C.O. Horgan, The remarkable Gent constitutive model for hyperelastic materials, *Int. J. Non-Linear Mech.* 68 (2015) 9–16.
- [154] G. Hou, J. Wang, A. Layton, Numerical methods for fluid-structure interaction - a review, *Commun. Comput. Phys.* 12 (2) (2012) 337–377.
- [155] J. Hron, S. Turek, *A Monolithic FEM/multigrid Solver for an ALE Formulation of Fluid-Structure Interaction with Applications in Biomechanics*, Springer Berlin Heidelberg, 2006.
- [156] T.J.R. Hughes, G.R. Feijoo, L. Mazzei, J.-B. Quincy, The variational multiscale method a paradigm for computational mechanics, *Comput. Methods Appl. Mech. Eng.* 166 (1–2) (1998) 3–24.
- [157] V. John, *Finite Element Methods for Incompressible Flow Problems*, Springer, 2016.
- [158] V. John, A. Linke, C. Merdon, M. Neilan, L.G. Rebholz, On the divergence constraint in mixed finite element methods for incompressible flows, *SIAM Rev.* 59 (3) (2017) 492–544.
- [159] J. Kim, B. Ahn, S. De, M.A. Srinivasan, An efficient soft tissue characterization algorithm from in vivo indentation experiments for medical simulation, *Int. J. Med. Robot. Comput. Assist. Surg.* 4 (3) (2008) 277–285.
- [160] F. Kong, X.-C. Cai, A scalable nonlinear fluid-structure interaction solver based on a Schwarz preconditioner with isogeometric unstructured coarse spaces in 3D, *J. Comput. Phys.* 340 (2017) 498–518.
- [161] I. Konshin, M. Olshanskii, Y. Vassilevski, ILU preconditioners for non-symmetric saddle point matrices with application to the incompressible Navier-Stokes equations, *SIAM J. Sci. Comput.* 37 (2015) A2171–A2197.
- [162] I. Konshin, M. Olshanskii, Y. Vassilevski, LU factorizations and ILU preconditioning for stabilized discretizations of incompressible Navier-Stokes equations, *Numer. Linear Algebra Appl.* 24 (3) (2017) e2085.
- [163] I.N. Konshin, M.A. Olshanskii, Y.V. Vassilevski, An algebraic solver for the Oseen problem with application to hemodynamics, in: *Contributions to Partial Differential Equations and Applications*, Springer, 2019, pp. 339–357.
- [164] U. Küttler, W.A. Wall, Fixed-point fluid-structure interaction solvers with dynamic relaxation, *Comput. Mech.* 43 (1) (2008) 61–72.

- [165] M. Landajuela, M. Vidrascu, D. Chapelle, M.A. Fernandez, Coupling schemes for the FSI forward prediction challenge: comparative study and validation, *Int. J. Numer. Method. Biomed. Eng.* 33 (4) (2017).
- [166] L.D. Landau, E.M. Lifshitz, Theory of elasticity, in: Course of Theoretical Physics, third ed., vol. 7, Butterworth-Heinemann, 1986.
- [167] L.D. Landau, E.M. Lifshitz, Fluid Mechanics. Course of Theoretical Physics, second ed., vol. 6, Butterworth-Heinemann, 1987.
- [168] B.E. Launder, D.B. Spalding, Mathematical Models of Turbulence, Academic press, 1972.
- [169] J. Liesen, Z. Strakos, Krylov Subspace Methods: Principles and Analysis, Oxford University Press, 2013.
- [170] K. Lipnikov, Y. Vassilevski, A. Danilov, et al. Advanced Numerical Instruments 2D. <http://sourceforge.net/projects/ani2d>.
- [171] K. Lipnikov, Y. Vassilevski, A. Danilov, et al. Advanced Numerical Instruments 3D. <http://sourceforge.net/projects/ani3d>.
- [172] A. Lozovskiy, M. Olshanskii, Y. Vassilevski, Analysis and assessment of a monolithic FSI finite element method, *Computers & Fluids* 179 (2019) 277–288.
- [173] A. Lozovskiy, M. Olshanskii, V. Salamatova, Y. Vassilevski, An unconditionally stable semi-implicit FSI finite element method, *Comput. Methods Appl. Mech. Eng.* 297 (2015) 437–454.
- [174] A. Lozovskiy, M. Olshanskii, Y. Vassilevski, A quasi-Lagrangian finite element method for the Navier-Stokes equations in a time-dependent domain, *Comput. Methods Appl. Mech. Eng.* 333 (2018) 55–73.
- [175] A.G. Malan, O.F. Oxtoby, An accelerated, fully-coupled, parallel 3D hybrid finite-volume fluid-structure interaction scheme, *Comput. Methods Appl. Mech. Eng.* 253 (2013) 426–438.
- [176] P.A.L.S. Martins, R.M.N. Jorge, A.J.M. Ferreira, A comparative study of several material models for prediction of hyperelastic properties: application to silicone-rubber and soft tissues, *Strain* 42 (3) (2006) 135–147.
- [177] C. Michler, S.J. Hulshoff, E.H. van Brummelen, R. de Borst, A monolithic approach to fluid-structure interaction, *Comput. Fluid* 33 (5) (2004) 839–848.
- [178] C.L.M.H. Navier, Mémoire sur les lois de l'équilibre et du mouvement des corps solides élastiques, 1827.
- [179] M.A. Olshanskii, E.E. Tyrtyshnikov, Iterative Methods for Linear Systems: Theory and Applications, vol. 138, SIAM, 2014.
- [180] A. Prohl, Projection and Quasi-Compressibility Methods for Solving the Incompressible Navier-Stokes Equations, Springer, 1997.
- [181] A. Quarteroni, T. Lassila, S. Rossi, R. Ruiz-Baier, Integrated heart coupling multiscale and multiphysics models for the simulation of the cardiac function, *Comput. Methods Appl. Mech. Eng.* 314 (2017) 345–407.
- [182] G. Querzoli, S. Fortini, A. Cenedese, Effect of the prosthetic mitral valve on vortex dynamics and turbulence of the left ventricular flow, *Phys. Fluids* 22 (4) (2010) 041901.
- [183] H.-G. Roos, M. Stynes, T. Lutz, Robust Numerical Methods for Singularly Perturbed Differential Equations: Convection-Diffusion-Reaction and Flow Problems, vol. 24, Springer Science & Business Media, 2008.
- [184] W. Rudin, Real and Complex Analysis, Tata McGraw-Hill Education, 1987.
- [185] P.B. Ryzhakov, R. Rossi, S.R. Idelsohn, E. Onate, A monolithic Lagrangian approach for fluid-structure interaction problems, *Comput. Mech.* 46 (6) (2010) 883–899.
- [186] Y. Saad, M. Schultz, GMRES: A generalized minimal residual algorithm for solving nonsymmetric linear systems, *SIAM J. Sci. Stat. Comput.* 7 (3) (1986) 856–869.
- [187] Y. Saad, Iterative Methods for Sparse Linear Systems, vol. 82, SIAM, 2003.
- [188] P.A. Sackinger, P.R. Schunk, R.R. Rao, A Newton-Raphson pseudo-solid domain mapping technique for free and moving boundary problems: a finite element implementation, *J. Comput. Phys.* 125 (1) (1996) 83–103.

- [189] P. Sagaut, Large Eddy Simulation for Incompressible Flows: An Introduction, Springer Science & Business Media, 2006.
- [190] W.E. Schiesser, The Numerical Method of Lines: Integration of Partial Differential Equations, Elsevier, 2012.
- [191] L.I. Sedov, Mechanics of Continuous Media, World Scientific, 1997 (In 2 Volumes).
- [192] A. Segal, M. Rehman, C. Vuik, Preconditioners for incompressible Navier-Stokes solvers, *Numer. Math. Theory Method. Appl.* 3 (3) (2010) 245–275.
- [193] A. Sequeira, A. Fasano, Hemomath. The Mathematics of Blood, Springer International Publishing, 2017.
- [194] K. Stein, T.E. Tezduyar, R. Benney, Mesh moving techniques for fluid-structure interactions with large displacements, *J. Appl. Mech.* 70 (1) (2003) 58–63.
- [195] A. Tagliabue, L. Dedè, A. Quarteroni, Fluid dynamics of an idealized left ventricle: the extended Nitsche's method for the treatment of heart valves as mixed time varying boundary conditions, *Int. J. Numer. Methods Fluids* 85 (3) (2017) 135–164.
- [196] K. Takizawa, Y. Bazilevs, T.E. Tezduyar, Space-time and ALE-VMS techniques for patient-specific cardiovascular fluid-structure interaction modeling, *Arch. Comput. Methods Eng.* 19 (2) (2012) 171–225.
- [197] F.P.P. Tan, G. Soloperto, S. Bashford, N.B. Wood, S. Thom, A. Hughes, X.Y. Xu, Analysis of flow disturbance in a stenosed carotid artery bifurcation using two-equation transitional and turbulence models, *J. Biomech. Eng.* 130 (2008), 061008–1.
- [198] R. Temam, Navier-Stokes Equations: Theory and Numerical Analysis, vol. 343, American Mathematical Soc., 2001.
- [199] T. E Tezduyar, S. Sathe, T. Cragin, B. Nanna, B.S. Conklin, J. Pausewang, M. Schwaab, Modelling of fluid-structure interactions with the space-time finite elements: arterial fluid mechanics, *Int. J. Numer. Methods Fluids* 54 (6–8) (2007) 901–922.
- [200] T.E. Tezduyar, S. Sathe, K. Stein, Solution techniques for the fully discretized equations in computation of fluid-structure interactions with the space-time formulations, *Comput. Methods Appl. Mech. Eng.* 195 (41) (2006) 5743–5753.
- [201] P.A. Thompson, S.M. Troian, A general boundary condition for liquid flow at solid surfaces, *Nature* 389 (6649) (1997) 360.
- [202] S. Turek, J. Hron, M. Madlik, M. Razzaq, H. Wobker, J.F. Acker, Numerical simulation and benchmarking of a monolithic multigrid solver for fluid-structure interaction problems with application to hemodynamics, in: H.-J. Bungartz, M. Mehl, M. Schfer (Eds.), Fluid Structure Interaction II, Volume 73 of Lecture Notes In Computational Science and Engineering, Springer Berlin Heidelberg, 2010, pp. 193–220.
- [203] K. Valen-Sendstad, K.A. Mardal, M. Mortensen, B.A.P. Reif, H.P. Langtangen, Direct numerical simulation of transitional flow in a patient-specific intracranial aneurysm, *J. Biomech.* 44 (2011) 2826–2832.
- [204] H.A. Van der Vorst, Bi-CGSTAB: a fast and smoothly converging variant of Bi-CG for the solution of nonsymmetric linear systems, *SIAM J. Sci. Stat. Comput.* 13 (2) (1992) 631–644.
- [205] C. Vuik, G. Segal, et al., A comparison of preconditioners for incompressible Navier-Stokes solvers, *Int. J. Numer. Methods Fluids* 57 (12) (2008) 1731–1751.
- [206] A.J. Wathen, Preconditioning, *Acta Numerica* 24 (2015) 329–376.
- [207] T. Wick, Fluid-structure interactions using different mesh motion techniques, *Comput. Struct.* 89 (13–14) (2011) 1456–1467.
- [208] J.R. Womersley, Method for the calculation of velocity, rate of flow and viscous drag in arteries when the pressure gradient is known, *J. Physiol.* 127 (3) (1955) 553–563.
- [209] N. Xiao, J. Alastrauey, C.A. Figueroa, A systematic comparison between 1D and 3D hemodynamics in compliant arterial models, *Int. J. Numer. Method. Biomed. Eng.* 30 (2) (2014) 204–231.

- [210] O.H. Yeoh, Some forms of the strain energy function for rubber, *Rubber Chem. Technol.* 66 (5) (1993) 754–771.
- [211] E. Crepeau, M. Sorine, A reduced model of pulsatile flow in an arterial compartment, *Chaos Solit. Fractals* 34 (2) (2007) 594–605.
- [212] T. Korakianitis, Y. Shi, Numerical simulation of cardiovascular dynamics with healthy and diseased heart valves, *J. Biomech.* 39 (11) (2006) 1964–1982.
- [213] A.S. Kholodov, Some dynamical models of multi-dimensional problems of respiratory and circulatory systems including their interaction and matter transport, in: *Computer Models and Medicine Progress*, Nauka, Moskva, 2001, pp. 127–163.
- [214] D.V. Parshin, I.V. Ufimtseva, A.A. Cherevko, A.K. Khe, K.Y. Orlov, A.L. Krivoshapkin, A.P. Chupakhin, Differential properties of Van der Pol - Duffing mathematical model of cerebrovascular haemodynamics based on clinical measurements, *J. Phys. Conf. Ser.* 722 (1) (2016), 012030:1–7.
- [215] A.S. Kholodov, A.V. Evdokimov, S.S. Simakov, Numerical simulation of peripheral circulation and substance transfer with 2D models, in: P. Chandra, R. Kumar (Eds.), *Mathematical Biology: Recent Trends*, 2006, pp. 22–29. Anshan.
- [216] A.G. Borzov, S.I. Mukhin, N.V. Sosnin, Conservative schemes of matter transport in a system of vessels closed by the heart, *Differential Equations* 48 (7) (2012) 919–928.
- [217] D. Canuto, K. Chong, C. Bowles, E.P. Dutson, J.D. Eldredge, P. Benharash, A regulated multiscale closed-loop cardiovascular model, with applications to hemorrhage and hypertension, *Int. J. Numer. Methods Biomed. Eng.* 34 (6) (2018) e2975:1–25.
- [218] F. Liang, H. Liu, Simulation of hemodynamic responses to the valsalva maneuver: an integrative computational model of the cardiovascular system and the autonomic nervous system, *J. Physiol. Sci.* 56 (1) (2006) 45–65.
- [219] F. Liang, S. Takagi, R. Himeno, H. Liu, Biomechanical characterization of ventricular-arterial coupling during aging: a multi-scale model study, *J. Biomech.* 42 (6) (2009) 692–704.
- [220] F. Liang, S. Takagi, R. Himeno, H. Liu, Multi-scale modeling of the human cardiovascular system with applications to aortic valvular and arterial stenosis, *Med. Biol. Eng. Comput.* 47 (7) (2009) 743–755.
- [221] S.S. Simakov, A.S. Kholodov, Computational study of oxygen concentration in human blood under low frequency disturbances, *Math. Models Comput. Simulat.* 1 (2) (2009) 283–295.
- [222] P.R. Trenhago, L.G. Fernandes, L.O. Müller, P.J. Blanco, R.A. Feijóo, An integrated mathematical model of the cardiovascular and respiratory systems, *Int. J. Numer. Methods Biomed. Eng.* 32 (1) (2016) e02736:1–25.
- [223] M. Capoccia, Development and characterization of the arterial Windkessel and its role during left ventricular assist device, *Artif. Organs* 39 (8) (2015) E138–E153.
- [224] Y. Shi, P. Lawford, R. Hose, Review of zero-D and 1D models of blood flow in the cardiovascular system, *Biomed. Eng. Online* 10 (33) (2011) 1–38.
- [225] E.B. Shim, J.Y. Sah, C.H. Youn, Mathematical modeling of cardiovascular system dynamics using a lumped parameter method, *Jpn. J. Physiol.* 54 (2004) 545–553.
- [226] S.S. Simakov, Modern methods of mathematical modeling of blood flow using reduced order methods, *Comput. Res. Model.* 10 (5) (2018) 581–604.
- [227] V. Milisic, A. Quarteroni, Analysis of lumped parameter models for blood flow simulations and their relation with 1D models, *ESAIM Math. Model. Numer. Anal.* 38 (4) (2004) 613–632.
- [228] A.G. Borzov, S.I. Mukhin, N.V. Sosnin, Conservative algorithm of substance transport over a closed graph of cardiovascular system, *Russ. J. Numer. Anal. Math. Model.* 27 (5) (2012) 413–429.
- [229] T. Dobroserdova, M. Olshanskii, S. Simakov, Multiscale coupling of compliant and rigid walls blood flow models, *Int. J. Numer. Methods In Fluids* 82 (12) (2016) 799–817.
- [230] A. Quarteroni, G. Rozza, *Reduced Order Methods for Modeling and Computational Reduction*, Springer International Publishing, 2014.

- [231] M.V. Abakumov, I.V. Ashmetkov, N.B. Esikova, V.B. Koshelev, S.I. Mukhin, N.V. Sosnin, V.F. Tishkin, A.P. Favorskii, A.B. Khrulenko, Strategy of mathematical cardiovascular system modeling, *Matem. Mod.* 12 (2) (2000) 106–117.
- [232] K.B. Campbell, A.M. Simpson, S.G. Campbell, H.L. Granzier, B.K. Slinker, Dynamic left ventricular elastance: a model for integrating cardiac muscle contraction into ventricular pressure-volume relationship, *J. Appl. Physiol.* 104 (4) (2008) 958–975.
- [233] H. Suga, Theoretical analysis of a left-ventricular pumping model based on the systolic time-varying pressure-volume relationship, *IEEE Trans. Biomed. Eng.* 18 (1) (1971) 47–55.
- [234] H. Suga, Cardiac energetics: from  $E_{MAX}$  to pressure-volume area, *Clin. Exp. Pharmacol. Physiol.* 30 (2003) 580–585.
- [235] K.R. Walley, Left ventricular function: time-varying elastance and left ventricular aortic coupling, *Crit. Care* 20 (270) (2016) 1–11.
- [236] T. Korakianitis, Y. Shi, A concentrated parameter model for the human cardiovascular system including heart valve dynamics and atrioventricular interaction, *Med. Eng. Phys.* 28 (2006) 613–628.
- [237] J.C. Butcher, P. Sehnalová, Predictor-corrector Obreshkov pairs, *Computing* 95 (5) (2013) 355–371.
- [238] A.S. Khodolov, A.I. Lobanov, A.V. Evdokimov, Numerical Schemes for Solving Stiff Ordinary Differential Equations in the Space of Undetermined Coefficients, MFTI, Moskva, 1985.
- [239] K. Barret, H. Brooks, S. Boitano, S. Barman, Ganong's Review of Medical Physiology, twenty third edition, The McGraw-Hill, 2010.
- [240] R.F. Schmidt, G. Thews, Human Physiology, second edition, Springer-Verlag, Berlin, 1989.
- [241] P.J. Blanco, S.M. Watanabe, M.A.R.F. Passos, P.A. Lemos, R.A. Feijóo, An anatomically detailed arterial network model for one-dimensional computational hemodynamics, *IEEE Trans. Biomed. Eng.* 62 (2) (2015) 736–753.
- [242] T. Gamilov, Y. Ivanov, P. Kopylov, S. Simakov, Y. Vassilevski, Patient specific haemodynamic modeling after occlusion treatment in leg, *Math. Model. Nat. Phenom.* 9 (6) (2014) 85–97.
- [243] Y. Vassilevski, A. Danilov, Y. Ivanov, S. Simakov, T. Gamilov, Personalized anatomical meshing of human body with applications, in: Modeling the Heart and the Circulatory System, Springer, 2015, pp. 221–236.
- [244] J. Alastrauey, S.M. Moore, K.H. Parker, T. David, J. Peiró, S.J. Sherwin, Reduced modelling of blood flow in the cerebral circulation, *Int. J. Numer. Methods Fluids* 56 (8) (2008) 1061–1067.
- [245] A.P. Avolio, Multi-branched model of the human arterial system, *Med. Biol. Eng. Comput.* 18 (1980) 709–718.
- [246] A.Y. Bunicheva, M.A. Menyailova, S.I. Mukhin, N.V. Sosnin, A.P. Favorskii, Studying the influence of gravitational overloads on the parameters of blood flow in vessels of greater circulation, *Math. Model. Comput. Simul.* 5 (1) (2013) 81–91.
- [247] S.J. Sherwin, L. Formaggia, J. Peiró, V. Franke, Computational modelling of 1D blood flow with variable mechanical/properties and its application to the simulation of wave propagation in the human arterial system, *Int. J. Numer. Methods Fluids* 43 (2003) 673–700.
- [248] L. Formaggia, A. Quarteroni, A. Veneziani, Cardiovascular Mathematics: Modeling and Simulation of the Circulatory System, vol. 1, Springer, Heidelberg, DE, 2009.
- [249] T.W. Secomb, Hemodynamics, *Compr. Physiol.* 6 (2) (2016) 975–1003.
- [250] F.N. van de Vosse, N. Stergiopoulos, Pulse wave propagation in the arterial tree, *Annu. Rev. Fluid Mech.* 43 (2011) 467–499.
- [251] S. Čanić, E.H. Kim, Mathematical analysis of the quasilinear effects in a hyperbolic model blood flow through compliant axi-symmetric vessels, *Math. Methods Appl. Sci.* 26 (2003) 1161–1186.
- [252] L.O. Müller, E. Toro, A global multiscale mathematical model for the human circulation with emphasis on the venous system, *Int. J. Numer. Methods Biomed. Eng.* 30 (7) (2014) 681–725.
- [253] S.S. Simakov, T.M. Gamilov, Y.N. Soe, Computational study of blood flow in lower extremities under intense physical load, *Russ. J. Numer. Anal. Math. Model.* 28 (5) (2013) 485–503.

- [254] Y.V. Vassilevski, V.Y. Salamatova, S.S. Simakov, On the elasticity of blood vessels in one-dimensional problems of hemodynamics, *Comput. Math. Math. Phys.* 55 (9) (2015) 1567–1578.
- [255] E.F. Toro, A. Siviglia, Simplified blood flow model with discontinuous vessel properties: analysis and exact solutions, *Model. Simul. Appl.* 5 (2012) 19–39.
- [256] I. Sazonov, P. Nithiarasu, A novel, FFT-based one-dimensional blood flow solution method for arterial network, *Biomechanics Model. Mechanobiol.* (2019) 1–24.
- [257] J. Alastrauey, A.W. Khir, K.S. Matthys, P. Segers, S.J. Sherwin, P.R. Verdonck, K.H. Parker, J. Peiró, Pulse wave propagation in a model human arterial network: assessment of 1D visco-elastic simulations against in vitro measurements, *J. Biomech.* 44 (12) (2011) 2250–2258.
- [258] J.P. Mynard, J.J. Smolich, One-dimensional haemodynamic modeling and wave dynamics in the entire adult circulation, *Ann. Biomed. Eng.* 43 (6) (2015) 1443–1460.
- [259] K. Sugimoto, F. Liang, Y. Takahara, K. Mogi, K. Yamazaki, S. Takagi, H. Liu, Assessment of cardiovascular function by combining clinical data with a computational model of the cardiovascular system, *J. Thorac. Cardiovasc. Surg.* 145 (5) (2013) 1367–1372.
- [260] J. Carson, S. Pant, C. Roobottom, et al., Noninvasive coronary CT angiography derived fractional flow reserve (FFR): a benchmark study comparing the diagnostic performance of four different computational methodologies, *Int. J. Numer. Methods Biomed. Eng.* 35 (2019) e3235.
- [261] D. Guan, F. Liang, P.A. Gremaud, Comparison of the Windkessel model and structured-tree model applied to prescribe outflow boundary conditions for a one-dimensional arterial tree model, *J. Biomech.* 49 (9) (2016) 1583–1592.
- [262] D. Amadori, S. Ferrari, L. Formaggia, Derivation and analysis of a fluid-dynamical model in thin and long elastic vessels, *Biophys. J.* 2 (1) (2007) 99–125.
- [263] A.C.L. Barnard, W.A. Hunt, W.P. Timlake, E. Varley, A theory of fluid flow in compliant tubes, *Biophys. J.* 6 (6) (1966) 717–724.
- [264] T. Gamilov, P. Kopylov, R. Pryammonosov, S. Simakov, Virtual fractional flow reserve assessment in patient-specific coronary networks by 1D hemodynamic model, *Russ. J. Numer. Anal. Math. Model.* 30 (5) (2015) 269–276.
- [265] L. Formaggia, D. Lamponi, M. Tuveri, A. Veneziani, Numerical modeling of 1D arterial networks coupled with a lumped parameters description of the heart, *Comput. Methods Biomed. Eng.* 9 (5) (2006) 273–288.
- [266] I. Larabidea, P.J. Blanco, S.A. Urquiza, E.A. Dari, M.J. Véneref, N.A. de Souza e Silvac, R.A. Feijóo, Hemolab — hemodynamics modelling laboratory: an application for modelling the human cardiovascular system, *Comput. Biol. Med.* 42 (2012) 993–1004.
- [267] W. Cousins, P.A. Gremaud, D.M. Tartakovsky, A new physiological boundary condition for hemodynamics, *SIAM J. Appl. Math.* 73 (3) (2013) 1203–1223.
- [268] M.S. Olufsen, C.S. Peskin, W.Y. Kim, E.M. Pedersen, A. Nadim, J. Larsen, Numerical simulation and experimental validation of blood flow in arteries with structured-tree outflow conditions, *Ann. Biomed. Eng.* 28 (2000) 1281–1299.
- [269] J. Alastrauey, K.H. Parker, J. Peiró, S.J. Sherwin, Lumped parameter outflow models for 1D blood flow simulations: effect on pulse waves and parameter estimation, *Commun. Comput. Phys.* 4 (2) (2008) 317–336.
- [270] L. Formaggia, D. Lamponi, A. Quarteroni, One-dimensional models for blood flow in arteries, *J. Eng. Math.* 47 (2003) 251–276.
- [271] J.P. Mynard, P. Nithiarasu, A 1D arterial blood flow model incorporating ventricular pressure, aortic valve and regional coronary flow using the locally conservative Galerkin (LCG) method, *Commun. Numer. Methods Eng.* 24 (5) (2008) 367–417.
- [272] K. Lagana, R. Balossino, F. Migliavacca, G. Pennati, E.L. Bove, M.R. de Leval, G. Dubini, Multiscale modeling of the cardiovascular system: application to the study of pulmonary and coronary perfusions in the univentricular circulation, *J. Biomech.* 38 (5) (2005) 1129–1141.
- [273] S.A. Urquiza, P.J. Blanco, M.J. Vénere, R.A. Feijóo, Multidimensional modelling for the carotid artery blood flow, *Comput. Methods Appl. Mech. Eng.* 195 (33–36) (2006) 4002–4017.

- [274] L. Formaggia, A. Moura, F. Nobile, On the stability of the coupling of 3D and 1D fluid structure interaction models for blood flow simulation, *Math. Model. Numer. Anal.* 41 (4) (2007) 743–769.
- [275] T. Dobroserdova, M. Olshanskii, A finite element solver and energy stable coupling for 3D and 1D fluid models, *Comput. Methods Appl. Mech. Eng.* 259 (2013) 166–176.
- [276] T. Passerini, M. de Luca, L. Formaggia, A. Quarteroni, A. Veneziani, A 3D/1D geometrical multiscale model of cerebral vasculature, *J. Eng. Math.* 64 (4) (2009) 319–330.
- [277] K. Low, R. van Loon, I. Sazonov, R.L.T. Bevan, P. Nithiarasu, An improved baseline model for a human arterial network to study the impact of aneurysms on pressure–flow waveforms, *Int. J. Numer. Methods Biomed. Eng.* 28 (2012) 1224–1246.
- [278] Y. Vassilevski, S. Simakov, V. Salamatova, Y. Ivanov, T. Dobroserdova, Numerical issues of modelling blood flow in networks of vessels with pathologies, *Russ. J. Numer. Anal. Math. Model.* 26 (6) (2011) 605–622.
- [279] J. Flores, J. Alastrauey, P.E. Corvera, A novel analytical approach to pulsatile blood flow in the arterial network, *Ann. Biomed. Eng.* 44 (10) (2016) 3047–3068.
- [280] K.M. Magomedov, A.S. Kholodov, Grid-Characteristics Numerical Methods, second ed., Urait, Moscow, 2018.
- [281] S. Simakov, T. Gamilov, Computational study of the cerebral circulation accounting for the patient-specific anatomical features, in: Smart Innovation, Systems and Technologies, vol. 133, Springer, Cham, 2019, pp. 309–330.
- [282] G.A. Holzapfel, R.W. Ogden, Constitutive modelling of arteries, *Proc. R. Soc. Lond. Ser. A* 466 (2118) (2010) 1551–1597.
- [283] P. Kalita, R. Schaefer, Mechanical models of artery walls, *Arch. Comput. Methods Eng.* 15 (1) (2008) 1–36.
- [284] P. Dobrin, F.N. Littooy, J. Golan, J. Fareed, Mechanical and histologic changes in canine vein grafts, *J. Surg. Res.* 44 (3) (1988) 259–265.
- [285] T.J. Pedley, X.Y. Luo, Modelling flow and oscillations in collapsible tubes, *Theor. Comput. Fluid Dyn.* 10 (1998) 277–294.
- [286] S.S. Simakov, A.S. Kholodov, Computational analysis of acoustical impacts to the lungs function and pulmonary circulation, in: Medicine in the Mirror of Informatics, Nauka, Moskva, 2001, pp. 124–144.
- [287] J. Fernandez, P. Hunter, V. Shim, K. Mithraratne, A subject-specific framework to inform musculoskeletal modeling: outcomes from the IUPS physiome project, in: Patient-Specific Computational Modeling, Springer, 2012, pp. 39–60.
- [288] P. Studinger, Z. Lénárd, Z. Kováts, L. Kocsis, M. Kollai, Static and dynamic changes in carotid artery diameter in humans during and after strenuous exercise, *J. Physiol.* 550 (2003) 575–583.
- [289] A.K. Tsaturjan, S.S. Grigorjan, Y.Z. Saakjan, On the mechanisms of generation of Korotkoff sounds, *Dokl. Acad. Sci. SSSR* 251 (1980) 570–574.
- [290] P.J. Blanco, R.A. Feijóo, A 3D-1D-0D computational model for the entire cardiovascular system, *Comput. Mech.* XXIX (2010) 5887–5911.
- [291] E. Ozawa, K. Bottom, X. Xiao, R.D. Kamm, Numerical simulation of enhanced external counterpulsation, *Ann. Biomed. Eng.* 29 (2001) 284–297.
- [292] E. VanBavel, J.P. Wesselman, J.A. Spaan, Myogenic activation and calcium sensitivity of cannulated rat mesenteric small arteries, *Circ. Res.* 82 (2) (1998) 210–220.
- [293] N.A. Kudryashov, I.L. Chernyavsky, A mathematical model for autoregulation of the arterial lumen by endothelium-derived relaxing factor, *Adv. Sci. Lett.* 1 (2) (2008) 226–230.
- [294] T. Bodnár, A. Sequeira, M. Prosi, On the shear-thinning and viscoelastic effects of blood flow under various flow rates, *Appl. Math. Comput.* 217 (11) (2011) 5055–5067.
- [295] B.M. Johnston, P.R. Johnston, S. Corney, D. Kilpatrick, Non-Newtonian blood flow in human right coronary arteries: transient simulations, *J. Biomech.* 39 (6) (2006) 1116–1128.

- [296] F.N. van de Vosse, J. de Hart, C.H.G.A. van Oijen, D. Bessems, T.W.M. Gunther, A. Segal, B.J.B.M. Wolters, J.M.A. Stijnen, F.P.T. Baaijens, Finite-element-based computational methods for cardiovascular fluid-structure interaction, *J. Eng. Math.* 47 (2003) 335–368.
- [297] E. Fatahian, N. Kordani, H. Fatahian, The application of computational fluid dynamics (CFD) method and several rheological models of blood flow: a review, *Gazi Univ. J. Sci.* 31 (4) (2018) 1213–1227.
- [298] J.M. Keijsers, C.A. Leguy, W. Huberts, A.J. Narracott, J. Rittweger, F.N. van de Vosse, A 1D pulse wave propagation model of the hemodynamics of calf muscle pump function, *Int. J. Numer. Methods Biomed. Eng.* 31 (7) (2015) e02716, 1–20.
- [299] J.M. Keijsers, C.A. Leguy, W. Huberts, A.J. Narracott, J. Rittweger, F.N. van de Vosse, Global sensitivity analysis of a model for venous valve dynamics, *J. Biomech.* 49 (13) (2016) 2845–2853.
- [300] X. Zhang, S. Noda, S. Himeno, H. Liu, Gravitational effects on global hemodynamics in different postures: a closed-loop multiscale mathematical analysis, *Acta Mech. Sin.* 33 (3) (2017) 595–618.
- [301] M.F. Snyder, V.C. Rideout, Computer simulation studies of the venous circulation, *IEEE Trans. Biomed. Eng.* 16 (4) (1969) 325–334.
- [302] G.A. Buxton, N. Clarke, Computational phlebology: the simulation of a vein valve, *J. Biol. Phys.* 32 (6) (2006) 507–521.
- [303] T.M. Gamilov, F. Liang, S.S. Simakov, Mathematical modeling of the coronary circulation during cardiac pacing and tachycardia, *Lobachevskii J. Math.* 40 (4) (2019) 448–458.
- [304] M.A. Vis, P.H. Bovendeerd, P. Sipkema, N. Westerhof, Effect of ventricular contraction, pressure, and wall stretch on vessels at different locations in the wall, *Am. J. Physiol. Heart Circ. Physiol.* 272 (1997) H2963–H2975.
- [305] W. Jin, F. Liang, H. Liu, Hemodynamic response to exercise in supine and standing attitudes: an integrated model, *J. Biomech. Sci. Eng.* 11 (1) (2016), 15–00523:1–12.
- [306] A. Parton, V. McGilligan, M. OKane, F.R. Baldrick, S. Watterson, Computational modelling of atherosclerosis, *Briefings Bioinf.* 17 (4) (2016) 562–575.
- [307] Z. Duanmu, M. Yin, X. Fan, X. Yang, X. Luo, A patient-specific lumped-parameter model of coronary circulation, *Sci. Rep.* 8 (2018) 874.
- [308] T. Köppel, G. Santin, B. Haasdonk, R. Helmig, Numerical modelling of a peripheral arterial stenosis using dimensionally reduced models and machine learning techniques, *Int. J. Numer. Methods Biomed. Eng.* 34 (8) (2018) e3095.
- [309] R.E. Mates, R.L. Gupta, A.C. Bell, F.J. Klocke, Fluid dynamics of coronary artery stenosis, *Circ. Res.* 42 (1) (1978) 152–162.
- [310] R.N. Pralhad, D.H. Schultz, Modeling of arterial stenosis and its applications to blood diseases, *Math. Biosci.* 190 (2004) 203–220.
- [311] M. Oshima, R. Torii, S. Tokuda, S. Yamada, A. Koizumi, Patient-specific modeling and multi-scale blood simulation for computational hemodynamic study on the human cerebrovascular system, *Curr. Pharmaceut. Biotechnol.* 13 (11) (2012) 2153–2165.
- [312] P.J. Blanco, C.A. Bulant, LO Müller, G. Talou, C.G. Bezerra, P.L. Lemos, R.A. Feijóo, Comparison of 1D and 3D models for the estimation of fractional flow reserve, *Sci. Rep.* 8 (1) (2018) 17275.
- [313] E. Boileau, S. Pant, C. Roobottom, I. Sazonov, J. Deng, X. Xie, P. Nithiarasu, Estimating the accuracy of a reduced-order model for the calculation of fractional flow reserve (FFR), *Int. J. Numer. Methods Biomed. Eng.* 34 (1) (2018) e2908.
- [314] D.V. Burenchev, F.Y. Kopylov, A.A. Bykova, T.M. Gamilov, D.G. Gognieva, S.S. Simakov, Y.V. Vasilevsky, Mathematical modelling of circulation in extracranial brachiocephalic arteries at pre-operation stage in carotid endarterectomy, *Russ. J. Cardiol.* 144 (4) (2017) 88–92.
- [315] A.R. Ghigo, S. Abou Taam, X. Wang, P.-Y. Lagrée, J.-M. Fullana, A one-dimensional arterial network model for bypass graft assessment, *Med. Eng. Phys.* 43 (2017) 39–47.
- [316] Y. Vassilevski, S. Simakov, V. Salamatova, Y. Ivanov, T. Dobroserdova, Blood flow simulation in atherosclerotic vascular network using fiber–spring representation of diseased wall, *Math. Model. Nat. Phenom.* 6 (5) (2011) 333–349.

- [317] Y. Vassilevski, S. Simakov, V. Salamatova, Y. Ivanov, T. Dobroserdova, Vessel wall models for simulation of atherosclerotic vascular networks, *Math. Model. Nat. Phenom.* 6 (7) (2011) 82–99.
- [318] M. Rosar, C. Peskin, Fluid flow in collapsible elastic tubes: a three-dimensional numerical model, *N.Y. J. Math.* (2001) 281–302.
- [319] M.K. Banerjee, D. Nag, R. Ganguly, A. Datta, Stenotic interaction on haemodynamic parameters in double stenoses, *Int. J. Comput. Fluid Dyn.* 22 (9) (2008) 609–622.
- [320] S.S. Simakov, T.M. Gamilov, F.Y. Kopylov, Y.V. Vasilevskii, Evaluation of hemodynamic significance of stenosis in multiple involvement of the coronary vessels by mathematical simulation, *Bull. Exp. Biol. Med.* 162 (1) (2016) 111–114.
- [321] A.K. Singh, Effects of shape parameter and length of stenosis on blood flow through improved generalized artery with multiple stenoses, *Adv. Appl. Math. Biosci.* 3 (1) (2012) 41–48.
- [322] J.-M. Zhang, L. Zhong, T. Luo, A.M. Lomarda, Y. Huo, J. Yap, et al., Simplified models of non-invasive fractional flow reserve based on CT images, *PLoS One* 11 (5) (2016) e0153070.
- [323] I.P. Dudanov, S.V. Ordynets, I.A. Lukinskiy, B.C. Abuazab, V.V. Akhmetov, A.A. Shabonov, O.P. Verbitskiy, Extracranial non-atherosclerotic pathology of the carotid artery in the causes of acute ischemic stroke, *Res. Pract. Med.* 4 (4) (2017) 35–49.
- [324] L. Wang, F. Zhao, D. Wang, S. Hu, J. Liu, Z. Zhou, J. Lu, P. Qi, S. Song, Pressure drop in tortuosity/kinking of the internal carotid artery: simulation and clinical investigation, *BioMed Res. Int.* 2016 (2016) 1–8, 2428970.
- [325] G.L. Tomei (Ed.), *Steam, Its Generation and Use*, 41 ed., The Babcock & Wilcox Company, 2015.
- [326] F.W. Prinzen, W.C. Hunter, B.T. Wyman, E.R. McVeigh, Mapping of regional myocardial strain and work during ventricular pacing: experimental study using magnetic resonance imaging tagging, *J. Am. Coll. Cardiol.* 33 (6) (1999) 1735–1742.
- [327] T. Bombardini, V. Gemignani, E. Bianchini, L. Venneri, C. Petersen, E. Pasanisi, L. Pratali, D. Alonso-Rodriguez, M. Pianelli, F. Faita, M. Giannoni, G. Arpesella, E. Picano, Diastolic time - frequency relation in the stress echo lab: filling timing and flow at different heart rates, *Cardiovasc. Ultrasound* 6 (2008).
- [328] T. Taguchi, K. Ogawa, T. Kanaya, R. Matsuda, H. Kuga, M. Nakatsugawa, Effects of enhanced external counterpulsation on hemodynamics and its mechanism, *Circ. J.* 68 (11) (2004) 1030–1034.
- [329] Q. Kairong, Z. Xinzhang, L. Zhaorong, The effects of external counterpulsation on the pulse waves in human aorta, *Acta Mech. Sin.* 11 (3) (1995) 275–283.
- [330] P.O. Bonetti, G.W. Barsness, P.C. Keelan, Enhanced external counterpulsation improves endothelial function in patients with symptomatic coronary artery disease, *J. Am. Coll. Cardiol.* 41 (10) (2003) 1761–1768.
- [331] R.P. Araujo, D.L.S. McElwain, New insights into vascular collapse and growth dynamics in solid tumors, *J. Theor. Biol.* 228 (3) (2004) 335–346.
- [332] J.M.P.C. Holash, P.C. Maisonpierre, D. Compton, P. Boland, C.R. Alexander, D. Zagzag, G.D. Yancopoulos, S.J. Wiegand, Vessel cooption, regression, and growth in tumors mediated by angiopoietins and VEGF, *Science* 284 (5422) (1999) 1994–1998.
- [333] D. Hanahan, R.A. Weinberg, The hallmarks of cancer, *Cell* 100 (1) (2000) 57–70.
- [334] F. Dai, R.K. Jain, Tumor microvasculature and microenvironment: targets for anti-angiogenesis and normalization, *Microvasc. Res.* 74 (2) (2007) 72–84.
- [335] H. Maeda, J. Wu, T. Sawa, Y. Matsumura, K. Hori, Tumor vascular permeability and the EPR effect in macromolecular therapeutics: a review, *J. Control. Release* 65 (1) (2000) 271–284.
- [336] B.M. Fu, S. Shen, Structural mechanisms of acute VEGF effect on microvessel permeability, *Am. J. Physiol. Heart Circ. Physiol.* 284 (6) (2003) H2124–H2135.
- [337] M.S. Gee, W.N. Procopio, S. Makonnen, M.D. Feldman, N.M. Yeilding, W.M.F. Lee, Tumor vessel development and maturation impose limits on the effectiveness of anti-vascular therapy, *Am. J. Pathol.* 162 (1) (2003) 183–193.

- [338] Y. Fan, Y. Chen, M. Dellian, N. Safabakhsh, N. Ferrara, R.K. Jain, Time-dependent vascular regression and permeability changes in established human tumor xenografts induced by an anti-vascular endothelial growth factor/vascular permeability factor antibody, *Proc. Natl. Acad. Sci. U.S.A.* 93 (25) (1996) 14765–14770.
- [339] S.K. Stamatelos, E. Kim, A.P. Pathak, S.P. Aleksander, A bioimage informatics based reconstruction of breast tumor microvasculature with computational blood flow predictions, *Microvasc. Res.* 91 (2014) 8–21.
- [340] M.J. Eymontt, G. Grant, F.A. Kruger, D.E. Maynard, G.J. Hamwi, Cushing' syndrome with hypoglycemia caused by adrenocortical carcinoma, *J. Clin. Endocrinol. Metab.* 25 (1) (1965) 46–52.
- [341] A.R. Pries, T.W. Secomb, P. Gaehrtgens, Structure and hemodynamics of microvascular networks: heterogeneity and correlations, *Am. J. Physiol.* 269 (1995) H1713–H1722.
- [342] C.D. Murray, The physiological principle of minimum work: I. The vascular system and the cost of blood volume, *Proc. Natl. Acad. Sci. U.S.A.* 12 (3) (1926) 207–214.
- [343] E. Gabrys, M. Rybaczuk, A. Kedzia, Blood flow simulation through fractal models of circulatory system, *Chaos Solit. Fractals* 27 (1–7) (2006).
- [344] C.D. Murray, On the fractality of the biological tree-like structures, *Discrete Dyn. Nat. Soc.* 3 (1999) 297–306.
- [345] C. Pozrikidis, Numerical simulation of blood flow through microvascular capillary networks, *Bull. Math. Biol.* 71 (2009) 1520–1541.
- [346] T. Takahashi, *Microcirculation in Fractal Branching Networks*, Springer Japan, 2014.
- [347] M. Welter, H. Rieger, Physical determinants of vascular network remodeling during tumor growth, *Eur. Phys. J. E* 33 (2010) 149–163.
- [348] N.O. Gorodnova, A.V. Kolobov, O.A. Mynbaev, S.S. Simakov, Mathematical modeling of blood flow alteration in microcirculatory network due to angiogenesis, *Lobachevskii J. Math.* 37 (5) (2016) 541–549.
- [349] D. Hu, D. Cai, A.V. Rangan, Blood vessel adaptation with fluctuations in capillary flow distribution, *PLoS One* 7 (2012) e45444.
- [350] A.R. Pries, T.W. Secomb, Microcirculatory network structures and models, *Ann. Biomed. Eng.* 28 (2000) 916–921.
- [351] A.R. Pries, T.W. Secomb, Modeling structural adaptation of microcirculation, *Microcirculation* 15 (2008) 753–764.
- [352] A.R. Pries, T.W. Secomb, Making microvascular networks work: angiogenesis, remodeling, and pruning, *Physiology* 29 (2014) 446–455.
- [353] T.W. Secomb, M.W. Dewhirst, A.R. Pries, Structural adaptation of normal and tumour vascular networks, *Basic Clin. Pharmacol. Toxicol.* 110 (2011) 63–69.
- [354] A.S. Kholodov, A.V. Evdokimov, S.S. Simakov, Y.A. Kholodov, Matter transport simulations using 2D model of peripheral circulation coupled with the model of large vessels, in: H. Rodrigues, et al. (Eds.), *Proceedings of II International Conference on Computational Bioengineering*, vol. 1, IST Press, 2005, pp. 479–490.
- [355] X. Ge, Z. Yin, Y. Fan, Y. Vassilevski, F. Liang, A multi-scale model of the coronary circulation applied to investigate transmural myocardial flow, *Int. J. Numer. Methods Biomed. Eng.* 34 (2018) e3123.
- [356] M. Peyrounette, Y. Davit, M. Quintard, S. Lorthois, Multiscale modelling of blood flow in cerebral microcirculation: details at capillary scale control accuracy at the level of the cortex, *PLoS One* 13 (2018) e0189474.
- [357] S.L. Waters, J. Alastrauey, D.A. Beard, P.H. Bovendeerd, P.F. Davies, G. Jayaraman, et al., Theoretical models for coronary vascular biomechanics: progress & challenges, *Prog. Biophys. Mol. Biol.* 104 (2011) 49–76.
- [358] E.K. Erbertseder, J. Reichold, B. Flemisch, P. Jenny, R. Helmig, A coupled discrete/continuum model for describing cancer-therapeutic transport in the lung, *PLoS One* 7 (2012) e31966.
- [359] J.W. Prothero, A.C. Burton, The physics of blood flow in capillaries. I. The nature of the motion, *Biophys. J.* 1 (1961) 565–579.

- [360] J.W. Prothero, A.C. Burton, The physics of blood flow in capillaries. II. The capillary resistance to flow, *Biophys. J.* 2 (1962) 199–212.
- [361] J.W. Prothero, A.C. Burton, The physics of blood flow in capillaries. III. The pressure required to deform erythrocytes in acid-citrate-dextrose, *Biophys. J.* 2 (1962) 213–222.
- [362] M.M. Guest, T.P. Bond, G. Cooper, J.R. Derrick, Red blood cells: change in shape in capillaries, *Science* 142 (3597) (1963) 1319–1321.
- [363] R.D. Kamm, Cellular fluid mechanics, *Annu. Rev. Fluid Mech.* 34 (1) (2002) 211–232.
- [364] T.W. Secomb, Blood flow in the microcirculation, *Annu. Rev. Fluid Mech.* 49 (2017) 443–461.
- [365] A.C.L. Barnard, L. Lopez, J.D. Hellmus, Basic theory of blood flow in capillaries, *Microvasc. Res.* 1 (1968) 23–34.
- [366] W. Dzwinek, K. Boryczko, D.A. Yuen, A discrete-particle model of blood dynamics in capillary vessels, *J. Colloid Interface Sci.* 258 (1) (2003) 163–173.
- [367] K.L. Lin, L. Lopez, J.D. Hellmus, Blood flow in capillaries, *Microvasc. Res.* 5 (7–19) (1973).
- [368] T.W. Secomb, B. Styp-Rekowska, A.R. Pries, Two-dimensional simulation of red blood cell deformation and lateral migration in microvessels, *Ann. Biomed. Eng.* 35 (5) (2007) 755–765.
- [369] K. Tsubota, S. Wada, H. Liu, Elastic behavior of a red blood cell with the membranes nonuniform natural state: equilibrium shape, motion transition under shear flow, and elongation during tank-treading motion, *Biomech. Model. Mechanobiol.* 13 (4) (2014) 735–746.
- [370] K. Tsubota, S. Wada, T. Yamaguchi, Particle method for computer simulation of red blood cell motion in blood flow, *Comput. Methods Progr. Biomed.* 83 (2) (2006) 139–146.
- [371] K. Vahidkhah, P. Balogh, P. Bagchi, Flow of red blood cells in stenosed microvessels, *Sci. Rep.* 6 (28194) (2016).
- [372] T. Wang, Z. Xing, Characterization of blood flow in capillaries by numerical simulation, *J. Mod. Phys.* 1 (2010) 349–356.
- [373] A.R. Pries, T.W. Secomb, P. Gaehtgens, J.F. Gross, Blood flow in microvascular networks. Experiments and simulation, *Circ. Res.* 67 (1990) 826–834.
- [374] A.R. Pries, D. Neuhaus, P. Gaehtgens, Blood viscosity in tube flow: dependence on diameter and hematocrit, *Am. J. Physiol.* 263 (1992) H1770–H1778.
- [375] A.R. Pries, T.W. Secomb, Microvascular blood viscosity in vivo and the endothelial surface layer, *Am. J. Physiol. Heart Circ. Physiol.* 289 (2005) H2657–H2664.
- [376] A.R. Pries, T.W. Secomb, T. Gessner, M.B. Sperandio, J.F. Gross, P. Gaehtgens, Resistance to blood flow in microvessels in vivo, *Circ. Res.* 75 (1994) 904–915.
- [377] B.C. Fry, J. Lee, N.P. Smith, T.W. Secomb, Estimation of blood flow rates in large microvascular networks, *Microcirculation* 19 (6) (2012) 530–538.
- [378] P.M. Rasmussen, T.W. Secomb, A.R. Pries, Modeling the hematocrit distribution in microcirculatory networks: a quantitative evaluation of a phase separation model, *Microcirculation* 25 (2018) e12445.
- [379] R.J. Person, R. Thies, R.C. Beesley, S. Benyajati, R.W. Blair, K.J. Dormer, J.P. Farber, R.D. Foreman, O.R. Kling, P.A. McHale, et al., *Physiology, Oklahoma Notes*, Springer, New York, 2012.
- [380] M.B. Kuznetsov, A.V. Kolobov, Transient alleviation of tumor hypoxia during first days of antiangiogenic therapy as a result of therapy-induced alterations in nutrient supply and tumor metabolism – analysis by mathematical modeling, *J. Theor. Biol.* 451 (2018) 86–100.
- [381] M.F. Milosevic, A.W. Fyles, R.P. Hill, The relationship between elevated interstitial fluid pressure and blood flow in tumors: a bioengineering analysis, *Int. J. Radiat. Oncol. Biol. Phys.* 43 (5) (1999) 1111–1123.
- [382] R. Ansiaux, C. Baudelot, B.F. Jordan, B. Nelson, P. Sonveaux, J. De Wever, P. Martinive, V. Grégoire, F. Olivier, B. Gallez, Thalidomide radiosensitizes tumors through early changes in the tumor microenvironment, *Clin. Cancer Res.* 11 (2) (2005) 743–750.
- [383] R.P.M. Dings, M. Loren, H. Hanke, E. McNeil, A. W Griffioen, K.H. Mayo, R.J. Griffin, Scheduling of radiation with angiogenesis inhibitors anginex and avastin improves therapeutic outcome via vessel normalization, *Clin. Cancer Res.* 13 (11) (2007) 3395–3402.

- [384] M. Franco, S. Man, L. Chen, U. Emmenegger, Y. Shaked, A.M. Cheung, A.S. Brown, D.J. Hicklin, F.S. Foster, R.S. Kerbel, Targeted anti-vascular endothelial growth factor receptor-2 therapy leads to short-term and long-term impairment of vascular function and increase in tumor hypoxia, *Cancer Res.* 66 (7) (2006) 3639–3648.
- [385] K.J. Williams, B.A. Telfer, S. Brave, Jane Kendrew, L. Whittaker, I.J. Stratford, R.W. Stephen, Zd6474, a potent inhibitor of vascular endothelial growth factor signaling, combined with radiotherapy, *Clin. Cancer Res.* 10 (24) (2004) 8587–8593.
- [386] H. Wildiers, G. Guetens, G. De Boeck, E. Verbeken, B. Landuyt, W. Landuyt, E.A. De Brujin, A.T. Van Oosterom, Effect of antivascular endothelial growth factor treatment on the intratumoral uptake of CPT-11, *Br. J. Cancer* 88 (12) (2003) 1979.
- [387] L.T. Baxter, R.K. Jain, Transport of fluid and macromolecules in tumors. I. Role of interstitial pressure and convection, *Microvasc. Res.* 37 (1) (1989) 77–104.
- [388] S.M. Bair, T.K. Choueiri, J. Moslehi, Cardiovascular complications associated with novel angiogenesis inhibitors: emerging evidence and evolving perspectives, *Trends Cardiovasc. Med.* 23 (4) (2013) 104–113.
- [389] J.R. Less, M.C. Posner, Y. Boucher, D. Borochovitz, W. Norman, R.K. Jain, Interstitial hypertension in human breast and colorectal tumors, *Cancer Res.* 52 (22) (1992) 6371–6374.
- [390] T. Stylianopoulos, J.D. Martin, M. Snuderl, F. Mpekris, S.R. Jain, R.K. Jain, Co-evolution of solid stress and interstitial fluid pressure in tumors during progression: implications for vascular collapse, *Cancer Res.* 73 (13) (2013) 3833–3841.
- [391] T. Alarcón, H.M. Byrne, P.K. Maini, A cellular automaton model for tumour growth in inhomogeneous environment, *J. Theor. Biol.* 225 (2) (2003) 257–274.
- [392] M.R. Owen, T. Alarcón, P.K. Maini, H.M. Byrne, Angiogenesis and vascular remodelling in normal and cancerous tissues, *J. Math. Biol.* 58 (4–5) (2009) 689.
- [393] A.R.A. Anderson, M.A.J. Chaplain, Continuous and discrete mathematical models of tumor-induced angiogenesis, *Bull. Math. Biol.* 60 (5) (1998) 857–899.
- [394] S.R. McDougall, A.R.A. Anderson, M.A.J. Chaplain, Mathematical modelling of dynamic adaptive tumour-induced angiogenesis: clinical implications and therapeutic targeting strategies, *J. Theor. Biol.* 241 (3) (2006) 564–589.
- [395] H. Perfahl, H.M. Byrne, T. Chen, V. Estrella, T. Alarcón, A. Lapin, R.A. Gatenby, R.J. Gillies, M.C. Lloyd, P.K. Maini, et al., Multiscale modelling of vascular tumour growth in 3D: the roles of domain size and boundary conditions, *PLoS One* 6 (4) (2011) e14790.
- [396] D. Drasdo, N. Jagiella, I. Ramis-Conde, I. Vignon-Clementel, W. Weens, Modeling steps from a benign tumor to an invasive cancer: examples of intrinsically multi-scale problems, in: *Cell Mechanics: From Single Scale-Based Models to Multiscale Modeling*, Chapman & Hall/CRC, 2010, pp. 379–417.
- [397] J.L. Gevertz, S. Torquato, Modeling the effects of vasculature evolution on early brain tumor growth, *J. Theor. Biol.* 243 (4) (2006) 517–531.
- [398] M. Hazewinkel, Spline Interpolation. Encyclopedia of Mathematics, vol. 1, 2001.
- [399] W.E.L. Brown, A.V. Hill, The oxygen-dissociation curve of blood, and its thermodynamical basis, *Proc. R. Soc. Lond. Ser. B Contain. Pap. Biol. Character* 94 (661) (1923) 297–334.
- [400] J.C.L. Alfonso, A. Köhn-Luque, T. Stylianopoulos, F. Feuerhake, A. Deutsch, H. Hatzikirou, Why one-size-fits-all vaso-modulatory interventions fail to control glioma invasion: in silico insights, *Sci. Rep.* 6 (2016) 37283.
- [401] H.M. Byrne, M.R. Owen, Tomas Alarcon, J. Murphy, P.K. Maini, Modelling the response of vascular tumours to chemotherapy: a multiscale approach, *Math. Model. Methods Appl. Sci.* 16 (Suppl. 1) (2006) 1219–1241.
- [402] D.G. Gognieva, T.M. Gamilov, R.A. Pryamonskov, F.Y. Kopylov, S.S. Simakov, Y.V. Vassilevski, et al., Noninvasive assessment of the fractional reserve of coronary blood flow with a one-dimensional mathematical model. Preliminary results of the pilot study, *Russ. J. Cardiol.* 24 (3) (2019) 60–68.
- [403] X. Ge, F. Liang, Y. Vassilevski, S. Simakov, Sensitivity of coronary flow reserve to cardiovascular parameters: a computational model-based study, in: *2018 IEEE EMBS Conference on Biomedical Engineering and Sciences, IECBES 2018 - Proceedings*, 2019, pp. 32–35.

- [404] D.G. Gognieva, A.L. Syrkin, Y.V. Vassilevski, S.S. Simakov, A.V. Melerzanov, F. Liang, A.A. Lomonosova, A.A. Bykova, H.E. El Manaa, P.Y. Kopylov, Noninvasive assessment of fractional flow reserve using mathematical modeling of coronary flow, *Kardiologiya* 58 (12) (2018) 85–92.
- [405] T. Gamilov, P. Kopylov, S. Simakov, Computational simulations of fractional flow reserve variability, in: Numerical Mathematics and Advanced Applications - ENUMATH 2015, Lecture Notes in Computational Science and Engineering, vol. 112, 2016, pp. 499–508.
- [406] F.Y. Kopylov, A.A. Bykova, Y.V. Vasilevsky, S.S. Simakov, Role of measurement of fractional flow reserve in coronary artery atherosclerosis, *Ter. Arkhiv* 87 (9) (2015) 106–113.
- [407] T.M. Gamilov, R.A. Pryamonosov, S.S. Simakov, Modeling of patient-specific cases of atherosclerosis in carotid arteries, in: Proceedings of the VII European Congress on Computational Methods in Applied Sciences and Engineering, ECCOMAS Congress 2016, Crete, Greece, 5–10 June, vol. 1, 2016, pp. 79–89.
- [408] F.Y. Kopylov, A.A. Bykova, D.Y. Shchekochikhin, K.E. El Manaa, A.N. Dzyundzya, Y.V. Vasilevsky, S.S. Simakov, Asymptomatic atherosclerosis of the brachiocephalic arteries: current approaches to diagnosis and treatment, *Ter. Arkhiv* 89 (4) (2017) 95–100.
- [409] D. Zheng, A. Murray, Non-invasive quantification of peripheral arterial volume distensibility and its non-linear relationship with arterial pressure, *J. Biomech.* 42 (8) (2009) 1032–1037.
- [410] I. Ozolanta, et al., Changes in the mechanical properties, biochemical contents and wall structure of the human coronary arteries with age and sex, *Med. Eng. Phys.* 20 (7) (1998) 523–533.
- [411] J. Sugawara, K. Hayashi, T. Yokoi, H. Tanaka, Carotid-femoral pulse wave velocity: impact of different arterial path length measurements, *Artery Res.* 4 (1) (2010) 27–31.
- [412] S. Millasseau, A.D. Stewart, S.J. Patel, S.R. Redwood, P.J. Chowienczyk, Evaluation of carotid-femoral pulse wave velocity: influence of timing algorithm and heart rate, *Hypertension* 45 (2005) 222–226.
- [413] R. Sala, C. Rossel, P. Encinas, P. Lahiguera, Continuum of pulse wave velocity from young elite athletes to uncontrolled older patients with resistant hypertension, *J. Hypertens.* 28 (2010), pp. 19.216.
- [414] J. Aguado-Sierra, K.H. Parker, J.E. Davies, D. Francis, A.D. Hughes, J. Mayet, Arterial pulse wave velocity in coronary arteries, in: Proceedings of the 28th IEEE EMBS Annual International Conference, New York City, USA, Aug 30–Sept 3, 2006, pp. 867–870.
- [415] E.S.J. Krner, H.J. Lamb, H.-M.J. Siebelink, S.C. Cannegieter, P.J. Van Den Boogaard, E.E. Van Der Wall, A. De Roos, J.J.M. Westenberg, Pulse wave velocity and flow in the carotid artery versus the aortic arch: effects of aging, *J. Magn. Reson. Imaging* 40 (2) (2014) 287–293.
- [416] T. Otsuki, S. Maeda, M. Iemitsu, Y. Saito, Y. Tanimura, R. Ajisaka, T. Miyauchi, Relationship between arterial stiffness and athletic training programs in young adult men, *Am. J. Hypertens.* 16 (2003) 168–174.
- [417] E.J. Kim, C.G. Park, J.S. Park, S.Y. Suh, C.U. Choi, J.W. Kim, S.H. Kim, H.E. Lim, S.W. Rha, H.S. Seo, D.J. Oh, Relationship between blood pressure parameters and pulse wave velocity in normotensive and hypertensive subjects: invasive study, *J. Hum. Hypertens.* 21 (2) (2007) 141–148.
- [418] A. Mahmud, J. Feely, Effect of smoking on arterial stiffness and pulse pressure amplification, *Hypertension* 41 (1) (2003) 183–187.
- [419] A. Tajaddini, et al., Impact of age and hyperglycemia on the mechanical behavior of intact human coronary arteries: an *ex vivo* intravascular ultrasound study, *Am. J. Physiol. Heart Circ. Physiol.* 288 (1) (2005) 250–255.
- [420] C. Velican, D. Velican, Progression of coronary atherosclerosis from adolescents to mature adults, *Atherosclerosis* 47 (2) (1983) 131–144.
- [421] T. Länne, et al., Increased arterial stiffness in women, but not in men, with IDDM, *Diabetologia* 38 (9) (1995) 1082–1089.
- [422] K. Devault, P.A. Gremaud, M.S. Olufsen, V. Novak, P. Zhao, G. Vernires, Blood flow in the circle of Willis: modeling and calibration, *Multiscale Model. Simul.* 7 (2) (2008) 888–909.
- [423] V. Ganz, A. Hlavova, A. Fronek, J. Linhart, I. Prerovsky, Measurement of blood flow in the femoral artery in man at rest and during exercise by local thermodilution, *Circulation* 30 (1964) 86–89.

- [424] Y. Vassilevski, T. Gamilov, P. Kopylov, Personalized computation of fractional flow reserve in case of two consecutive stenoses, in: Proceedings of the VII European Congress on Computational Methods in Applied Sciences and Engineering, ECCOMAS Congress 2016, Crete, Greece, 5–10 June, vol. 1, 2016, pp. 90–97.
- [425] M. Gottsauner-Wolf, H. Sochor, D. Moertl, M. Gwechenberger, F. Stockenhuber, P. Probst, Assessing coronary stenosis, *Eur. Heart J.* 17 (9) (1996) 1167–1174.
- [426] L. Page, B. Riegel, S.B.K. Kern III, et al., ACC/AHA/SCAI 2005 guideline update for percutaneous coronary intervention: a report of the American College of Cardiology/American Heart Association task force on practice guidelines, *J. Am. Coll. Cardiol.* 47 (1) (2006) e1–e121.
- [427] Y. Adiputra, S.-L. Chen, Clinical relevance of coronary fractional flow reserve: art-of-state, *Chin. Med. J.* 128 (10) (2015) 1399–1406.
- [428] T.K. Zarins, C.A. Taylor, J.K. Min, Computed fractional flow reserve (FFCT) derived from coronary CT angiography, *J. Cardiovasc. Transl. Res.* 6 (5) (2013) 708–714.
- [429] P.D. Morris, D. Ryan, A.C. Morton, R. Lycett, P.V. Lawford, D.R. Hose, J.P. Gunn, Virtual fractional flow reserve from coronary angiography: modeling the significance of coronary lesions. Results from the VIRTU-1 (virtual fractional flow reserve from coronary angiography) study, *JACC Cardiovasc. Interv.* 6 (2) (2013) 149–157.
- [430] E.S. Bernad, S.I. Bernad, M.L. Craina, Hemodynamic parameters measurements to assess severity of serial lesions in patient specific right coronary artery, *Bio Med. Mater. Eng.* 24 (1) (2014) 323–334.
- [431] C.A. Taylor, T.A. Fonte, J.K. Min, Computational fluid dynamics applied to cardiac computed tomography for noninvasive quantification of fractional flow reserve: scientific basis, *J. Am. Coll. Cardiol.* 61 (22) (2013) 2233–2241.
- [432] J.-M. Zhang, T. Luo, S.Y. Tan, A.M. Lomarda, A.S.L. Wong, F.Y.J. Keng, J.C. Allen, Y. Huo, B. Su, X. Zhao, M. Wan, G.S. Kassab, R.S. Tan, L. Zhong, Hemodynamic analysis of patient-specific coronary artery tree, *Int. J. Numer. Methods Biomed. Eng.* 31 (4) (2015) e02708.
- [433] HeartFlow, HeartFlow-FFRct-analysis. <https://www.heartflow.com/heartflow-ffrct-analysis/>.
- [434] R. Rajani, Y. Wang, A. Uss, D. Perera, S. Redwood, M. Thomas, J.B. Chambers, R. Preston, G.S. Carr-White, P. Liatsis, Virtual fractional flow reserve by coronary computed tomography - hope or hype? *EuroIntervention* 9 (2) (2013) 277–284.
- [435] A. Coenen, Y.-H. Kim, M. Kruk, et al., Diagnostic accuracy of a machine-learning approach to coronary computed tomographic angiography-based fractional flow reserve, *Circulation* 11 (2018) e007217.
- [436] E. Boileau, P. Nithiarasu, One-dimensional modelling of the coronary circulation. Application to noninvasive quantification of fractional flow reserve (FFR), in: J.M.R.S. Tavares, R.N. Jorge (Eds.), *Computational and Experimental Biomedical Sciences: Methods and Applications*, Volume 21 of LN Comput. Vis. Biomech., Springer International, 2015, pp. 137–155.
- [437] B. De Bruyne, N.H.J. Pijsls, G.R. Heyndrickx, D. Hodeige, R. Kirkeeide, K.L. Gould, Pressure-derived fractional flow reserve to assess serial epicardial stenoses: theoretical basis and animal validation, *Circulation* 15 (2000) 1840–1847.
- [438] N. Prasad, P. Chhetri, A. Poudel, Normal variants of the circle of Willis in patients undergoing CT angiography, *J. Coll. Med. Sci. Nepal* 13 (1) (2017) 190–192.
- [439] Laboratory of Medical Computer Systems and Gammamed Co., Picture Archiving and Communication System “Gamma Multivox”. <https://multivox.ru/>.
- [440] Y. Lazebnik, What are the hallmarks of cancer? *Nat. Rev. Cancer* 10 (4) (2010) 232.
- [441] C. Sonnenschein, A.M. Soto, The aging of the 2000 and 2011 hallmarks of cancer reviews: a critique, *J. Biosci.* 38 (3) (2013) 651–663.
- [442] G. Steel, Species-dependent growth patterns for mammalian neoplasms, *Cell Prolif.* 13 (4) (1980) 451–453.
- [443] H. Schmidt, W. Siems, M. Müller, R. Dumdey, S.M. Rapoport, ATP-producing and consuming processes of Ehrlich mouse ascites tumor cells in proliferating and resting phases, *Exp. Cell Res.* 194 (1) (1991) 122–127.
- [444] J. Freyer, E. Tustanoff, A. Franko, R. Sutherland, *In situ* oxygen consumption rates of cells in V-79 multicellular spheroids during growth, *J. Cell. Physiol.* 118 (1) (1984) 53–61.

- [445] R.K. Jain, N.S. Forbes, Can engineered bacteria help control cancer? *Proc. Natl. Acad. Sci. U.S.A.* 98 (26) (2001) 14748–14750.
- [446] S. Doblas, T. He, D. Saunders, J. Pearson, J. Hoyle, N. Smith, M. Lerner, R.A. Towner, Glioma morphology and tumor-induced vascular alterations revealed in seven rodent glioma models by *in vivo* magnetic resonance imaging and angiography, *J. Magn. Reson. Imaging* 32 (2) (2010) 267–275.
- [447] S.M. Weis, D.A. Cheresh, Tumor angiogenesis: molecular pathways and therapeutic targets, *Nat. Med.* 17 (11) (2011) 1359.
- [448] J. Folkman, Tumor angiogenesis: therapeutic implications, *N. Engl. J. Med.* 285 (21) (1971) 1182–1186.
- [449] J.M. Ebos, R.S. Kerbel, Antiangiogenic therapy: impact on invasion, disease progression, and metastasis, *Nat. Rev. Clin. Oncol.* 8 (4) (2011) 210–221.
- [450] I. Genentech, Highlights of Prescribing Information, 2017. [https://www.gene.com/download/pdf/avastin\\_prescribing.pdf](https://www.gene.com/download/pdf/avastin_prescribing.pdf).
- [451] J. Ma, S. Pulfer, S. Li, J. Chu, K. Reed, J.M. Gallo, Pharmacodynamic-mediated reduction of temozolomide tumor concentrations by the angiogenesis inhibitor TNP-470, *Cancer Res.* 61 (14) (2001) 5491–5498.
- [452] A. Claes, P. Wesseling, J. Jeuken, C. Maass, A. Heerschap, W.P. Leenders, Antiangiogenic compounds interfere with chemotherapy of brain tumors due to vessel normalization, *Mol. Cancer Ther.* 7 (1) (2008) 71–78.
- [453] W.V. Mayneord, On a law of growth of Jensen's rat sarcoma, *Am. J. Cancer* 16 (4) (1932) 841–846.
- [454] A.K. Laird, Dynamics of tumour growth, *Br. J. Cancer* 18 (3) (1964) 490.
- [455] T.D. Gaddy, Q. Wu, A.D. Arnhem, S.D. Finley, Mechanistic modeling quantifies the influence of tumor growth kinetics on the response to anti-angiogenic treatment, *PLoS Comput. Biol.* 13 (12) (2017) e1005874.
- [456] A.C. Burton, Rate of growth of solid tumours as a problem of diffusion, *Growth* 30 (2) (1966) 157–176.
- [457] H. Greenspan, Models for the growth of a solid tumor by diffusion, *Stud. Appl. Math.* 51 (4) (1972) 317–340.
- [458] P. Tracqui, From passive diffusion to active cellular migration in mathematical models of tumour invasion, *Acta Biotheor.* 43 (4) (1995) 443–464.
- [459] K. Swanson, E. Alvord Jr., J. Murray, Virtual resection of gliomas: effect of extent of resection on recurrence, *Math. Comput. Model.* 37 (11) (2003) 1177–1190.
- [460] H. Byrne, M.A. Chaplain, Free boundary value problems associated with the growth and development of multicellular spheroids, *Eur. J. Appl. Math.* 8 (6) (1997) 639–658.
- [461] A. Kolobov, A. Polezhaev, G. Solyanik, The role of cell motility in metastatic cell dominance phenomenon: analysis by a mathematical model, *Comput. Math. Methods Med.* 3 (1) (2000) 63–77.
- [462] K.R. Swanson, R.C. Rockne, J. Claridge, M.A. Chaplain, E.C. Alvord, A.R. Anderson, Quantifying the role of angiogenesis in malignant progression of gliomas: *in silico* modeling integrates imaging and histology, *Cancer Res.* 71 (24) (2011) 7366–7375.
- [463] P. Macklin, S. McDougall, A.R. Anderson, M.A. Chaplain, V. Cristini, J. Lowengrub, Multiscale modelling and nonlinear simulation of vascular tumour growth, *J. Math. Biol.* 58 (4–5) (2009) 765–798.
- [464] S. Sanga, J.P. Sinek, H.B. Frieboes, M. Ferrari, J.P. Fruehauf, V. Cristini, Mathematical modeling of cancer progression and response to chemotherapy, *Expert Rev. Anticancer Ther.* 6 (10) (2006) 1361–1376.
- [465] A. Swierniak, M. Kimmel, J. Smieja, Mathematical modeling as a tool for planning anticancer therapy, *Eur. J. Pharmacol.* 625 (1–3) (2009) 108–121.
- [466] R. Rockne, J. Rockhill, M. Mrugala, A. Spence, I. Kalet, K. Hendrickson, A. Lai, T. Cloughesy, E. Alvord Jr., K. Swanson, Predicting the efficacy of radiotherapy in individual glioblastoma patients *in vivo*: a mathematical modeling approach, *Phys. Med. Biol.* 55 (12) (2010) 3271.
- [467] S. Benzekry, G. Chapuisat, J. Ciccolini, A. Erlinger, F. Hubert, A new mathematical model for optimizing the combination between antiangiogenic and cytotoxic drugs in oncology, *Compt. Rendus Math.* 350 (1–2) (2012) 23–28.

- [468] R. Grossman, H. Brastianos, J.O. Blakeley, A. Mangraviti, B. Lal, P. Zadnik, L. Hwang, R.T. Wicks, R.C. Goodwin, H. Brem, et al., Combination of anti-VEGF therapy and temozolomide in two experimental human glioma models, *J. Neurooncol.* 116 (1) (2014) 59–65.
- [469] A.W. El-Kareh, T.W. Secomb, A theoretical model for intraperitoneal delivery of cisplatin and the effect of hyperthermia on drug penetration distance, *Neoplasia* 6 (2) (2004) 117–127.
- [470] Y. Miyagi, K. Fujiwara, J. Kigawa, H. Itamochi, S. Nagao, E. Aotani, N. Terakawa, I. Kohno, Intraperitoneal carboplatin infusion may be a pharmacologically more reasonable route than intravenous administration as a systemic chemotherapy. A comparative pharmacokinetic analysis of platinum using a new mathematical model after intraperitoneal vs. intravenous infusion of carboplatin – A Sankai Gynecology Study Group (SGSG) study, *Gynecol. Oncol.* 99 (3) (2005) 591–596.
- [471] P.G. Corrie, Cytotoxic chemotherapy: clinical aspects, *Medicine* 36 (1) (2008) 24–28.
- [472] J. Chen, B. Liu, J. Yuan, J. Yang, J. Zhang, Y. An, L. Tie, Y. Pan, X. Li, Atorvastatin reduces vascular endothelial growth factor (VEGF) expression in human non-small cell lung carcinomas (NSCLCS) via inhibition of reactive oxygen species (ROS) production, *Mol. Oncol.* 6 (1) (2012) 62–72.
- [473] A.V. Kolobov, V.V. Gubernov, M.B. Kuznetsov, The study of antitumor efficacy of bevacizumab antiangiogenic therapy using a mathematical model, *Russ. J. Numer. Anal. Math. Model.* 30 (5) (2015) 289–298.
- [474] A. Giese, R. Bjerkvig, M. Berens, M. Westphal, Cost of migration: invasion of malignant gliomas and implications for treatment, *J. Clin. Oncol.* 21 (8) (2003) 1624–1636.
- [475] O. Pyaskovskaya, D. Kolesnik, A. Kolobov, S. Vovyanko, G. Solyanik, Analysis of growth kinetics and proliferative heterogeneity of Lewis lung carcinoma cells growing as unfed culture, *Exp. Oncol.* 30 (4) (2008) 269–275.
- [476] H. Byrne, D. Drasdo, Individual-based and continuum models of growing cell populations: a comparison, *J. Math. Biol.* 58 (4–5) (2009) 657.
- [477] M.G. Vander Heiden, L.C. Cantley, C.B. Thompson, Understanding the Warburg effect: the metabolic requirements of cell proliferation, *Science* 324 (5930) (2009) 1029–1033.
- [478] H. Suahimi, D.B. Das, Glucose diffusivity in cell-seeded tissue engineering scaffolds, *Biotechnol. Lett.* 38 (1) (2016) 183–190.
- [479] J.P. Rock, L. Scarpace, D. Hearshen, J. Gutierrez, J.L. Fisher, M. Rosenblum, T. Mikkelsen, Associations among magnetic resonance spectroscopy, apparent diffusion coefficients, and image-guided histopathology with special attention to radiation necrosis, *Neurosurgery* 54 (5) (2004) 1111–1119.
- [480] D. Shweiki, M. Neeman, A. Itin, E. Keshet, Induction of vascular endothelial growth factor expression by hypoxia and by glucose deficiency in multicell spheroids: implications for tumor angiogenesis, *Proc. Natl. Acad. Sci. U.S.A.* 92 (3) (1995) 768–772.
- [481] J. Freyer, R. Sutherland, A reduction in the in situ rates of oxygen and glucose consumption of cells in EMT6/Ro spheroids during growth, *J. Cell. Physiol.* 124 (3) (1985) 516–524.
- [482] K. Izuishi, K. Kato, T. Ogura, T. Kinoshita, H. Esumi, Remarkable tolerance of tumor cells to nutrient deprivation: possible new biochemical target for cancer therapy, *Cancer Res.* 60 (21) (2000) 6201–6207.
- [483] American Diabetes Association, et al., Screening for type 2 diabetes, *Diabetes Care* 27 (Suppl. 1) (2004) s11–s14.
- [484] P.G. Baker, R. Mottram, Metabolism of exercising and resting human skeletal muscle, in the post-prandial and fasting states, *Clin. Sci.* 44 (5) (1973) 479–491.
- [485] J. Casciari, S. Sotirchos, R. Sutherland, Mathematical modelling of microenvironment and growth in EMT6/Ro multicellular tumour spheroids, *Cell Prolif.* 25 (1) (1992) 1–22.
- [486] V. Tuchin, A. Bashkatov, E. Genina, Y.P. Sinichkin, N. Lakodina, *In vivo* investigation of the immersion-liquid-induced human skin clearing dynamics, *Tech. Phys. Lett.* 27 (6) (2001) 489–490.
- [487] J.M. Kelm, C.D. Sanchez-Bustamante, E. Ehler, S.P. Hoerstrup, V. Djonov, L. Ittner, M. Fussenegger, VEGF profiling and angiogenesis in human microtissues, *J. Biotechnol.* 118 (2) (2005) 213–229.
- [488] F. Mac Gabhann, A.S. Popel, Interactions of VEGF isoforms with VEGFR-1, VEGFR-2, and neuropilin *in vivo*: a computational model of human skeletal muscle, *Am. J. Physiol. Heart Circ. Physiol.* 292 (1) (2007) H459–H474.

- [489] A. Köhn-Luque, W. De Back, Y. Yamaguchi, K. Yoshimura, M. Herrero, T. Miura, Dynamics of VEGF matrix-retention in vascular network patterning, *Phys. Biol.* 10 (6) (2013) 066007.
- [490] N. Papadopoulos, J. Martin, Q. Ruan, A. Rafique, M.P. Rosconi, E. Shi, E.A. Pyles, G.D. Yancopoulos, N. Stahl, S.J. Wiegand, Binding and neutralization of vascular endothelial growth factor (VEGF) and related ligands by VEGF trap, ranibizumab and bevacizumab, *Angiogenesis* 15 (2) (2012) 171–185.
- [491] D. Zemlickis, J. Klein, G. Moselhy, G. Koren, Cisplatin protein binding in pregnancy and the neonatal period, *Pediatr. Blood Cancer* 23 (6) (1994) 476–479.
- [492] P. Van de Vaart, N. Van der Vange, F. Zoetmulder, A. Van Goethem, O. Van Tellingen, W. ten Bokkel Huinink, J. Beijnen, H. Bartelink, A. Begg, Intraperitoneal cisplatin with regional hyperthermia in advanced ovarian cancer: pharmacokinetics and cisplatin–DNA adduct formation in patients and ovarian cancer cell lines, *Eur. J. Cancer* 34 (1) (1998) 148–154.
- [493] P.V. Dickson, J.B. Hamner, T.L. Sims, C.H. Fraga, C.Y. Ng, S. Rajasekeran, N.L. Hagedorn, M.B. McCarville, C.F. Stewart, A.M. Davidoff, Bevacizumab-induced transient remodeling of the vasculature in neuroblastoma xenografts results in improved delivery and efficacy of systemically administered chemotherapy, *Clin. Cancer Res.* 13 (13) (2007) 3942–3950.
- [494] E.M. Renkin, Filtration, diffusion, and molecular sieving through porous cellulose membranes, *J. Gen. Physiol.* 38 (2) (1954) 225–243.
- [495] G. Clough, L. Smaje, Exchange area and surface properties of the microvasculature of the rabbit submandibular gland following duct ligation, *J. Physiol.* 354 (1) (1984) 445–456.
- [496] A. Bouchoux, H. Roux-de Balmann, F. Lutin, Nanofiltration of glucose and sodium lactate solutions: variations of retention between single- and mixed-solute solutions, *J. Membr. Sci.* 258 (1) (2005) 123–132.
- [497] L.M. Hirvonen, G.O. Fruhwirth, N. Srikantha, M.J. Barber, J.E. Neffendorf, K. Suhling, T.L. Jackson, Hydrodynamic radii of ranibizumab, afibbercept and bevacizumab measured by time-resolved phosphorescence anisotropy, *Pharm. Res.* 33 (2016) 2025.
- [498] D. Venturoli, B. Rippe, Ficoll and dextran vs. globular proteins as probes for testing glomerular permselectivity: effects of molecular size, shape, charge, and deformability, *Am. J. Physiol. Renal. Physiol.* 288 (4) (2005) F605–F613.
- [499] P. Carmeliet, VEGF as a key mediator of angiogenesis in cancer, *Oncology* 69 (Suppl. 3) (2005) 4–10.
- [500] H.-L. Liu, H.-W. Yang, M.-Y. Hua, K.-C. Wei, Enhanced therapeutic agent delivery through magnetic resonance imaging–monitored focused ultrasound blood-brain barrier disruption for brain tumor treatment: an overview of the current preclinical status, *Neurosurg. Focus* 32 (1) (2012) E4.
- [501] J.P. Boris, D.L. Book, Flux-corrected transport. I. SHASTA, a fluid transport algorithm that works, *J. Comput. Phys.* 11 (1) (1973) 38–69.
- [502] M.M. Mrugala, Advances and challenges in the treatment of glioblastoma: a clinicians perspective, *Discov. Med.* 15 (83) (2013) 221–230.
- [503] J. Segers, V. Di Fazio, R. Ansiaux, P. Martinive, O. Feron, P. Wallemacq, B. Gallez, Potentiation of cyclophosphamide chemotherapy using the anti-angiogenic drug thalidomide: importance of optimal scheduling to exploit the normalization window of the tumor vasculature, *Cancer Lett.* 244 (1) (2006) 129–135.
- [504] A. Hall, M. Tilby, Mechanisms of action of, and modes of resistance to, alkylating agents used in the treatment of haematological malignancies, *Blood Rev.* 6 (3) (1992) 163–173.
- [505] H. Chen, T. Luo, X. Zhao, X. Lu, Y. Huo, G.S. Kassab, Microstructural constitutive model of active coronary media, *Biomaterials* 34 (31) (2013) 7575–7583.
- [506] Y. Hollander, D. Durban, X. Lu, G.S. Kassab, Y. Lanir, Constitutive modeling of coronary arterial media – comparison of three model classes, *J. Biomech. Eng.* 133 (6) (2011), 061008.
- [507] D.P. Sokolis, Experimental investigation and constitutive modeling of the 3D histomechanical properties of vein tissue, *Biomech. Model. Mechanobiology* 12 (3) (2013) 431–451.

# **Index**

*Note:* ‘Page numbers followed by “f” indicate figures and “t” indicates tables’.

## **A**

- Added mass effect, 103
- Adenosine triphosphate (ATP), 8
- Adjacency rule, 37
- Aneurysms, 24–26, 25f
- Angiogenesis, 22
- Angiogenic capillaries, 173–174, 178–180, 180f, 182–183, 182f
- Antiangiogenic therapy (AAT), 219–220, 233–241
- Antitumor therapy
  - chemo- and antiangiogenic therapy
  - bevacizumab, 219–220, 221f, 227t–229t, 232
  - cisplatin, 220–222
  - glucose, 220–222
- governing equations, 220–227, 221f
- initial and boundary conditions, 232–233
- model parameters, 227–230, 227t–229t, 233–237, 234f
- multicellular tumor spheroids (MCTS), 217–220
- numerical scheme, 116–118, 135–140, 232–233
- permeability, 230–232
- tumor growth, 218–220, 218f, 221f, 226–227, 238
- vascular permeability factor (VPF), 218–219
- Aortic regurgitation, 122–123, 122f, 123f
- Arbitrary Lagrangian-Eulerian (ALE) formulation, 64
- Arterial regulation, 15–16

- Asynchronous myocardial stimulation effect, 156–157
- Atherosclerotic plaque, 150
- Autoregulation, 143–145

## **B**

- Bevacizumab, 219–220, 221f, 225, 227t–229t, 232–236
- Blood flow across stenosis model, 150–153
- Blood flow simulation in heart
  - finite element method, 96–98
  - heart beat reconstruction, 96
  - mathematical model, 96–98
  - patient-specific simulation of blood flow, left ventricle, 99–100
- Blood flow simulation in vessel compliant wall
  - examples, 92–95
  - fluid–structure interaction, 89–91
  - mathematical model, 88–89
  - monolithic finite element method, 89–91
  - wall shear stress (WSS), 92–94
- nondeformable walls
  - examples, 87–88
  - finite element method (FEM), 81–83
  - mathematical model, 79–81, 80f
  - numerical stability, 83–86
- Blood rheology, 19–20
- Blood vessel junctions, 132, 145–146

- Blood vessels segmentation, 42–48
- automatic segmentation of aorta, 42–44, 45f
- automatic segmentation of cerebral arteries, 46–48
- automatic segmentation of coronary arteries, 44–46

- Blood viscosity, 145–146, 173–174
- Boundary conditions, 61–63, 131–132, 137–140

## **C**

- Capillary blood flow model
  - angiogenic capillaries, 173–174, 178–180, 180f, 182–183, 182f
  - antiangiogenic therapy, 219–220, 233–236
  - oxygen concentration, 174, 184–186
- Cardiac pacing, 149f, 150, 156–159
- Cardiomyocytes, 8–9
- Cardiovascular system
  - blood elements, 6f
  - coronary artery disease (CAD), 10
  - heart pumping, 6–11
    - anatomy, 7–8, 7f
    - electrical activity, 8–10, 9f
    - infarction, 10–11
    - ischemia, 10–11
    - myocardial perfusion, 10–11
  - large vessels
    - arterial regulation, 15–16
    - pulse wave propagation and reflection, 16–17

Cardiovascular system (*Continued*)  
vascular network anatomy, 11–12, 12f  
vascular wall elasticity, 12–14, 13f, 140–143  
vascular wall structure, 12–14, 13f  
microvascular dysfunction, 10  
microvasculature, 17–22  
anatomy, 17–19, 18f  
angiogenesis, 22  
blood rheology, 19–20  
transvascular transport, 20–21  
myocardium perfusion, 6  
vascular pathologies, 22–29  
aneurysms, 24–26, 25f  
hypertension, 27–28  
hypotension, 27–28  
stenosis, 22–24, 24f  
vascular aging, 26–27  
vein thrombosis, 28–29  
Carotid and vertebral arteries, 153  
Cauchy stress tensor, 56–57  
Cisplatin, 220–222  
Compliant wall  
blood flow simulation in vessel examples, 92–95  
fluid–structure interaction, 89–91  
mathematical model, 88–89  
monolithic finite element method, 89–91  
wall shear stress (WSS), 92–94  
Computational meshes, 48–53  
1D meshes, 50–53, 53f  
dynamic 3D mesh generation, 49–50, 50f  
tetrahedral mesh generation techniques, 48–49  
Computational phantoms, 32  
Computed tomography (CT), 33  
Conservation laws, 57–59  
Continuum mechanics, 166, 170–171  
basics, 55–57  
conservation laws, 57–59

deformation gradient tensor, 58–59  
*Eulerian* description, 55–56  
*Lagrangian* description, 55–56  
partial differential equations (PDEs), 57–59  
rate-of-deformation tensor, 58–59  
Reynolds transport theorem, 57  
Stokes theorem, 57  
Coronary circulation, 156–159  
Coupled multiscale model, 181

**D**

Darcy's law, 166

Deformable bodies equations  
hyperelastic materials  
general framework, 67–70  
models, 70–72

Deformation gradient tensor, 58–59

Digital Imaging and Communications in Medicine (DICOM), 36

1D vascular hemodynamics  
applicability, 125–126  
derivation of equations, 128–132  
boundary and junction conditions, 131–132  
geometric multiscale methods, 132–135  
Navier–Stokes averaging, single vessel, 128–131, 129f  
model reduction, 125–126  
numerical methods, 135–140  
boundary conditions  
implementation, 137–140  
grid-characteristic method, 135–137  
pathologies accounting  
asynchronous myocardial stimulation effect, 156–157  
blood flow across stenosis model, 150–153  
cardiac pacing, 156–159  
coronary circulation, 156–159

enhanced external counterpulsation, 159–161, 160f, 161t  
external forces, 145–150  
friction, 145–146  
gravity force, 147–148  
internal forces, 145–150  
muscle pump, 148–150  
pacemaker position effect, 157, 158t  
tachycardia, 156–159  
tortuous vessels blood flow, 153–156, 154f–155f  
venous valves function, 146–147, 147f

**E**

Electrical activity, 8–10, 9f

Electromechanical analogy, 111–112

Energy balance, 60–61

Enhanced external counterpulsation, 159–161, 160f, 161t

*Eulerian* description, 55–56

External compression, 148–150

External forces, 145–150

**F**

Finite element method (FEM), 81–83, 96–98

Flow regimes, 64–66, 66f

Fluid–structure interaction (FSI), 89–91  
equations and energy balance, 75–78  
fluid domain motion, 74–75  
interface conditions, 73–74

Fractional flow reserve (FFR), 199–200

Frangi vesselness filter, 44–46

**G**

Gent model, 72

Geometric multiscale methods, 132–135

Glucose, 21

Green–Lagrange strain tensor, 70  
Grid-characteristic method, 135–137

**H**

Hagen–Poiseuille pressure drop condition, 132, 139  
Heart model, 113f, 116–117  
Heart pumping, 6–11  
anatomy, 7–8, 7f  
electrical activity, 8–10, 9f  
infarction, 10–11  
ischemia, 10–11  
Heart segmentation, 38–41  
dynamic images, 40–41,  
41f–44f  
heart cavities, 39, 39f  
myocardium, 39–40, 39f–40f  
Hounsfield units (HU), 35  
Hydraulic equations, 170–175  
capillary blood flow model,  
174–175  
microcirculatory flow models,  
170–172  
microvascular network flow,  
173–174  
statistical properties, 168–169,  
174–175  
Hydrodynamic radii, 232  
Hypertension, 27–28  
Hypotension, 27–28, 153,  
155–156

**I**

Image-based patient-specific models, 32  
Image modalities, 33–34  
Incompressible elastic materials, 69  
Infarction, 10–11  
Interface conditions, 73–74  
Ischemia, 10–11

**K**

Kirchhoff's law, 111–112

**L**

*Lagrangian* description, 63–64

Large vessels  
arterial regulation, 15–16  
pulse wave propagation and reflection, 16–17  
vascular network anatomy, 11–12, 12f  
vascular wall elasticity, 12–14, 13f  
vascular wall structure, 12–14, 13f  
Lumped parameter models, 109–116  
electromechanical analogy, 111–112  
lumped heart model, 112–116, 113f  
valve pathologies accounting, 118–123  
aortic regurgitation, 122–123,  
122f, 123f  
mitral valve stenosis, 120–122, 121f  
valve closing models, 118–120, 119f–120f  
vascular network coupling, 117–118

**M**

Magnetic resonance imaging (MRI), 34  
Material derivative, 56  
Medical imaging, 33–38  
basic operations, 36–38  
contrast enhancement protocols/phases, 34  
image modalities, 33–34  
voxel-based representation, 34–36

Microcirculatory flows, 170  
Microcirculatory network  
hydraulic equations, 170–175  
capillary blood flow model, 174–175  
microcirculatory flow models, 170–172  
statistical properties, 174–175  
structure  
algorithm, 166–168  
generation methods, 165–166  
statistical properties, 168–169

Microvasculature, 17–22  
anatomy, 17–19, 18f  
angiogenesis, 22  
blood rheology, 19–20  
transvascular transport, 20–21  
Mitral valve stenosis, 120–122, 121f  
Model reduction, 125–126  
Monolithic finite element method, 89–91  
Morphological operators, 38  
closing, 38  
dilation, 38  
erosion, 38  
opening, 38  
Multicellular tumor spheroids (MCTS), 217–218  
Murray's law, 165–166  
Muscle pump, 148–150  
Myocardial perfusion, 10–11  
Myocardium, 148

**N**

Navier–Stokes averaging, single vessel, 128–131, 129f  
Navier–Stokes equations  
arbitrary Lagrangian–Eulerian formulation, 64  
boundary conditions, 61–63  
energy balance, 60–61  
flow regimes, 64–66, 66f  
governing equations, 59–60  
Lagrangian coordinates, 63–64

Neo-Hookean model, 71  
Newtonian viscous fluid, 59–60  
Nondeformable walls  
blood flow simulation in vessel examples, 87–88  
finite element method, 81–83  
mathematical model, 79–81  
numerical stability, 83–86  
Non-Newtonian blood rheology models, 145–146

**O**

Oxygen concentration, 174, 184–186  
Oxygen levels, 164–165

**P**

Pacemaker position effect, 157, 158t

Patient-specific geometric modeling  
blood vessels segmentation, 42–48  
heart segmentation, 38–41

Patient-specific simulation of blood flow, left ventricle, 99–100

Poiseuille pressure drop, 132, 139, 173–174

Pressure-related diseases, 27–28

Pulse wave propagation/reflection, 16–17

**Q**

Quasi-Lagrangian coordinates, 63–64

**R**

Rate-of-deformation tensor, 58–59

Red blood cells (RBCs), 5

Reflux-provoking maneuvers, 149–150

Renkin equation, 231

Reynolds transport theorem, 57

**S**

Saint Venant–Kirchhoff model, 71

Shear stress, 56–57

Skeletonization process, 50, 52

Stenosis, 22–24, 24f

Stokes theorem, 57

**T**

Tachycardia, 156–159

Tetrahedral mesh generation techniques, 48–49

Tortuous vessels blood flow, 153–156, 154f–156f

Transvascular transport, 20–21

**V**

Valve closing models, 118–120, 119f–120f

Valve pathologies accounting, 118–123

aortic regurgitation, 122–123, 122f, 123f

mitral valve stenosis, 120–122, 121f

Vascular aging, 26–27

Vascular network, anatomy, 11–12, 12f

Vascular pathologies, 22–29

aneurysms, 24–26, 25f

hypertension, 27–28

hypotension, 27–28

stenosis, 22–24, 24f

vascular aging, 26–27

vein thrombosis, 28–29

Vascular permeability factor (VPF), 218–219

Vascular smooth muscle cells, 143–144

Vascular surgery  
cerebral arteries, 207–214

coronary arteries, 189, 192, 193f, 197–208, 199t, 214–215

decision support software, 214–215

endovascular interventions, 208

fractional flow reserve (FFR), 197–207, 199t, 201f–202f, 206f

leg artery stenting, 195–197  
parameters identification, 189–195

postsurgical flow velocities, 211–212

presurgical blood flow rates, 208–211

Willis Circle structure, 213–214, 213f

Vascular wall  
elasticity, 12–14, 13f, 140–143  
structure, 12–14, 13f

Vein thrombosis, 28–29

Venous valves function, 146–147, 147f

Voxel-based representation, 34–36

**W**

Wall shear stress (WSS), 92–94

Windkessel models, 197–198

**Y**

Yeoh model, 72

**Z**

Zero-level edges, 166–167

# PERSONALIZED COMPUTATIONAL HEMODYNAMICS

Yuri Vassilevski · Maxim Olshanskii · Sergey Simakov  
Andrey Kolobov and Alexander Danilov

*Personalized Computational Hemodynamics: Models, Methods, and Applications for Vascular Surgery and Antitumor Therapy* offers practices and advances surrounding the multiscale modeling of hemodynamics and their personalization with conventional clinical data. Focusing on three physiological disciplines, readers will learn how to derive a suitable mathematical model and personalize its parameters to account for pathologies and diseases. Written by leading experts, this book mirrors the top trends in mathematical modeling with clinical applications. In addition, this book features the major results of the "Research group in simulation of blood flow and vascular pathologies" at Marchuk Institute of Numerical Mathematics of the Russian Academy of Sciences. Two important features distinguish this book from other monographs on numerical methods for biomedical applications. First, the variety of medical disciplines targeted by the mathematical modeling and computer simulations, including cardiology, vascular neurology, and oncology. Second, for all mathematical models, the authors consider extensions and parameter tuning that account for vascular pathologies. The book:

- Examines a variety of medical disciplines targeted by mathematical modeling and computer simulation
- Discusses how the results of numerical simulations are used to support clinical decision-making
- Covers hemodynamics relating to various subject areas, including vascular surgery and oncological tumor treatments

**Yuri Vassilevski** is a professor and corresponding member of the Russian Academy of Sciences. He is the deputy director of Marchuk Institute of Numerical Mathematics of the Russian Academy of Sciences, the head of the Laboratory of mathematical modeling in medicine at Sechenov University, and the head of the Department of computational technologies and modeling in geophysics and biomathematics at the Moscow Institute of Physics and Technology.

**Maxim Olshanskii** is currently a professor of Mathematics at the University of Houston. He also holds adjunct professorships at the Department of Mathematics and Computer Science at Emory University and Sechenov University. Prior to joining the University of Houston in 2012, he worked as a professor at the Department of Mathematics and Mechanics at Lomonosov Moscow State University.

**Sergey Simakov** is the deputy chair and associated professor of the Department of computational physics at the Moscow Institute of Physics and Technology. He is also a senior researcher at the Laboratory of mathematical modelling in medicine at Sechenov University, and the Laboratory of human physiology at the Moscow Institute of Physics and Technology.

**Andrey Kolobov** is the scientific secretary of Lebedev Physical Institute of the Russian Academy of Sciences. He is also a senior scientist at the Laboratory of nonlinear dynamics and theoretical biophysics at the same institute.

**Alexander Danilov** is a senior researcher at Marchuk Institute of Numerical Mathematics of the Russian Academy of Sciences, the Laboratory of mathematical modeling in medicine at Sechenov University, and the Laboratory of human physiology at the Moscow Institute of Physics and Technology.

In 2014-2018 the authors were a part of the "Research group in simulation of blood flow and vascular pathologies" at Marchuk Institute of Numerical Mathematics of the Russian Academy of Sciences, which was supported by the Russian Science Foundation.



ACADEMIC PRESS

An imprint of Elsevier

[elsevier.com/books-and-journals](http://elsevier.com/books-and-journals)

ISBN 978-0-12-815653-7



9 780128 156537